FERMILAB-THESIS-2001-45

Scuola Normale Superiore
Anno Accademico 2000-2001

Classe di Scienze
Corso di Perfezionamento in Fisica

Tesi:

Trigger Strategies for the Measurement of CP Violation in CDF Run II

Candidato:
Alessandro Cerri

Relatore:
Chiar.mo Prof.
Luciano Ristori

Per nonno Goffredo

Roadmap

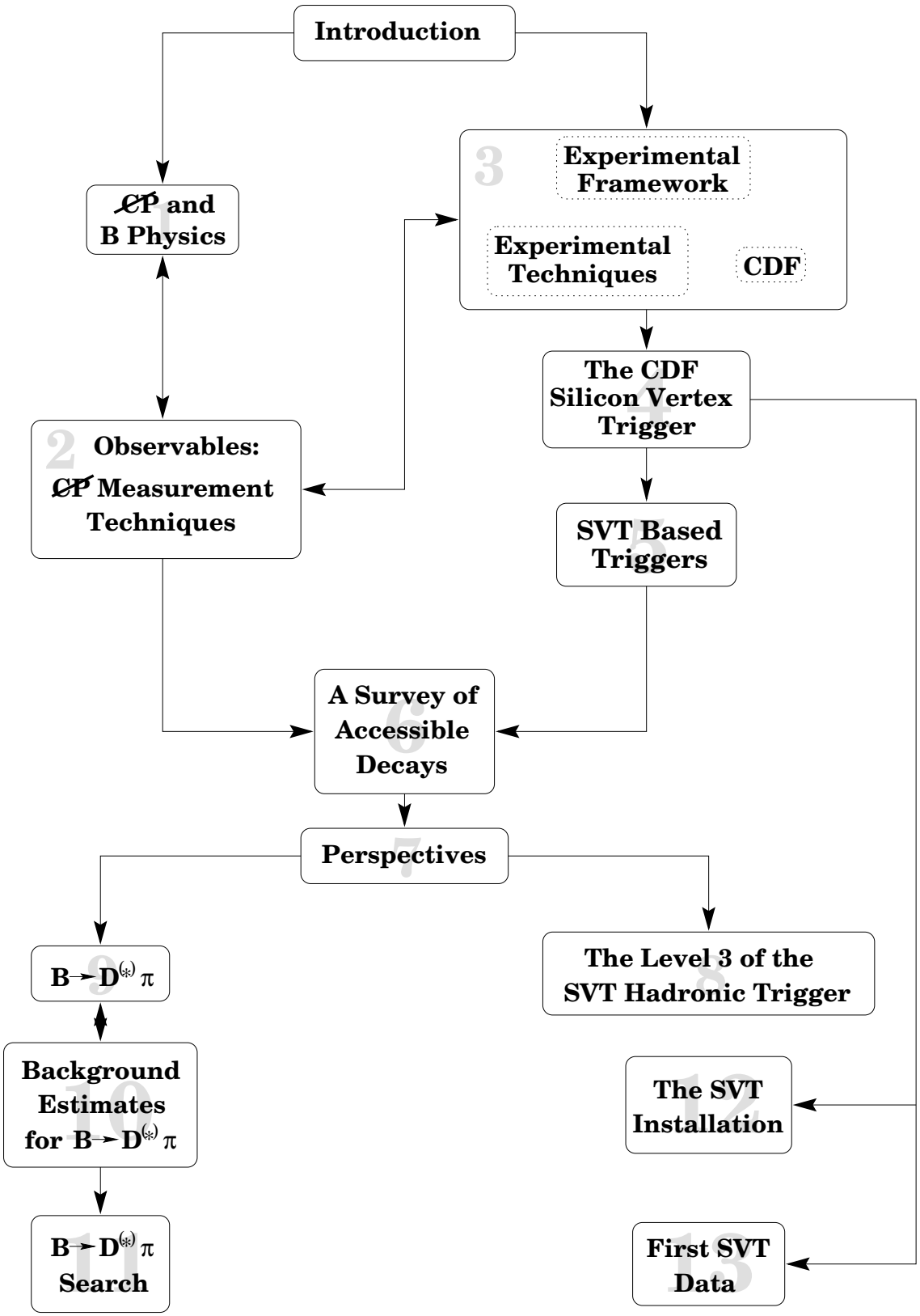
Introduction
1
CP and B Physics
2
Observables: CP Measurement Techniques
3
Experimental Framework
Experimental Techniques
CDF
4
The CDF Silicon Vertex Trigger
5
SVT Based Triggers
6
A Survey of Accessible Decays
7
Perspectives
8
The Level 3 of the SVT Hadronic Trigger
9
B→D(*)π
10
Background Estimates for B→D(*)π
11
B→D(*)π Search
12
The SVT Installation
13
First SVT Data

Contents

Introduction

Measuring CP violation in its manifestations and comparing the results with the *Standard Model* predictions is one of the most important consistency tests of the standard model itself. This fact is so clear that contributing to this effort has become one of the main objectives in practically all the new generation experiments. Moreover, experiments have been specifically designed for this purpose (see, for example, [1], [2] and [3]).

The CDF experiment [4] has been upgraded and will be competitive in many HEP issues. Among these, it will be possible for our experiment to contribute to CP violation measurements in the b quark sector.

A traditional handicap of $p\bar{p}$ experiments has been the presence of a huge hadronic background. This is especially true for high precision b physics measurements, which for this reason have been often considered virtually impossible in such a framework. The opportunity of doing these measurements in the $p\bar{p}$ environment is indeed very attractive because of the high b production rate. CDF has already demonstrated its capability of contributing to the measurement of CP violation parameters in b physics with the measurement of $Sin\,(2\beta)$ [5].
The CDF upgrade (CDF II) plans to extend its results in this sector, exploiting as much as possible the rich b production.
Due to the large event rate, only a small fraction of the events produced by $p\bar{p}$ collisions can be stored for analysis; in order to do b-physics, the ability to select events efficiently on the basis of their *flavour*, and thus choose *beautiful* events, is crucial. For this reason, a great care has been placed in designing and realizing the CDF trigger for selecting the events to be stored for analisis.

The making of new trigger strategies is difficult from many points of view: the technological aspect represents a challenge in itself, often asking for techniques beyond the established edge. Even just the practical aspect of defining trigger strategies and cuts becomes a challenge because their choice often relies on uncertain predictions of the physics and background of the events we want to collect.
The physics, the analysis approach, the hardware limitations and the trigger strategies often influence each other in a nontrivial manner.

Unfortunately, many interesting B decay channels are fully hadronic; this was a great limitation for CDF I, where hadronic triggers at low P_t were nearly impossible. For this reason the Silicon Vertex Trigger was designed as a CDF upgrade.
The precise online measurement of impact parameters in the silicon detector allows a beauty tag early in the trigger chain, and allows the experimenters to selectively acquire low P_t events rich in b content. All this can happen without introducing

leptonic cuts, and thus opening the gates to a variety of previously inaccessible B decays (and CP violation measurements).

CDF II gives then in principle access to non leptonic B decays, but its possibilities are mainly unexplored. A few studies, which will be outlined in the following chapters, have been detailed at a level sufficient to produce a well defined proposal for the trigger algorithm. The goal of our work will be that of investigating the use of these trigger templates as starting points for new analyses. In fact, with the advent of B factories and the identification of B physics as a primary tool for investigating the Standard Model, many phenomenological approaches have been proposed for the measurement of the relevant parameters. The exploitability of these techniques within the CDF II framework has been so far investigated only in few cases. That's where our work starts.

This work is organized in two parts:

- A general introduction to the theoretical highlights of CP violation (chapter 1) is followed by an analysis of the techniques and the constraints on B physics in the SM (chapter 2), CDF II detector and techniques are discussed (chapter 3) before introducing the Silicon Vertex Tracker (chapter 4) and the possibilities opened by this innovative device (chapter 5)

- A description of the author's original contribution to the experiment, both in the field of B physics and in the hardware development and setup of the Silicon Vertex Tracker.
  We start from a detailed study of the new possibilities that SVT brings to CDF II (chapters 6 and 7). Chapter 8 discusses the optimization of the SVT based selections for the purpose of obtaining a generic tool for hadronic B physics at CDF II.
  This will lead us to the study of a specific decay mode of the B meson: $B \to D^*\pi$, which is expected to give the highest yield among the hadronic channels. It is an important benchmark for the SVT performance and for several aspects of B physics at CDF. We will discuss the physics reach of this channel (chapter 9) and then figure out the detailed performance of CDF II for this mode, concentrating our efforts in obtaining a background expectation based on real data (chapters 10 and 11).
  On the hardware side, we will discuss the SVT installation (chapter 12) and the first results obtained with Run II data (chapter 13), which are part of the author's contribution.

Part I

The Framework

Part I: The Framework

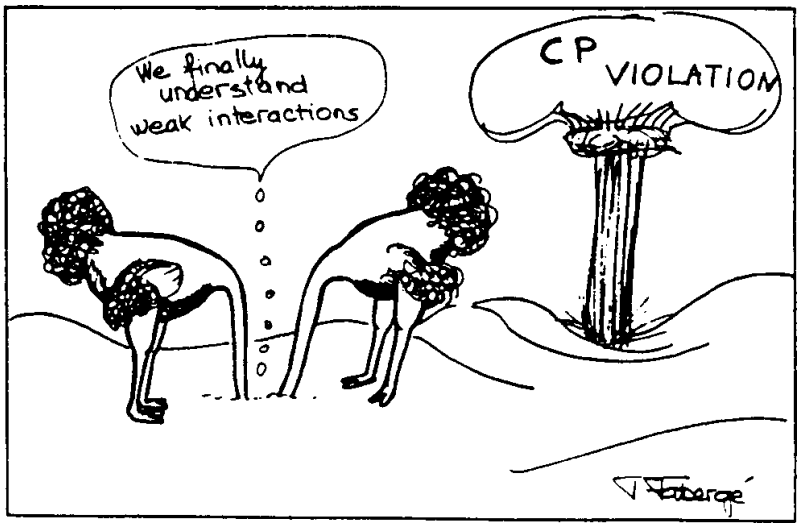

In this part we will discuss the framework in which our work is contained: chapter 1 is intended as a general description of the physics behind CP violation in the B meson sector, while chapter 3 describes the general structure and analysis approach of CDF II, with special emphasis on the issues more relevant for B physics studies. Chapters 2 and 4 will get closer to our field of interest: chapter 2 covers in more detail the phenomenological issues related to CP violation measurements in B physics, while chapter 4 details the working principle and the performances of SVT: the tool that will allow a significant enhancement of CDF's capabilities in B physics measurements.

Chapter 1

The Physics Framework

In this chapter we will go over the theoretical results which are at the foundation of our work. We will first quickly show how the Standard Model allows the existence of a CP violation effect. We will then concentrate on the B meson physics, showing how the same model can be used to describe CP violation effects in the B and K meson sector. This will led us to the measurable effects, and to what and how can be measured using the CDF detector.
The last years have been characterized by a great theoretical effort towards the exploration of new techniques for the measurement of CP violation related standard model parameters. We will point out the ones which look more appealing in our case, specifically concentrating on those more relevant for the studies that will be described later. A further insight in some of these techniques will be given in the following chapters, and in particular in chapter 2.

1.1 CP Violation in Nature

The invariance of physical phenomena under discrete symmetries like *charge conjugation* C, *parity transformation* P and *time reversal* T, has been implicitly assumed true for a long time. The basic assumption that left and right are potentially different in natural phenomena has been formally stated only in the second half of our century [6] (1956). Experimental study of the charged kaon decay modes into two pions and into three pions indicated that the extra pion carried a negative intrinsic parity, un-compensated by the relevant spatial parities, and hence that two different decay modes from the same parent carried opposite parities. This remarkable observation was interpreted by Lee and Yang [6] as evidence that mirror symmetry (manifested by P conservation) was not a symmetry of the weak interaction. This was confirmed by the Wu et al. [7] observation of the angular asymmetry of beta particles emitted from polarized ^{60}Co, and by the Garwin et al. measurement of the asymmetry in the electron angular distribution of muon decay [8]. These observations also established the violation in weak interactions of C invariance. Symmetry with respect to the combined operation CP appeared preserved: even the wonderful experiment for the measurement of neutrino helicity [9] showed C and P violation without evidence of CP violation.

1964 was the year of the big explosion: Christenson, Cronin, Fitch and Turlay found the first evidence of CP violation in K° decays.

1.2 CP Violation in the Standard Model: the Cabibbo-Kobayashi-Maskawa Matrix

One year before the astonishing evidence of Christenson et al., Cabibbo [10] first observed that CP violation can be accommodated in the standard model as an arbitrary nonzero value of the relative phase of coupling constants in the W-quark sector.
The electroweak (EW) Lagrangian couples quarks to the W boson through a term of the form:

$$\mathcal{L}_{\mathcal{C}.\mathcal{C}.} \propto W_\mu^+ \left(\bar{u}_L^\alpha V^{\alpha\beta} \gamma^\mu d_L^\beta \right) + h.c. \tag{1.1}$$

The $V_{\alpha\beta}$ coefficients allow for a non factorisable relative phase factor for $n \geq 3$ (n is the number of quark families of the model). This phase factor can't be re-absorbed in the field definition for massive fields (which is the case for the physics we want to model). This leaves the SM Lagrangian with a non-factorisable phase factor in the $V_{\alpha\beta}$ matrix. This 3×3 matrix is usually referred to as the *Cabibbo-Kobayashi-Maskawa* matrix (CKM) [10, 11].
The most common parameterization of the CKM matrix is the one introduced by Wolfenstein [12]:

$$\begin{aligned} V_{\text{CKM}} &= \begin{pmatrix} V_{ud} & V_{us} & V_{ub} \\ V_{cd} & V_{cs} & V_{cb} \\ V_{td} & V_{ts} & V_{tb} \end{pmatrix} \\ &= \begin{pmatrix} 1 - \lambda^2/2 & \lambda & A\lambda^3 (\rho - i\eta) \\ -\lambda & 1 - \lambda^2/2 & A\lambda^2 \\ A\lambda^3 (1 - \rho - i\eta) & -A\lambda^2 & 1 \end{pmatrix} + \mathcal{O}(\lambda^4) \end{aligned} \tag{1.2}$$

In this parameterization phase effects show up only in the V_{td} and V_{ub} coefficients up to $\mathcal{O}(\lambda^4)$.
The unitarity of the CKM matrix is a property which is physically stringent: it would be not very meaningful to include in a model a set of coupling constants which not satisfying unitarity. This of course applies to the *whole* set of coupling constants: the V_{CKM} matrix might for example be actually just a sub-element of a 4×4 matrix of the form (1.1) whose unitarity would not imply the unitarity of each of its 3×3 sub-matrices.
What are the implications of the V_{CKM} unitarity? These can be summarized in the relation:

$$\sum_k V_{ki} V_{kj}^* = \delta_{ij}. \qquad i, j \in \{u, c, t\} \qquad k \in \{d, s, b\} \tag{1.3}$$

The 6 equations with $i \neq j$ each require that the sum of three complex numbers is 0. This is equivalent to the existence of 6 triangles in the complex plane.
The six triangles are described by:

Figure 1.1: Sketch of the three independent relations coming from eqs. 1.4 in the Wolfenstein approximation.

$$\begin{array}{lccccccc}
ds & V_{ud}V_{us}^* & + & V_{cd}V_{cs}^* & + & V_{td}V_{ts}^* & = 0 \\
 & \lambda & & \lambda & & \lambda^5 & \\
sb & V_{us}V_{ub}^* & + & V_{cs}V_{cb}^* & + & V_{ts}V_{tb}^* & = 0 \\
 & \lambda^4 & & \lambda^2 & & \lambda^2 & \\
db & V_{ud}V_{ub}^* & + & V_{cd}V_{cb}^* & + & V_{td}V_{tb}^* & = 0 \\
 & \lambda^3 & & \lambda^3 & & \lambda^3 & \\
uc & V_{ud}V_{cd}^* & + & V_{us}V_{cs}^* & + & V_{ub}V_{cb}^* & = 0 \\
 & \lambda & & \lambda & & \lambda^5 & \\
ct & V_{cd}V_{td}^* & + & V_{cs}V_{ts}^* & + & V_{cb}V_{tb}^* & = 0 \\
 & \lambda^4 & & \lambda^2 & & \lambda^2 & \\
ut & V_{ud}V_{td}^* & + & V_{us}V_{ts}^* & + & V_{ub}V_{tb}^* & = 0 \\
 & \lambda^3 & & \lambda^3 & & \lambda^3 &
\end{array} \tag{1.4}$$

Below each term we report, as a reference, the corresponding order in λ. In Wolfenstein's approximation, the independent equations in (1.4) are 3 (e.g. the first three). These three relations can be viewed as three triangles in the complex plane (each side of them being one of the terms in the sum) which are often almost-degenerate (with sides of the order $\lambda, \lambda, \lambda^5$ and $\lambda^2, \lambda^2, \lambda^5$). Typical configuration for these triangles are qualitatively sketched in figure 1.1. Note also that all triangles degenerate onto segments if $\bar{\eta} = 0$. In the second order Wolfenstein parameterization ($\mathcal{O}(\lambda^2)$) only one triangle doesn't degenerate onto a segment: that's the conventional *Bjorken Triangle*, which has all sides of $\mathcal{O}(\lambda^3)$.
The usual representation of Bjorken's triangle is made by normalizing one of its sides:

$$1 + \frac{V_{ud}V_{ub}^*}{V_{cd}V_{cb}^*} + \frac{V_{td}V_{tb}^*}{V_{cd}V_{cb}^*} = 0 \tag{1.5}$$

which is equivalent (up to $\mathcal{O}(\lambda^4)$) to:

$$1 + \frac{V_{ud}V_{td}^*}{V_{us}V_{ts}^*} + \frac{V_{ub}V_{tb}^*}{V_{us}V_{ts}^*} = 0 \tag{1.6}$$

Keeping in mind figure 1.2 we can introduce the following quantities, generally

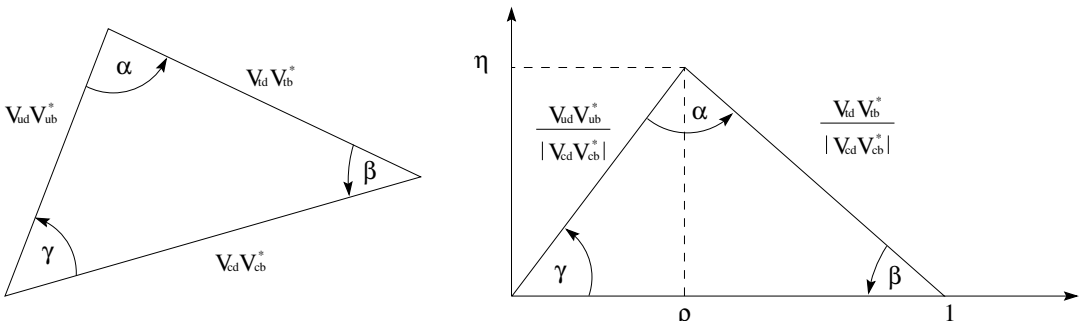

Figure 1.2: The Bjorken triangle with the corresponding V_{ij} for each triangle parameter.

adopted in literature[1]:

$$\begin{aligned} R_u &= \left|\frac{V_{ub}^* V_{ud}}{V_{cb}^* V_{cd}}\right| = \sqrt{\bar{\rho}^2 + \bar{\eta}^2} \\ R_t &= \left|\frac{V_{tb}^* V_{td}}{V_{cb}^* V_{cd}}\right| = \sqrt{(1-\bar{\rho})^2 + \bar{\eta}^2} \end{aligned} \tag{1.7}$$

and:

$$\begin{aligned} \alpha &= \arg\left[-\frac{V_{td}V_{tb}^*}{V_{ud}V_{ub}^*}\right] \qquad \bar{\rho} = \left(1 - \frac{\lambda^2}{2}\right)\rho \\ \beta &= \arg\left[-\frac{V_{cd}V_{cb}^*}{V_{td}V_{tb}^*}\right] \qquad \bar{\eta} = \left(1 - \frac{\lambda^2}{2}\right)\eta \\ \gamma &= \arg\left[-\frac{V_{ud}V_{ub}^*}{V_{cd}V_{cb}^*}\right] \end{aligned} \tag{1.8}$$

Each of the above angles is the phase difference between two V_{CKM} elements and is thus connected to a physics observable (see chapter 2). A non vanishing (and different from π) value for one of these angles would mean that the SM accommodates some kind of CP violation.

The particle physics phenomenology implies constraints on many V_{ij} (see [13]):

- $|V_{ud}| = 0.9740 \pm 0.0010$ Is determined by comparing β decays with $\mu^\pm$ decay.
- $|V_{us}| = 0.2196 \pm 0.0023$ Measuring $\Delta S = 1$ transitions in semileptonic decays of K mesons and hyperons, like in $K \to \pi\ell\nu$.
- $|V_{cs}| = 1.04 \pm 0.16$ From semileptonic decays of charmed mesons ($D^\circ \to K^- e^+ \nu_e$ and $D^- \to K^\circ e^- \bar{\nu}_e$), using evaluated hadronic form factors.

[1]Note that since we are interested in the B sector, we will use from now on the Bjorken triangle as parametrized in equation (1.5)

- $|V_{cd}| = 0.224 \pm 0.016$ From the ratio of strange and non strange decays of charmed mesons, like $D^\circ \to \pi^- e^+ \nu_e$ and $D^\circ \to K^- e^+ \nu_e$, the ratio $\left|\frac{V_{cd}}{V_{cs}}\right|$ is extracted, and thus $|V_{cd}|$ is obtained.

- $|V_{cb}| = 0.0395 \pm 0.0017$ From semileptonic decays of B mesons, keeping into account the uncertainty on the hadronic form factors.

- $|V_{ub}| = 0.08 \pm 0.02$ From semileptonic charmless decays $b \to u\ell^- \nu_\ell$

- $|V_{tb}| \approx 1$, $|V_{ts}| \approx 0.04$, $|V_{td}| \approx 0.003$ Direct determination of V_{td} and V_{ts} is practically impossible because the BR for the process $t \to bW^+$ is practically 100% in the SM. Combining flavor oscillation parameters (see chapter 2) and unitarity of V_{CKM} allows the indirect determination of these three parameters.

Using the above described estimates, together with the flavor oscillation parameters [13], we can write 90% confidence limits on the magnitude of the elements of V_{CKM}:

$$\begin{pmatrix} 0.9745 \text{ to } 0.9760 & 0.217 \text{ to } 0.224 & 0.0018 \text{ to } 0.0045 \\ 0.217 \text{ to } 0.224 & 0.9737 \text{ to } 0.9753 & 0.036 \text{ to } 0.042 \\ 0.004 \text{ to } 0.013 & 0.035 \text{ to } 0.042 & 0.9991 \text{ to } 0.9994 \end{pmatrix} \tag{1.9}$$

1.3 Phenomenological Approach

Kaon physics was the starting point for CP violation insight. The theoretical interpretation of such intriguing phenomena is still debated, while the phenomenological interpretation has become universally accepted. Since the same parameterization can be used in the case of the $\bar{K}^\circ - K^\circ$ and $\bar{B}^\circ - B^\circ$ system, we will first outline it for a generic neutral particle-anti-particle system and then detail the model using the peculiarities of the particular system under study.

1.3.1 An Effective Hamiltonian

Let's consider a generic particle-anti-particle system $A^\circ - \bar{A}^\circ$, which is an eigenstate of the electromagnetic and strong part (H_0) of the model Hamiltonian $H = H_0 + \mathcal{H}$. We assume that A° and $\bar{A}^\circ$ are eigenstates of H_0: given the CPT invariance of the system, we can firmly state that

$$H_0 = \begin{pmatrix} m_0 & 0 \\ 0 & m_0 \end{pmatrix} \tag{1.10}$$

where, assuming that the A° decays only through $\mathcal{H}$, we have $\mathcal{I}m\,(H_0) = 0$.

The effective Hamiltonian is thus in the form:

$$H = H_0 + \mathcal{H}$$

We assume now that $\mathcal{H}$ is the byproduct of $A^\circ - \bar{A}^\circ$ coupling through some intermediate state, due to a weak interaction coupling. Given a generic intermediate state $|f\rangle$, the time evolution of an arbitrary $|A^\circ\rangle - |\bar{A}^\circ\rangle$ mix is:

$$|\psi\,(t)\rangle = a\,(t)\,|A^\circ\rangle + b\,(t)\,|\bar{A}^\circ\rangle + \int df\; c_f\,(t)\,|f\rangle$$

the same state $|\psi\rangle$ obeys Schrödinger's equation:

$$i\hbar\frac{\partial}{\partial t}|\psi\rangle = (H_0 + \mathcal{H})\,|\psi\rangle \tag{1.11}$$

which can be rewritten as:

$$i\hbar\frac{\partial}{\partial t}\left(e^{\frac{iH_0t}{\hbar}}|\psi\rangle\right) = \left[e^{\frac{iH_0t}{\hbar}}\mathcal{H}e^{-i\frac{H_0t}{\hbar}}\right]\left[e^{\frac{iH_0t}{\hbar}}|\psi\rangle\right]$$

we thus define:

$$\begin{aligned}
\tilde{a}(t) &= e^{\frac{iH_0t}{\hbar}}a(t)\\
\tilde{b}(t) &= e^{\frac{iH_0t}{\hbar}}b(t)\\
\chi_f(t) &= e^{\frac{iH_0t}{\hbar}}c_f(t)\\
V(t) &= e^{\frac{iH_0t}{\hbar}}\mathcal{H}e^{-i\frac{H_0t}{\hbar}}\\
|\psi\rangle &= \tilde{a}(t)|A^\circ\rangle + \tilde{b}(t)|\bar{A}^\circ\rangle + \int df\;\chi_f(t)|f\rangle
\end{aligned}$$

obtaining:

$$i\hbar\frac{\partial}{\partial t}|\psi\rangle = V(t)|\psi\rangle$$

We rewrite this relation for each time-dependent function:

$$\begin{aligned}
i\hbar\frac{\partial}{\partial t}\tilde{a}(t) &= i\hbar\frac{\partial}{\partial t}\langle A^\circ|\psi\rangle = \langle A^\circ|V(t)|\psi\rangle =\\
&= \langle A^\circ|V(t)|A^\circ\rangle\tilde{a}(t) + \langle A^\circ|V(t)|\bar{A}^\circ\rangle\tilde{b}(t) + \textstyle\int df\;\chi_f(t)\langle A^\circ|V(t)|f\rangle \qquad (1.12)\\
i\hbar\frac{\partial}{\partial t}\tilde{b}(t) &= i\hbar\frac{\partial}{\partial t}\langle \bar{A}^\circ|\psi\rangle = \langle \bar{A}^\circ|V(t)|\psi\rangle =\\
&= \langle \bar{A}^\circ|V(t)|A^\circ\rangle\tilde{a}(t) + \langle \bar{A}^\circ|V(t)|\bar{A}^\circ\rangle\tilde{b}(t) + \textstyle\int df\;\chi_f(t)\langle \bar{A}^\circ|V(t)|f\rangle \qquad (1.13)\\
i\hbar\frac{\partial}{\partial t}\chi_f(t) &= i\hbar\frac{\partial}{\partial t}\langle f|\psi\rangle = \langle f|V(t)|\psi\rangle =\\
&= \langle f|V(t)|A^\circ\rangle\tilde{a}(t) + \langle f|V(t)|\bar{A}^\circ\rangle\tilde{b}(t) + \textstyle\int df'\;\chi_{f'}(t)\langle f|V(t)|f'\rangle = \qquad (1.14)\\
&= \langle f|V|A^\circ\rangle e^{i\frac{(E_f-m_0)t}{\hbar}}\tilde{a}(t) + \langle f|V|\bar{A}^\circ\rangle e^{i\frac{(E_f-m_0)t}{\hbar}}\tilde{b}(t) + \textstyle\int df'\;\chi_{f'}(t)e^{i\frac{(E_{f'}-E_f)t}{\hbar}}\langle f|V|f'\rangle
\end{aligned}$$

Ignoring transitions between intermediate states $\langle f'|V|f\rangle = 0 \quad \forall\ |f\rangle, |f'\rangle \neq$

$|A^\circ\rangle$, $|\bar{A}^\circ\rangle$:

$$\begin{aligned}\chi_f(t) &\simeq -\frac{i}{\hbar}\int_0^t dt' \left(\langle f|\mathcal{H}|A^\circ\rangle\tilde{a}(t') + \langle f|\mathcal{H}|\bar{A}^\circ\rangle\tilde{b}(t')\right) e^{i\frac{(E_f-m_0)t'}{\hbar}} = \\ &= \lim_{\epsilon\to 0}\frac{-i}{\hbar}\left[\frac{\langle f|\mathcal{H}|A^\circ\rangle\tilde{a}(t') + \langle f|\mathcal{H}|\bar{A}^\circ\rangle\tilde{b}(t')}{E_f - m_0 + i\epsilon}\, e^{i\frac{(E_f-m_0)t'}{\hbar}}\right]_{t'=0}^{t'=t} + \\ &- \int_0^t dt' \frac{e^{i\frac{(E_f-m_0)t'}{\hbar}}}{E_f - m_0 + i\epsilon}\frac{d}{dt'}\left\{\langle f|\mathcal{H}|A^\circ\rangle\tilde{a}(t') + \langle f|\mathcal{H}|\bar{A}^\circ\rangle\tilde{b}(t')\right\}\end{aligned} \tag{1.15}$$

where ϵ means that we regularise the integral[2] ignoring $\mathcal{O}(\mathcal{H}^2)$:

$$\begin{aligned}\chi_f(t) &\simeq -\mathcal{P}\frac{\langle f|\mathcal{H}|A^\circ\rangle\tilde{a}(t) + \langle f|\mathcal{H}|\bar{A}^\circ\rangle\tilde{b}(t)}{E_f - m_0}e^{i\frac{(E_f-m_0)t}{\hbar}} + \\ &- \pi i\delta(E_f - m_0)\left(\langle f|\mathcal{H}|A^\circ\rangle\tilde{a}(t) + \langle f|\mathcal{H}|\bar{A}^\circ\rangle\tilde{b}(t)\right) e^{i\frac{(E_f-m_0)t}{\hbar}}\end{aligned} \tag{1.16}$$

merging (1.12) and (1.13) with (1.16):

$$\begin{aligned}i\hbar\frac{\partial}{\partial t}\tilde{a}(t) &= \tilde{a}(t)\left\{\langle A^\circ|\mathcal{H}|A^\circ\rangle - \frac{i}{\hbar}\mathcal{P}\int df\, \frac{\langle A^\circ|\mathcal{H}|f\rangle\langle f|\mathcal{H}|A^\circ\rangle}{E_f - m_0} + \right. \\ &- \left.\pi i\left[|\langle A^\circ|\mathcal{H}|A^\circ\rangle|^2 + \left|\langle\bar{A}^\circ|\mathcal{H}|A^\circ\rangle\right|^2\right]\right\} + \\ &+ \tilde{b}(t)\left\{\langle A^\circ|\mathcal{H}|\bar{A}^\circ\rangle - \frac{i}{\hbar}\mathcal{P}\int df\, \frac{\langle A^\circ|\mathcal{H}|f\rangle\langle f|\mathcal{H}|\bar{A}^\circ\rangle}{E_f - m_0} + \right. \\ &- \left.\pi i\left[\langle A^\circ|\mathcal{H}|A^\circ\rangle\langle A^\circ|\mathcal{H}|\bar{A}^\circ\rangle + \langle A^\circ|\mathcal{H}|\bar{A}^\circ\rangle\langle\bar{A}^\circ|\mathcal{H}|\bar{A}^\circ\rangle\right]\right\}\end{aligned} \tag{1.17}$$

$$\begin{aligned}i\hbar\frac{\partial}{\partial t}\tilde{b}(t) &= \tilde{a}(t)\left\{\langle\bar{A}^\circ|\mathcal{H}|A^\circ\rangle - \frac{i}{\hbar}\mathcal{P}\int df\, \frac{\langle\bar{A}^\circ|\mathcal{H}|f\rangle\langle f|\mathcal{H}|A^\circ\rangle}{E_f - m_0} + \right. \\ &- \left.\pi i\left[\langle\bar{A}^\circ|\mathcal{H}|A^\circ\rangle\langle A^\circ|\mathcal{H}|A^\circ\rangle + \langle\bar{A}^\circ|\mathcal{H}|\bar{A}^\circ\rangle\langle\bar{A}^\circ|\mathcal{H}|A^\circ\rangle\right]\right\} + \\ &+ \tilde{b}(t)\left\{\langle\bar{A}^\circ|\mathcal{H}|\bar{A}^\circ\rangle - \frac{i}{\hbar}\mathcal{P}\int df\, \frac{\langle\bar{A}^\circ|\mathcal{H}|f\rangle\langle f|\mathcal{H}|\bar{A}^\circ\rangle}{E_f - m_0} + \right. \\ &- \left.\pi i\left[\left|\langle\bar{A}^\circ|\mathcal{H}|A^\circ\rangle\right|^2 + \left|\langle\bar{A}^\circ|\mathcal{H}|\bar{A}^\circ\rangle\right|^2\right]\right\}\end{aligned} \tag{1.18}$$

This suggests that we define:

$$\begin{cases} M_{ij} \equiv m_0\delta_{ij} + \langle i|\mathcal{H}|j\rangle - \mathcal{P}\int df\, \frac{\langle i|\mathcal{H}|f\rangle\langle f|\mathcal{H}|j\rangle}{E_f - m_0} \\ \\ \Gamma_{ij} \equiv 2\pi\int df\, \delta\left(E_f - m_0\right)\langle i|\mathcal{H}|f\rangle\langle f|\mathcal{H}|j\rangle \end{cases} \tag{1.19}$$

[2]Remembering that

$$\lim_{\epsilon\to 0}\frac{1}{x + i\epsilon} = \mathcal{P}\frac{1}{x} - \pi i\delta(x)$$

thus expressing $\mathcal{H}$:

$$H_0 + \mathcal{H} = M - \frac{i}{2}\Gamma \tag{1.20}$$

Note that M and Γ, thanks to equations (1.19), are hermitian operators:

$$M^\dagger = M \qquad \Gamma^\dagger = \Gamma \tag{1.21}$$

while CPT invariance requires:

$$M_0 \equiv M_{11} = M_{22} \qquad \Gamma_0 \equiv \Gamma_{11} = \Gamma_{22} \implies \mathcal{H}_0 \equiv \mathcal{H}_{11} = \mathcal{H}_{22}$$

In analogy with the single particle system, we call M and Γ respectively *mass* and *decay* matrix. After integrating over the intermediate states, Schrödinger's equation in the $A^\circ - \bar{A}^\circ$ space finally becomes:

$$i\hbar\frac{\partial}{\partial t}\begin{pmatrix} a \\ b \end{pmatrix} = \begin{pmatrix} \mathcal{H}_0 & \mathcal{H}_{12} \\ \mathcal{H}_{12}^* & \mathcal{H}_0 \end{pmatrix}\begin{pmatrix} a \\ b \end{pmatrix} = \left[\begin{pmatrix} M_0 & M_{12} \\ M_{12}^* & M_0 \end{pmatrix} - \frac{i}{2}\begin{pmatrix} \Gamma_0 & \Gamma_{12} \\ \Gamma_{12}^* & \Gamma_0 \end{pmatrix}\right]\begin{pmatrix} a \\ b \end{pmatrix} \tag{1.22}$$

1.3.2 Mixing and CP Violation

Let's now use equation (1.22) as a starting point. We first identify the *eigenstates* of the system, parameterizing them as:

$$\begin{cases} A_a^\circ = pA^\circ + q\bar{A}^\circ \\ A_b^\circ = pA^\circ - q\bar{A}^\circ \end{cases} \longleftrightarrow \begin{cases} A^\circ = \dfrac{A_a^\circ + A_b^\circ}{p} \\ \bar{A}^\circ = \dfrac{A_a^\circ - A_b^\circ}{q} \end{cases} \tag{1.23}$$

this constrains the p, q value to:

$$\frac{q}{p} = \sqrt{\frac{M_{12}^* - \frac{i}{2}\Gamma_{12}^*}{M_{12} - \frac{i}{2}\Gamma_{12}}} \tag{1.24}$$

The A_a°, A_b° definition immediately tells us that their time evolution is simply:

$$|A_{a,b}^\circ(t)\rangle = |A_{a,b}^\circ(0)\rangle \cdot e^{-i\mu_{a,b}t} \tag{1.25}$$

where $\mu_{a,b} = m_{a,b} - \frac{i}{2}\Gamma_{a,b}$ are the eigenvalues of the effective Hamiltonian operator (1.20).
We can introduce the parameters:

$$\begin{cases} M = \dfrac{m_a + m_b}{2} \\ \Gamma = \dfrac{\Gamma_a + \Gamma_b}{2} \end{cases} \qquad \begin{cases} \Delta M = m_b - m_a = -2\mathcal{R}e\,(p \cdot q) \\ \Delta\Gamma = \Gamma_a - \Gamma_b = -4\mathcal{I}m\,(p \cdot q) \end{cases} \tag{1.26}$$

This allows us to express the time evolution of an initial $|A^\circ\rangle$ or $|\bar{A}^\circ\rangle$ as:

$$\begin{cases} |A^\circ(t)\rangle = \frac{1}{2}e^{iMt}e^{-\frac{\Delta\Gamma}{2}t}\left[|A^\circ\rangle Cos\left(\frac{\Delta Mt - i\frac{\Delta\Gamma}{2}t}{2}\right) - |\bar{A}^\circ\rangle\frac{q}{p}Sin\left(\frac{\Delta Mt - i\frac{\Gamma}{2}t}{2}\right)\right] \\ |\bar{A}^\circ(t)\rangle = \frac{p}{q}\frac{1}{2}e^{iMt}e^{-\frac{\Delta\Gamma}{2}t}\left[-|A^\circ\rangle Sin\left(\frac{\Delta Mt - i\frac{\Delta\Gamma}{2}t}{2}\right) + |\bar{A}^\circ\rangle\frac{q}{p}Cos\left(\frac{\Delta Mt - i\frac{\Gamma}{2}t}{2}\right)\right] \end{cases} \tag{1.27}$$

it is now clear that a particle which is initially in the $|A^\circ\rangle$ (or $|\bar{A}^\circ\rangle$) state will evolve into a mixed $A^\circ - \bar{A}^\circ$ state. This is the so called *mixing* phenomena.

1.3.2.1 Asymmetry

The decay amplitudes $\Gamma(A^\circ \to f)$ and $\Gamma\left(\bar{A}^\circ \to f\right)$ can be written, using (1.27):

$$\begin{cases} \Gamma(A^\circ \to f) \propto e^{-\Gamma t}|\langle f|A^\circ\rangle|^2 \cdot |g_+(t) + \lambda g_-(t)|^2 \\ \Gamma\left(\bar{A}^\circ \to f\right) \propto e^{-\Gamma t}\left|\frac{p}{q}\right|^2 |\langle f|A^\circ\rangle|^2 \cdot |g_-(t) + \lambda g_+(t)|^2 \end{cases} \tag{1.28}$$

Here and in the following we will omit for the sake of simplicity the decay operator between the initial and the final state. We also introduced

$$\begin{aligned} g_\pm(t) &= \frac{1}{2}e^{iMt}e^{-\frac{\Gamma t}{2}}\left(e^{i\frac{\Delta Mt}{2}}e^{-\frac{\Delta\Gamma t}{4}} \pm e^{-i\frac{\Delta Mt}{2}}e^{\frac{\Delta\Gamma t}{4}}\right) \\ \lambda &= \frac{q}{p}\frac{\langle f|\bar{A}^\circ\rangle}{\langle f|A^\circ\rangle} \end{aligned} \tag{1.29}$$

We can thus introduce the *asymmetry* parameter:

$$\mathcal{A} = \frac{\Gamma(A^\circ \to f) - \Gamma\left(\bar{A}^\circ \to f\right)}{\Gamma(A^\circ \to f) + \Gamma\left(\bar{A}^\circ \to f\right)} \tag{1.30}$$

Which can be rewritten:

$$\mathcal{A} = \frac{\begin{array}{c}\cosh\left(\frac{\Delta\Gamma t}{2}\right)\left[1 - \left|\frac{p}{q}\lambda\right|^2 + |\lambda|^2 - \left|\frac{p}{q}\right|^2\right] + Cos(\Delta Mt)\left[1 - \left|\frac{p}{q}\lambda\right|^2 - |\lambda|^2 + \left|\frac{p}{q}\right|^2\right] + \\ +2|\lambda|\sqrt{\sinh^2\frac{\Delta\Gamma t}{2} + Sin^2(\Delta Mt)}\left[Cos(\phi_m + \phi_\lambda) - \left|\frac{p}{q}\right|^2 Cos(\phi_m - \phi_\lambda)\right]\end{array}}{\begin{array}{c}\cosh\left(\frac{\Delta\Gamma t}{2}\right)\left[1 + \left|\frac{p}{q}\lambda\right|^2 + |\lambda|^2 + \left|\frac{p}{q}\right|^2\right] + Cos(\Delta Mt)\left[1 + \left|\frac{p}{q}\lambda\right|^2 - |\lambda|^2 - \left|\frac{p}{q}\right|^2\right] + \\ +2|\lambda|\sqrt{\sinh^2\frac{\Delta\Gamma t}{2} + Sin^2(\Delta Mt)}\left[Cos(\phi_m + \phi_\lambda) + \left|\frac{p}{q}\right|^2 Cos(\phi_m - \phi_\lambda)\right]\end{array}} \tag{1.31}$$

with $\phi_\lambda \equiv \arg\lambda$ and $\phi_m \equiv \arg\left[\sinh\frac{\Delta\Gamma t}{2} + iSin\left(\Delta M t\right)\right]$.

Given a final decay state $|f\rangle$ which is CP eigenstate

$$|\bar{f}\rangle = \mathsf{CP}|f\rangle = \eta|f\rangle \qquad \eta = \pm 1 \tag{1.32}$$

and assuming that a pure $|A^\circ\rangle$ state has a decay amplitude:

$$\langle f|A^\circ\rangle = A_0 e^{i\delta} e^{i\Phi_w} \tag{1.33}$$

where δ represents the electromagnetic and strong phase contribution and Φ_w the CP violating weak phase factor, we have:

$$\langle f|\bar{A}^\circ\rangle = \eta\langle\bar{f}|\bar{A}^\circ\rangle = \eta A_0 e^{i\delta} e^{-i\Phi_w} \tag{1.34}$$

And thus, introducing $\phi_M \equiv \frac{1}{2}\arg\frac{q}{p}$

$$\begin{aligned} |\lambda| &= \left|\tfrac{q}{p}\right| A_0 \\ \arg\lambda &= 2\phi_M - 2\phi_w + (1-\eta)\tfrac{\pi}{2} \end{aligned} \tag{1.35}$$

we can rewrite equation (1.31):

$$\begin{aligned} \mathcal{A} = \frac{\sqrt{\sinh^2\frac{\Delta\Gamma t}{2} + Sin^2\left(\Delta M t\right)}}{\cosh\left(\frac{\Delta\Gamma t}{2}\right)\left[1 + A_0^2 + A_0^2\left|\frac{q}{p}\right|^2 + \left|\frac{p}{q}\right|^2\right] + Cos\left(\Delta M t\right)\left[1 + A_0^2 - A_0^2\left|\frac{q}{p}\right|^2 - \left|\frac{p}{q}\right|^2\right] +} \\ +2\left|\lambda\right|\left[Cos\left(\phi_m + 2\phi_M - 2\phi_w + (1-\eta)\frac{\pi}{2}\right) + \left|\frac{p}{q}\right|^2 Cos\left(\phi_m - 2\phi_M + 2\phi_w - (1-\eta)\frac{\pi}{2}\right)\right] \\ \cosh\left(\frac{\Delta\Gamma t}{2}\right)\left[1 - A_0^2 + A_0^2\left|\frac{q}{p}\right|^2 + \left|\frac{p}{q}\right|^2\right] + Cos\left(\Delta M t\right)\left[1 - A_0^2 - A_0^2\left|\frac{q}{p}\right|^2 + \left|\frac{p}{q}\right|^2\right] + \\ +2\left|\lambda\right|\left[Cos\left(\phi_m + 2\phi_M - 2\phi_w + (1-\eta)\frac{\pi}{2}\right) + \left|\frac{p}{q}\right|^2 Cos\left(\phi_m - 2\phi_M + 2\phi_w - (1-\eta)\frac{\pi}{2}\right)\right] \\ \sqrt{\sinh^2\frac{\Delta\Gamma t}{2} + Sin^2\left(\Delta M t\right)} \end{aligned} \tag{1.36}$$

This last relation shows what are the sources of CP violation effects, in the form of asymmetry in the particle-anti-particle instantaneous decay rates:

- $\lambda = 1$ and $p = q$ implies **no CP violation effects** (no measurable asymmetry)
- $\lambda = \frac{q}{p}$ and $p \neq q$ implies that CP is violated as a consequence of the **mixing** of the $A^\circ - \bar{A}^\circ$ particles.

- **Direct CP violation**: $\lambda \neq \frac{q}{p}$ and $p = q$ implies that CP is violated as a consequence of a violation in the particle **decay** amplitudes.
- $|\lambda| = 1$ but $\mathcal{I}m\lambda \neq 0$ implies CP violation in the **interference** between decays with an without mixing.

1.3.3 Kaons

In the case of Kaons, we have:

$$\begin{array}{ll} \Gamma_{K_s} = 7.379 \cdot 10^{-12} MeV & \Delta M = m_{K_s} - m_{K_L} = 3.510 \pm 0.018 \cdot 10^{-12} MeV \\ \Gamma_{K_L} = 1.27 \cdot 10^{-14} MeV & \Delta\Gamma\,(\approx \Gamma_{K_s}) = 7.366 \cdot 10^{-12} MeV \end{array} \tag{1.37}$$

These values explain why the empirical assumption $\Delta\Gamma \approx 2\Delta M$ is used.
The phenomenological description of CP violation in the K system often refers to the quantity:

$$\epsilon_K \equiv \frac{p-q}{p+q} \tag{1.38}$$

Which directly parameterizes the shift of the mass eigenstates from CP eigenstates. Note also that $\epsilon \neq 0$ implies CP violation in the mixing of kaons, but doesn't contain any information on the *direct* phenomena.
The parameters which measure *direct* CP violation for the kaons are usually referred to as ϵ'_K, η_{00} and η_{+-}. In fact, CP violation implies that $\Gamma\,(K_L \to \pi^+\pi^-) \neq \Gamma\,(K_s \to \pi^+\pi^-)$ and $\Gamma\,(K_L \to \pi^\circ\pi^\circ) \neq \Gamma\,(K_s \to \pi^\circ\pi^\circ)$. But if we assume the presence of direct CP violation:

$$\begin{aligned} \eta_{+-} &\equiv \tfrac{\langle \pi^+\pi^-|T|K_L\rangle}{\langle \pi^+\pi^-|T|K_s\rangle} \approx \epsilon_K + \epsilon'_K \\ \eta_{00} &\equiv \tfrac{\langle \pi^\circ\pi^\circ|T|K_L\rangle}{\langle \pi^\circ\pi^\circ|T|K_s\rangle} \approx \epsilon_K - 2\epsilon'_K \end{aligned} \tag{1.39}$$

Which thus leads to the well known observable:

$$\left|\frac{\eta_{+-}}{\eta_{00}}\right|^2 \approx \left|\frac{\epsilon_K + \epsilon'_K}{\epsilon_K - 2\epsilon'_K}\right|^2 \simeq 1 + 6\mathcal{R}e\frac{\epsilon'_K}{\epsilon_K} \tag{1.40}$$

1.3.4 The Beauty Case

B mesons are simpler to deal with because $\Delta\Gamma_B \approx 0$ and $\Delta M \approx 2\,|M_{12}|$ while $\frac{q}{p} \approx e^{-2i\phi_M}$. Equation (1.36) then simplifies to:

$$\mathcal{A} = \frac{\left[1 - |\lambda|^2\right] Cos\,(\Delta M t) - 2\,|\lambda|\, Sin\,(\Delta M t)\, Sin\,(\phi_\lambda)}{1 + |\lambda|^2} \tag{1.41}$$

There exists a set of so called "*golden modes*" (like $B \to J/\psi K_s$) for which $|\lambda| \approx 1$ and the decay amplitude is dominated by one single process. In these cases:

$$\mathcal{A} \approx Sin\,(\Delta M t)\, Sin\,(\phi_\lambda) = \eta Sin\,(\Delta M t)\, Sin\,(2\phi_M - 2\phi_w) \tag{1.42}$$

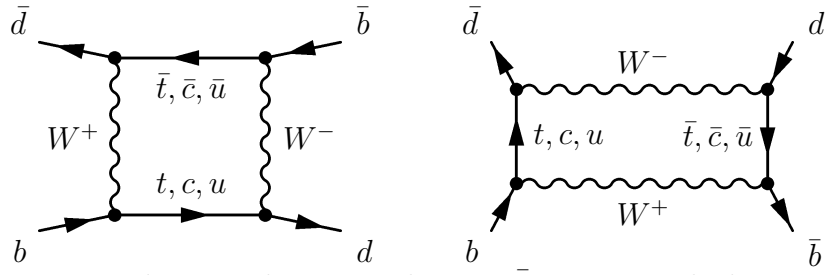

Figure 1.3: Lowest order contribution to the $B_d^\circ - \bar{B}_d^\circ$ mixing. The loops contributions are dominated by the t quark loop.

Decay Mode	ϕ_M	ϕ_w	$\phi_M - \phi_w$	Channel
$b \to c\bar{c}s$	ϕ_{td}	≈ 0	β	$B \to J/\psi K_s$
$b \to d\bar{d}d$	ϕ_{ts}	ϕ_{ub}	γ	$B_s \to \rho K_s$
$b \to u\bar{u}d$	ϕ_{td}	ϕ_{ub}	α	$B_d \to \pi\pi$

Table 1.1: Examples of ϕ_M and ϕ_λ values for some leading term weak decays of B mesons.

Now note that ϕ_M is the phase factor due to the mixing between B° and $\bar{B}^\circ$ states. Since the B meson mixing diagrams 1.3 are *top quark* dominated, ϕ_M corresponds to the phase of the V_{tx} coefficient (with x either d or s). Table 1.1 reports a list of some B decay modes with the leading terms in the Wolfenstein expansion and the corresponding ϕ_M, ϕ_λ and $\phi_M - \phi_\lambda$ values. Measuring the asymmetry $\mathcal{A}$ of such modes should in principle allow a straightforward determination of the Bjorken triangle parameters.

1.4 Conclusions: Beautiful Physics

CP violation in the b flavor became of interest after the studies which shed light on CP violation in the SM. The main consequence of this fact is that the connection between K physics and the CKM scenario is much harder than in the beauty case: the historical parameterization used in kaon physics is difficult to relate to the SM parameters, while B physics is usually pictured using more strictly the SM language. In spite of this, we can build a strict analogy between the K and B mixing formalism, due to the fact that the two systems are consequences of the same model in different approximations.
Going beyond the formalism and specifying the peculiarities of B mesons, shows that B physics is potentially a powerful instrument for the direct determination of SM parameters.

Chapter 2

Observables

What are the measurable quantities in the B meson sector which are relevant for CP violation studies? This is the question towards which this chapter is devoted. We will first discuss how the SM self-consistency can be tested through an over-determination of the interesting parameters. We will then briefly expose what are the ways in which CP violation in the B sector can be measured. Over determination of the CP violation parameters can be foreseen with these tools, thus providing either a strong SM check or an evidence for new physics.

2.1 How to Constrain the Standard Model

Two categories of measurements must be considered: those more strictly involving the relative phase of the CKM coupling constants, and those which are simply functions of their relative amplitude.
The former group can be essentially related to the measurement of angles in the Bjorken triangle (see section 1.2), while the latter implies the measurement of *sides* of the same triangle.
Since $|V_{ij}|$ determination has already been described in chapter 1, we will now mainly focus on the other category of measurements.

Let's consider the Bjorken triangle in figure 2.1: a pure measurement of the pa-

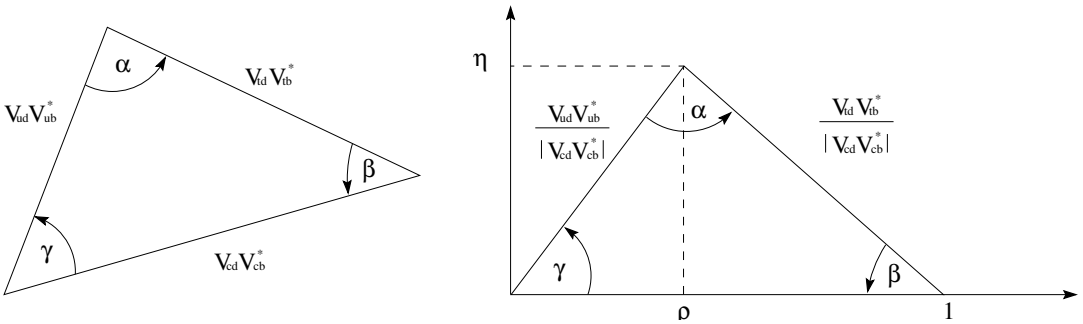

Figure 2.1: The Bjorken triangle with the corresponding V_{ij} for each triangle parameter.

rameters involved in these figures can be done by the determination of two quantities (e.g. α and η, α and γ or ρ and η). The over determination of the model can then be simply done by adding one measurement to the above: α β and γ must satisfy $\alpha+\beta+\gamma=\pi$, while γ, ρ and η must satisfy $\tan\gamma=\eta/\rho$ and so on.
Current model-dependent and model-independent analyses of the available experimental results end up in the restriction of the allowed region in the $(\bar{\rho},\bar{\eta})$ plane. Alternatively the $(Sin\,(2\beta)\,, Sin\,(2\alpha))$ plane can be used to represent physics constraints.

This $2D$ representation is possible thanks to the fact that the λ and A parameters in the Wolfenstein $(\lambda, A, \bar{\rho}, \bar{\eta})$ parameterization[1], are know at a far better level than ρ and η. We express here for convenience the relevant relations of the V_{ij} parameters with $(\lambda, A, \bar{\rho}, \bar{\eta})$:

$$\begin{array}{rcl} V_{ud}V_{ub}^{*} & = & A\lambda^{3}\left(\bar{\rho}+i\bar{\eta}\right) \\ V_{cd}V_{cb}^{*} & = & -A\lambda^{3} \\ V_{td}V_{tb}^{*} & = & A\lambda^{3}\left(1-\bar{\rho}-i\bar{\eta}\right) \end{array} \tag{2.1}$$

The sides of the unitarity triangle with vertices $\{(0,0)\,,\,(1,0)\,,\,(\bar{\rho},\bar{\eta})\}$ are:

$$\begin{array}{rcl} R_{u} & = & \left|\dfrac{V_{ub}^{*}V_{ud}}{V_{cb}^{*}V_{cd}}\right| = \sqrt{\bar{\rho}^{2}+\bar{\eta}^{2}} \\ R_{t} & = & \left|\dfrac{V_{ub}^{*}V_{ud}}{V_{cb}^{*}V_{cd}}\right| = \sqrt{\left(1-\bar{\rho}\right)^{2}+\bar{\eta}^{2}} \end{array} \tag{2.2}$$

While the angles α, β, γ are defined:

$$\begin{array}{rcl} \alpha & = & \arg\left[-\dfrac{V_{td}V_{tb}^{*}}{V_{ud}V_{ub}^{*}}\right] \\ \beta & = & \arg\left[-\dfrac{V_{cd}V_{cb}^{*}}{V_{td}V_{tb}^{*}}\right] \\ \gamma & = & \arg\left[-\dfrac{V_{ud}V_{ub}^{*}}{V_{cd}V_{cb}^{*}}\right] \end{array} \tag{2.3}$$

Finally, the relation between the $(Sin\,(2\alpha)\,, Sin\,(2\beta))$ and $(\bar{\rho},\bar{\eta})$ parameters:

$$\begin{array}{rcl} Sin\,(2\alpha) & = & \dfrac{2\bar{\eta}\left[\bar{\eta}^{2}+\bar{\rho}\left(\bar{\rho}-1\right)\right]}{\left[\bar{\eta}^{2}+\left(1-\bar{\rho}^{2}\right)\right]\left[\bar{\eta}^{2}+\bar{\rho}^{2}\right]} \\ Sin\,(2\beta) & = & \dfrac{2\bar{\eta}\left(1-\bar{\rho}\right)}{\bar{\eta}^{2}+\left(1-\bar{\rho}^{2}\right)} \end{array} \tag{2.4}$$

Let's focus for a moment on the hypothesis that an over-determination of the Bjorken triangle parameters yields incompatible results. In other words, we assume a total

[1] given that $(\bar{\rho},\bar{\eta}) = \left(1-\frac{\lambda^{2}}{2}\right)(\rho,\eta)$ we will use interchangeably during our discussion

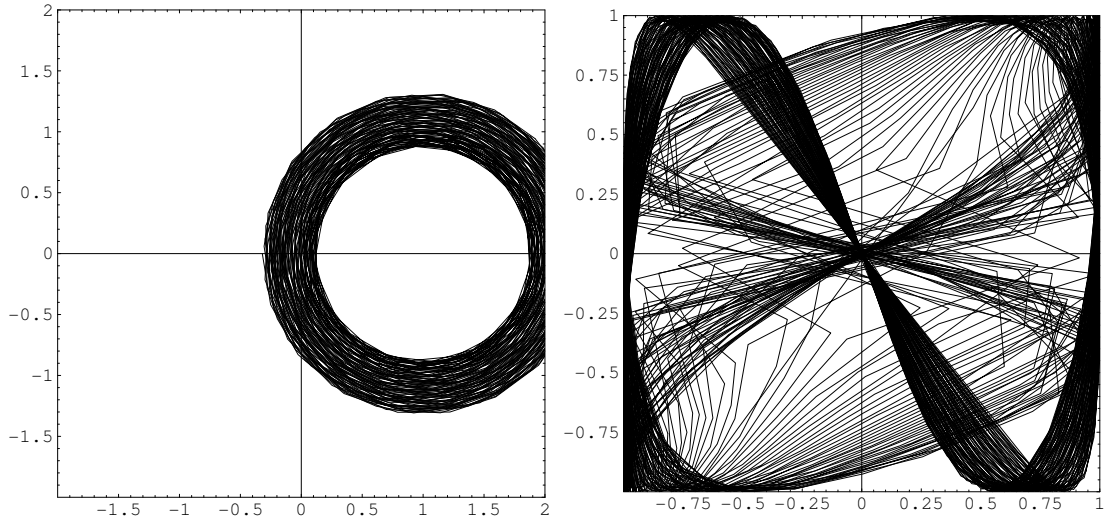

Figure 2.2: the effect of the measurement of Δm_d $(0.471 \pm 0.016\, ps^{-1})$ in terms of the corresponding allowed region (hatch) in the ρ, η plane (left) and in the $Sin\,(2\alpha)\,, Sin\,(2\beta)$ plane (right). Hatching of the allowed region in the right plot isn't uniform: the excluded region is the union of the quasi-triangular white regions near the top left and bottom right corners.

exclusion of the ρ, η and $Sin\,(2\alpha)\,, Sin\,(2\beta)$ planes. This would of course mean that the SM as we know it is incompatible with the CP violation phenomena. It is customary to call these effects *unitarity violation*, even if a physicist is much more reluctant to drop off unitarity instead of the SM. In other words, *testing the unitarity of the CKM matrix* is our goal in the sense that in the case of V_{CKM} non-unitarity we would be led to the rejection of the SM interpretation of CP violation rather than keeping a non unitary SM.

It should now be clear that direct or indirect measurements of V_{CKM} coefficients so far available restrict the allowed regions for the $\bar{\rho}, \bar{\eta}$ (or $Sin\,(2\alpha)\,, Sin\,(2\beta)$) quantities. What we want to discuss next are the general outlines of the methods so far established for the measurement of some of these quantities, together with examples of the restrictions implied by such measurements.

2.2 Asymmetry, Oscillations and Angles

Flavor oscillation is a well known consequence of the non diagonal form of the V_{CKM} matrix. Oscillation parameters are a first example of constraints on the V_{CKM} coefficients. Not being directly related to CP violation, such constraints are sometimes included in the well established world limits on the absolute values of CKM elements. The x_d oscillation frequency, for example, is related to $V_{tb}V_{td}^*$ because this process is accounted for by the standard model through box diagrams involving the top quark [14] and this yields an indirect limit on $|V_{tb}V_{td}^*|$.

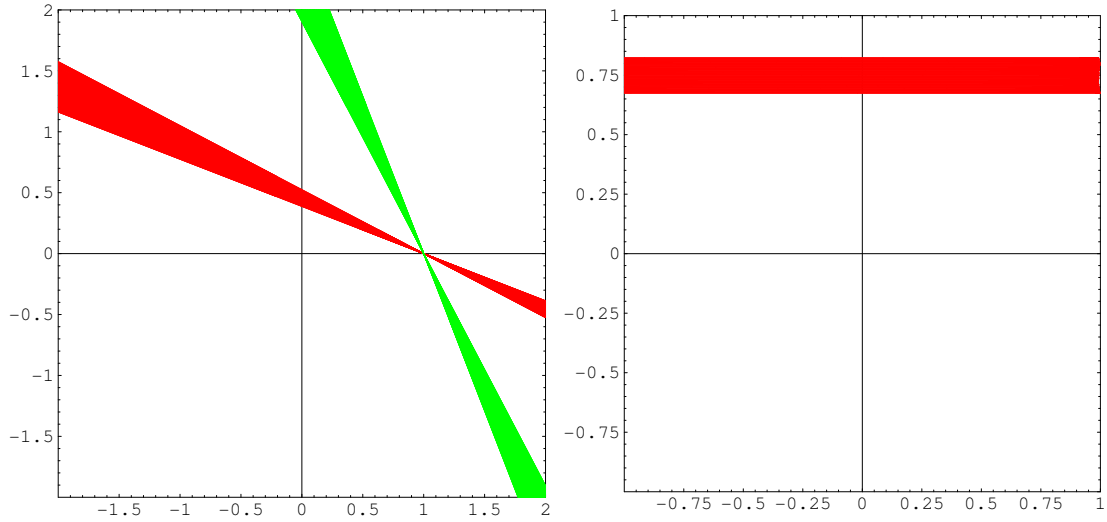

Figure 2.3: the effect of an hypothetic measurement of $Sin\,(2\beta)$ (0.75 ± 0.076) in terms of the corresponding allowed region (hatch) in the ρ, η plane (left) and in the $Sin\,(2\alpha)\,, Sin\,(2\beta)$ plane (right).

If this limit is not included in the overall determination of the V_{ij} coefficients, we can use it as a restriction in the ρ, η plane: figure 2.2 shows the effect of the measurement of Δm_d $(0.471 \pm 0.016\, ps^{-1})$ in terms of the corresponding allowed region in the two parameter planes defined above.

A deeper discussion is devoted to the case of CP violation related measurements involving the α, β and γ angles. The direct measurement of the Bjorken angles is foreseen as experimentally feasible (with difficulty) for α and β through the measurement of $Sin\,(2\alpha)$ and $Sin\,(2\beta)$. This explains the phenomenological preference for the $Sin\,(2\alpha)\,, Sin\,(2\beta)$ plane in the discussion.
The $Sin\,(2\beta)$ measurement (and analogously $Sin\,(2\alpha)$) is usually performed in the B_d sector via the measurement of a *decay asymmetry* $\mathcal{A}$ of the neutral meson into a CP eigenstate. For example, a well known clean measurement of the $Sin\,(2\beta)$ parameter comes from the asymmetry $\mathcal{A}_{B\to J/\psi K_s}$ in the decay $B \to J/\psi K_s$ (see section 3.3 pg. 45 for details).

The measurement result is directly [2] $Sin\,(2\beta)$ and yields a straightforward restriction in the $Sin\,(2\alpha)\,, Sin\,(2\beta)$ plane. In the case of a $Sin\,(2\beta)$ measurement visualizing the allowed region is quite immediate, given the privileged position of β in the Bjorken triangle (see fig. 2.3). Note that the measurement of $Sin\,(2\beta)$ leaves a 4-fold ambiguity in the determination of β: $\beta, \pi+\beta, \frac{3}{2}\pi-\beta$ and $\frac{\pi}{2}-\beta$ give the same $Sin\,(2\beta)$ value. This reflects, in the case of the $Sin\,(2\beta)$ measurement in a two-fold compatibility region.

[2] Note that in many cases the proper direct result is contaminated by a spurious phase $(Sin\,(2\beta)+\delta)$. In these cases we assume that an extraction of $Sin\,(2\beta)$ is however feasible through a theoretical/experimental estimate of δ.

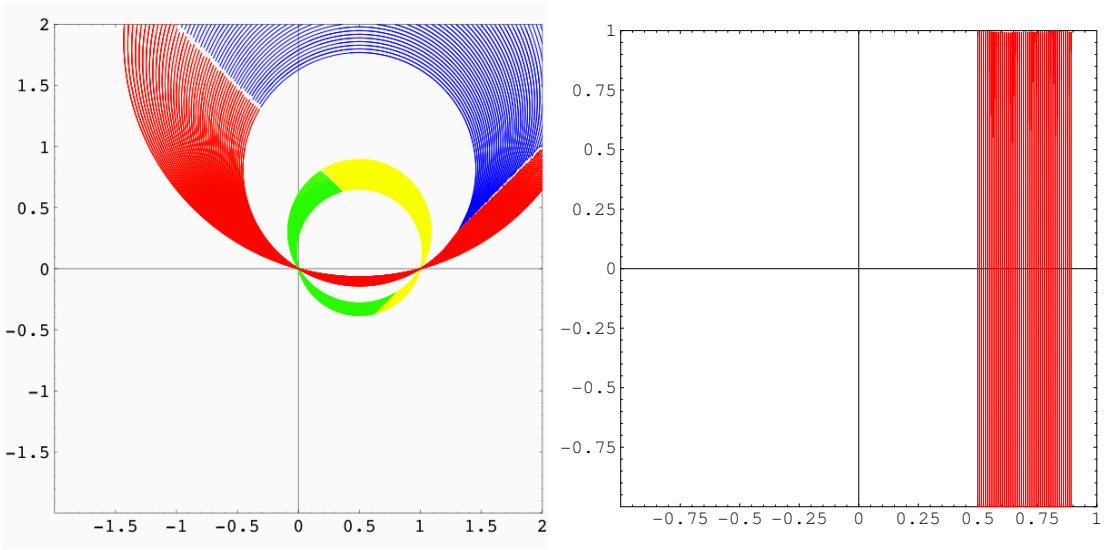

Figure 2.4: the effect of an hypothetic measurement of $Sin\,(2\alpha)$ (0.7 ± 0.2) in terms of the corresponding allowed region (hatch) in the ρ, η plane (left) and in the $Sin\,(2\alpha)\,, Sin\,(2\beta)$ plane (right). The outer circle corresponds to α and $\pi + \alpha$ while the smaller one is given by the values $\frac{\pi}{2} - \alpha$ and $\frac{3}{2}\pi - \alpha$. Coloring of the different parts of the allowed regions isn't relevant in this discussion.

The resulting ρ, η constraint of a $Sin\,(2\alpha)$ measurement needs a little geometrical discussion. α is the angle under which the points $(0,0)$ and $(1,0)$ are seen by the Bjorken triangle vertex. The definition of a single value of α reflects into the restriction of the ρ, η point on a circular arc passing through $(0,0)$ and $(1,0)$ [3]. The consequence is that the region bounded by a $Sin\,(2\alpha)$ measurement in the ρ, η plane (see fig. 2.4) is composed of 4 circular arcs (corresponding to the angles $\alpha, \pi + \alpha, \frac{3}{2}\pi - \alpha$ and $\frac{\pi}{2} - \alpha$) *smeared* by the measurement error.

$Sin\,(2\gamma)$ is indirectly accessible through the $Sin\,(2\alpha)$ and $Sin\,(2\beta)$ estimates, if one assumes unitarity. Recently methods have been proposed for the direct determination of γ (see, for example, [15]).
A limit on $Sin\,(2\gamma)$ would have an impact similar to the $Sin\,(2\beta)$ measurement as far as the ρ, η variables are concerned (see fig. 2.5). In the $Sin\,(2\alpha)\,, Sin\,(2\beta)$ plane a $Sin\,(2\gamma)$ constrained region defines two elliptical corona because of the usual degeneracy in the γ determination given $Sin\,(2\gamma)$.

The direct determination of $Cos\,(\gamma)$ has been suggested in [15] through the measurement of the ratio $\frac{\Gamma\left(B^{\pm} \to K^{\circ}\pi^{\pm}\right)}{\Gamma(B^{\pm} \to K^{\pm}\pi^{\circ})}$. This would lead to a constraint in the ρ, η plane not different from the one of figure 2.5 (see figure 2.6). Note also that a simultaneous determination of $Cos\,(\gamma)$ and $Sin\,(2\gamma)$ would allow the partial removal of the

[3] This is a straightforward consequence of the fact that given a segment AB, the set of points under which the segment AB is seen with the same angle α is a circular arc passing through A and B. The circular arc lies all to the same side with respect to A and B: its symmetric with respect to AB corresponds to the opposite angle $-\alpha$. Note also that the arc which complements the one described to a circle corresponds to an angle which is $\pi + \alpha$.

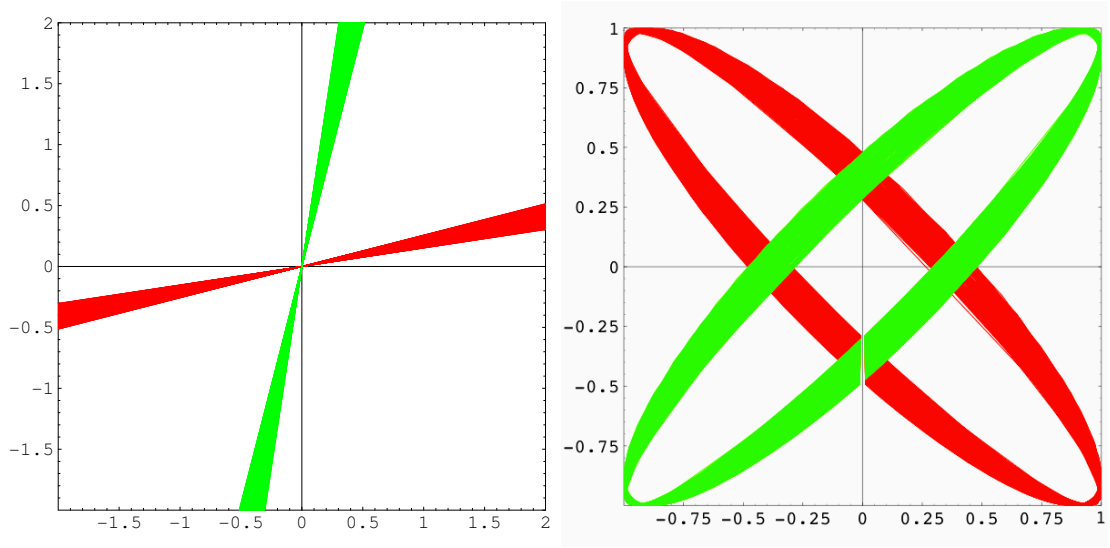

Figure 2.5: the effect of an hypothetic measurement of $Sin\,(2\gamma)$ (0.2 ± 0.05) in terms of the corresponding allowed region (hatch) in the ρ, η plane (left) and in the $Sin\,(2\alpha)\,, Sin\,(2\beta)$ plane (right).

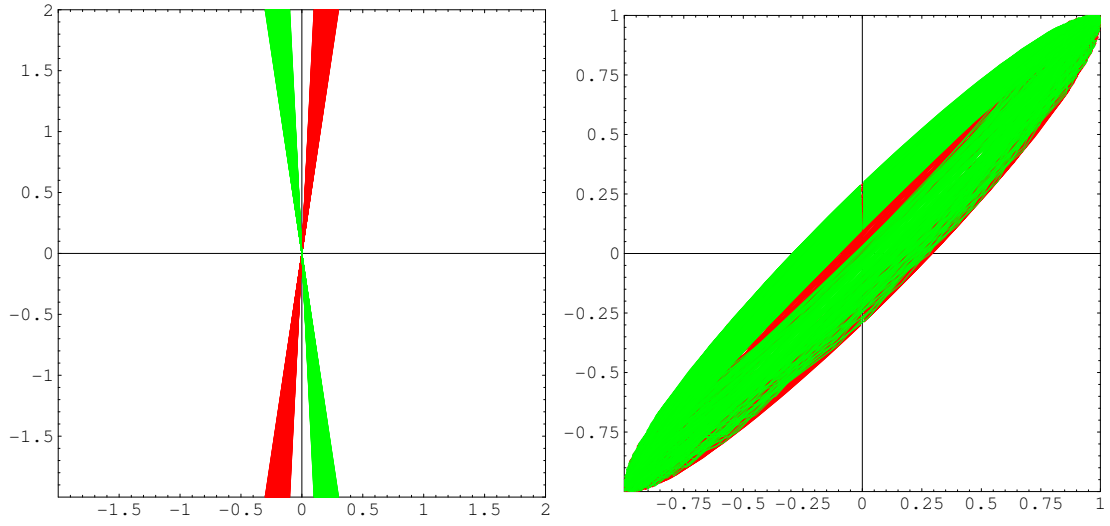

Figure 2.6: the effect of an hypothetic measurement of $Cos\,(\gamma)$ (0.1 ± 0.05) in terms of the corresponding allowed region (hatch) in the ρ, η plane (left) and in the $Sin\,(2\alpha)\,, Sin\,(2\beta)$ plane (right).

Decay	V_{ij} involved	Suppression	Relative Scale
$B^+ \to \bar{D}^\circ K^+$	$V_{us}V_{cb}^*$	$A\lambda^3$	1
$B^- \to D^\circ K^-$	$V_{cb}V_{us}^*$	$A\lambda^3$	1
$B^+ \to D^\circ K^+$	$V_{cs}V_{ub}^*$	$A\lambda^3\left(\bar{\rho}+i\bar{\eta}\right)$	~ 0.01
$B^- \to \bar{D}^\circ K^-$	$V_{ub}V_{cs}^*$	$A\lambda^3\left(\bar{\rho}-i\bar{\eta}\right)$	~ 0.01
$B^+ \to D_+^\circ K^+$	$V_{cs}V_{ub}^*$	$A\lambda^3\left(\bar{\rho}+i\bar{\eta}\right)$	~ 0.01
$B^- \to D_+^\circ K^-$	$V_{cs}V_{ub}^*$	$A\lambda^3\left(\bar{\rho}+i\bar{\eta}\right)$	~ 0.01

Table 2.1: Relative scale and ordering using the Wolfenstein parameterization for the BR of the various decay channels discussed in the text.

degeneracy induced by the $Sin\left(2\gamma\right)$ measurement in the ρ,η plane. The degeneracy in the $Sin\left(2\alpha\right), Sin\left(2\beta\right)$ plane and the ones produced by the other measurements ($Sin\left(2\alpha\right)$ and $Sin\left(2\beta\right)$) in the ρ,η plane aren't however removed.

2.3 *Self Tagging* Modes

The latter method proposed for the measurement of $Cos\left(\gamma\right)$ has a peculiarity which we want to stress further. The measurement of $Sin\left(2\alpha\right)$, $Sin\left(2\beta\right)$ and $Sin\left(2\gamma\right)$ is often addressed through measurement of time dependent or time integrated CP -*asymmetry*: the underlying idea is that of choosing a CP eigenstate for the B (either B_d or B_s) meson decay products, thus measuring the time-dependent or time integrated CP asymmetry. This asymmetry is often given by an expression of the form $Sin\left(2\Phi+\delta\right)$ (where $\Phi \in \{\alpha,\beta,\gamma\}$ and δ is an additional phase factor often difficult to determine). With an estimate of δ, this yields the desired measurement of Φ.
The asymmetry measurement requires the restriction of the reconstructed event sample to the cases in which the B flavor at origin can be determined. This usually means a further reduction of the sample of about one order of magnitude due to tagging efficiency effects.

Recent studies ([16], [15], [17], [18]) shed light on the possibility of determining γ through the simple measurement of *branching ratios*. The appeal of this approach is that the decay modes involved don't require the use of *tagging algorithms*. This means that *efficiency* and *dilution* don't contribute to the degradation of the measurement resolution. Generally speaking these methods usually reduce to a bare event counting operation, maximizing the experiment acceptance. This is a significant improvement with respect to the *oscillation* analyses, where only a few percent of the signal can be used (see for example section 3.3.3 at page 47).

Let's discuss as an example the procedure for the determination of γ as described in [19]. The basic approach is that of using charged B decays into a $K^\pm D^\circ$ pair[4]. The decays chosen are (see table 2.1):

1. $B^+ \to \bar{D}^\circ K^+$

[4]Remember that $\gamma = \arg V_{ub}^*$

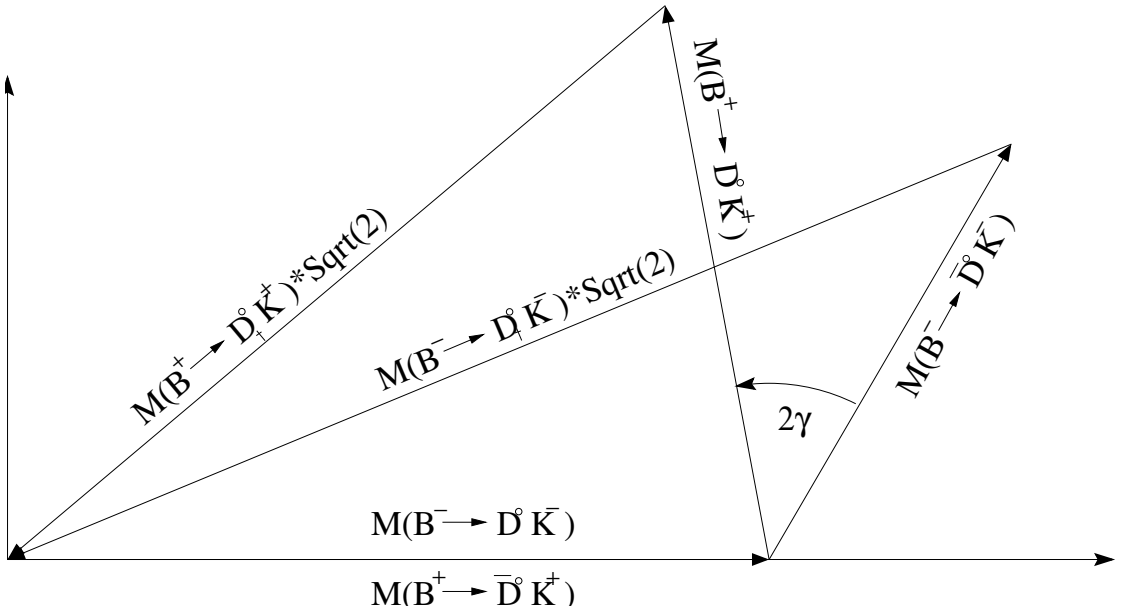

Figure 2.7: Complex plane sketch of the relations 2.7 and 2.8.

2. $B^- \to D^\circ K^-$
3. $B^+ \to D^\circ K^+$
4. $B^- \to \bar{D}^\circ K^-$
5. $B^+ \to D^\circ_\dagger K^+$
6. $B^- \to D^\circ_\dagger K^-$

Where a † identifies CP **even** eigenstates. The decay amplitudes (1,2) and (4,3) are CP conjugated[5]:

$$\mathcal{M}\left(B^- \to D^\circ K^-\right) = |V_{us}|\,|V_{cb}|\,|A|\,e^{i\Delta_A} \propto \mathcal{M}\left(B^+ \to \bar{D}^\circ K^+\right) \tag{2.5}$$

$$\mathcal{M}\left(B^- \to \bar{D}^\circ K^-\right) = |V_{ub}|\,e^{-i\gamma}\,|V_{cs}|\,|a|\,e^{i\Delta_a} \propto \mathcal{M}\left(B^+ \to D^\circ K^+\right) e^{-2i\gamma} \tag{2.6}$$

The decay amplitudes (1,3,5) and (2,4,6) are expected to satisfy (disregarding CP violating effects in the D meson sector) the relations:

$$\sqrt{2}\mathcal{M}\left(B^+ \to D^\circ_\dagger K^+\right) = \mathcal{M}\left(B^+ \to \bar{D}^\circ K^+\right) + \mathcal{M}\left(B^+ \to D^\circ K^+\right) \tag{2.7}$$

$$\sqrt{2}\mathcal{M}\left(B^- \to D^\circ_\dagger K^-\right) = \mathcal{M}\left(B^- \to \bar{D}^\circ K^-\right) + \mathcal{M}\left(B^- \to D^\circ K^-\right) \tag{2.8}$$

Which imply the existence of two triangles in the complex plane with one side in common (see figure 2.7). This relation in principle allows the extraction of γ from the determination of the branching ratios connected with the elements in equations 2.7 and 2.8. Two difficulties arise with this method:

[5] A and a denote the magnitude of the hadronic matrix elements for the corresponding states, and Δ_a, Δ_A their phase

- The triangles in figure 2.7 are flattened: $BR\left(B^+ \to \bar{D}^\circ K^+\right) \approx BR\left(B^+ \to D^\circ K^+\right)/100$. This means that the process of extracting γ involves the combination of two quantities of different orders of magnitude (the two BR) and makes it practically challenging.

- Because of the way in which the method is designed, it suffers not only for the previous statistical effects but also from an ineludible source of background: to use eqns. 2.7 and 2.8 we must choose a specific decay channel for the D° meson; the most interesting one, notably $D^\circ \to K^-\pi^+$, gives as final decay chain for the B^+ meson: $B^+ \overset{\sim 10^{-6}}{\longrightarrow} K^+ D^\circ \overset{\sim 10^{-1}}{\longrightarrow} K^+\left[K^-\pi^+\right]$. Now the problem is that the same final products are obtained: $B^+ \overset{\sim 10^{-4}}{\longrightarrow} K^+ \bar{D}^\circ \overset{\sim 10^{-3}}{\longrightarrow} K^+\left[K^-\pi^+\right]$. Due to the conspiracy of Cabibbo suppressions and the branching ratios mentioned above, these two final states have a total BR of the same order of magnitude (10^{-7}) and the same final states.

These objections are such that even if theoretically clean, this method becomes unpractical. However, we will see in the next subsection that we can take advantage of the very same problems to build a method of measuring γ based on the same scheme.

2.3.1 An Evolution

The obstacles which arose with the method described above can help [16] in the determination of γ. Let's define:

$$\begin{array}{ll} a = BR\left(B^+ \to K^+ \bar{D}^\circ\right) & b = BR\left(B^+ \to K^+ D^\circ\right) \\ c\left(f\right) = BR\left(\bar{D}^\circ \to f\right) & c\left(\bar{f}\right) = BR\left(\bar{D}^\circ \to \bar{f}\right) \\ d = BR\left(B^+ \to K^+\left[f\right]\right) & \bar{d} = BR\left(B^+ \to K^+\left[\bar{f}\right]\right) \end{array}$$

Where $B^+ \to K^+\left[x\right]$ is a short for $B^+ \to K^+\left[\bar{D}^\circ \to x\right]$. These quantities must satisfy[6]:

$$d = ac\left(f\right) + bc\left(\bar{f}\right) + 2\sqrt{abc\left(f\right)c\left(\bar{f}\right)}Cos\left(\xi + \gamma\right) \tag{2.9}$$

$$\bar{d} = ac\left(f\right) + bc\left(\bar{f}\right) + 2\sqrt{abc\left(f\right)c\left(\bar{f}\right)}Cos\left(\xi - \gamma\right) \tag{2.10}$$

Where the phase ξ has been introduced to account for other effects (hadronic and non CP violating interactions). All the terms in these relations have now the same order of magnitude, since we are alternating doubly Cabibbo-suppressed and Cabibbo-allowed decays of the D° meson. This cancels the first difficulty.

[6] Given that:

$$\mathcal{M}\left(B^+ \to K^+ f\right) = \mathcal{M}\left(B^+ \to K^+ \bar{D}^\circ\right) \cdot \mathcal{M}\left(\bar{D}^\circ \to f\right) + \mathcal{M}\left(B^+ \to K^+ D^\circ\right) \cdot \mathcal{M}\left(D^\circ \to f\right)$$
$$\mathcal{M}\left(B^- \to K^- \bar{f}\right) = \mathcal{M}\left(B^- \to K^- \bar{D}^\circ\right) \cdot \mathcal{M}\left(\bar{D}^\circ \to \bar{f}\right) + \mathcal{M}\left(B^+ \to K^+ D^\circ\right) \cdot \mathcal{M}\left(D^\circ \to \bar{f}\right)$$

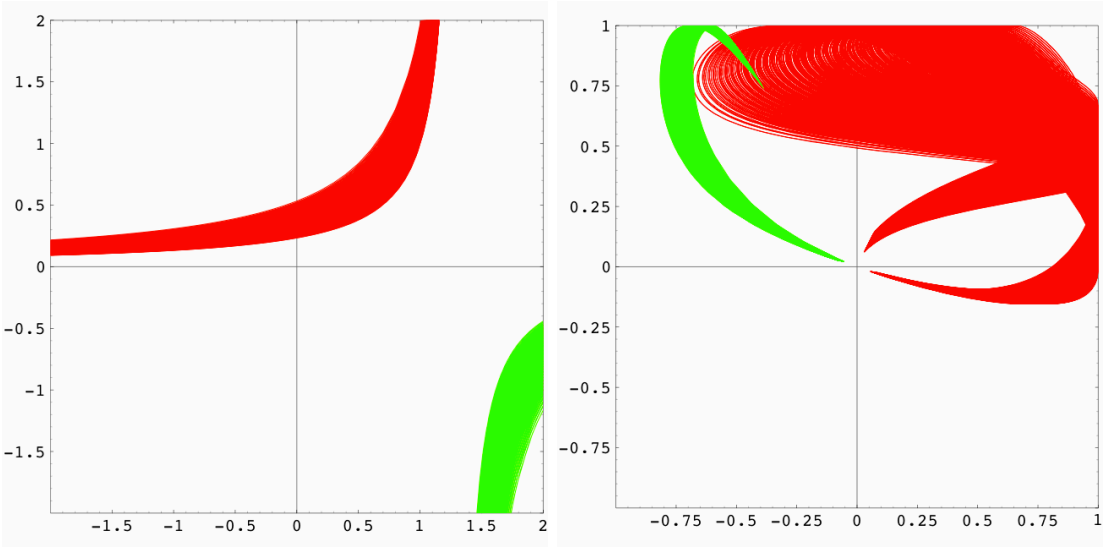

Figure 2.8: the effect of the measurement of ε_K in terms of the corresponding allowed region (hatch) in the ρ, η plane (left) and in the $Sin\left(2\alpha\right), Sin\left(2\beta\right)$ plane (right).

Note also that adding new D° decay modes to the measurement means introducing for each of them a pair of equations like 2.9 and 2.10. This can eventually compensate the fact that one or more of the BR involved is unknown.
This method needs the measurement of branching ratios only, and returns a set of measurements of γ (and the possibly mode-specific phases ξ_n): $\pm\left(\gamma \pm \xi_n\right)$. This would leave only a sign ambiguity on the value of γ, just like the measurement of $Cos\left(\gamma\right)$ (see figure 2.6).

2.4 Bjorken and the Kaons

Restrictions of the $(\bar{\rho}, \bar{\eta})$ allowed region are obtained also from the study of non-*beauty* mesons. CP violation has been historically introduced because of the *strange* behavior of K mesons and in fact the parameters ε_K and ε'_K can be related to $\bar{\rho}$ and $\bar{\eta}$.
ε_K is related to $\bar{\rho}, \bar{\eta}$ by an hyperbola in the $\bar{\rho}, \bar{\eta}$ space (see [20]). Using the values reported in [20] and [13] we obtain the confidence region reported in figure 2.8. It should be noted that the dominating uncertainty is that on the calculations of the hadronic interactions involved and on $|V_{cb}|$ [20].

Recently, a measurement[7] of $\varepsilon'_K/\varepsilon_K$ has been claimed by the KTeV collaboration [21]. The quoted result is $\mathcal{R}e\,\varepsilon'_K/\varepsilon_K = (28.0 \pm 3.0 \pm 2.8)\,10^{-4}$.
The prediction of the SM yields [20]:

$$\varepsilon'_K/\varepsilon_K = \mathcal{I}m\lambda_t F\left(x_t\right) = |V_{cb}|^2\,\lambda\bar{\eta}F\left(x_t\right) \tag{2.11}$$

[7] due to editorial issues we could not cover the more recent NA48 measurement which is consistent with the previous NA31 measurements, confirmed by the KTeV collaboration

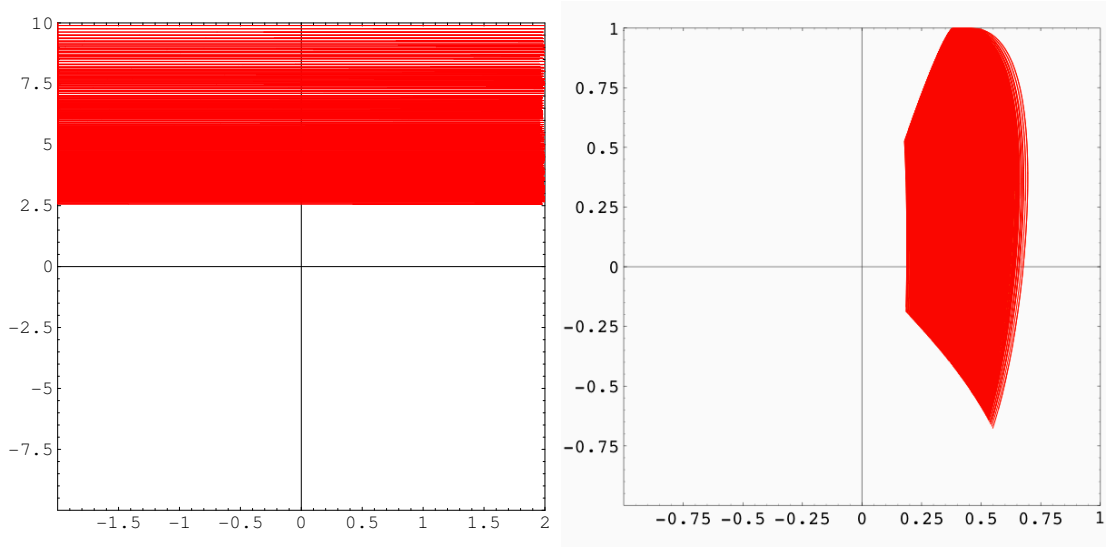

Figure 2.9: the effect of the measurement of ε'_K in terms of the corresponding allowed region (hatch) in the ρ, η plane (left) and in the $Sin\,(2\alpha)\,, Sin\,(2\beta)$ plane (right).

Where $F\,(x_t)$ represents a sum of top-mass-dependent functions that also depend on $\Lambda_{\bar{MS}}$ and hadronic matrix elements, which in turn depend on the charm-quark mass and the strange-quark mass.
The larger uncertainty in these conditions is shared between the measurement of $\varepsilon'_K/\varepsilon_K$ and the theoretical estimate of $F\,(x_t)$. The resulting constrained region in the ρ, η plane and in the $Sin\,(2\alpha)\,, Sin\,(2\beta)$ plane is the one reported in figure 2.9. Note that since equation 2.11 is proportional to $\bar{\eta}$, the confidence interval in the $\bar{\rho}, \bar{\eta}$ plane is simply an horizontal band.

2.5 CDF II *Shopping List*

Which CKM elements are measurable by CDF II? Which physics channels are usable? No firm answer can be given in principle, but reach estimates are needed in order to define trigger strategies and techniques.
The new Silicon Vertex Trigger gives access to non leptonic B decays, but its possibilities are largely unexplored. Only few studies, some of which will be outlined in the following chapters, have been detailed at a level sufficient to yield specific trigger proposal.
The identification of new candidate analyses and possibilities is in progress. Channels currently investigated are:

- $B \to \pi^+\pi^-$: the historical reference for the determination of $Sin\,(2\alpha)$. This channel is now known to be plagued by the presence of electromagnetic penguin contributions. Work-arounds for this "defect" have been studied.
  Two set of "cures" have been found: the first one [20], [22] is hard to implement at CDF, since it requires a detailed isospin analysis of the decay in order to

isolate a sample immune from penguin contributions. The second cure [23] is more interesting in our case, since it simultaneously determines β and γ from the measurement of the *time-dependent asymmetry in the decays* $B_d \to \pi^+\pi^-$ *and* $B_s \to K^+K^-$.

The possibility of building a completely hadronic B trigger is the fundamental fact giving CDF II access to these decay channel.

- $B \to J/\psi K_s$ This is the universally recognized *golden* B_d channel for the determination of $Sin\,(2\beta)$. This channel has already been discussed in section 3.3. Here we add only the observation that a measurement of the $B_s \to J/\psi K_s$ decay could serve as a check on asymmetry effects independent from the tree level contribution given by β. It has also been suggested [24] that direct CP violation in $B_s \to J/\psi K_s$ could be measurable, thus allowing a measurement of $Sin\,(2\gamma)$.
  The improved detector performance and accelerator luminosity will allow CDF to reach a resolution $\delta Sin\,(2\beta) \approx 0.1$.

- $B_s \to D_s^{\pm} K^{\mp}$ Is one of the accessible modes for the measurement of γ at CDF II [25]. Recent estimates [26] suggest that the signal/background ratio might be acceptable and should allow an error in $Sin\,(\gamma)$ ranging from 0.43 to 0.79. Even if the final state is not a CP eigenstate, the study of the time-dependence of the four BR (distinguished for the flavor of the initial state and the charge distribution in the final state) should allow to measure γ. The decay mode is mainly hadronic, and its feasibility is once more connected to a careful exploit of the hadronic B trigger. The analysis uncertainty in this case is higher, since the time scale to be studied is that of the B_s flavor oscillation, still to be determined but presumably rather small.

- $B \to \rho\pi$ ($B \to \rho^\circ\pi^\circ, B \to \rho^+\pi^-, B \to \rho^-\pi^+$) is expected to allow a measurement of α without the ambiguities due to penguin contributions. The strategy [27] is that of fitting all the unknown parameters in the decays $B \to \rho^\circ\pi^\circ, B \to \rho^+\pi^-, B \to \rho^-\pi^+$ through the study of the Dalitz plot in the final state $\pi^+\pi^-\pi^\circ$. In [27] it is shown that a good accuracy on α can be obtained with a sample as small as 1000 $B \to \rho\pi$ events.
  Also in the case of $B \to \rho\pi$ an hadronic B trigger is the only hope for the measurement of this channel. The main difficulty of this analysis is due to the presence of a neutral pion in the final state, which is difficult to identify and reconstruct in our environment.

- $B^{\pm} \to K^\circ\pi^{\pm}, B^{\pm} \to K^{\pm}\pi^\circ$ The measurement of the fraction $R_* = \frac{\Gamma\left(B^{\pm}\to K^\circ\pi^{\pm}\right)}{2\Gamma(B^{\pm}\to K^{\pm}\pi^\circ)}$ alone, or completed with the asymmetries in the two channels would allow to constrain in a model-independent way the phase γ [15]. Detection of the neutral pions is the main issue also in this case. A fully hadronic trigger is also needed.

- $B_s \to J/\psi\phi$ The SM predicts small CP violation effects in this channel: significant asymmetry would be an unambiguous signal of new physics. Moreover,

this is a good candidate for the determination of ΔM_s and $\Delta\Gamma_s$ from the corresponding angular distributions [28]. The hadronic contribution to the uncertainties of SM calculations for this channel can be estimated through the study of the $B_d \to J/\psi\rho^\circ$ channel [29]. Estimates performed using Run I data [4] suggest that the yield for $B_d \to J/\psi\rho^\circ$ is roughly 60% that for $B \to J/\psi K_s$. This means that we should expect about 9000 events for this decay mode. An efficiency improvement ranging from 2% to 5% and an $\epsilon D^2 \approx 10\%$ are expected with the use of the TOF system. The precision on the asymmetry is expected to be about ± 0.09, but this estimate is optimistic because it doesn't take into account the additional difficulty of resolving the B_s oscillations.

2.6 Conclusions

In this chapter we described how the SM can be constrained and possibly over-constrained using experimental data. In particular we have shown what's the working principle of the measurements based on the so-called *self-tagging* modes. For each measurement type we have shown the confidence regions in the (ρ, η) and $(Sin\,(2\alpha)\,, Sin\,(2\beta))$ planes.
From the brief discussion on the B decay channels under study at CDF, the importance of fully hadronic B decays clearly emerged: most leptonic channels have already been exploited in CDF I, and the CDF II improvement will be mostly statistical. On the contrary, hadronic B decays are totally new to CDF.
The list of possibilities must not be considered exhaustive: new phenomenological approaches are actively being studied and might soon produce new ways to measure SM parameters.

Chapter 3

The Experimental Framework: Detectors and Techniques

This chapter contains a quick description of the CDF II experiment, particularly focused on the parts more relevant for our work. A complete CDF II description can be found in [4]: this subject has been thoroughly described in so many places that the reader probably does not need to find here another detailed description of our detector. For this reason we find more practical and useful to quickly point out what are the essentials needed to go on reading the following chapters. The chapter provides also a few examples of detectors of the same generation, pointing out what are the main issues and expected results in the measurements we are interested in. The second part of this chapter will introduce some analysis techniques of general interest in CP violation measurements and their specific implementation in CDF, using the Run I $Sin\,(2\beta)$ measurement as a benchmark example.

3.1 General Comparison

Modern *beauty* production techniques can be classified on the basis of the different S/N ratio at production, the type of mesons and/or baryons produced, and also for the different production Lorentz boost (see table 3.1). The latter, when significant, allows lifetime measurements. Production cross section ($\sigma_{b\bar{b}}$) values suggest that $p\overline{p}$ colliders are the ideal environment for B physics. The universal plague of these environments is the small $\sigma_{b\bar{b}}/\sigma_{tot}$ ratio, which translates in the fact that B signals must be dug up from the huge hadronic background. Moreover, at reconstruction level the event is still polluted by the soft exchanges accompanying the hard interaction: the *underlying event*.
The larger statistics of the hadronic environment (with respect to a leptonic machine) can be exploited only for those decay channels for which a good efficiency and an high background rejection factor are achievable.

The main advantage of fixed target experiments is the possibility of achieving a good geometrical coverage with small detectors.

The $\Upsilon\,(4S)$ resonance decay is dominated ($\approx 96\%$) by the production of a $B\bar{B}$

Machine	Experiment	$\sqrt{s}\,(GeV)$	Type	$\mathcal{L}\,(fb/y)$	$\sigma_{b\bar{b}}\,(nb)$	$\sigma_{b\bar{b}}/\sigma_t$	$N_{b\,\bar{b}}/y$
DORIS	?	10.6	$e^+\,e^-$	0.2	1.15	0.25	$2{\cdot}10^5$
CESR	CLEO	10.6	$e^+\,e^-$	1	1.15	0.25	$1{\cdot}10^6$
LEP	Delphi, ...	93.0	$e^+\,e^-$	0.1	5.0	0.14	$5{\cdot}10^5$
Tevatron	CDF,D0	$1.8{\cdot}10^3$	$p\,\overline{p}$	0.05	$40{\cdot}10^3$	$7{\cdot}10^{-4}$	$2{\cdot}10^9$
KEKB	BELLE†	10.6	$e^+\,e^-$	100	1.15	0.2	$1{\cdot}10^8$
PEPII	BaBar	12	$e^+\,e^-$	30	1.15	0.2	$3.5{\cdot}10^7$
HERA	HeraB†	820*	$p\;e^\pm$	0.3	12	$9{\cdot}10^{-7}$	$3.7{\cdot}10^8$
Tevatron	BTEV†	$2.0{\cdot}10^3$	$p\bar{p}$	1	$100{\cdot}10^3$	$\sim 10^{-3}$	$1{\cdot}10^{11}$
" Upgr.	CDF, D0	$2.0{\cdot}10^3$	$p\,\overline{p}$	1	$50{\cdot}10^3$	$7{\cdot}10^{-4}$	$5{\cdot}10^{10}$
LHC†	LHCB†	$1.4{\cdot}10^4$	$p\,p$	5	$500{\cdot}10^3$	$5{\cdot}10^{-3}$	10^{12}

Table 3.1: b-quark production main features for various accelerator/detector configurations. A † indicates detectors and/or accelerators still under development/construction. *: HeraB is a $p-target$ experiment where the target interacts with the proton beam halo: the proton beam energy is reported in the $\sqrt{s}$ column.

coherent state[1]. This suggests that an e^+e^- collider tuned at the $\Upsilon\,(4S)$ resonance with an adequate luminosity might be one of the best tools for investigating CP violation in the B meson decays. The advantages of this possibility are a cleaner signal and an easier trigger system, which are however paid with a smaller production rate.

3.1.1 B Factories: BaBar and BELLE

Current $\Upsilon\,(4s)$ experiments produce this resonance in a moving reference frame with respect to the laboratory rest frame: this allows to spatially separate the decay vertices of the two B mesons decaying at different times. In the case of BABAR/PEP-II, for example, the Υ is on average produced with a boost of $\beta\gamma = 0.56$ which corresponds to an average separation of $\beta\gamma c\tau = 250\,\mu m$ between the two B vertices.
There are currently two similar devices at work in the world: the BaBar detector observing collisions produced by the PEP II accelerator at the Stanford Linear Accelerator Laboratory (SLAC), and the BELLE experiment at the KEKB collider in Japan. The typical $B\bar{B}$ production cross section in this environment is of the order of $1\,nb$, with design integrated luminosities of the order of $100\,fb^{-1}/year$. Compared to the CDF hadronic environment this translates typically into cleaner samples with smaller statistics at production.

[1] *à la Einstein-Podolsky-Rosen*

Superlayer	Inner Radius [cm]	Cells/Layer	Stereo Angle [$mrad$]
1	26.04	96	0
2	31.85	112	+[44.9-50.0]
3	37.05	128	-[52.3-57.4]
4	42.27	144	0
5	48.08	176	+[55.6-59.7]
6	53.32	192	-[62.8-66.9]
7	58.54	208	0
8	64.30	224	+[65.0-68.5]
9	69.52	240	-[72.1-75.8]
10	74.72	256	0

Table 3.2: Layer arrangement for the BaBar Drift Chamber

3.1.1.1 BaBar

BaBar [1, 20] is the detector observing collisions of $9\,GeV$ electrons and $3.1\,GeV$ positrons accumulated in the storage rings of the PEP-II B-factory.
The structure of the BaBar detector is that of a huge spectrometer, with an asymmetric organization driven by the boost direction of the Υ. BaBar collected the first data in May 1999.
The BaBar detector is currently organized as follows:

- The **tracking system** is built within a $1.5\,T$ superconducting solenoid, producing an axial magnetic field. Two devices provide high resolution tracking with excellent efficiency:

  - the **Silicon Vertex Tracker** is a five-layer silicon-strip vertex detector which provides both the required vertex resolution for resolving B displaced decay vertices and stand-alone tracking for low p_t ($< 120\,MeV/c$) particles which cannot be measured by the central tracking chamber. The achieved impact parameter resolution is of the order of $35\,\mu m$ in the transverse plane and about $50\,\mu m$ along the longitudinal axis for $2\,GeV/c$ tracks. The polar angle coverage is $-0.87 < cos\theta_{lab} < 0.96$, with a Two-track vertex resolution of about $50\,\mu m$ for reconstructed J/ψ, and a z resolution on the B vertices separation of the order of $110\,\mu m$.

  - The **Drift Chamber** (DCH [30]) is a cylindrical wire chamber placed in the $26\,cm - 75\,cm$ radial interval. It consists of 10 wire layers, organized in stereo and axial groups (see table 3.2).
    The average single point resolution achieved is about $125\,\mu m$, with a dE/dx resolution of about 7.5%. The DCH provides charged particle tracking for objects with $p_t > 100\,MeV/c$. Since the distribution of the decay products is asymmetric, the drift chamber center is longitudinally displaced of $36.7\,cm$ with respect to the nominal PEP-II interaction point. This allows covering the polar angle range $-0.92 < cos\theta_{lab} < 0.96$.

- The heart of the *particle identification* system is the Detector of Internally Reflected Cherenkov light (**DIRC** [31, 32, 33, 34, 35, 36]). Charged particles exiting the DCH encounter a cylindrical distribution of 144 fused silica quartz bars of $17\,mm \times 35\,mm \times 4.9m$ ($\delta r \times \delta\phi \times \delta z$). A special low magnetic field volume outside the BaBar return yoke hosts 10752 photomultiplier tubes which are coupled through a water bath to the end of the quartz bars. These PMT's are used to measure the angles of Cherenkov photons with respect to the particle direction for particles above the Cherenkov threshold.
  The average single-photon angular resolution is about $10.2\,mrad$. An average track produces 30 Cherenkov photons and gives a Cherenkov angle resolution of about $2.8\,mrad$ rms, allowing a 3σ $K-\pi$ separation for particles with momenta as large as $3\,GeV/c$.

- Electromagnetic Calorimetry is provided by 6580 CsI crystals $T\ell I$-doped [37]. Each crystal is a truncated trapezoidal pyramid $16-17.5$ radiation lengths thick. The whole calorimeter is organized in a quasi-projective structure covering $-0.78 < cos\theta_{lab} < 0.96$. Each crystal read-out is provided by 2 large ($2\,cm^2$) PIN photodiodes. The resulting electromagnetic energy resolution is:

$$\frac{\sigma(E)}{E} = \sigma_1 E_{GeV}^{-0.25} \oplus \sigma_2$$

  with $\sigma_1 = (1.33 \pm 0.16)\,\%$ and $\sigma_2 = (2.1 \pm 0.06)\,\%$

- Muon Identification is provided by nearly 900 resistive plate chambers (RPC) which instrument the magnetic flux return yoke. This is the Instrumented Flux Return (IFR) detector. 19 RPC layers (18 in the detector endcap region) are interleaved with iron plates from the flux return. Each RPC is filled with a $567:388:45$ Ar-Freon-Isobutane mixture and operated at $7.6\,kV$. Readout from orthogonal strips provides $z-\phi$ granularity (which becomes $X-Y$ in the endcaps).

3.1.1.2 BELLE

The BELLE/KEKB complex [2, 38] is in principle similar to BaBar/PEP-II: $8\,GeV$ electrons and $3.5\,GeV$ positrons are stored in two parallel $3\,Km$ storage rings, fed by an e^+/e^- linac. Given the similar environment, also similar detector performance is required. We will thus quickly point out the main points of the detector structure in analogy or contrast with the ones already shown for BaBar, leaving to the references a deeper discussion of the BELLE internals.
e^+e^- collisions in the BELLE interaction point are at a small ($11\,mrad$) angle, chosen to minimize parasitic collisions near the Interaction Point. The BELLE **tracking** is made of a 3-layer (at radii of 3, 4.55 and $6.05\,cm$) Silicon Vertex Detector (SVD [39]) covering $-0.76 < cos\theta_{lab} < 0.94$ together with a 32 (axial)+18 (stereo)+3 (cathode strip) layer Central Drift Chamber (CDC) covering $-0.87 < cos\theta_{lab} < 0.96$ in the radial region $8\,cm < r < 88\,cm$. This system provides tracking in a solenoidal $1.5\,T$ magnetic field, parallel to the electron beam axis. Tracking resolution is $\sigma_{d_0} =$

$21 + 69/p\beta Sin^{3/2}(\theta)$, $\sigma_{z_0} = 41 + 48/p\beta Sin^{5/2}(\theta)$ and $\frac{\delta p_t}{p_t} = (0.36 \oplus 0.28\, p_t\,[GeV])\%$ with a $\frac{dE}{dx}$ resolution of 6.9%

Particle identification is based on the CDC dE/dx information, an Aerogel Cerenkov Counter (ACC) and a Time of Flight (TOF) system (both placed just outside the CDC volume). ACC consists of blocks of silica aerogel (SAG) in $0.2\,mm$ Al boxes, read-out by fine-mesh photomultipliers (FMPMT). The unique possibility offered by the SAG of controlling its refractive index ($1.01 < n < 1.05$) has been used by modulating n as a function of the polar angle to optimize the performance. A nonuniform response is in fact desired in order to match the kinematics of two-body decays[2] from the boosted B mesons.
ACC gives excellent $K - \pi$ separation in the $1.5\,GeV/c < p_t < 3.5\,GeV/c$ range. This device is complemented by a TOF detector, placed just outside the ACC, at $r = 120\,cm$. The TOF is made of 128 scintillating bars each $4\,cm \times 6\,cm \times 255\,cm$, allowing a $\approx 100\,ps$ time resolution and thus $K - \pi$ separation for particles with p_t below $1.2\,GeV/c$.

Electromagnetic Calorimetry is done with 8736 CsI crystals each long 16.1 radiation lengths, placed in the region $125\,cm < r < 162\,cm$. The energy resolution is $\frac{\sigma_E}{E} = \left(1.3 \oplus \frac{0.07}{E_{GeV}} \oplus \frac{0.8}{E^{0.25}_{GeV}}\right)\%$ with an exact coverage of the CDC angular region. ECL is integrated by a small-angle BGO calorimeter with 12.0 and 10.5 radiation lengths in the forward ($0.98 < cos\theta_{lab} < 0.994$) and backward ($-0.989 < cos\theta_{lab} < -0.957$) regions, respectively. EFC is used as a luminosity monitoring device, and for the study of Bhabba and small angle-scattering processes ($e^+e^- \to e^+e^-\gamma$, $e^+e^-\mu^+\mu^-$, $e^+e^-\gamma\gamma$).

Muon and K_L detection is performed [40, 41] with the KLM (K Long and Muon) detector. KLM consists of 14 layers of RPC placed outside the BELLE coil, sandwiched between iron plates. This detector is analogous to the BaBar IFR device. K_L identification is done requiring the presence of a KLM shower with no charged track matching from the CDC.

3.1.1.3 Recent Results and Near Future Plans

At the moment of writing this thesis, even with the accidents occurred in the first detector warm-ups, beauty factories have well demonstrated their ability of measuring CKM parameters and published the first measurements of CP violation in the B sector [42, 43, 44, 45, 46, 47]. BaBar [48] and BELLE [49] have provided the most precise $Sin(2\beta)$ measurements so far available, together with many branching fractions measurements ($B_d(t) \to D^{(*)\mp}\pi^{\pm}$, $D^{*\mp}\rho^{\pm}$ [50] exclusive and inclusive charmonium decays [51, 52, 53], $K^*\gamma$, $\pi\pi$, $K\pi$ [54] and many more [55, 56, 57, 58, 59, 60, 61, 62]), lifetime and oscillation frequency determinations [63, 64, 65, 66, 67, 68, 69, 70].

The near future plans of B factories, are rather aggressive. The pursuit of the extensive B physics plan [1, 20, 2] has just begun. Moreover, after the $\Upsilon(4S)$ data taking, an $\Upsilon(5S)$ period can be easily foreseen. This will give BaBar and BELLE

[2]The measurement of CP violation in two body decays of the B meson relies on the discrimination of the $\pi\pi$ and $K\pi$ decay modes

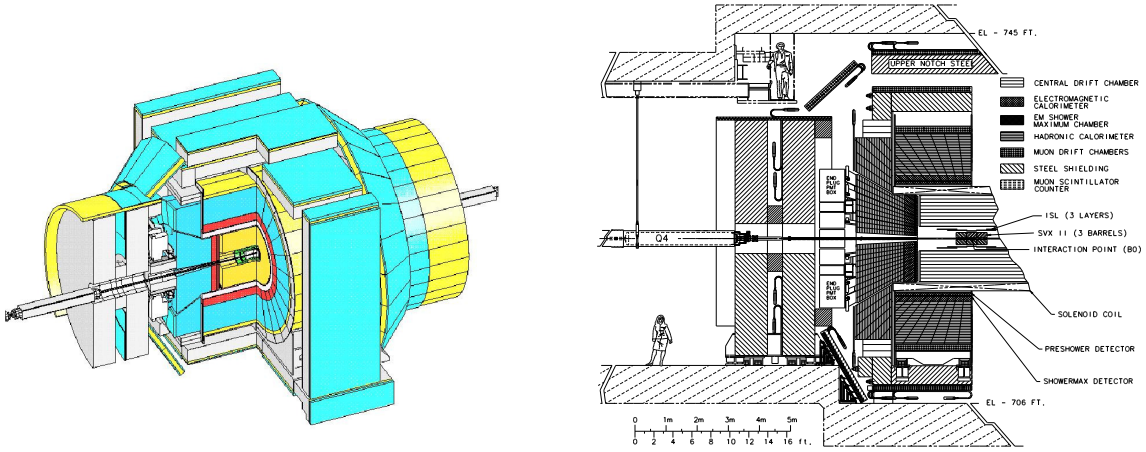

Figure 3.1: Schematic view of the CDF II detector with its main components. (Left) An isometric view and (Right) elevation view.

access to B_s mesons, so far only achievable at high energy machines like LEP and the Tevatron.

3.2 CDF II

CDF II (see fig. 3.1) is a general purpose $p\overline{p}$ experiment placed on the $B0$ interaction point of the Tevatron collider. The collider and detector performance have evolved from 1985 to today, meeting and surpassing the design goals. The needs for more performing tools have led to the current detector and collider improvements, generally referred to as "Run II".
The Tevatron collider is expected to reach a luminosity of $2 \cdot 10^{32} cm^{-2} s^{-1}$, a minimum inter-bunch time of $132 ns$ and a mean number of overlapping events ranging between 2 and 6. The CDF detector has been upgraded to take advantage of the full power of the new collider, with the goal of accumulating an integrated luminosity of $2 fb^{-1}$. The CDF II detector started data taking in spring 2001.
In the next subsections we will describe the CDF detector parts and techniques expected to be useful for b physics analyses of Run II.
b physics works at CDF II will be essentially based on two detector components: the tracking system and the particle identification system. Data taking and on-the-fly sample selection criteria are decided by the trigger and DAQ systems, much more important in the case of a $p\overline{p}$ experiment than for e^+e^- detectors.
The three devices listed above are the main tools of the B physicist at CDF. We must complete this list with another tool of general interest. This is the *ensemble* of techniques so far developed for a task which is needed in most B physics measurements: flavor tagging.

3.2.1 Tracking

The tracking systems (see fig. 3.1) are contained in a super-conducting solenoid ($1.5m$ in radius and $4.8m$ in length) generating a $1.4T$ magnetic field parallel to the beam axis (z). In order to obtain a good resolution on the parameters of central tracks, two independent detectors are used:

- The Central Outer Tracker (COT) : a large open cell drift chamber designed to significantly outperform in response time its Run I predecessor (usually referred to as CTC)
- The Silicon VerteX detector (SVX II): a six[3] layer silicon micro-strip detector, placed near to the interaction region

The combined information from these detectors allows CDF to obtain a good impact parameter resolution $\sigma_d \approx 30\mu m$.
One of the main goals of the CDF upgrade is that of increasing the geometrical coverage of its detectors. Geometrical acceptance of the tracking system was in fact one of the limiting factor of CDF I. In CDF II an additional intermediate layer of silicon micro-strip detectors (ISL) will increase the b tagging acceptance up to $|\eta| < 2$.

3.2.1.1 The Central Outer Tracker

The core of the Run II CDF tracking system is a large open cell drift chamber for charged particle reconstruction in the central region $|\eta| < 1$ (see fig. 3.1 and 3.2).
The basic drift cell of the COT will perform 12 measurements along each central track, and will have a maximum drift distance of $\approx 0.9\,cm$. In the COT four axial and four stereo super-layers with 12 wires each will provide 96 measurements between 48 and 131 cm, using a total of 30,240 readout channels for the entire detector. The number of stereo measurements is increased from 24 to 48 with respect to Run I, removing the historical stereo deficiency of this detector.
The complete chamber is roughly 1.3% of a radiation length at normal incidence.

3.2.1.2 SVX II and ISL

The high resolution tracking is achieved with a "second generation" silicon detector which is optimized for the CDF/Tevatron environment. SVX II (see fig. 3.3) is composed of three cylindrical barrels (*mechanical barrels*) with a total length of $96cm$. Each barrel is divided into 12 mechanical *wedges* along ϕ and longitudinally divided into two *electrical barrel* . It covers $\approx 2.5\sigma$ of the luminous region, raising the geometrical acceptance for b tagging from the Run I value of 60% to almost 100%. Each barrel supports five layers of double-sided silicon micro-strip detectors (*ladders*) between radii of 2.45 and $10.6cm$. One side of all layers measures $r-\phi$; on the other sides three layers measure $r-z$ and two are small angle stereo. Readout

[3]The inmost layer of SVX II is often referred to as a separate detector ("Layer 00"), therefore sometimes SVX II is said to be a 5 layer detector.

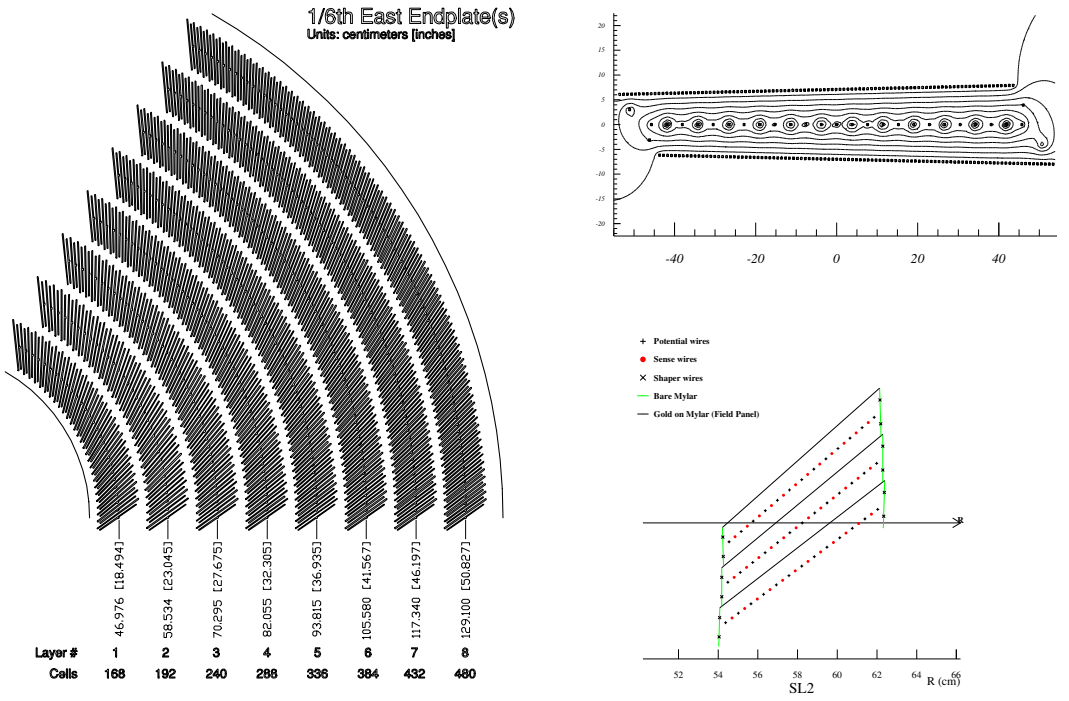

Figure 3.2: COT Structure: (left) cell arrangement, (bottom right) single cell structure and (top right) electric field structure within each cell.

and signal digitization is embedded on the detector, which contains readout hybrids directly at the end of each electrical ladder.
The Intermediate Silicon Layers (ISL, see the rightmost schematic view of fig. 3.3) use similar technology to that of SVX II, from the silicon itself through the readout electronics. In the central region, a layer of double-sided silicon is placed at a radius of $22\,cm$. In the region $1.0 \leq |\eta| \leq 2.0$ two layers of double-sided silicon are placed at radii of $20\,cm$ and $28\,cm$. All layers make $r - \phi$ and a small angle stereo measurement.

3.2.1.3 Layer 00

The addition of a low-mass silicon detector layer at small radius (inside the SVX II) improves the purity of reconstructed tracks and yields a more precise and uniform measurement of track impact parameters.

Layer 00 will improve the impact parameter resolution for $1\,GeV/c$ tracks from roughly $50\,\mu m$ to $\approx 25\,\mu m$. The improvement of impact parameter resolution at lower momentum leads to a substantial increase in b-tagging efficiency and will also help with the separation of b and c flavored events. Moreover, the expected improvement of the vertex-finding resolution will lower the proper time resolution on b hadron decays and thus enhance CP violation and B_s mixing measurements.

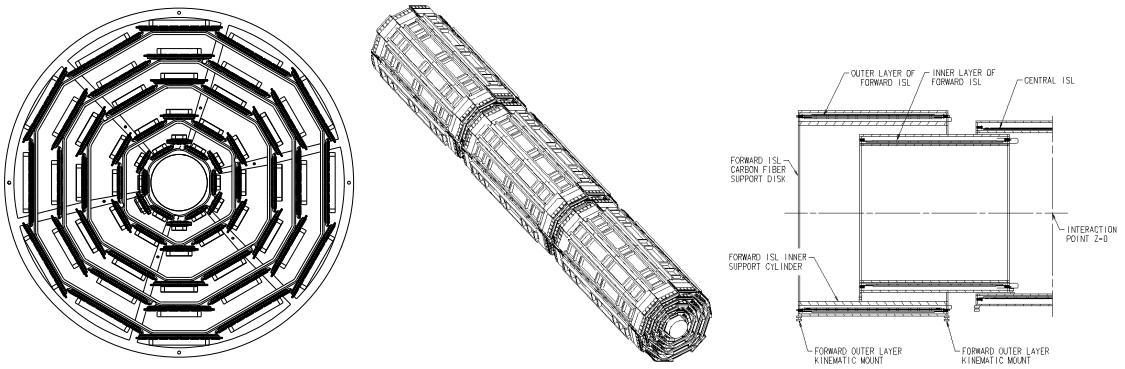

Figure 3.3: Organization of the SVX II and ISL detectors: (left) $r-\phi$ view of the bulkhead of SVX II, (center) schematic view of the full SVX II detector and (right) $r-z$ view of one half in z of the ISL detector.

3.2.1.4 Resulting Tracking Performance

The performance of the CDF II tracking upgrades has been thoroughly studied using simulation tools tuned to similar systems used in CDF during Run I.
The results are:

- The COT reconstruction is highly efficient and gives good helix parameter resolutions[4] $\sigma_{P_t}/P_t^2 \approx 0.007^2 + (0.000009\,P_t)^2$, $\sigma_{d_0} \approx 13 + 40/P_t\,\mu m$ (see figure 3.4), up to the full Run II design luminosity of $2 \cdot 10^{32} cm^{-2} s^{-1}$.

- Track finding in the SVX II+ISL inner tracking system will be efficient, and yield stand-alone silicon track segments over the full region $|\eta| \leq 2.0$. For tracks with $1.0 \leq |\eta| \leq 2.0$, the seven silicon layers will provide helix parameter resolution adequate to extend electron and muon identification to the plug and IMU (see [4]), and to allow efficient stand-alone b-tagging.

- Stand-alone SVX II+ISL track segments can be linked to the COT with high efficiency, and the full tracks have excellent helix parameter resolution. The efficiency and resolution are maintained up to the luminosity of $2 \cdot 10^{32} cm^{-2} s^{-1}$.

- The ability to find stand-alone silicon segments over the region $|\eta| \leq 2.0$ allows the use of a fully integrated tracking strategy. We expect that as we gain experience with this system we will learn to raise the efficiency and precision of the tracking analyses in Run II far beyond the level achieved in Run I.

- Impact parameter resolution for tracks not passing through the SVX II hybrids and hitting Layer 00, SVX II and the CTC will improve from $\sigma_{d_0} = 9 \oplus 66/P_t$ to $\sigma_{d_0} = 6 \oplus 22/P_t$. In the case in which there is significant material interaction in SVX II, σ_{d_0} will go from $9 \oplus 66/P_t$ to $6 \oplus 27/P_t$.

[4] P_t is in units of GeV/c

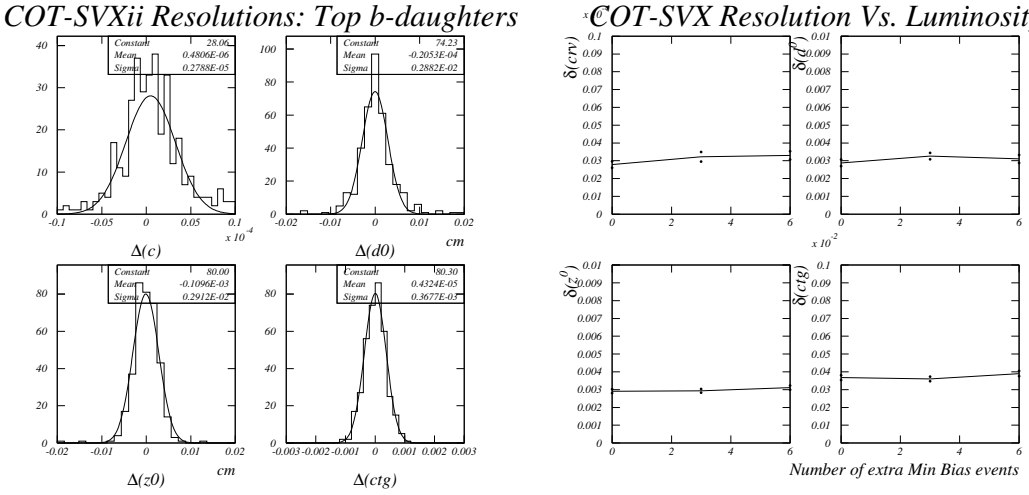

Figure 3.4: Helix parameter resolution for COT+SVX II at low luminosity (Left) and luminosity dependence (Right).

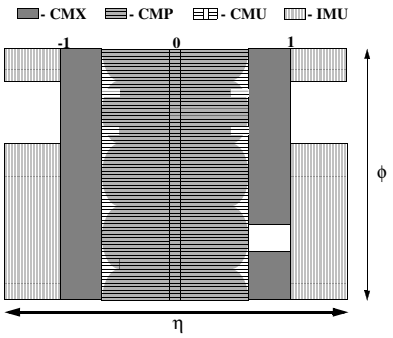

	CMU	CMP/CSP	CMX/CSX	IMU
η Coverage	≤ 0.6	≤ 0.6	$0.6 \leq \eta \leq 1$	$1 \leq \eta \leq 1.5$
Max Drift Time (μs)	0.8	1.4	1.4	0.8
Total Drift Tubes	2304	1076	2208	1728
Total Scint. Counters		269	324	864
Pion Inter. Lengths	5.5	7.8	6.2	6.2-20
Min. μ P_t (GeV/c)	1.4	2.2	1.4	1.4-2.0

Figure 3.5: Location of the central muon upgrade components in azimuth ϕ and pseudo-rapidity η for Run II. The table reports the design parameters of the CDF II muon detectors.

3.2.2 Particle Identification

CDF II has 3 particle identification systems: the muon chambers, the electromagnetic calorimeter and the Time Of Flight detector. In addition, the charge deposited on the COT wires samples the electromagnetic energy lost by charged particles, providing an additional handle for particle identification: the so called dE/dx measurement.

3.2.2.1 Muon Identification

Muon identification in CDF II relies on their distinctive ability to pass through material. Muons are detected by scintillating counters or drift tubes placed outside the iron structure of the CDF II detector.

Momentum measurement is simultaneously done using the COT chamber. The muon detectors are historically distinguished in *central* and *forward*.

For the $|\eta| > 1$ region CDF has elected to cover a smaller and lower rapidity interval ($\eta = 1 - 1.5$) with sufficient granularity to survive high luminosity. The design closely parallels that of the central detectors.
Between $\eta = 1.5$ and $\eta = 2.0$ there is also muon identification, with granularity (and therefore occupancy) insufficient for triggering, but adequate for identifying high P_T tracks in this region as muons.
There are four detectors for muon identification in CDF II. Design parameters of these detectors are summarized in figure 3.5.

3.2.2.2 Electron Identification

Electrons are identified using two distinct informations: the ratio of *electromagnetic* to *hadronic* signal in the calorimeters (see table 3.3) and the shower shape as identified by two layers of wire proportional chambers placed at two different radii.
The first proportional chamber (CPR) projectively corresponds to the CEM calori-

Name	*Region* $\lvert\eta\rvert$	*Type*	$\sigma_E\,(\%)$	*Thickness*	$\Delta\eta \times \Delta\varphi$
CEM	< 1	Pb-scint.	$13.7/\sqrt{E_t} \oplus 2$	18 X_0	0.1×15^o
PEM	1.1-2.4	Pb-wire ch.	$22.0/\sqrt{E_t} \oplus 2$	18-21 X_0	0.1×5^o
FEM	2.4-4.2	Pb-wire ch.	$26.0/\sqrt{E_t} \oplus 2$	25 X_0	0.1×15^o
CHA	< 0.9	Fe-scint.	$50.0/\sqrt{E_t} \oplus 3$	4.5 λ_0	0.1×15^o
WHA	0.7-1.3	Fe-wire ch.	$75.0/\sqrt{E_t} \oplus 4$	4.5 λ_0	0.1×15^o
PHA	1.3-2.4	Fe-wire ch.	$106./\sqrt{E_t} \oplus 6$	5.7 λ_0	0.1×15^o
FHA	2.4-4.2	Fe-wire ch.	$137./\sqrt{E_t} \oplus 3$	7.7 λ_0	0.1×5^o

Table 3.3: Main features of the CDF Run I calorimeters. $E_t = E \cdot Sin\,(\theta)$, λ_0, X_0 are, respectively, the *transverse energy*, the *absorption length* and the *radiation length*. The Run II configuration excludes all the forward $4.2 \leq |\eta| \leq 2.4$ sections.

meter, and detects the shower shape after the particles interaction with the tracking detectors, the coil and the outer wall of the CDF solenoid.
Another proportional wire chamber is placed at the maximum development of the electromagnetic shower ($\sim 6X_0$), allowing a good γ/π° separation.
A track in the COT is matched to the position of the shower in the chambers in order to reject combinations of random charged tracks with low-E_t photons and neutral pions hitting a calorimeter tower.

3.2.2.3 TOF

One of the CDF historical weaknesses was the absence of hadron particle identification capabilities. This issue has become especially relevant in B physics, where particle identification can also increase the efficiency of certain *tagging algorithms* (see section 3.3.3). That's why a system capable of identifying pions, kaons and protons has been added to CDF II [71].

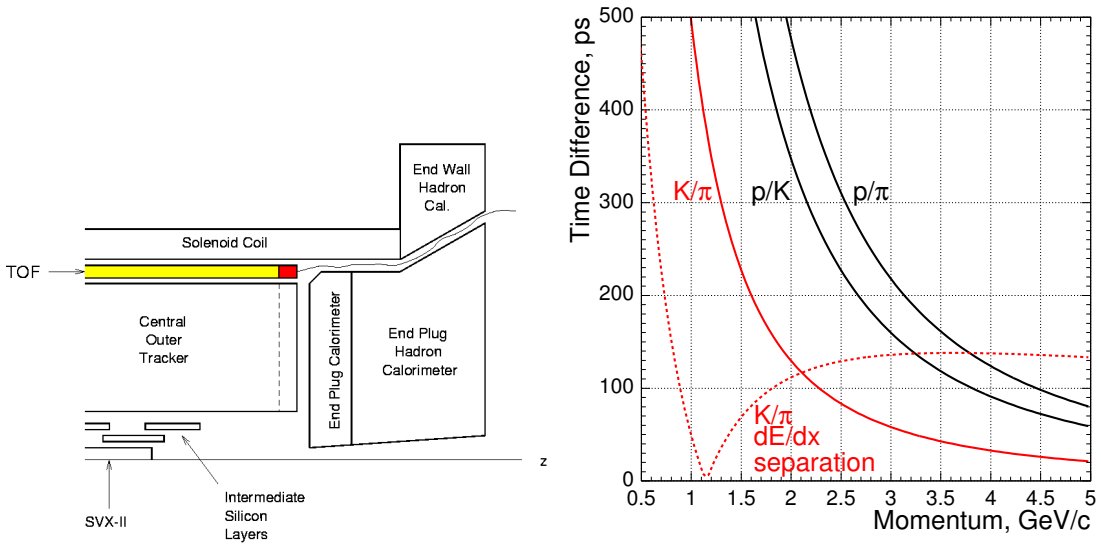

Figure 3.6: (Left) Cross section of the TOF detector position into CDF II and (Right) flight time difference for various particle types as a function of the transverse momentum. The figure also reports (lower curve) the performance of the dE/dx particle separation capability, showing it complementarity to the TOF system.

Particle identification is implemented by integrating time of flight and tracking information: the particle velocity and momentum are obtained from the charged particle signal in the COT and from the time employed by the particle in traveling from the interaction point to the outer edge of the COT. The Flight Time difference for different particle types is shown in fig. 3.6 as a function of particle P_t.
The relative timing of primary vertex and TOF hits will be measured with a resolution of about $100\,ps$, thus allowing an effective $K-\pi$ and $p-\pi$ separation.
Figure 3.6 shows that a system with a time resolution of the order of $100\,ps$ or better is needed to effectively distinguish pions from kaons below the $1.6\,GeV/c$ threshold. This is realized (see fig. 3.6) inserting a cylindrical array of scintillating bars between the COT and the CDF II solenoid. The mean traveling path for particles originating at the interaction point is $1.4\,m$.

3.2.2.4 dE/dx

Some non-leptonic particle identification was achieved in Run I [72]. This was performed measuring the profile of the energy lost by charged particles while traversing the central wire chamber. The measurement of the gas ionization charge at each of the sense wires is in fact an indirect measurement of the energy lost by the charged particle which interacts electromagnetically with the gas mixture in the chamber.
Appropriate elaboration of this charge profile thus gives insight in the energy loss profile which is known ([73]) to depend on the particle's velocity (through $\beta\gamma$). The simultaneous measurement of this quantity and of the particle's momentum allows

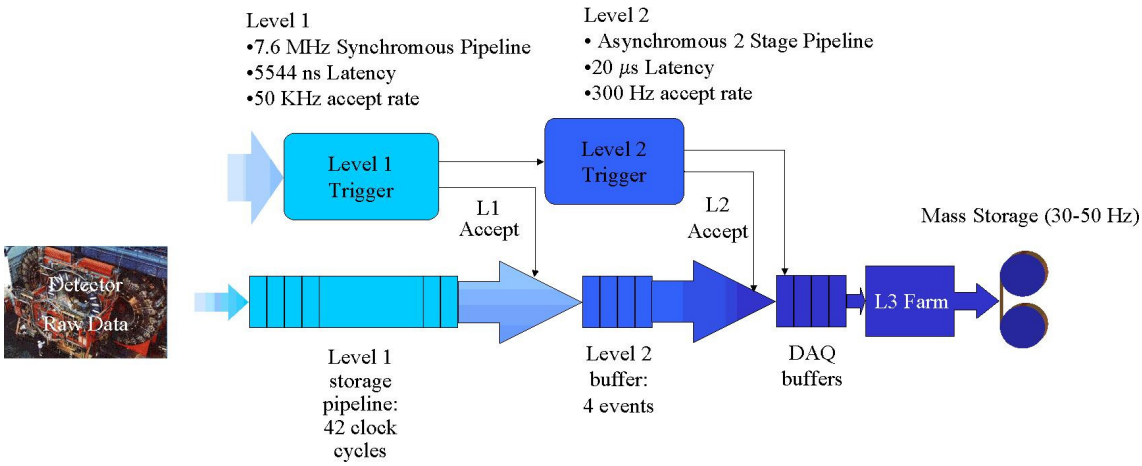

Figure 3.7: Schematic structure of the CDF trigger 3 level organization.

a determination of the mass of the particle.
This method is expected to equally apply also in run II, with the performance reported by the curve in figure 3.6 in terms of the achievable $K - \pi$ separation.

3.2.3 The CDF Trigger Architecture

Since the interaction rate in hadron collider experiments is well beyond the conceivable storage rate and analysis capabilities, background excess is a general plague of hadronic experiments. The well known cure is a DAQ system intelligent enough to select and discard events online on the basis of the information available from the detectors.
In the case of CDF II the collision rate at high luminosities is effectively equal to the crossing rate of $7.6\,MHz$, while tape writing speed is less than $50\,Hz$. The role of the trigger is that of efficiently extract the most interesting physics events from the large number of *minimum bias* events: for example the total $b\bar{b}$ production cross section is approximately 3 orders of magnitude smaller than the minimum bias one.
The CDF II trigger system (see figure 3.7) inherits the 3 level architecture of CDF I. At each trigger level more accurate information from the detectors is available and more complicate calculations can be implemented: *level 1* is based on limited resolution calorimetry and tracking, *level 2* uses full tracking resolution and calorimetric clustering, evaluating the event with a set of programmable processors, *level 3* uses a full detector reconstruction in a commercial processor farm to take the final decision on the processed events.
Given the complexity and size of the information available at the various stages, and the processing time necessary to make a decision based on this information, we can define the maximum processing rate for each trigger stage.
Assuming that accept rates for each level are well tuned, a pipelined architecture can be implemented with the various trigger stages.

3.2.3.1 Level 1

The *level 1* trigger processes in parallel calorimetry and detector information, and hits from the Central Outer Tracker. A decision stage then performs basic selections combining these informations. Tracks fitted by the level 1 COT fitter (XFT) are for example matched with the calorimeter and muon section of the trigger, in order to implement a better particle recognition.
COT information is translated in fitted track parameters by the XFT system, which makes them available for Level 1 and Level 2 processing. XFT reconstructs tracks parameters using COT hits and ignoring z information: XFT tracks are 2-dimensional and at low tracking resolution (SVX is not used). The track-finding efficiency of this device is greater than 96%, the momentum resolution is $\Delta P_t/P_t^2 \approx 2\%$ and the ϕ_0 resolution is better than $6\,mrad$. The minimum track P_t is $1.5\,GeV/c$.
The muon section identifies tracks in the muon chambers (*stubs*) and hits in the scintillator. Muons are flagged when *stubs* match (at a coarser resolution than offline) with XFT tracks.
The calorimetry trigger identifies two categories of events: object triggers (e^-, γ and jets) and global triggers (total transverse energy ΣE_T and missing transverse energy $\not\!\!E_T$). The object triggers are formed by applying thresholds to individual calorimeter towers and possibly matching the calorimetric hits with tracks from the XFT. The global triggers are done applying a threshold to the weighted sum of individual tower energy content.

3.2.3.2 Level 2

This trigger level can be pictured as divided in two parts: the first stage operates event building, while the second implements algorithms on dedicated CPUs in order to take trigger decisions based on joined level 1 and level 2 outputs. Each of these stages takes half of the total processing time for level 2.
Event building is done in parallel: level 2 processes the calorimeter data and implements the clustering algorithm needed to correctly identify hadronic jets. Simultaneously a track processor (SVT, see chapter 4) integrates XFT information with SVX II data producing 2D track parameters with offline level quality at $P_t > 2\,GeV/c$.
The key improvement with respect to the level 1 track fitting is in the measurement of the track impact parameter, which can be taken as a rough indication of the lifetime of the parent of the observed particle.
Customized algorithms are developed specifically for each trigger channel and are distributed on a set of four CPUs (Level-2 processors).

3.2.3.3 Level 3

The third trigger level is implemented in a farm of commercial processors, running the Linux operating system. The purpose of this farm is to reconstruct the event at full resolution, distribute the information to the online monitoring and data logger programs and feed it to the trigger algorithms, which make the decision of perma-

nently storing the event or not. At the same time event integrity is checked.
The reconstruction at full resolution is implemented using lower trigger levels to drive the algorithm: when the lower trigger levels generate an accept signal for that event, the level 3 farm calls the reconstruction routines needed to verify at full detector resolution the presence of that triggering event.
Selected events are finally output to tape, with a maximum rate of about $12.5\,MB/sec$ (which means about $50\,Hz$ or $250\,nb$ at $\mathcal{L} = 2 \cdot 10^{32}\,cm^{-2}\,s^{-1}$ assuming an event size of $\approx 250\,KB$).

3.2.3.4 Trigger Summary

What are the rates and rejection ratios required at each trigger stage? The initial constraint is of course that of reducing the $7.5\,MHz$ event rate into the sustainable output rate ($50\,Hz$).
Many interplaying constraints concur in the definition of the trigger architecture and performance. First of all the physics fenomena under investigation define the rate of desirable events. On the opposite side, bare technicalities define the maximum achievable storage rate: detector granularity, occupancy, and technological limits in I/O throughput to storage devices. Half way between these two are the technical limitations coming from the specific detector design: readout electronics dead time in particular.
The proposed CDF II implementation breaks up the needed rejection factor in three distinct layers, with processing times of $5.5\,\mu s$, $20\,\mu s$ and $10\,ms$. Latency varies among detector parts, thus making certain parameters available earlier or later in the trigger chain.
The need for building a deadtimeless device drives the grand design of the DAQ system, and brings us to the choice of having the trigger chain splitted in levels of increasing information accuracy and complexity.

From the point of view of the access to B physics and low P_t processes in general, the CDF trigger architecture allows three basic approaches: two of them are based on the lepton identification and require either a single lepton with a momentum threshold of the order of $6\,GeV$ or a pair of leptons with momenta above $2-3\,GeV$. In many B decays these selections are insufficient or inadequate. The third approach available is that of using the specific heavy flavor tag given by the Silicon Vertex Trigger, which will be the focus of our discussion in the following chapters.

3.3 $Sin\,(2\beta)$ in CDF I

We want to describe here one of the most striking results of CDF in Run I: the measurement of the CKM parameter known as $Sin\,(2\beta)$.
Our purpose in this description is that of showing the CDF capability of disentangling a problem which was considered very hard at hadron colliders, and that of describing some issues and tools that are relevant for other measurements that we will consider in our work. In this sense we will take $Sin\,(2\beta)$ as a prototype of the Run II measurements. The method with which this parameter was measured at

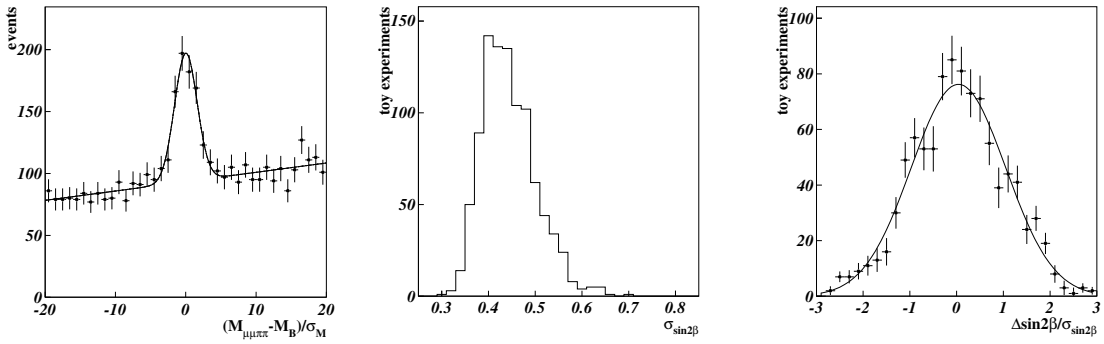

Figure 3.8: Signal reconstruction in the $B \to J/\psi K_s$ analysis: (left) normalized invariant mass $\left(M_{candidate} - M_B^{PDG}\right)/\sigma_M$ of the sample, (center) final $Sin\,(2\beta)$ resolution in a toy simulation of the analysis described and (right) $\left(Sin\,(2\beta)_{fit} - Sin\,(2\beta)_{input}\right)/\sigma_{Sin(2\beta)}$.

CDF is based on the measurement of the CP asymmetry $\mathcal{A}$ (see section 1.3.2.1) in the $B \to J/\psi K_s$ decay: this will give us the occasion to discuss an issue common to all oscillation and asymmetry measurements: *flavor tagging*.

Given the qualitative similarity of the CDF I and CDF II detector frameworks for what concerns this analysis, we will not go into the details of the differences between the Run I and the Run II environments.

3.3.1 Sample Selection

The analysis is based on about 400 fully reconstructed $B \to J/\psi K_s$ decays. They were collected through the J/Ψ trigger, which requires two stubs in the muon detectors for a level one trigger decision. At level 2 each muon stub is required to match a track in the central tracking chamber with $P_t > 2\,GeV/c$. Both tracks are then required to have an invariant mass between $2.8\,GeV/c^2 < M_{\mu\mu} < 3.4\,GeV/c^2$. This trigger results in a clean sample of $440,000$ J/Ψ's from $110\,pb^{-1}$ of data, about 20% of which are estimated to come from B decays.

3.3.2 Signal Reconstruction

The signal is reconstructed by requiring each muon from the J/Ψ trigger candidate to have $P_t > 0.7\,GeV$ and $L_{xy}/\sigma_{L_{xy}} > 5.0$ where L_{xy} and $\sigma_{L_{xy}}$ are the transverse decay length and its error. Two additional tracks are combined, searching the $K_s \to \pi\pi$ signal and a four particle vertex fit is performed using mass, vertex and pointing constraints. The resulting $B^\circ/\bar{B}^\circ$ candidate is required to have $P_t\,(B) > 4.5\,GeV/c$. Quality cuts are applied to the vertex fit. Refit momentum and their errors are used to compute a normalized mass for the $B^\circ/\bar{B}^\circ$ candidate, defined as the deviation of the $B^\circ/\bar{B}^\circ$ mass from the PDG value, divided by the estimated error.

From section 2.3 we know that the asymmetry in $B \to J/\psi K_s$ channel is strictly connected with $Sin\,(2\beta)$:

$$\mathcal{A}_{CP}\,(t) = Sin\,(2\beta)\,Sin\,(\Delta m_d t) \tag{3.1}$$

To measure $\mathcal{A}_{CP}\,(t)$ we need to reconstruct two parameters: the flight path length of the B decaying in $B \to J/\psi K_s$ and the flavor of that B meson. The flight path length is measured reconstructing the primary vertex position and the J/ψ decay position (undistinguishable from the J/ψ production point) in the vertex fit. In order to measure $\mathcal{A}_{CP}\,(t)$ and thus $Sin\,(2\beta)$ we need to determine the flavor of the reconstructed B meson at production. This issue, known as *flavor tagging*, arises in all the asymmetry measurements and for this reason is of general interest. Since almost identical tools will be used in Run II, the CDF techniques for B flavor tagging will be now discussed in detail.
Given the solution to this problem, we will statistically infer from the measured $\mathcal{A}_{CP}\,(t)$ ($\mathcal{A}_{CP}^{meas}\,(t)$ from now on) the CL interval on $Sin\,(2\beta)$.

3.3.3 Flavor Tagging and Dilution

One of the main issues in the extraction of CP violation asymmetries is the determination of the B meson flavor at the production point: without this it is impossible to make use of the techniques discussed in chapters 1 and 2. Since this fact is common to many analyses, we will describe which algorithms CDF plans to use for this purpose.
Defining a specific algorithm for the identification of the B flavor at production has implications on the measurement result. These implications are parametrized in a quantity called "dilution". We will discuss these first, followed by a brief description of the flavor tagging techniques that demonstrated successful in Run I and review those expected to show good performance in Run II.

3.3.3.1 Dilution

Whatever the algorithm we use to identify the flavor of the reconstructed B at the point of creation, we must face the fact that our tagging algorithm may fail, thus allowing the probability $\mathcal{P}$ that the tag obtained is correct to be less than 1. This modifies the experimentally measured asymmetry:

$$\mathcal{A}_{CP}^{meas}\,(t) = DSin\,(2\beta)\,Sin\,(\Delta m_d t) \tag{3.2}$$

where the factor $D = 2\mathcal{P} - 1$ is called the *dilution* and obeys $0 \leq |D| \leq 1$: errors in the tagging algorithm effectively reduce the measured asymmetry.
A rough estimate on the statistical error for the true asymmetry $\mathcal{A}$ can be easily derived:

$$\delta\mathcal{A} \simeq \sqrt{\frac{1}{\epsilon D^2 N}} \tag{3.3}$$

Where N is the sample size and ϵ is the *efficiency* of the tagging algorithm, defined as the fraction of the sample to which our tagging algorithm actually gives an answer:

each tagging algorithm is applicable only to a fraction of the events. The product ϵD^2 is effectively the figure of merit of any tagging algorithm.
Eq. 3.3 clearly shows the keys to a good asymmetry measurement:

1. A sample of events as large as possible (large N)
2. A large algorithm acceptance with respect to our sample (which means ϵ as close as possible to 1)
3. A tagging algorithm as reliable as possible, which means the lowest possible rate of mistags (D as close as possible to 1).

For what concerns (1) there is not much to say, the sample size depends mainly on the analysis cuts and the strategy applied.
(2) and (3) are completely in our hands: it's up to the experimenter to identify the best possible algorithm.
CDF has identified three good tagging algorithms. Two of them (opposite side tags) use the fact that in a $p\overline{p}$ environment the b quarks are always produced in $b\bar{b}$ pairs. The flavor tagging of the quark not reconstructed (*opposite*) then gives indications on the production flavor of the reconstructed quark.
The third algorithm (same side tag) uses the charge correlation of particles produced in the fragmentation process of the b quark leading to the reconstructed B meson.

3.3.3.2 Opposite Side Tags

If the opposite b decays in a leptonic channel like $b \to \ell^+ X$ ($\approx 10\%$ of the total width) then the lepton charge is a direct tag of the b charge and thus the flavor. This is the principle on which the *soft lepton tagging* algorithm is based. This is an algorithm with a good dilution (about 60%) but poor efficiency (about 5.5% when reconstruction efficiencies are included).
Another tag of the opposite b quark charge is the so-called *jet charge* algorithm. This uses the fact that even if the opposite b decays hadronically, the hadronization products show a charge correlation with the opposite quark flavor.
The commonly used parameter is the momentum weighted charge average Q_{jet} (often called *jet charge*) of the hadronization and decay products of the opposite b. Q_{jet}'s sign is correlated with the opposite b flavor: on average a $b/\bar{b}$ quark will produce negative/positive jet charge.

This algorithm has larger efficiency than the *soft lepton* ($\approx 40\%$) but worser dilution ($\approx 23\%$). The ϵD^2 factor for the two OST algorithms is approximately 2%. These two techniques have been successfully used in CDF Run I for the measurement of $B\bar{B}$ flavor oscillations [74].

3.3.3.3 Same Side Tags

Another possible flavor tag approach is based on the idea of using hadronization products on the b quark on the *same side* (the one originating the B meson reconstructed). This idea has the advantage of improving the algorithm efficiency,

since the tag is based on particles geometrically close to the b that is already reconstructed, which therefore have higher chance to fall within detector acceptance.
This kind of tagging was first proposed by Gronau et al. [75]. It was tested and used in a CDF measurement of Δm_d [76], using as a tag the charge of a track with the following characteristics:

- The track is reconstructed with good tracking accuracy
- The particle is not part of the B decay products
- Originates from the same primary vertex of the B meson and lies within a predefined $\Delta R = \sqrt{(\Delta\eta)^2 + (\Delta\phi)^2}$ window from the reconstructed B direction
- Its momentum is as close as possible to the one of the originating b quark[5]

This last choice is practically equivalent to the choice of a track with maximum P_t or minimum ΔR from the B, and is preferred essentially for its highest immunity to B products contamination in the case of partially reconstructed B decays.
The resulting algorithm has a measured efficiency of $\epsilon \approx 84\%$ and a dilution $D \approx 18\%$ [76].

3.3.3.4 Run II Projections

In Run II the above tagging algorithms are expected to perform equally or better than in Run I.
To the algorithms mentioned we must add the improvements coming from the information provided by the TOF system: tagging particles are soft enough to make the TOF resolution sufficient to separate kaons from pions.
This means that TOF information is available for the candidate taggers. Given the principles on which SST and OST are based, the algorithm dilution will be improved excluding from the set of candidate taggers specific particles: if we do SST, for example, a better dilution is obtained requiring the particles not to be kaons, since kaons have an high probability to be unidentified B decay products. SST dilution will be improved requiring that the particle used as flavor tag is chosen among candidate pions.
We will implement also a new OST tagging algorithm in which we use as a tag the charge of a particle the TOF has identified as a kaon.
For comparison we report in table 3.4 the results for the various tagging algorithm so far discussed and the projections for Run II.

3.3.4 The Run I $Sin\,(2\beta)$ Measurement

All the pieces for the Run I $Sin\,(2\beta)$ measurement are now in place and we can thus have a look at the results. In figure 3.9 we report the $B \to J/\psi K_s$ asymmetry

[5] As an approximation of the b quark momentum the sum of the reconstructed B meson momentum and the tagging track momentum is taken

Algorithm	ϵD^2 (Run I)	ϵD^2 (Run II)
Same Side	1.4	1
Same Side with TOF	1.9	-
Soft Lepton (e)	0.8	0.8
Soft Lepton (μ)	1.0	0.9
Jet Charge	3.0	2.1
Opposite side K (requires TOF)	2.4	-

Table 3.4: Projected ϵD^2 values for the various tagging algorithms proposed in the Run II environment (the reference decay is still $B \to J/\psi K_s$) and corresponding Run I values.

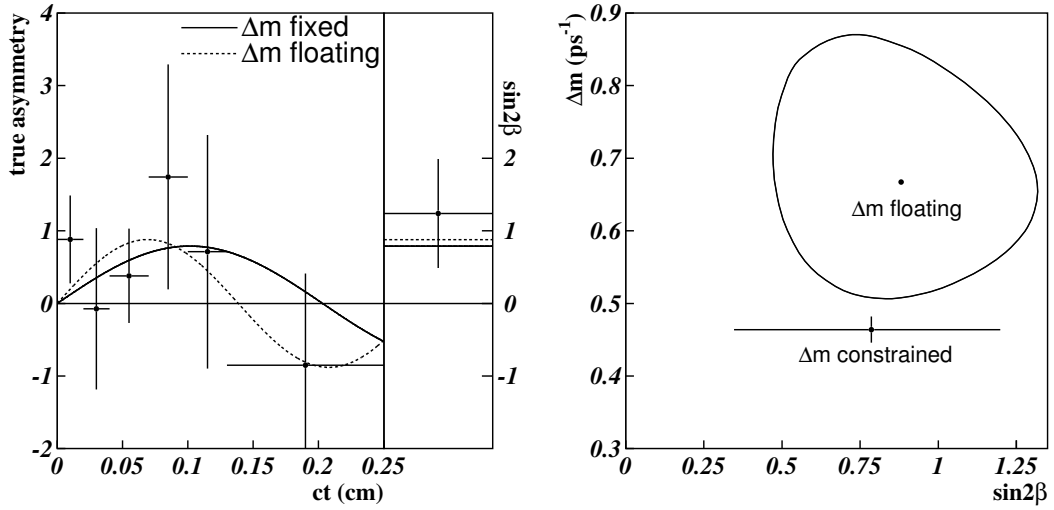

Figure 3.9: Analysis results: (left) time distribution of the asymmetry in the sample and integrated asymmetry. Superimposed on the plot are the fit results in the case of fixed and floating Δm_d. (right) 1σ contour plot of Δm_d vs $Sin\,(2\beta)$.

measured in Run I as a function of proper time ct. A simultaneous log-likelihood fit to the mass, lifetime and asymmetry distributions returns:

$$Sin\,(2\beta) = 0.79 \pm 0.39\,(stat) \pm 0.16\,(syst) = 0.79^{+0.41}_{-0.44} \tag{3.4}$$

if Δm_d is tied to the world average value [13], and becomes:

$$Sin\,(2\beta) = 0.88^{+0.44}_{-0.41} \tag{3.5}$$

$$\Delta m_d = 0.68 \pm 0.17 ps^{-1} \tag{3.6}$$

if Δm_d is considered a fit parameter.
A final cross-check is done by fitting the *time integrated asymmetry*:

$$\int_{ct=0}^{ct=+\infty} \mathcal{A}\,(t)\; dt = 0.71 \pm 0.63 \tag{3.7}$$

The results of these fits are visualized in figure 3.9.
The systematic term in equation 3.4 reflects the uncertainty in the result due to the uncertainty in the dilution parameters. Since the latter improves with the increase in statistics foreseen for Run II, its contribution to the $Sin\,(2\beta)$ measurement error is expected not to dominate.
The statistical significance of whether this results supports $Sin\,(2\beta) > 0$ has been evaluated using three different methods: a Bayesian approach finds a probability 95% that $Sin\,(2\beta) > 0$ when a flat prior distribution for $Sin\,(2\beta)$ is assumed. The Feldman-Cousins method [77] gives a 93% confidence level for the interval $0.0 < Sin\,(2\beta) < 1.00$. Finally, if $Sin\,(2\beta) = 0$ is assumed, the probability of obtaining $Sin\,(2\beta) > 0.79$ is 3.6%.

3.4 Conclusions

CDF II represents a competitive tool for CP violation studies in the years before LHC. The fact of being an hadronic experiment is at the same time its strength (because of the variety of physics involved) and its weakness (because of the strong rejection required in the acquisition and analysis of the data samples). The collaboration has already demonstrated its ability to disentangle challenging physics channels previously thought to be prohibitive for our environment, and the brief account given in this chapter should have provided the reader with enough confidence in the experiment to trust what will come in the next chapters.

Chapter 4

The Silicon Vertex Tracker

The main characters of our work will be essentially two: B physics and the tools needed to take advantage of the high b production rate at the Tevatron Collider. Among these tools a key role is played by the Silicon Vertex Tracker, which is the true CDF *beauty* tagger. For this reason we find appropriate to devote a whole chapter to the description of this innovative device, discussing its working principle, the hardware implementation and the performances.
SVT is a specialized electronic device designed to perform real time track reconstruction using the silicon vertex detector (SVX II). This will strongly improve the CDF capability of triggering on events containing b quarks, usually characterized by the presence of secondary vertices.
The keyword in a trigger system is *efficiency*: any trigger system is useless if its signal efficiency is too low or the background rejection is too high. The SVT key is accurate track reconstruction but this would be again useless if the track detection efficiency gets too small compared to the fully deployed detector possibilities. This is the reason why after paying so much attention to the algorithm performance and its hardware implementation in CDF, we will end the chapter turning our attention to the SVT track detection efficiency.

4.1 Introduction

Charged particle trajectory reconstruction is a very common task in HEP experiments. The history of HEP could be traced along the evolution of detectors and techniques employed to improve the resolution on track parameters. The typical processing time scale has evolved from months (in bubble chamber experiments) down to tenths and hundredths of second (in modern DAQ systems) in a non monotonic way.
The need for even faster tracking tools stems from two main issues:

- the fact that experiments are carried out to measure smaller and smaller cross sections. This means an increase in the event rate, as a consequence of improvements both in detectors and accelerators.

- the finer granularity of modern detectors, needed to achieve good track resolution.

High energy physics experiments, especially those performed at hadronic colliders, are facing the need of more and more efficient triggering devices.
SVT has been designed as an high efficiency triggering device for events involving the production of long lived particles (like, for example, B meson production). The design has been constrained by the architecture of the whole CDF trigger, which requires SVT to process each event within $10\mu s$. A data driven pipelined architecture based on an asynchronous $630Mb/s$ data path is the chosen solution. SVT is implemented on custom VME9U boards.

4.2 Physics Motivation

B hadrons of sufficiently high transverse momentum are characterized by a large mean valued distribution of the impact parameter with respect to the beam axis. This means that events containing this kind of particles can be separated from non–long–lived background simply cutting on the track's impact parameter.
Tracking is in fact an essential ingredient for B physics studies, where long lived particles (the B meson travels about $450\mu m$ in the CDF environment) can be detected if a good enough tracking resolution is available. Up to now this resolution could only be efficiently achieved in the offline analysis, and was not fully exploited at trigger level.
One of the goals of CDF in Run II is to achieve online tracking resolution of the same order of magnitude as the offline; this might prove to be essential in order to be able to deal with the small ratio between the b-quark production cross section and the total inelastic $p\overline{p}$ cross section. Single track parameters (impact parameter in particular) are the most commonly used handles for the selection of b-flavored events.
The ability to trigger on this kind of events will extend the sensitivity to new phenomena, broaden the inventory of heavy flavor decay channels and provide important control samples for top quark related measurements.

4.2.1 SVT Resulting Constraints

Since we want to identify as many events as possible, SVT needs to be implemented as early as possible in the CDF pipeline. On the other hand SVT needs SVX II data to be available and thus can't be earlier than Level 2. The total Level 2 latency is $20\,\mu s$ on average, with $10\,\mu s$ reserved for the Level 2 processors, and thus about $10\,\mu s$ available for SVT processing. This defines the time constraints for SVT.
The resolution must be good enough to trigger on impact parameter and must therefore be of the same order of magnitude as the offline analysis.

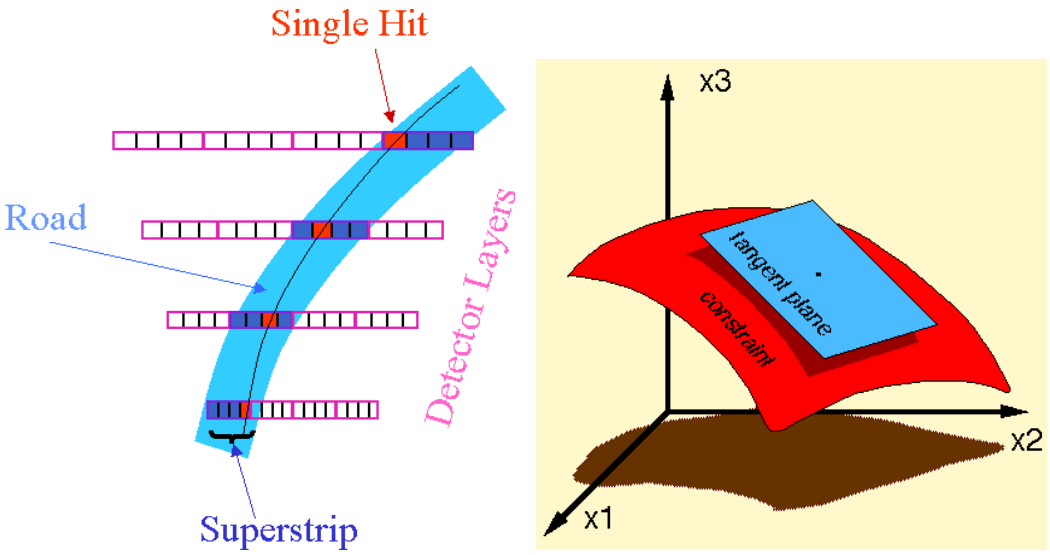

Figure 4.1: (left) Definition of the various fitting elements in the SVT algorithm. (right) Graphical sketch of the linearization principle (see section 4.3.2).

4.3 The SVT Algorithm

To obtain a good enough resolution in a short enough time we need a simple fitting algorithm that can be implemented directly in hardware as easily as possible.
The basic SVT architecture is that of an highly parallel data driven pipelined device. The algorithm implemented is conceived to distribute as much as possible the computational load in independent cascadable stages. It is divided into a pattern recognition stage and a track fitting stage.
The pattern recognition stage is performed by the Associative Memory (AM) [78, 79] using a coarser spatial resolution (see fig. 4.1). This is obtained by grouping silicon strips into wider *superstrips*. The AM identifies *roads* through the detector layers corresponding to combinations of *superstrips* (one for each layer), thus reducing combinatorics for the following fitting stage to combinations of hits contained in the same superstrip.
Typical superstrip size is $\approx 250\mu m$ while the detector resolution is typically one order of magnitude smaller.

The fitting problem can be solved analytically, but the results are functional dependencies of the track parameters on the hit coordinates that can be extremely heavy even for a very performing CPU. The SVT approach is to use a linear approximation: the linear approximation has been shown to be so good [79] that a single set of fitting constants can be used for each silicon detector mechanical wedge (30° in the detector azimuthal angle ϕ).
The combined use of pattern recognition and linearized fitting has been thoroughly simulated using Run I data [79], demonstrating the possibility of achieving offline resolution within the required time constraints. The trigger efficiency has also been studied on real Run I data samples, and found to be satisfactory (see [80], [81]).

4.3.1 Pattern Recognition

The pattern recognition stage is in charge of individuating candidate *roads* in the silicon detector. The candidate roads must contain a set of hits consistent with the presence of a candidate track: roads are similar to tracks at coarser resolution.
This fact allows to reduce combinatorics in the presence of a track. At the same time

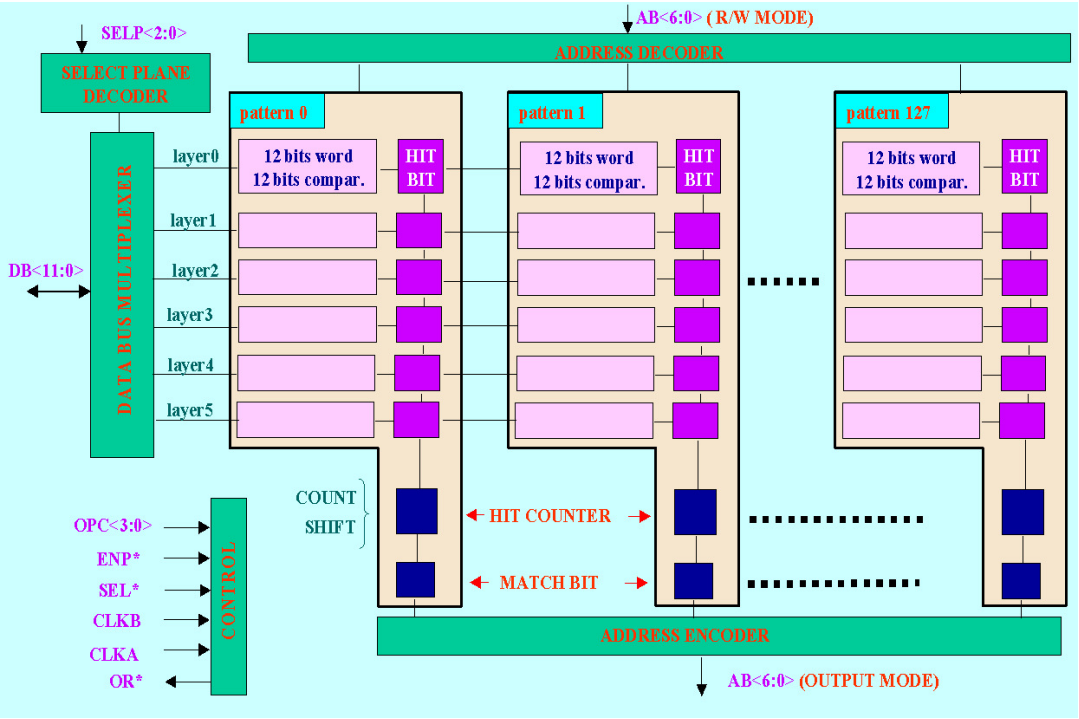

Figure 4.2: AM chip schematic design. Each pattern is organized into 6 *layers* (0 through 5). Each of them has a 1 bit flag *hit counter* telling whether that particular superstrip-layer combination has been hit. At the end of the hit stream hit bits are sequentially added into the hit counter: the *count* operation adds the effective value of the hit bit for the current layer, while a *shift* operation adds 1 whatever state the hit bit is. The Match bit is then flagged if the hit counter reaches the value 6 (possibly in coincidence with the hit bit of layer 5, if required). Single *layer* read/write operations are possible for pattern setup.

the large region of the detector where no tracks left hits is automatically excluded. In principle, given the fact that the detector is intrinsically granular, we might think to push pattern recognition to the natural scale of the detector. This would eliminate the need of a track fitting stage, but the set of patterns to be checked would be too large.

The heart of the pattern recognition technique is a device capable of checking *at the same time* how many and which pattern of *superstrips* (that is *roads*) are present. The most convenient implementation of this operation is a parallelized one, and that's why a customized device has been designed and built to implement such an operation. The Associative Memory (AM) chip is capable of simultaneously

checking 128 patterns, organized in 6 layers, 12 bits wide. Many AMchips can work in parallel, thus allowing in principle to check a set of patterns as large as desired. In practice, each SVT sector contains 256 AMchips, for a total of 32768 patterns.
The working principle of the AMchip (see fig. 4.2) is that of a content addressable memory: the superstrip coordinate is stored in the memory cells and flagged out when the superstrips hit in that event are fed to the memory.
The AMchip is a device acting in two cycles: in the first stage (input) all the roads corresponding to the same event are compared with the patterns stored, flagging the ones which have been hit. When the end of the hit stream for that event is detected, the AMchip is switched to the *output* state: all the flagged roads are sequentially output by the AMchip, ready for full resolution investigation by the fitting stage.
The AMchip works at a clock speed greater than $30\,MHz$. The chip is capable of comparing the incoming superstrip coordinate with all the patterns stored in a single clock cycle, that is less than $33\,ns$. Also the *output* operation sends out one word every clock cycle.
Since the detector itself is organized in *layers*, the AMchip has been designed to group up to 6 different superstrip coordinates in each pattern, assigning each of them to a specific layer.
In the simplest implementation all the layers in the pattern must be hit by the incoming superstrips in order to have the pattern flagged. In addition to the standard matching algorithm, which requires that all the superstrip coordinates (each pertaining to a different *layer*) are hit, also a *majority logic* mode has been implemented with AMchips: the hit can be flagged if all layers but one (either a specified one or no matter which) hasn't been hit. Moreover, one specific layer can be forcedly required to be present.

4.3.2 Linearized Track Fitting

After the pattern recognition stage, the fitting operation can be restricted to the subset of hits which pertain the particular road flagged. This simplifies the fitting work, but it's not sufficient for a fast enough implementation.
The working principle of the fitting algorithm is as follows. Each track is identified by six coordinates: four from different layers selected in the silicon detector and two derived from the track parameters fitted by the XFT.
We can assume that there exists a set of constraints the 6 parameters must satisfy in order to correspond to a physical track. Since the input coordinates are six while the track parameters to be determined are three (the transverse momentum of the track P_t, the azimuthal angle ϕ and the impact parameter d_0) three separate constraints must exist.
These constraints can be expressed by three equations:

$$F_i(\vec{x}) = 0 \quad i \in \{1, 2, 3\} \tag{4.1}$$

Where $\vec{x}$ is a six-dimensional vector whose components are the six coordinates discussed above. The constraint equations (4.1) can be linearized around the mean

value of the x_i parameters ($\vec{x}_c$ from now on) obtaining:

$$\nabla_{\vec{x}} F_i(\vec{x}_c) \cdot \Delta\vec{x} + F_i(\vec{x}_c) = 0 \tag{4.2}$$

Pattern recognition within a road is thus reduced to the calculation of the scalar product in equation 4.2, where the parameters $\nabla_{\vec{x}} F_i(\vec{x}_c)$ and $F_i(\vec{x}_c)$ are defined once for all in every subset of the space $\vec{x}$ where the approximation 4.2 is good enough. We don't discuss here the best criteria which defines this subset. The result is that the approximation described by equation 4.2 is good enough even if we use the same set of constants for a full 30° wedge of the SVX II. This result corresponds to the statement that the manifold which describes physical tracks in the six dimensional space of the $\vec{x}$ parameters is practically flat within each SVX II wedge (see fig. 4.1). We still have the problem of how to compute the constants which define the constraints in the linearized approximation.
Let's call $\vec{v}_i = \nabla_{\vec{x}} F_i(\vec{x}_c)$ and $c_i = F_i(\vec{x}_c)$. Given a "training" sample $\mathcal{S}$ for which track parameters and $\vec{x}$ are known, we can proceed as follows: first observe that these tracks obey the exact relation $F_i(\vec{x}) = 0$. As long as the linear approximation is good, also equation 4.2 holds, and thus $\vec{v}_i \cdot \vec{x} + c_i = 0$. Averaging this relation on the sample $\mathcal{S}$ we discover that $c_i = -v_i \cdot \langle\vec{x}\rangle_{\mathcal{S}}$.
On the other hand, 4.2 tells us that for real tracks the linear function $y_i(\vec{x}) = \vec{v}_i \cdot \vec{x} + c_i$ is zero and thus also its covariance is necessarily zero. This relation translates on the requirement that:

$$^t\vec{v}_i M \vec{v}_i = 0$$

where M is the covariance matrix of the components of the vector $\vec{x}$ evaluated on the "training" sample. This means that the vectors $\vec{v}_i$ belong to the kernel of the covariance matrix M.

So far we described how to *recognize* physical tracks. The point still to be clarified is how SVT measures their *parameters*.
A similar approach is proposed: the functional relation between the track parameters and the vector $\vec{x}$ is linearized

$$\tilde{p}_i = \mathcal{F}_i(\vec{x}) = b_i + \vec{w}_i \cdot \vec{x} + O\left(x^2\right) \quad i \in \{1,2,3\} \tag{4.3}$$

We thus introduce the linearized parameters:

$$p_i(\vec{x}) \equiv b_i + \vec{w}_i \cdot \vec{x} \quad i \in \{1,2,3\} \tag{4.4}$$

The linearization coefficients $\vec{w}_i$ and b_i are calculated once for all from a sample $\mathcal{S}$ of real tracks for which both track parameters and $\vec{x}$ are known. Given a set $\mathcal{S}$ which is an unbiased sample of real tracks with real parameters $\tilde{p}_i$, we can define the w_i's and the b_i's requiring that the distribution $\tilde{p}_i - p_i$ is *unbiased* and of minimum width:

$$\langle\tilde{p}_i - p_i\rangle_{\mathcal{S}} = 0 \tag{4.5}$$

$$\nabla_{\vec{w}_i} \left\langle(\tilde{p}_i - p_i)^2\right\rangle_{\mathcal{S}} = 0 \tag{4.6}$$

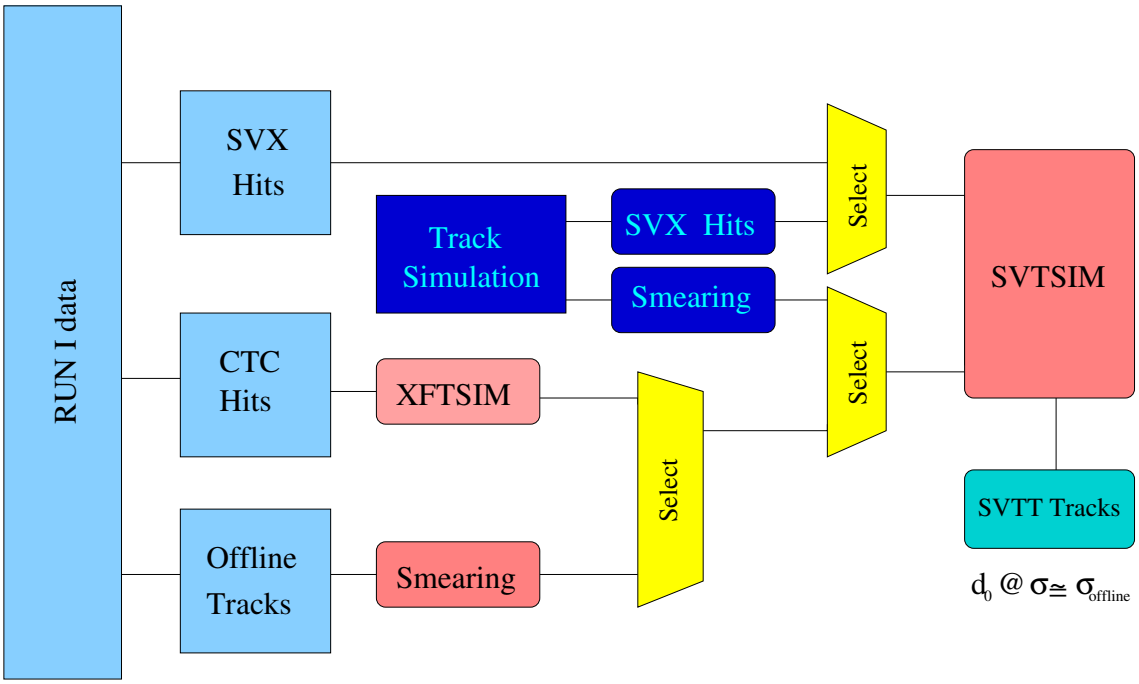

Figure 4.3: Schematic structure of the SVT simulator architecture.

Given the covariance matrix M of the track coordinates $\vec{x}$, we obtain:

$$\begin{array}{rcl} \vec{w}_i & = & M^{-1} \cdot \vec{\gamma}_i \\ M & \equiv & \frac{N}{N-1} \left\langle \left(x_\alpha - \langle x_\alpha \rangle_{\mathcal{S}}\right) \left(x_\beta - \langle x_\beta \rangle_{\mathcal{S}}\right) \right\rangle_{\mathcal{S}} \\ \vec{\gamma}_i & \equiv & \langle \vec{x} \tilde{p}_i \rangle_{\mathcal{S}} \\ b_i & = & \langle \tilde{p}_i \rangle_{\mathcal{S}} - \langle \vec{w}_i \cdot \vec{x} \rangle_{\mathcal{S}} \end{array} \tag{4.7}$$

The effect of detector misalignment has been thoroughly studied in [79]. The conclusions are that the algorithm performance is practically undistinguishable from the offline within the specified mechanical tolerances. This concludes the recipe to the pattern recognition and track fitting algorithm for SVT.

4.3.3 Resulting Performances

The resulting SVT algorithm performances have been thoroughly studied with the aid of a software simulator (SVTSIM). This simulator (see fig. 4.3) has been extremely useful in simulating and testing the hardware and in studying physics rates for the CDF II setup.
SVTSIM can in fact take as input both real or simulated data. The real data is in the old CDF I format, in that case we simulate the behavior of an hypothetic SVT connected to the SVX' detector. SVX' and CTC hit coordinates can be used as input, alternatively to the use of a smeared version of the SVX' and CTC tracks fitted in the CDF environment. In the case of simulated tracks (montecarlo data), a parametric simulation of the SVX detector is available. In any case the final SVTSIM output is a set of tracks (SVTT) with parameter resolutions similar to those

obtained by the offline algorithms. This study has been carried out on real data samples from Run I, but the same simulator architecture is configurable to work on any detector configuration. A study of the track parameter resolutions and the reconstruction efficiency of this algorithm is reported in section 4.8.

4.4 Overall SVT architecture

SVT (see fig. 4.4) is organized as a set of 12 parallel engines, each processing the stream coming from one 30° SVX II wedge. Each SVT wedge consists of 9 boards[1], with data flowing from board to board through front panel data lines. The error monitoring is handled in parallel for pairs of SVT wedges by a supervising board (Spy Control).
Data flow from one board to the other is handled with the same uniform protocol for all the SVT elements; any SVT data port complying to this protocol is monitorable through a *Spy Buffer*, which is a circular buffer keeping a VME accessible copy of the data flow. The Spy Control, together with the Spy Buffers thus acts as a sophisticated debugging tool for the SVT data streams: we can *freeze* the *spy–buffers* of all the SVT boards in coincidence with predefined events (error conditions) or under the supervision of an external program.
Input processing is done through 4 different boards: the Hit Finders for the SVX II data flow, and the XTF boards for the COT parameters.
The input stage is followed by the pattern recognition stage, implemented in four different boards: the associative memory group (AM sequencer and two AM boards) and the Hit Buffer. The AM system is composed of 3 boards: the AM sequencer (AMS), which controls the status and the operation of the AM chips, and the AM boards (AMb), which act as slaves hosting the AM chip banks for the AMS. The AMS feeds the AM chips with the hit stream and sends out the identifiers of the roads hit in that particular event (*road* stream). The Hit Buffer board (HB) attaches to each road output by the AMS the set of corresponding hits from the HF.
After the pattern recognition stage we have the track fitting stage, implemented into a single board (*Track Fitter*).

4.5 Single Board Functionality

The first processing stage in the SVT is performed by a set of three clustering boards (Hit Finders) for each SVT wedge. Raw SVX II data consists of hit strip coordinate, followed by the signal amplitude. Each Hit Finder (HF) receives 4 optical fibers (G-links) from the SVX II DAQ system. Each pair of fiber channel transmits the strip streams for one wedge in a single SVX II electrical barrel. Each hit finder is able to process 4 G-links. Since SVT merges the information from all electrical wedges in a single ϕ sector (six segments along z), the hit streams from 3 HF are merged together by a Merger board.

[1]The boards comply to the VME9U standard

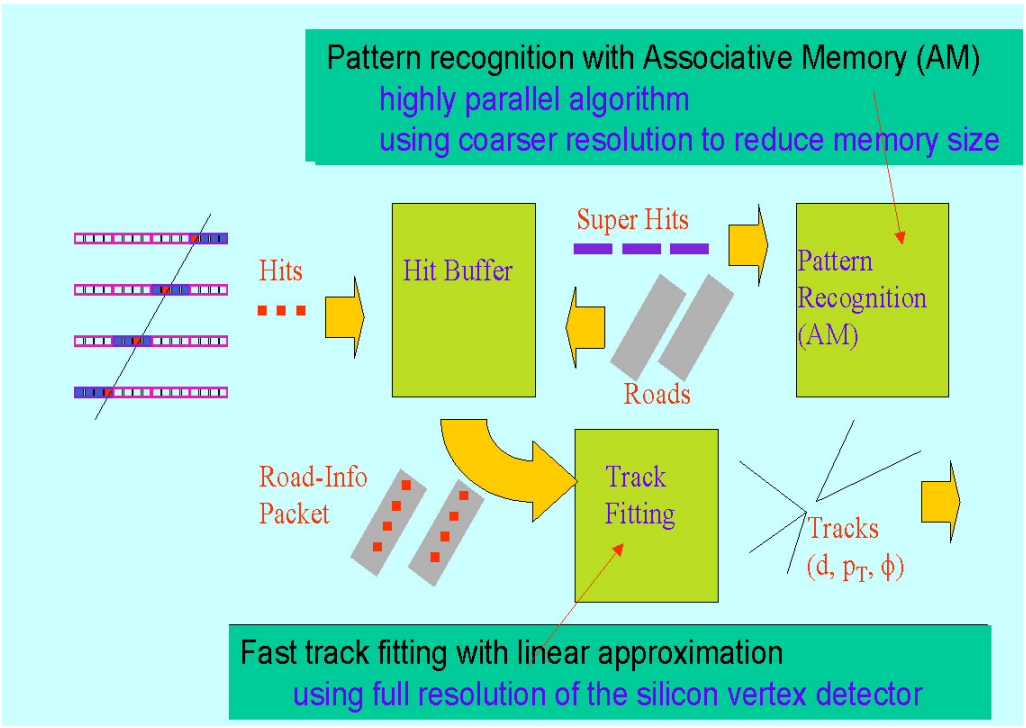

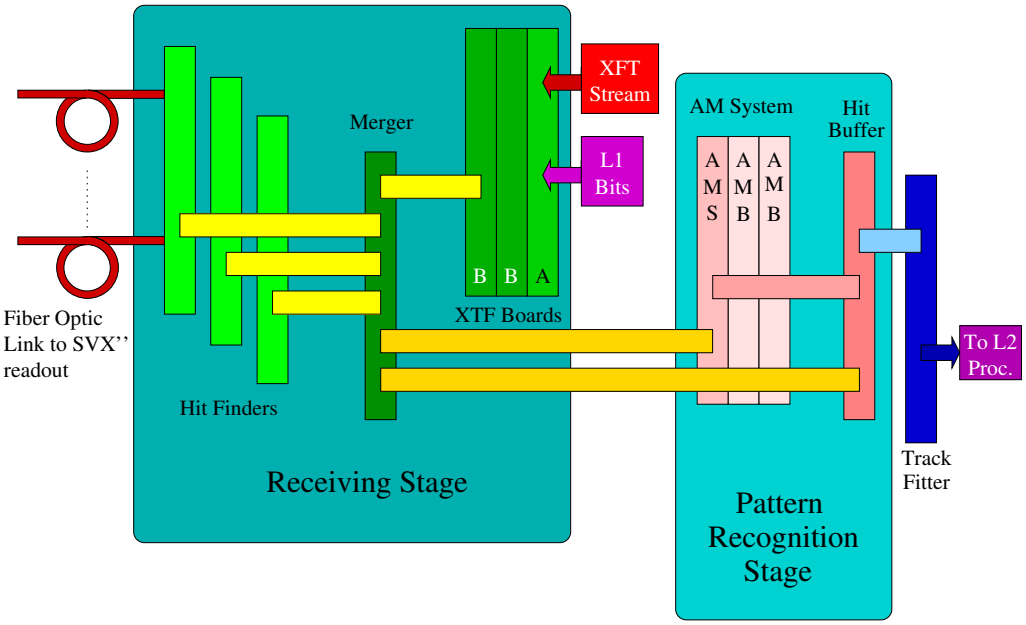

Figure 4.4: (top) Block diagram of the SVT algorithm implementation. (bottom) Board organization of an SVT wedge (1/12 of the whole system).

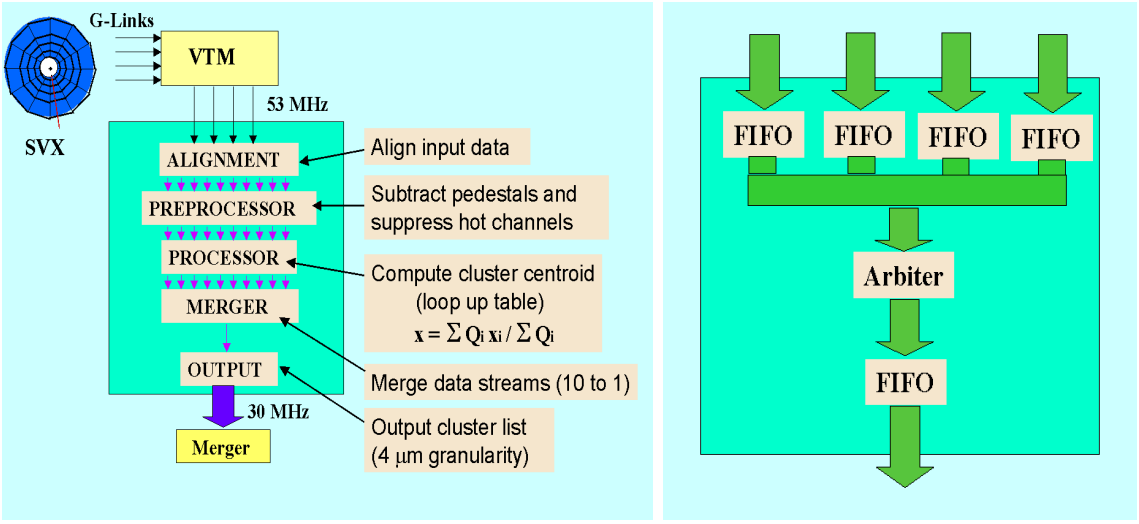

Figure 4.5: (left) Hit Finder and (right) Merger block diagram. See text for a detailed description.

The **HF** (see fig. 4.5) is organized as follows. An auxiliary card (VTM) converts the four G-links' serial data into four set of 20-bit words, clocked out at 53 MHz. This data is passed to the HF board through the crate backplane.
The first stage of the HF realigns the G-Link words into ten sets of 8-bit words corresponding to ten SVX readout streams. The stream is then coded in a 26.5 MHz sequence of 16-bit words. After this each data stream is parsed and simplified: only the axial strip coordinates and amplitudes are kept and fed to a set of parallel *clustering engines*. Clustering is then performed applying a pulse-height-weighted average of consecutive strip positions, at a resolution which is 1/16 of the silicon strip width. This makes the cluster position 14 bits wide.
Output of all the clustering engines is then merged and encoded as a 23 bit word following the SVT standard.

The XFT output consists of a single stream of track parameters, encoded in a protocol slightly different from the one needed by SVT. The translation into an SVT stream is operated by a set of three **XTF** boards (1 XTFA and 2 XTFB) common to all 12 SVT wedges. The XTFA board receives the XFT stream and the L1 trigger information, converts the relevant information into an SVT-like stream and sends it to the two XTFB boards through a custom backplane. The XTFB boards act each as a 6-fold fanout thus feeding 6×2 SVT wedges.
Relevant information from the XFT fitter is encoded differently for the pattern recognition and the track fitting stage: an identical copy of the XFT data is sent to the track fitters, while a coarser resolution mapping is used for the ϕ and curvature parameters in order to handle them with the pattern recognition engine.

Hits from the three Hit Finders are merged together with the XFT output into a single stream by a **Merger** board (see fig. 4.5). This consists of a 4-input 2-output board, capable of merging streams in the SVT format with a twofold fanout. The merger identifies data streams on the different inputs on the basis of the event they

belong to. Words from data streams belonging to the same event are merged together in a first-come first-serve basis (*non deterministic* merging) or in a predefined order (*deterministic* merging). The first option is preferred for improving the device speed, while the latter is desired for debugging purposes. Data for the same event is output by the merger as soon as it is received, on two identical output streams.

The first *hit* stream output by the merger goes to the **Associative Memory Sequencer** (see fig. 4.6), which performs the pattern recognition stage of SVT together with 2 slave AM boards. Communication with the AM boards flows through a custom backplane. The AMS remaps hits into coarser *superstrips*, which are then fed through the backplane bus to 2×128 AM Chips, distributed on two AM boards. Each AM chip is a full custom ASIC CMOS device [78] containing 128 roads, each road is defined as a combination of six superstrips, one for the XFT and 5 for the silicon layers. A road identifier is output back to the AMS through the backplane bus if the predefined set of superstrip coordinates for that specific road has been received. Matching *roads* start to flow back through the AMS to the output stream as soon as the last hit of the event has been received. The AMS board hosts a VME programmable device (*microsequencer*) in charge of processing each input stream executing the commands specified. The microsequencer is in charge of sending the correct sequence of commands to the AM chips. The microsequencer algorithm can depend on the L1 bits transmitted by the XTF boards, thus allowing greater flexibility in the event handling: one might desire, for example, to apply majority logic (see section 4.3.1) only to a subset of the L1 triggers.

The **AMboard** (see fig. 4.6) is a slave board, communicating with the rest of SVT through a custom backplane interface. Each amboard makes 128 AM chips accessible to the AMS, through a tree structure controlled by a set of logic interfaces called *glues*. Clock distribution to the AM chips and VME access for pattern read and write is also provided.

The oncoming hit stream is sorted by the **Hit Buffer** (see fig. 4.7) into an internal register (Hit List Memory) according to which road they trigger in the AM stage. After receiving the list of roads found by the AM, the HB appends all the hits found in each road and sends the whole packet to the TF.
The Hit Buffer works as a well organized library, where books arrive in arbitrary order and are quickly arranged on bookshelves by basics subjects - one shelf for each subject. The librarian also maintains a list of complex, interdisciplinary topics. Each complex topic (e.g. “CMOS VLSI Design”) points to several specific basic subjects (e.g. “MOS Transistor”, “VLSI Technology”, “Logic Design” and “System Design”). Usually the same basic subject will be pointed by many different topics. When a complex topic is later requested by the user, the librarian looks at the basic subjects pointed by the topic and all books on these subjects are quickly found and delivered. The book corresponds to the *hit*, the basic subject to the *superstrip*, the complex topic to the *road*, and the set of bookshelves to the *hit list memory*. During the *write mode hits* are copied from the input and immediately organized in the Hit List Memory, according to the *superstrip* they belong to. *Roads* are sets of *superstrips*, one for each layer. During *read mode*, each *road* received by the HB triggers an output sequence made of the road itself and the *hit list* corresponding to each *layer*

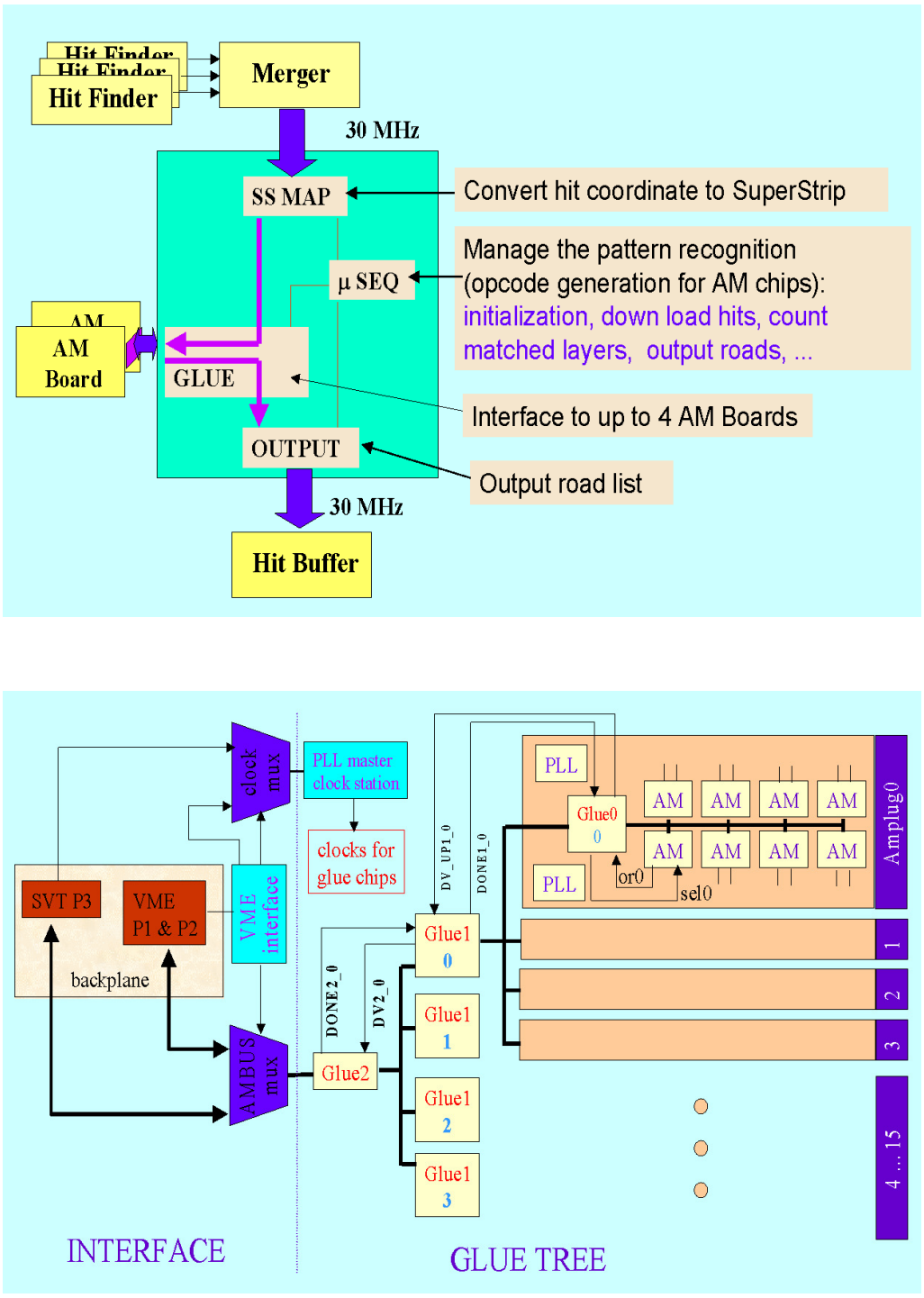

Figure 4.6: (top) Associative Memory Sequencer and (bottom) Associative Memory Board block diagram. See text for a detailed description.

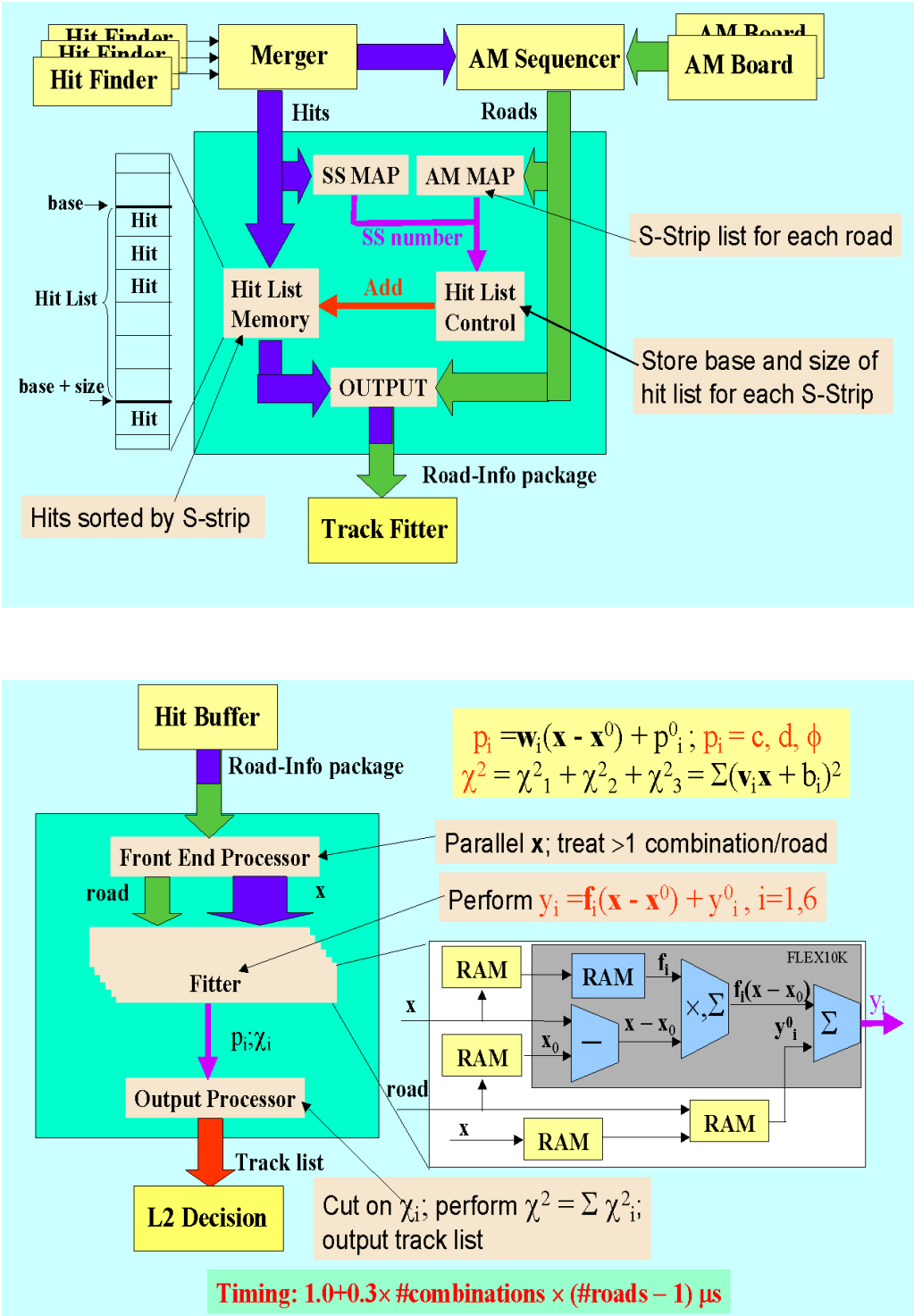

Figure 4.7: (top) Hit Buffer and (bottom) Track Fitter block diagram. See text for a detailed description.

in the *road*.

The **Track Fitter** board (see fig. 4.7) loops on all possible *hit* combination within a given road, applying for each of them the linearized fitting algorithm (see section 4.3.2). All the tracks falling within the preset χ^2 cut are then output and sent to the Level 2 processors.
The main function of the TF is that of performing the calculation 4.7. In order to further reduce the computational load, the linearization is performed separately on each SVT road. In that condition the $\vec{w}_i$ coefficients can still be factorized for the whole wedge, while the b_i coefficients are split in a wedge dependent part (b_i) and a road dependent part (p_i^0). Having the $\vec{w}_i$, b_i and p_i^0 mapped into memory leaves the track fitter only in charge of performing a memory lookup, few additions and the multiplication $\vec{w}_i \cdot \vec{x}$. Since the $\vec{x}$ are now restricted within a single road, the multiplication can be restricted to the lowest 8 bits of the 14 bits wide road coordinate.
6 parallel devices (*fitting engines*) are implemented in the TF board, 3 of them are used to calculate the 3 track parameters, while the other 3 perform a similar calculation for the fit χ^2.
An input processor is in charge of generating the various possible hit combinations if more than one hit is present within the same superstrip, while an output processor performs the χ^2 cut and data encoding in the SVT format.

4.6 SVT with Layer 00

We have described the baseline design for SVT, disregarding the Layer 00 upgrade. If Layer 00 hits are used in SVT two requirements must be met:

- Mechanical tolerances for Layer 00 must be compatible with SVT: any detector ladder must be within $100\,\mu rad$ from the nominal beam axis
- Some additional boards must be added to SVT

The current implementation is as follows (fig. 4.8). Six HF boards are added in order to receive and clusterize Layer 00 data (each pair of layer 00 wedges is transmitted with the same protocol as a single SVX II wedge). Then we need to split these streams for the 12 wedges. This is done in common with the XFT data. A set of 6 modified merger boards (XTFC) is added: each XTFC board receives the XFT stream for each 60° wedges (two XTFB outputs) and the output of an HF, separates the hits in the stream according to the SVX II wedge they belong to, and sends them separately on two outputs (one for each SVT wedge). Each output then replaces the corresponding XTF stream in the available input of the hit merger belonging to the receiving stage of each SVT wedge.

4.7 Current Project Status

All the SVT boards have been produced and tested. Each prototype has been successfully tested up to the nominal 30MHz clock speed, and a mock–up of an

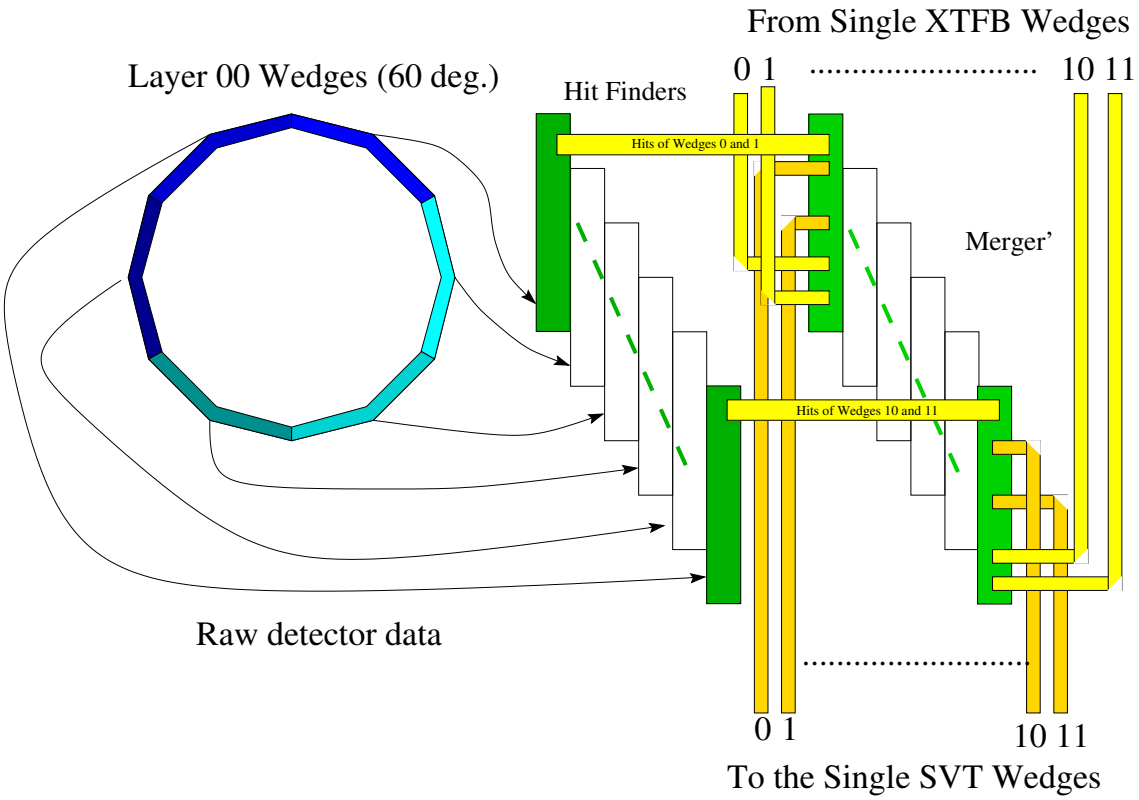

Figure 4.8: Update to include Layer 00 in the SVT stream. 6 HF boards receive the raw Layer 00 data, which is merged with two XTFB streams, separated in 30° wedges and sent to the 12 SVT layers.

SVT wedge (The "Vertical Slice Test") has been thoroughly tested at Fermilab. The complete hardware device has been assembled and is currently running as part of the CDF DAQ system: chapters 12 and 13 will show that SVT has been able to actually fit tracks in real time for the CDF II detector.

4.8 SVT Efficiency on Real Run I Data

We now turn our attention to the issue of the device efficiency. The key SVT parameter for any trigger based on this tool is the track detection efficiency (ϵ_{trk}). The performance of the SVT algorithm in terms of ϵ_{trk} can be investigated without the need of the Run II hardware: a study has been performed on SVT's efficiency, using a small Run IB data sample and the SVT simulator. The results are in good agreement with expectations. Part of the work has also been devoted to the comparison of the track parameters produced by the simulator with the ones extracted by the offline algorithms.

4.8.1 Introduction

This is the first attempt at evaluating ϵ_{trk} relying on a real data sample and the SVTSIM software simulator of SVT.
In general, *efficiency* is defined to be the fraction of some sample of *good* tracks that our system is able to detect. In the case of SVT, the ideal reference sample would be the subset of the world of "real" tracks (which is visible only through the offline reconstructed tracks) entering within our system's nominal acceptance.
We will thus try to define a suitable set of cuts on the offline (SVXS) tracks with the purpose of producing a reasonable and consistent reference sample for the estimate of the efficiency.
The version of the SVT simulator we use is able to use as the "fifth" layer input either the XFT simulator output or the offline tracks (operating, in this case, a rough smearing algorithm); we will exploit this ability to better understand the connection between offline and SVT tracking.

4.8.2 Samples and Selections

Let's first of all study the composition of our "standard" SVT simulation output. The *baseline* SVT (see [79]) will reconstruct tracks which have 4 hits in the same ϕ wedge of the Silicon VerteX detector with $P_t > 2\,GeV/c$. Moreover, since the AM storage is limited in capacity, the patterns don't have 100% coverage. The default pattern set gives (see [79]) nominal 90% efficiency for tracks pointing back towards a spot of size $500\,\mu m$ around the beam axis.
We might be led, from the previous consideration, to the conclusion that the beam position of the data set used plays a significant role in the estimate of the trigger's efficiency; however, we will show that there is a very loose dependency of the pattern efficiency from the beam position: the data set used in the simulation comes from

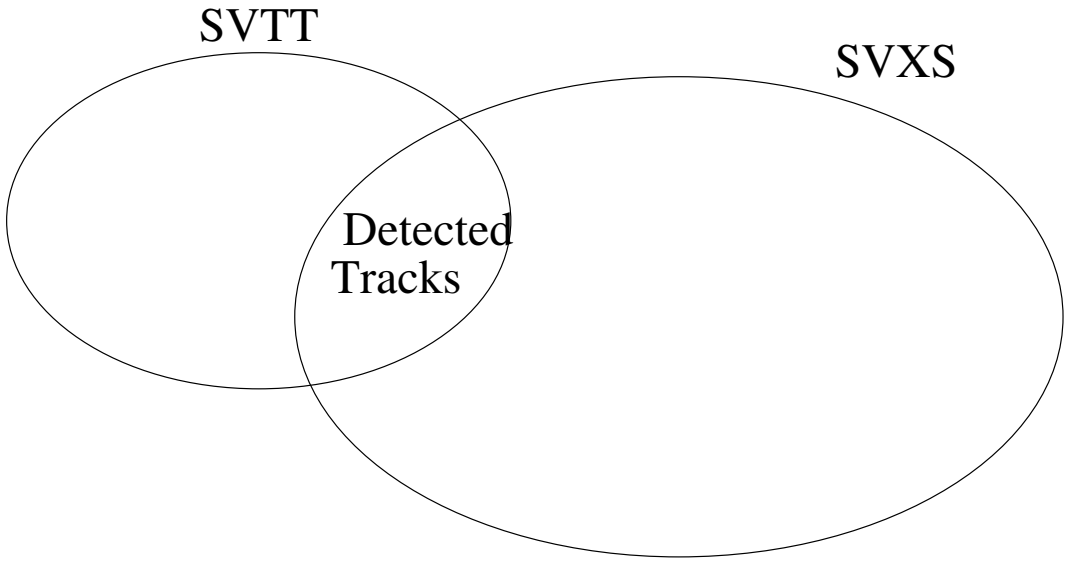

Figure 4.9: A simplified sketch of our different track sets: SVT fitted (SVTT) and offline-reconstructed (SVXS)

a run which has the beam $1.5mm$ far off from the nominal detector (and thus SVT spot) axis. Even in this extreme case no significant difference is noticeable in the trigger efficiency if we change the pattern size from $500\,\mu m$ to $2\,mm$.
The only free parameter available in the simulation is the cut on the χ^2 of the tracks, intended as the *linearized* χ^2 of SVT, nominally distributed as a 3 d.o.f. variable.
In this work the cut on this parameter has been set to 11.34 (corresponding to 99% efficiency for a 3 d.o.f. χ^2).
This is the full story for our SVT sample (SVTT), and thus the numerator of our *efficiency*.
Things are more complicated for the offline tracks, that is our denominator: we can't accept the whole set of SVXS tracks, which contains tracks with low P_t and/or 3 (and less) silicon hits. A reasonable requirement is to restrict ourself to the subset of SVXS tracks which have **4 hits** in the same ϕ-wedge of SVX', $P_t > 2$ and impact parameter within $500\,\mu m$ from the beam axis. We need also to fix a χ^2 cut on these tracks. The choice is made rather difficult by the fact that the χ^2 parameter for offline tracks is calculated differently way from SVT, using a rescaled covariance matrix from the CTC fit, and is nominally declared to have 4 d.o.f. in the case of 4 SVX hits tracks. We thus choose to introduce a χ^2 cut for the offline tracks corresponding to a 99% efficiency for a 4 d.o.f. χ^2 (thus about 13.28). These assumptions on the two χ^2 distributions will affect our results: a direct inspection (see the first two plots of fig. 4.14) shows deviations from what expected.

4.8.3 Preliminary considerations

Let's refer to figure 4.9: the two sets of tracks which we have defined above (we will refer to them, from now on, as *SVT* and *offline* tracks respectively) look at first sight like two intersecting sets, and our purpose seems simply that of counting sheeps which live in each set and in the intersection. Unfortunately, things are more complicated because our sheeps tend to live across the borders of the intersection: the trigger might have a 50% efficiency and look at the same time 100% efficient if it produces two tracks for each *offline* track going through the detector. An underestimate of the "intersection" is possible too (e.g. if the selection cuts for the two samples are not consistent).
Since we're interested in a good definition of the efficiency, what we are truly looking for is the size of the subset of *offline* tracks for which we are able to identify a corresponding one (in a sense later specified) in the *SVT* sample.
In parallel to this, we will also look for an estimate of the *over efficiency* of our simulation, which can be conveniently parametrized by the fraction of *SVT* tracks that *don't* look sufficiently 'similar' to *offline* tracks.
The only unsolved problem seems now that of defining an algorithm that tells us whether a given *SVT* track has a corresponding *offline* track. Two different algorithms have been explored, each one with advantages and disadvantages. The first one is simple: if the simulation has been performed using CTC tracks instead of the XFT output, both the SVT and the offline tracks have a link to the corresponding CTC track from which they've been generated. We can then simply say that the two entries correspond to the same real track going through the detector when they have been generated from the same CTC track. This seems a good definition, and in fact is, when we are not using the XFT simulator. In this second case SVT tracks are not originated from a CTC track, and thus cannot be back-connected with offline tracks. For this reason another method of *SVT -offline* tracks matching has been adopted and will be continuously compared with the one above described. This method is described in the next section.

4.8.3.1 A *distance* between tracks

Let's assume we are really looking at these tracks, in a sufficiently small scale, so that all the offline tracks look distant from each other, and let's now draw the SVT track for which we want to find a 'partner': it is intuitive that the best candidate is the track that looks less 'distant' from our SVT track.
Things can be formalized looking at the difference between track parameters among matched tracks, when the matching is done using the first algorithm described (*backlink*): all deviations (fig. 4.10) look Gaussian, with a width of the order of the SVT expected resolution[2] (see [79]): $35\mu m$ in d_0, $34 \cdot 10^{-6} cm^{-1}$ in curvature and $3.7\, mrad$ in ϕ_0 (the TDR resolutions are $\sigma_d \simeq 35\mu m$, $\sigma_\phi \simeq 1 mrad$ and $\sigma_{crv} \simeq 14 \cdot 10^{-6} cm^{-1}$

[2]Note that it is not at all obvious that the SVT resolution is $\sigma^2_{off} + \sigma^2_{off-SVT}$ (where σ^2_{off} is the resolution on the parameters of the offline tracking algorithms, and $sigma^2_{off-SVT}$ is the width of the differences foretold). This is essentially due to the fact that the two deviations (offline from *real* and SVT from offline) will be correlated.

for tracks with $P_t > 2\,GeV/c$)[3].
We might expect narrower distributions for these deviations, but there are some smearing effects which have to be taken in account: first of all, the simulator is applying the SVT algorithm to a set of tracks coming from a real run I sample, which is well known to suffer from a beam misalignment orders of magnitude greater than what required for a proper working of SVT. This effect has been partially compensated by a post-simulation subtraction of the beam position, which can't completely remove the effects of such a distortion. Also, it is well known that SVT can't compensate for Z misalignments of the detector, thus also the Z misalignment of the SVX elements could play a major role in the smearing of the residual distribution. The last effect we want to mention is the approximation introduced by the linearized fit operated by SVT: nonlinear effects are considered contributors to the observed smearing.
The Gaussian distributions shown suggest to define a χ^2-like distance among tracks which corresponds to the intuitive idea of similarity between them:

$$\Delta^2 \equiv \left(\frac{d_0^{SVT} - d_0^{real}}{\sigma_{\delta d_0}}\right)^2 + \left(\frac{\phi_0^{SVT} - \phi_0^{real}}{\sigma_{\delta \phi_0}}\right)^2 + \left(\frac{C^{SVT} - C^{real}}{\sigma_{\delta C}}\right)^2$$

Where we have used the track impact parameter with respect to the beam axis (d_0), the usual CDF definition of ϕ_0 (measured, like d_0 wrt the beam axis) and the track curvature (C). The superscripts identify the SVT and *offline* track, and each $\sigma_{\delta x}$ is the width of the distribution $x^{SVT} - x^{real}$.
If we assume to get, in most cases, the right pair of SVT -*offline* tracks, the deviation among track parameters (that is, the quantities δd_0, $\delta\phi_0$ and δC) has to be correlated.

Looking (fig. 4.10) at the distribution of this "distance" among tracks, for pairs matched using the first algorithm described ("back link" using the offline info) and comparing this with the expected χ^2 distribution, we immediately see that the Δ^2 profile looks more compressed toward the y axis than expected for a pure χ^2 distribution with 3 d.o.f.: this tells us that there is in fact some correlation between different parameters for "matched" pairs.

We will use this *distance* for two different purposes: the first one is that of matching SVT and *offline* tracks: we can identify a given real track with the nearest SVT track (or vice-versa) using the distance Δ.
Another important role will be played by this parameter: disregarding the algorithm used for matching tracks, we cannot consider a track to be well reconstructed if Δ is too large; it is thus convenient to look at the Δ^2 distribution of matched pairs, to exclude those pairs in which tracks don't look really similar. Given that Δ naturally parameterizes *track similarity*, it seems natural to apply a loose cut on that variable.

[3]Note that the rough XFT model we are using in the present study is expected to provide worse resolution than in the device design, since the covariance of XFT parameters is not correctly simulated

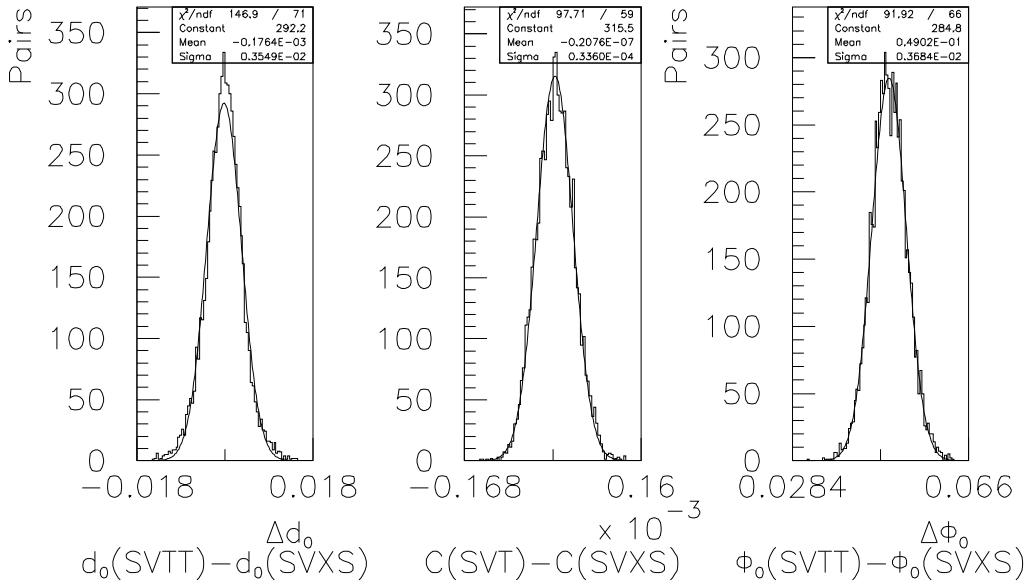

Figure 4.10: Distribution of the track parameters difference between *SVT* and *offline* tracks in the same pair (associated via the back-link to "XFT")

The cut is chosen to be $\Delta^2 < 10$, nominally corresponding to about 98% efficiency for a 3 d.o.f. χ^2 distribution.

4.8.3.2 A comparison of the matching algorithms

An encouraging result is obtained if we compare the Δ^2 distribution (fig. 4.11) for pairs matched with the two algorithms described above: the two distributions look virtually indistinguishable. This encourages our idea of applying the 2nd algorithm (*distance*) in the cases in which the first one is not available (e.g. when simulating the full XFT-SVT chain).

4.8.4 Results of the simulation

We will now present the results of our study, in the case of SVT-only simulation, which allows us not only to obtain an estimate for the system's efficiency, but also to compare the performance of the two methods described above.

4.8.4.1 Effect of the preliminary cuts

The preliminary cuts on *offline* and *SVT* tracks have been described above. In the case of *SVT* tracks, the only cut introduced is the fiducial cut on the impact-parameter: since the pattern's efficiency does not go to 0 for tracks outside the $500\mu m$ spot around the beam, we choose to exclude the tracks outside this range, to sample the nominal high-efficiency region of SVT. Table 4.1 reports the effect of this cut on our sample. In the case of SVXS tracks, we apply successively the five

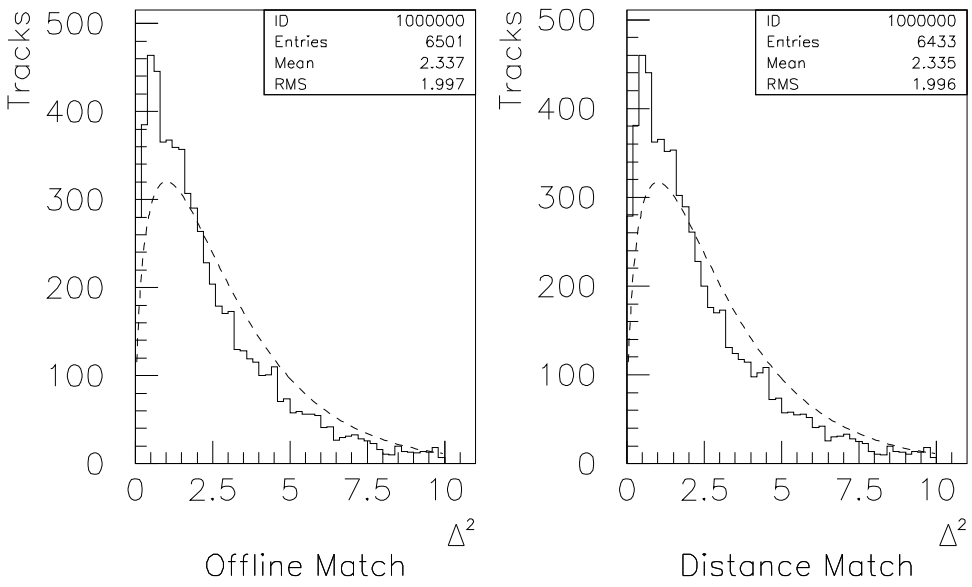

Figure 4.11: "Distance" distributions for pairs matched with the two different algorithms described in the text. The distributions are cut at $\Delta^2 < 10$. The dashed lines are 3 d.o.f. χ^2 distributions, conveniently rescaled.

Cut	Tracks	fraction %
Raw SVTT $\chi^2 < 11.3$	7951	100%
$\chi^2 < 11.3$ and $\lvert d_0 \rvert < 500 \mu m$	7852	98.7 %

Table 4.1: Effect of the preliminary cut discussed in the text on SVTT tracks of our sample (the numbers reported are tracks and not events). The fraction reported is wrt the numbers in the first row of the same table.

cuts described before, finally obtaining the sample of tracks in principle detectable by SVT (table 4.2). We would like to stress here a byproduct of our study: if we look in detail at the various effects that make a 4 hits track not *visible* for SVT, we might suspect that (after cutting on P_t) an important contribution to the device's *inefficiency* is due to the fact that we require that the 4 hits are in the same *phi* wedge[4] . We have then classified offline tracks, looking for those various pathologies, and the result is reported in table 4.3. From now on, we will use as the two reference samples (*SVT* and *offline*) the events obtained in last lines of the corresponding tables.

[4]Note also that SVT is in principle able to reconstruct also the tracks going through two barrels, provided that they are in the same phi wedge. In the present work, however, these tracks are not taken in account because the current internal alignment routine of SVT doesn't yet take in account the offset of the two barrels.

Cut	Tracks	fraction %	fraction %
SVXS $\chi^2 < 150$	84812		
$P_t > 2GeV/c$	20766	100%	
$\chi^2 < 13.3$	17361	84%	
4 hits	9606	46%	100 %
4 hits same wedge (ϕ and Z)	9062	44%	94%
$\|d_0\| < 500\mu m$	8918	43%	93%

Table 4.2: Effect of the cuts discussed above on the SVXS tracks of our sample. The first fraction column is relative to the number of SVXS reported in the second row of the table, while the second one refers to the 4th row. Each line includes all the cuts of the preceding ones.

Grouping	Tracks	fraction %
Whole set	9606	100%
Same ϕ wedge	9305	97%
Same ϕ and Z wedge	9062	94%
Same Z but different ϕ	268	2.7%
Same ϕ but different Z	243	2.5%
Different ϕ and Z wedge	33	0.3%

Table 4.3: Offline tracks with $P_t > 2$, $\chi^2 < 13.3$, and 4 hits classified looking at the position of the 4 hits inside the SVX' detector. The *fraction* column reports the fraction with respect to the fourth row of table 4.2.

4.8.4.2 SVT efficiency

Another choice to be made in SVTSIM is whether to use any charge cluster identified by the offline code in the silicon or only the *high quality* ones. For the actual SVT, the final choice has to be made on the basis of observed efficiency and trigger rates in running condition, which depends also on the quality of the SVX II detectors. The default in SVTSIM is to only use clusters with some quality cut, but since this criterion is not used in fitting the offline tracks, a more meaningful comparison to our offline reference sample requires turning off this quality cut in SVTSIM. We report here the results obtained in both ways.
Table 4.4 reports the number of *offline* tracks which have at least a *matching SVT* mate, that is, a track which passes the $\Delta^2 < 10$ pointing back to the same "XFT" track (first row). On the second row of the same table we report the same quantity for tracks matched using the *distance* algorithm, described in section 4.8.3.1.

As one might expect, the method called *distance* gives bigger efficiencies, because we start minimizing the parameter Δ^2 and then cut on it. The difference between the two estimates is, however, within few %.
In the same table we report also the results of a SVT simulation in which we have enlarged by a factor 16 the "hot" spot size of the trigger (from $500\mu m$ to $2mm$): it is clear that no significant improvement seems to be achieved in the trigger's efficiency, thus showing that the pattern's efficiency decreases very smoothly with the distance

Matching Method	# of Pairs	Efficiency
First (via "XFT") $\Delta^2 < 10$	6331	71%
Second (*distance*) $\Delta^2 < 10$	6383	72%
First (via "XFT") no Δ^2 cut	6568	74%
Second (*distance*) no Δ^2 cut	7828	87%
First (via "XFT") enl. patt.	6453	72%
Second (*distance*) enl. patt.	6400	72%

Table 4.4: Matched pairs using the two algorithms, and different SVT pattern sizes: the lines marked with *enl. patt.* come from the $2\,mm$ spot simulation, while the other come from the default $500\,\mu m$ simulation.

from the nominal "hot" spot's axis.
Note also (fig. 4.12) that if we don't cut on Δ^2 the *distance* match obviously gives even higher results (7828 pairs, corresponding to 88%) with respect to the "XFT" match (6568 pairs, 74%). This is a straightforward consequence of the fact that when we match two wrong tracks the Δ^2 distribution looks flatter and more extended toward big Δ^2 values.
We can affirm that SVTSIM efficiency relative to offline 4-hits is certainly larger than 81%. The *distance* distributions for this new simulation are shown in fig.4.13; the bottom-left plot shows some increase in the large-Δ^2 tail with respect to the case of the 'clean' simulation, presumably due to the presence of the *bad* clusters.

Matching Method	# of Pairs	Efficiency
First (via "XFT")	7202	81%
Second (*distance*)	7141	80%
First (via "XFT") no Δ^2 cut	7400	83%
Second (*distance*) no Δ^2 cut	8320	93%

Table 4.5: Matched pairs using the two algorithms, and the modified version of SVTSIM, without the cluster quality cuts. The last two lines show the same quantity obtained excluding the Δ^2 cut, as previously done in the case of the non-modified SVT simulation.

4.8.4.3 SVT *over*-efficiency

Another accessible and interesting information about SVT is the estimate of the number of tracks that can't be reasonably matched to offline tracks: assuming that the offline package does the best possible track reconstruction, we are led to the conclusion that these tracks are in some sense "wrong" (they might, for example, be a byproduct of the fact that SVT works on the transverse plane only, and thus has no z info). What we want to estimate is then the fraction of *SVT* tracks for which we can't find a mate within our requirements. Table 4.6 report the number of *SVT* tracks which have a *matching offline* mate, that is, a *offline* track which

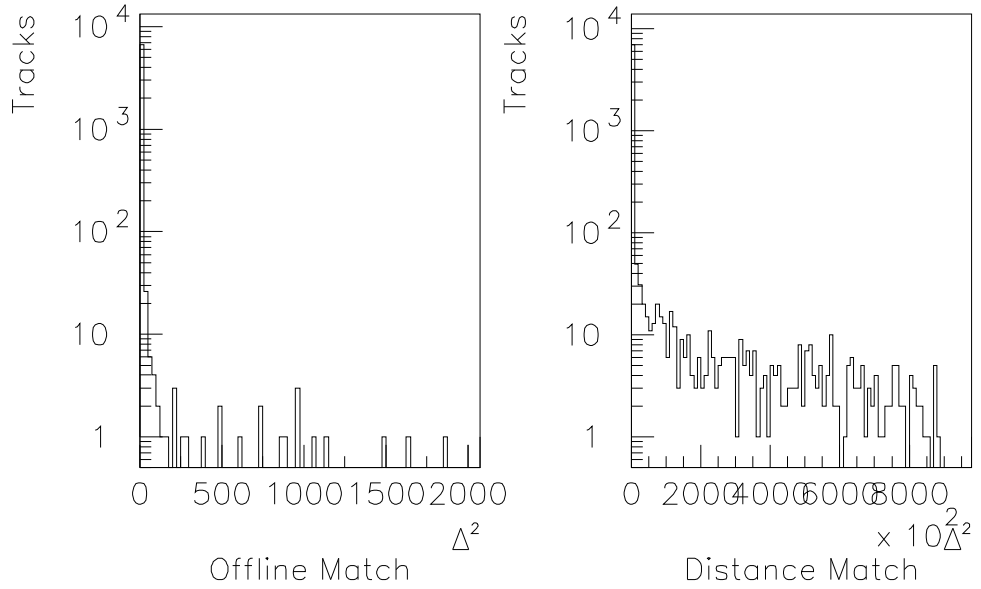

Figure 4.12: Δ^2 distributions for *SVX* tracks matched with *real* tracks using the algorithm described above. To stress the difference in high Δ^2 tails, the log scale is used on the y axis.

passes the $\Delta^2 < 10$ pointing back to the same "XFT" track (first row). On the second row of the same table we report the same quantity for tracks matched using the *distance* algorithm, described in section 4.8.3.1. We report also the difference between the size of our *SVT* sample (7852 tracks) and the number of pairs passing the Δ^2 cut, and finally the *over*-efficiency, here defined as this last column divided by the number of *SVT* tracks.

The high value of this parameter is essentially due to the presence of a "flat"

Type of Match	*SVT* passing the cut (N)	$\#\{SVTT\,\|d_0\| < 500\mu m\} - N$	*over*-efficiency
"XFT"	6455	1397	18 %
distance	6427	1425	18 %
"XFT" enl. patt.	6525	1365	17 %
distance enl. patt.	6497	1493	17 %

Table 4.6: Results for the estimate of the trigger *over*-efficiency. A detailed description of the columns can be found in the text.

background of fake tracks in the χ^2 distribution of SVT tracks (see fig. 4.14). The *over*-efficiency thus obviously depends on the χ^2 cut chosen, since there are regions in the χ^2 distribution naturally more populated by real tracks.
Like in the case of the efficiency estimate (see sec. 4.8.4.2), we report in two separate lines of the same table the results obtained enlarging the pattern size of SVT: also in this case no significant improvement is achieved.

4.9 Conclusions

SVT is designed to reconstruct in real time charged particles trajectories using data coming from the Silicon VerteX detector and the Central Outer Tracker drift chamber. The SVT architecture and algorithm have been specially tuned to minimize processing time without degrading parameter resolution. All the SVT hardware has been assembled and tested successfully during the first CDF II runs.

The efficiency of the SVT simulation is measured on the actual SVX' detector to be about 81% out of a maximal 90%, when calculated with respect to offline tracks within SVT nominal acceptance requirements. Z-misalignments are expected to give some inefficiency contribution, which was not estimated. The requirement of 4 hits in the SVX rejects about 50% of the total offline sample. The inefficiency brought by this requirement could only be improved by allowing majority logic in SVT, which is currently under study.
The device's *over*-efficiency is calculated to be about 20%. These numbers are dependent on the χ^2 cuts chosen on our samples, which may be to some extent arbitrary. In particular, there is an apparent lack of correlation (see fig. 4.14 and 4.15) in the χ^2 parameter for the matched pairs. This suggests that what estimated is to be taken as a lower bound for the actual SVT efficiency.

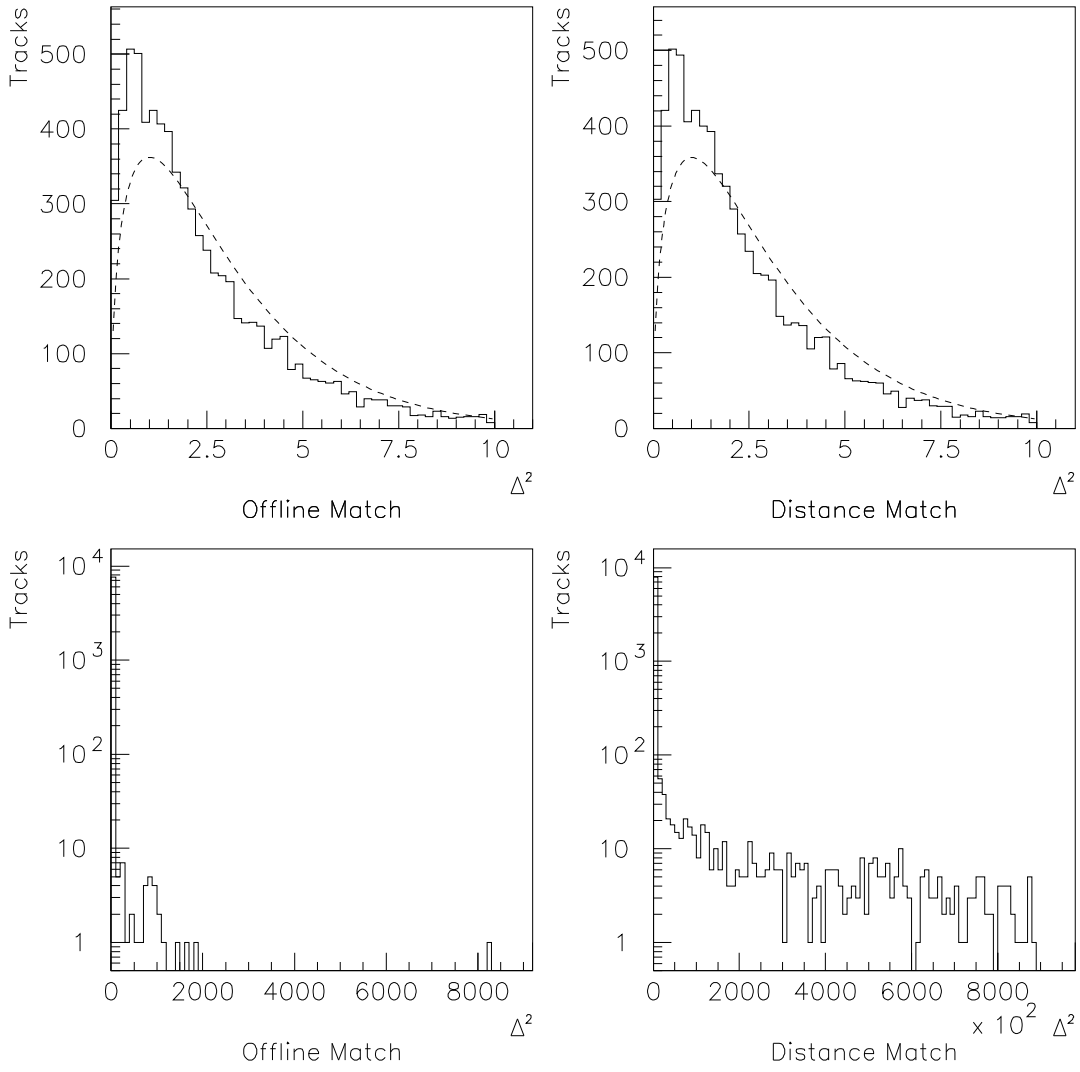

Figure 4.13: Δ^2 distributions for *SVX* tracks matched with *real* tracks using the algorithm described above, in the modified SVT simulation. The upper two plots show the plot restricted to the $\Delta^2 \in [0, 10]$ region, with the 3 d.o.f. distribution superimposed. The lower two plots show the full Δ^2 range spanned by our data.

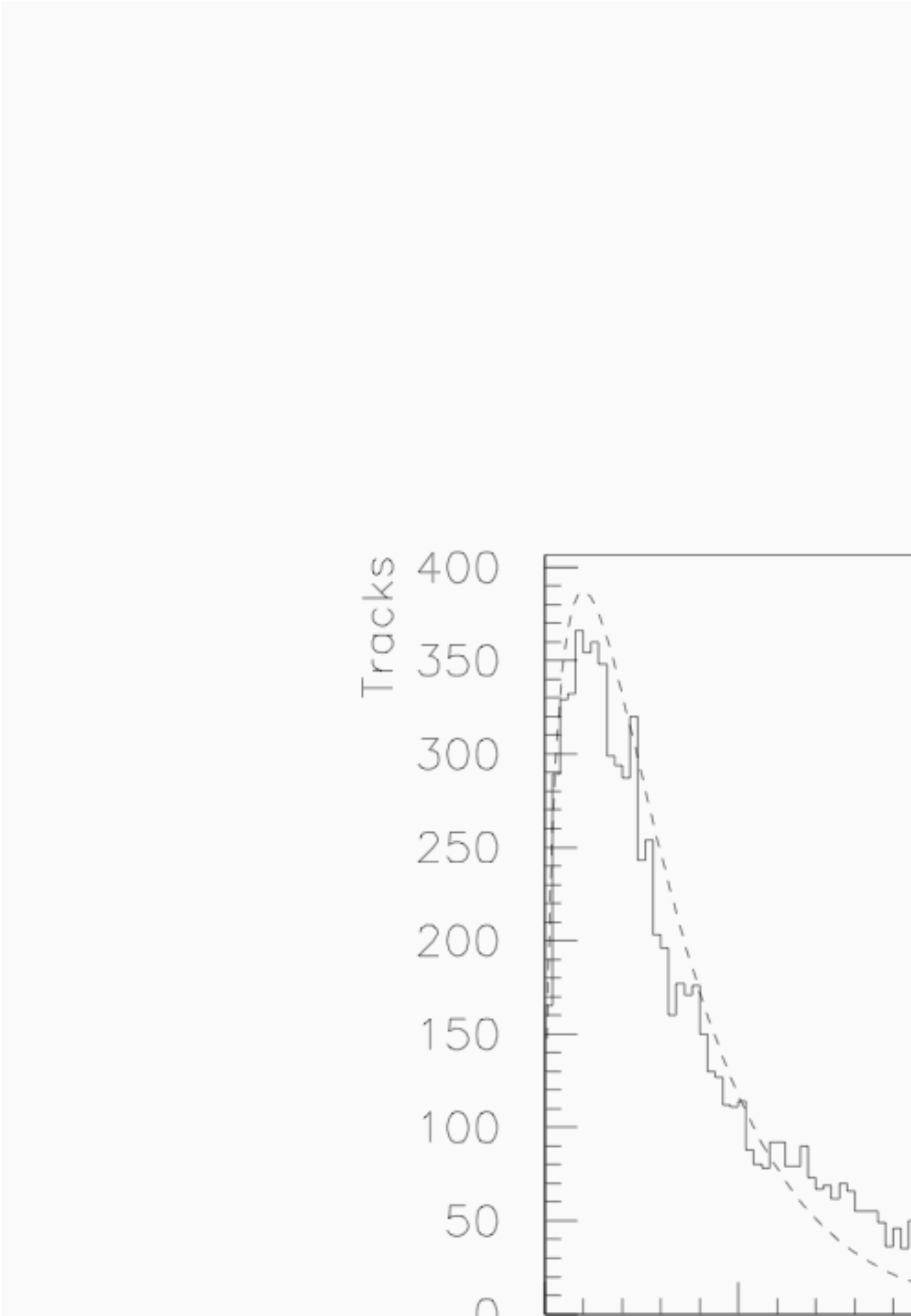
Tracks
400
350
300
250
200
150
100
50
0

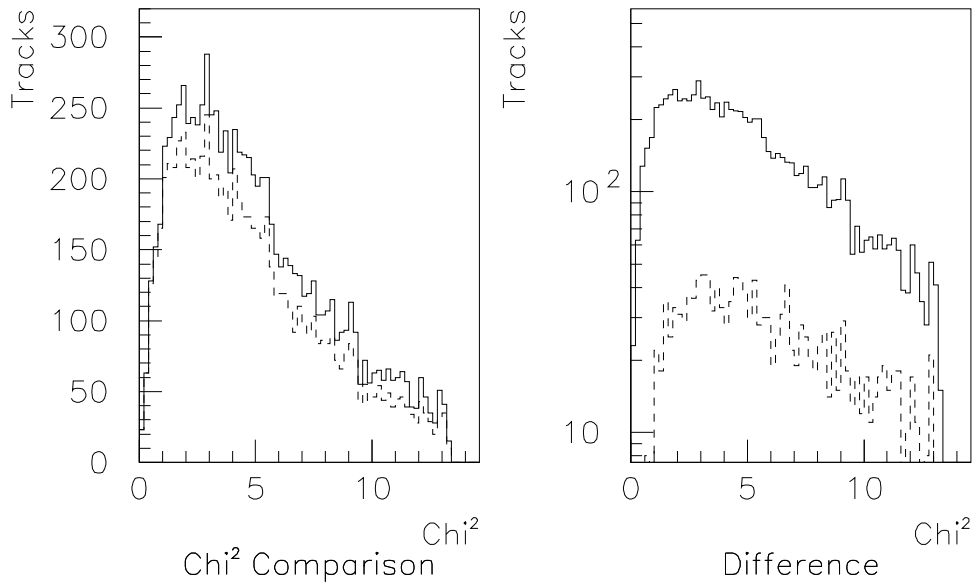

Figure 4.15: Comparison of the χ^2 distribution for the offline tracks passing our quality cuts (continuous line) and those (dashed line on the left plot) which have been matched to an SVT entry (in the *modified* SVT simulation). The difference is reported in the dashed line of the rightmost plot, which shows how the SVTT-SVXS match is uncorrelated with the χ^2 of the real tracks.

Chapter 5

SVT Based Triggers

This chapter describes the status of SVT based B triggers and what are the results so far obtained in their implementation.

The whole collaboration is paying much attention to these trigger channels (and the fully hadronic trigger in particular) because they are major improvements in CDF's capabilities in the B physics sector, and also because of the big resources required in terms of trigger bandwidth. This is why we will be mainly concerned with a sound justification of the required bandwidth.

5.1 Hadronic vs Leptonic Trigger

The B meson decay table [13] is essentially a long list of small contributions coming from heterogeneous decay modes. This is at the same time the weakness and the strength of B physics: having many decay channels means that there are many possibilities of measuring the weak mixing angles. The "reverse of the medal" is that only a small fraction of the total B production cross section contributes to a single channel and analysis: most measurements uncertainties are of statistical nature and therefore maximal care must be taken in the selection and reconstruction of such signals.
CDF I approach was driven by detector performance and limited by the trigger throughput: the selection and reconstruction efficiency for B physics was rather limited, especially for nonleptonic decay modes.
We can distinguish three categories of Run I samples useful for B physics, according to the way in which they were selected and the B modes reconstructed:

- The dilepton sample, selected by requiring two leptons in the event and mostly used for reconstructions based on the J/ψ resonance. This sample had good efficiency for the selection of B decays containing a J/ψ as intermediate state.

- The single lepton sample, selected by requiring at least one lepton in the trigger. This sample has worse efficiency than the previous for B decays. We can basically distinguish for it two B physics applications:

  - The reconstruction of *semileptonic* B decays, where the triggering lepton is part of the reconstructed B decay
  - *Away side* modes, where the lepton is not considered part of the final products of the B meson we want to reconstruct. In most of these cases the lepton is part of the decay of the opposite b quark and requiring its presence is an often undesired statistical limitation

  In both cases, the efficiency for the collection and reconstruction of B decays is poor and limited by the bandwidth limitations on the single lepton trigger, which impose a large ($\approx 5 - 10\,GeV$) threshold on the lepton transverse momentum. In away side modes, there is the additional limit coming from the small semileptonic BR involved.

Achieving a good background rejection was feasible but often trading for a low signal efficiency: leptons had to be stiff enough not to saturate the trigger throughput, while the natural average value of the lepton momentum for semileptonic B decays tends to be of the order of few GeV.
It has already been anticipated that SVT makes the main difference with respect to this problem, and we want to outline in this chapter what are the two most promising uses of this device.
The first one is a variation over the *leptonic* approach typical of Run I and will be discussed first. The second one takes advantage of the full power of SVT and completely avoids lepton identification, implementing impact parameter cuts in order to prevent bandwidth saturation without degrading the signal acceptance.

Why two different approaches? Even if restrictive, a first answer can be given based upon the distinction of strategies so far discussed in measuring CP violation: a first class, which corresponds to the "historical" approach is based on the measurement and fit of the asymmetry time dependence in some specific decays. This requires flavor tagging. The need of a flavor tagging algorithm can be exploited in the trigger design, requiring the identification of a lepton at trigger level. The underlying idea is that this lepton could be interpreted as a decay product of the *opposite* B involved in the event. This is not sufficient to avoid trigger bandwidth saturation, and much of the events selected in this way are not $b\bar{b}$ decays. A more specific b tag is then added with the requirement of an impact parameter cut.
There are two issues which push for an alternative approach, both basically coming from the fact that lepton-based flavor tagging isn't always a desired feature:

- Other tagging methods are available offline, which means that the efficiency of a "trigger level tagging algorithm" combined with the efficiency for any accompanying trigger requirements could be smaller than that of the offline tagging algorithms combined with different trigger selections

- Some recent approaches don't even require flavor tagging techniques and would only be damaged by the requirement of a soft lepton identification in the event[1]

[1]Remember that $\Gamma(B \to \ell + X) \approx 10\%$

These two considerations led to a purely hadronic trigger (the Two Track Trigger) strongly based on SVT for heavy flavor tagging.

Section 5.2 will deal with the perspectives of the SLT and its compatibility with the CDF environment. Since this thesis is mainly devoted to fully hadronic decays, we won't go in further details of the results recently obtained in the finalization of the SLT. Section 5.3 will then deal with the TTT, the ideas which led to its current structure and optimization. As we will show along section 5.3, the TTT has separated in two different streams. The first sub-stream is fine-tuned for the collection of $B \to \pi^+\pi^-$ events and will be discussed in section 5.3. The second sub-stream was separated from the previous one with the idea of collecting $B_s \to D_s\pi$ events. Its features are remarkably different from the ones of the $B \to \pi^+\pi^-$ and we will see its performance for B decays different from $B_s \to D_s\pi$ in the next chapters.

5.1.1 A Soft *Lepton plus Track* Trigger

This trigger has been so far presented as a way of triggering on the flavor tag of the *opposite* B decay. On the other hand, it gives also access to B decays containing leptons in the final state: with respect to the traditional *single lepton* and dilepton triggers this has the advantage of allowing a softer event reconstruction (muons can be identified only above the $2\,GeV/c$ threshold) and that events with one soft lepton in the final state are still accepted: the blind signal degradation due to the high P_t threshold applied in the case of a single muon trigger is replaced by a B specific trigger in the form of an impact parameter cut.
Depending on the analyses under study the same trigger channel might require different fine tunings. This applies also to the *soft lepton plus track trigger* (often referred to as $\mu +$ track trigger): a precise definition of the parameters and strategy has to be carefully identified on the basis of the physics channels of interest. Mode-specific improvements of this baseline idea are still under study, while we took care of the feasibility of such an approach in the CDF trigger framework.
First of all we must in fact make sure that rate limitations don't make this trigger practically unuseful (e.g. constraining the threshold on impact parameter to a value too high for the physics we are interested in). After this, specific implementations can be qualified.

5.1.2 The Two Track Trigger

The TTT was initially developed for a specific analysis and decay channel of the B meson: $B \to \pi^+\pi^-$. We will later show that slight modifications of the requirements result in a general purpose tool, useful for many hadronic B decays.
The TTT principle is based on three fundamental facts:

1. The large life time for B hadrons and its connection with the products impact parameter: once again we will be dealing with SVT

2. The kinematic correlation between the decay products in $B \to \pi^+\pi^-$: opposite sign tracks with a defined angular correlation must be expected. In particular the tracks are expected to be back to back in a small fraction of $B \to \pi^+\pi^-$ events

3. The inclusive P_t spectrum of charged particles in $p\bar{p}$ collisions at $\sqrt{s} \approx 2\,TeV$ falls approximately as P_t^{-8} [82], while the charged particle P_t spectrum for B hadron decay produced by the hard-scattering process $p\bar{p} \to b\bar{b}X$ is significantly harder

5.2 Preliminary Results on the Soft Lepton Trigger

In this section we will discuss the results of a first simulation of the muon+track trigger [83]. This simulation is based on a real data sample and the XFT+SVT simulator. The details of this trigger are still undefined, but the general framework is clear: the basic idea is that of selecting events in which a muon and a high-lifetime particle have been produced. The muon tag can be obtained in a manner substantially equivalent to the one used in the leptonic triggers of Run I, taking care of having its momentum threshold as small as possible; in the following we will be concerned with the fact that the *long-lifetime* tag is obtained using the SVT. We will in fact require that the event contains at least one track with impact parameter (d_0) larger than a certain fixed value D_0.
Key questions concern the best value of D_0, the merit of requiring that the high-d_0 track has been/not been tagged as a muon, the merit of requiring a $\Delta\phi$ cut between the muon and the track [2]; the answers somehow depend on the particular physics study for which the sample is used. However, the basic idea is that of applying the D_0 cut as a bandwidth-limiter. For this reason we will focus on the first question, and on the restrictions coming on the range of possible D_0 values from trigger-rate limitations: this information is crucial, since a too high D_0 (the only free parameter in the SVT selection for this trigger) dictated, for example, by the presence of too many "fake" tracks coming out from the XFT-SVT system, might strongly affect the trigger's signal efficiency and its usefulness. It is therefore crucial that the study has been carried out on real data using the software simulators of both XFT and SVT.
We will first briefly discuss the strategy of this study and then cover the results obtained.

[2] in the following, we will conventionally call muon the particle which has been identified by the muon trigger, and track the one on which the cut is applied; note that what we call muon and track might actually be the same physical track.

5.2.1 Simulation Strategy

Real Run I data is the most reliable model we can choose to observe the trigger behavior, therefore we base the study on a Run I data sample collected requiring only the presence of a muon at trigger level. In order to simulate the SVT behavior we then have to simulate the trigger's level 1 (L1) requirements: we use the trigger muon as a simulation of the L1 muon requirement, while different approaches of simulating the tracking requirements at trigger level will be explored.
The inclusive muon trigger in the Run I sample we use was selected requiring a $4\,GeV$ muon: we cannot directly study the bandwidth for a lower P_t muon requirement. While an even lower threshold is probably desirable, we choose to give the results for this hypothetic $4\,GeV$ *muon plus track trigger* rather than attempting an uncertain and doubtful extrapolation to lower momenta.
The remaining trigger requirements (like the presence of an additional track at L1 and the whole Level 2) are simulated in several steps, choosing various simulator options:

- **Offline Simulation:** This is a toy simulation of the trigger system obtained applying cuts on offline quantities: we completely skip the trigger software simulators and apply some rough cuts to take into account the effect of SVT and XFT. This is a quick tool which has the advantage of being of straightforward interpretation;

- *partial* **simulation:** this is a software option of the SVT simulator, which can use as input for the level 1 simulation the offline (TRKS) tracks, so that we use the SVT simulator on the same data sample, avoiding the XFT simulator;

- *full* **simulation:** the last step is to use both the XFT and SVT simulation: this simulates the whole trigger chain up to the 2nd trigger level

The *full* simulation is expected to give the most realistic estimate of the trigger rates on the Run I setup. We will then extrapolate the desired quantities to the Run II setup.

5.2.2 Simulation Results

Figure 5.1 reports the results of the simulation in terms of required trigger bandwidth as a function of the impact parameter cut. The consistency of the three simulation steps has been thoroughly checked [83].
Since we rely on Run I data, the bandwidth (and the corresponding cross section) has to be read as what we would obtain implementing this trigger in the Run I detector configuration; we can roughly extrapolate this estimate to the Run II setup by increasing the cross section by a factor 1.5 for the increased SVX II acceptance and by another factor 1.5 for the increased muon detector coverage; the results show that the trigger rate estimate is still compatible with CDF level 2 trigger requirements (see table 5.1).
We expect that a naive extrapolation from the $4\,GeV$ trigger threshold for the muon

Sim. Configuration	Xsect. in nb	rate estimate Hz
Offline	90	18
SVT+TRKS	180	36
SVT+XFT	180	36

Table 5.1: Equivalent trigger cross sections for the Run II setup, estimated with the various simulations described in the text. Results are for the simulation of a trigger requiring a $4\,GeV/c$ muon and a track with impact parameter $d_0 > 100\,\mu m$. The last column reports the rate estimate for an instantaneous luminosity of $2 \cdot 10^{32}\,Hz\,cm^{-2}$.

down to $1.5-2GeV$ would increase the required bandwidth of an order of magnitude. This means that the L2 bandwidth needed for a $2\,GeV$ muon+track trigger should be of the order of the total L2 bandwidth: additional (probably mode-specific) cuts should render this selection really acceptable in the CDF II framework.

5.3 The Hadronic Trigger

In this section we summarize the studies of the Two Track trigger for run II [84, 85]. These include the definition of efficient trigger cuts for the collection of a $B \to \pi\pi$ sample, studies and improvements for the estimate of the required trigger bandwidth. A close relative to this trigger path was suggested [86, 85] for the collection of $B_s \to D_s\pi/3\pi$. We will see that such a trigger requires resources comparable to the $B \to \pi^+\pi^-$ trigger, with a significant overlap. A common L1 strategy has been developed, requiring the separation of the two streams only at level 2.

5.3.1 Trigger Rates

All the trigger rates that we quote were estimated using true data samples taken during CDF Run I. The use of real data is crucial since the evaluation of the background is very uncertain when high rejection factors, as in this case, are needed. When possible, a detailed SVT simulation (SVTSIM) is employed to reconstruct SVX tracks, while standard offline tracks are used when the SVT simulation was particularly hard. The two procedures give very similar results [79].
From the analysis of the whole Run Ia Minimum Bias (MB) sample (1,169,000 events) the L1 trigger rate was estimated and an upper bound on the L2 rate was set [87]. These studies on MB were done using offline quantities: no SVT simulation could be performed.
A similar simulation was then carried on with a data sample collected on purpose. The sample was collected applying cuts similar to the ones of the L1 TTT. This sample allows better studies of the L2 bandwidth required by the TTT.

5.3.2 The $B \to \pi^+\pi^-$ Trigger

The $B \to \pi^+\pi^-$ decay mode is one of the historical benchmarks for the SVT performance: the collection of this charmless two body decay of the B meson totally relies

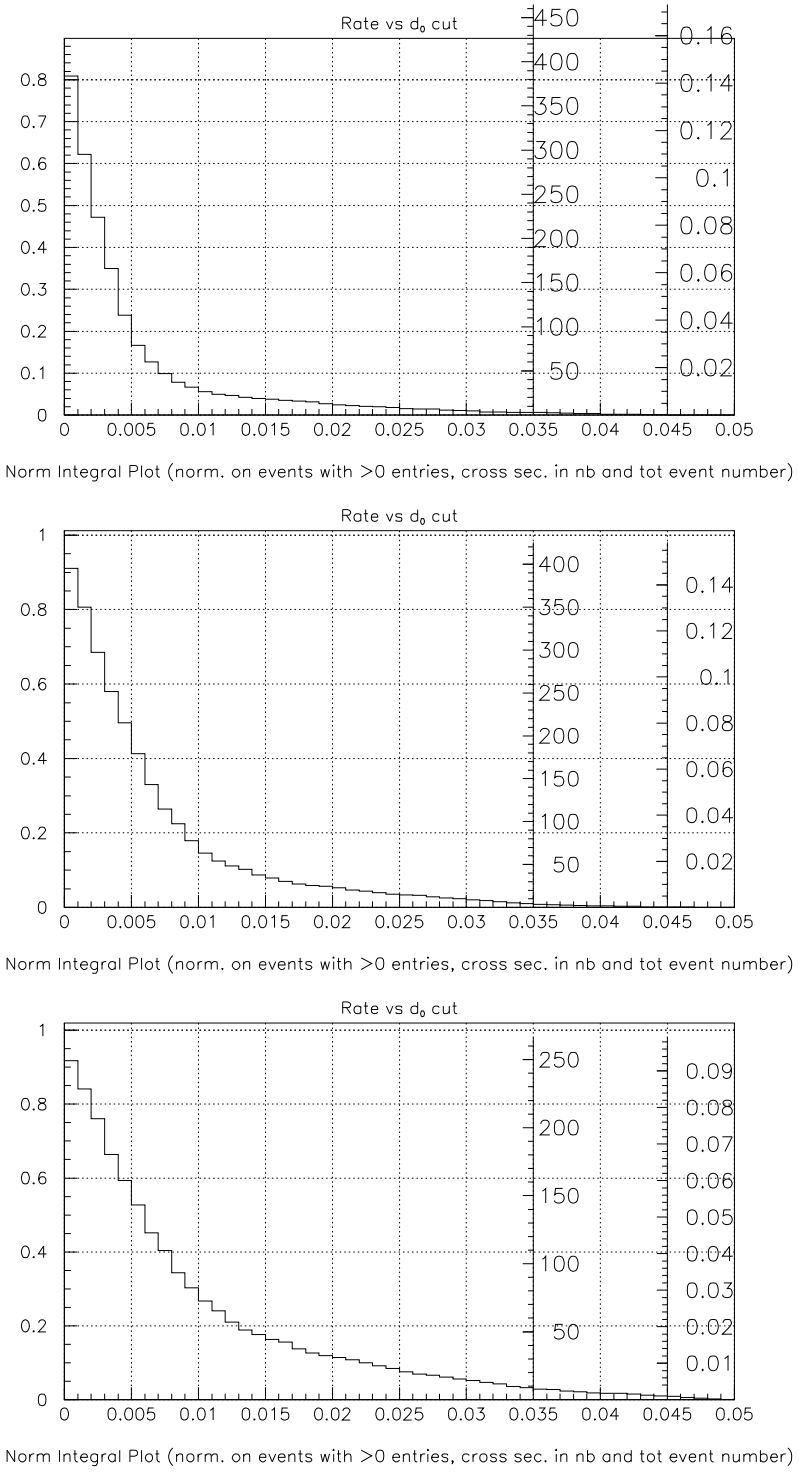

Figure 5.1: Fraction of events passing the muon+track trigger as a function of D_0 for different trigger simulations: full offline (top) SVT (center) and SVT+XFT (bottom). The leftmost vertical scale reports the fraction with respect to the events which have at least an SVXS entry within our requirements. The mid vertical scale reports the trigger cross section in *nb*. The rightmost scale reports the fraction of events in the simulation sample.

on the SVT capabilities. This is one of the main reasons for which its feasibility in CDF II has been studied for a long time [79, 85].
The two most important quantities we need to understand are the trigger efficiency on the signal and the bandwidth required by a selection which is efficient enough to be useful.
We will first deal with the trigger cuts, which have been defined with the aid of real data as a model of the background and a sample of simulated signal for $B \to \pi^+\pi^-$ events. After the trigger cuts are defined, we will give the best available trigger bandwidth estimate for this trigger.

5.3.2.1 Cuts Tuning

The signal efficiency is evaluated [85] using a montecarlo simulated signal selected to fall within the nominal detector acceptance. Measured parameters are smeared according to the nominal CDF II detector and accelerator performance.

Level 1
Level 1 cuts are required to reduce the minimum bias rate of at least two orders of magnitude. The only useful information at this level is the tracking information. Since the tracking information on the two pions will be needed at L2, those are also required to be visible also at L1: the XFT information is strictly required in SVT.
The most important candidates for cutting at L1 are the tracks momenta, the relative angular separation ($\Delta\phi$) in the transverse plane and the relative charge.
Requiring two tracks within the COT fiducial volume ($|\eta| < 1$) and $P_t > 2\,GeV/c$ has 12% efficiency on the signal and 2.5% on minimum bias. Most of the signal loss is due to the η acceptance of the tracker.
Another 2/3 factor in background rejection is obtained with no loss in signal simply requiring that the two tracks have opposite charge.
These cuts alone are not sufficient: the resulting bandwidth occupation at L1 is about 80% of the total L1 resources at the nominal CDF II instantaneous luminosity.
The next candidate for L1 cuts is $\Delta\phi$. We expect that a cut on the relative azimuthal angle between the two tracks ($\Delta\phi$) will help in beating noise: a huge fraction of background is due to jet events that typically have many high P_t tracks. A peak at small angles can be noticed in the $\Delta\phi$ distribution for Minimum Bias events that pass P_t and η L1 cuts (Figure 5.2). A similar effect due to tracks in back-to-back jets is present at large angles.

The left plot in figure 5.2 shows that the $\Delta\phi$ distribution for signal events before (continuous line) and after (dashed line) an impact parameter cut are very different. In order to take this additional effect into account, it is convenient to choose the $\Delta\phi$ cut by comparing its distribution for the background at L1 with the $\Delta\phi$ for the signal after L2. This is done in the right plot of figure 5.2.

The final choice is to require $30° < \Delta\phi < 160°$, reducing the trigger rate to $\sim 48\ KHz$[3] with acceptable signal degradation (Table 5.2).

[3] assuming $L \approx 10^{32}\,cm^{-2}\,s^{-1}$

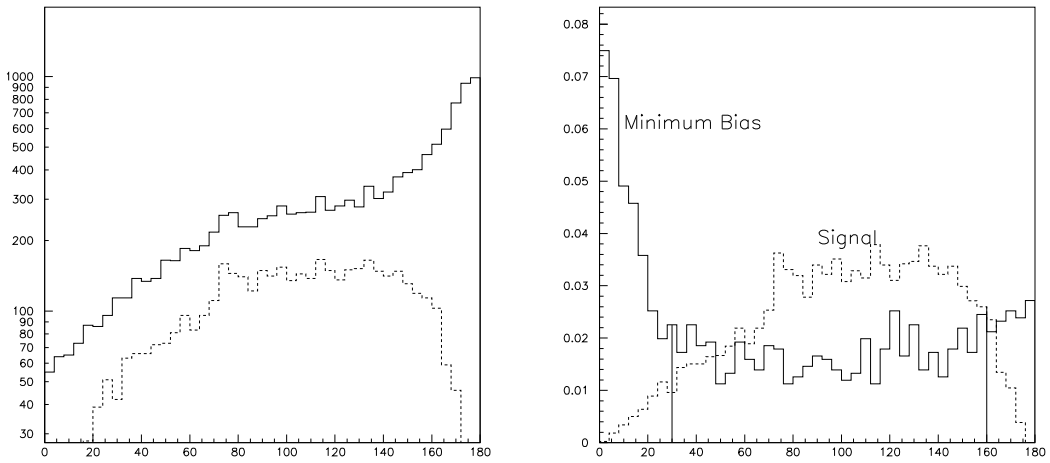

Figure 5.2: (left) $\Delta\phi$ Distribution [degrees] for $B \to \pi^+\pi^-$ events after η and P_t cuts (solid line) and after η, P_t and impact parameter cuts (dashed line). (right) $\Delta\phi$ Distribution [degrees] of Minimum Bias events (solid line), after Level 1 cuts and of $B \to \pi^+\pi^-$ events (dashed line), after Level 1 and Level 2 cuts.

The L1 trigger rate (∼48 kHz) after $\Delta\phi$ cuts is still too high and additional cuts are necessary. The only way out is that of rising the P_t thresholds. A good strategy is that of performing an asymmetric combination of cuts which requires both tracks over a minimum threshold and at least one track over a higher threshold. This selection can even lower the lowest P_t threshold below $2\,GeV/c$: combinations would still be implementable in SVT even if the baseline project is that with a P_t threshold of $2\,GeV/c$.

In Figure 5.3 we report the L1 cross section for background and the L2 cross section for signal as a function of P_t cuts. A good choice appears that of keeping the lower threshold at $2.0\,GeV/c$ and setting the higher one at $3.0\,GeV/c$.

This choice gives $220\,\mu b$ as L1 cross section that corresponds to 22 kHz (at a luminosity $10^{32}\,Hz\,cm^{-2}$). The L1 trigger strategy is summarized in Table 5.2.

Level 2

The two tracks picked at L1 are selected at L2 if they show significant impact parameter: $100\,\mu m <\mid d \mid < 1\,mm$ (the cut at $1\,mm$ is introduced to reduce background due to long-lived particles, like K and Λ, and fake tracks).

Only 3 Minimum Bias events out of the initial 1,169,000 events pass the L2 impact parameter cuts. We estimate the L2 efficiency on background to be $6.4 \cdot 10^{-6}$ (Table 5.2). The $B_d \to \pi^+\pi^-$ trigger efficiency on signal (ϵ) is found to be 1.2 % ($\approx$ 5600 events per fb^{-1}).

So far none of the imposed cuts really keeps into account the common origin of the two pions. A quantity typically efficient for this kind of selection is the

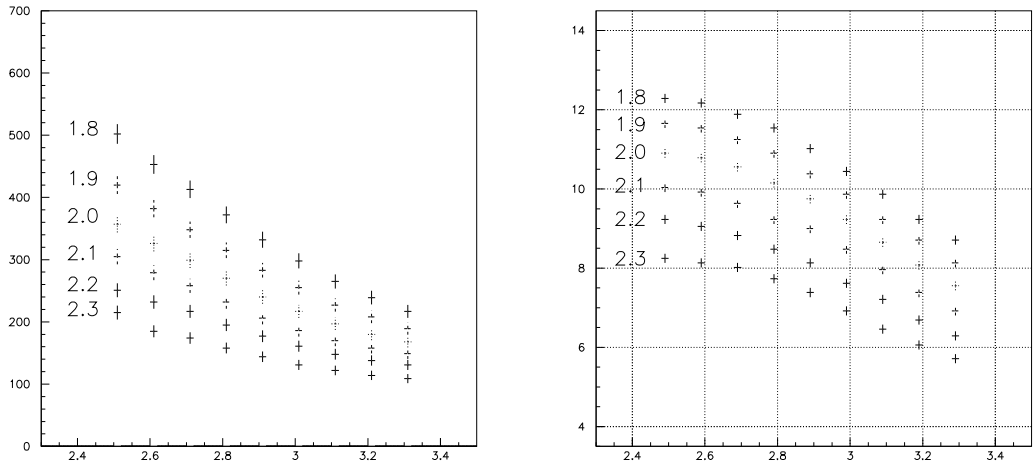

Figure 5.3: Level 1 *trigger* cross section [μb] (left) and L2 *signal* cross section [pb] (right) as a function of the threshold on Max $(P_{t\pi 1}, P_{t\pi 2})$ $[GeV/c]$. Different curves are for different choices of the threshold on Min $(P_{t\pi 1}, P_{t\pi 2})$ $[GeV/c]$ (from 1.8 to $2.3 GeV/c$). Only statistical errors are plotted.

	$B_d^0 \to \pi^+\pi^-$		Minimum Bias		
	Effic.	σ(pb)	Effic.	$\sigma(\mu$b)	Rate (@10^{32})
Level 1					
2 XFT tracks $\mid \eta \mid$<1					
P_t > 2 GeV/c	0.12	120 ± 25	0.025	1280	
Opposite Charge	0.12	120 ± 25	0.016	820	
$30^o < \Delta\phi < 160^o$	0.083	77 ± 16	0.0093	475	
Max(P_{t1},P_{t2}) >3.0 GeV/c	0.061	62 ± 13	0.0042	220	22 kHz
Level 2					
2 SVX II tracks					
100 μm<$\mid$ d $\mid$< 1 mm	0.012	12 ± 2.5	$6.4{\cdot}10^{-6}$	0.33±0.19	
$\vec{P_{tB}} \cdot \vec{X_v}$ >0, $\mid d_B \mid$<140 μm	0.012	12 ± 2.5	$<4.9{\cdot}10^{-6}$	<0.25	<25 Hz

Table 5.2: Background, signal efficiency and cross section obtained from the Minimum Bias analysis. Signal efficiency and cross section refer to the sum of $B_d \to \pi^+\pi^-$ and $\overline{B}_d^0 \to \pi^+\pi^-$ channels. The signal cross section assumes $1.0 \cdot 10^{-5}$ as branching ratio.

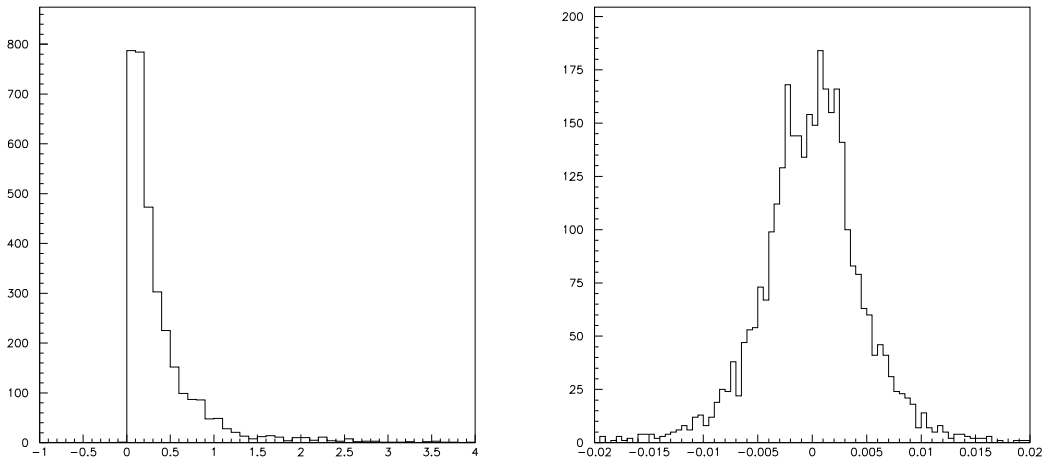

Figure 5.4: Distribution of $\vec{P}_t \cdot \vec{X}_v$ $[GeV \cdot cm/c]$ (left) and impact parameter [cm] (right) for $B_d^0 \to \pi^+\pi^-$ events passing Level 2 impact parameter cuts.

candidate B momentum projected along its measured decay path: in the case of real $B \to \pi^+\pi^-$ events this quantity must be positive.

Figure 5.4 shows the $\vec{P}_t^B \cdot \vec{X}_v$ distribution for $B_d \to \pi^+\pi^-$ events that pass L1+L2 cuts [4]. Figure 5.4 shows also the B_d^0 impact parameter distribution for $B_d \to \pi^+\pi^-$ events that pass L1+L2 cuts.

We choose to apply the cut $\vec{P}_t^B \cdot \vec{X}_v > 0$ and require the impact parameter of the candidate B meson to satisfy $\mid d_B \mid < 140\,\mu m$. These cuts have $> 99\%$ efficiency on signal. No MB event is left after these cuts; we can thus set an upper bound on L2 trigger cross section of $250\,nb$ (2.3 events) at 90% confidence level corresponding to a $25\,Hz$ trigger rate[5] (Table 5.2).

5.3.2.2 Wrap Up

In Figure 5.5 the L2 cross section for the signal is reported as a function of impact parameter cuts. The impact parameter is probably the best candidate for a further reduction of the required L2 bandwidth, if needed. Given that the minimum bias sample was insufficient for significant studies of the L2 output, a special sample was collected at the end of Run I specifically for studies connected to the two track trigger. Table 5.3 shows the background efficiency and cross section for the L2 output simulated using either offline quantities or the SVT software simulator on this sample.

[4] $\vec{P}_t^B$ is the P_t of the reconstructed B_d^0 and $\vec{X}_v$ is the vector that points from the beam axis to the B_d^0 decay vertex.

[5] estimated at a luminosity $10^{32} Hz cm^{-2}$.

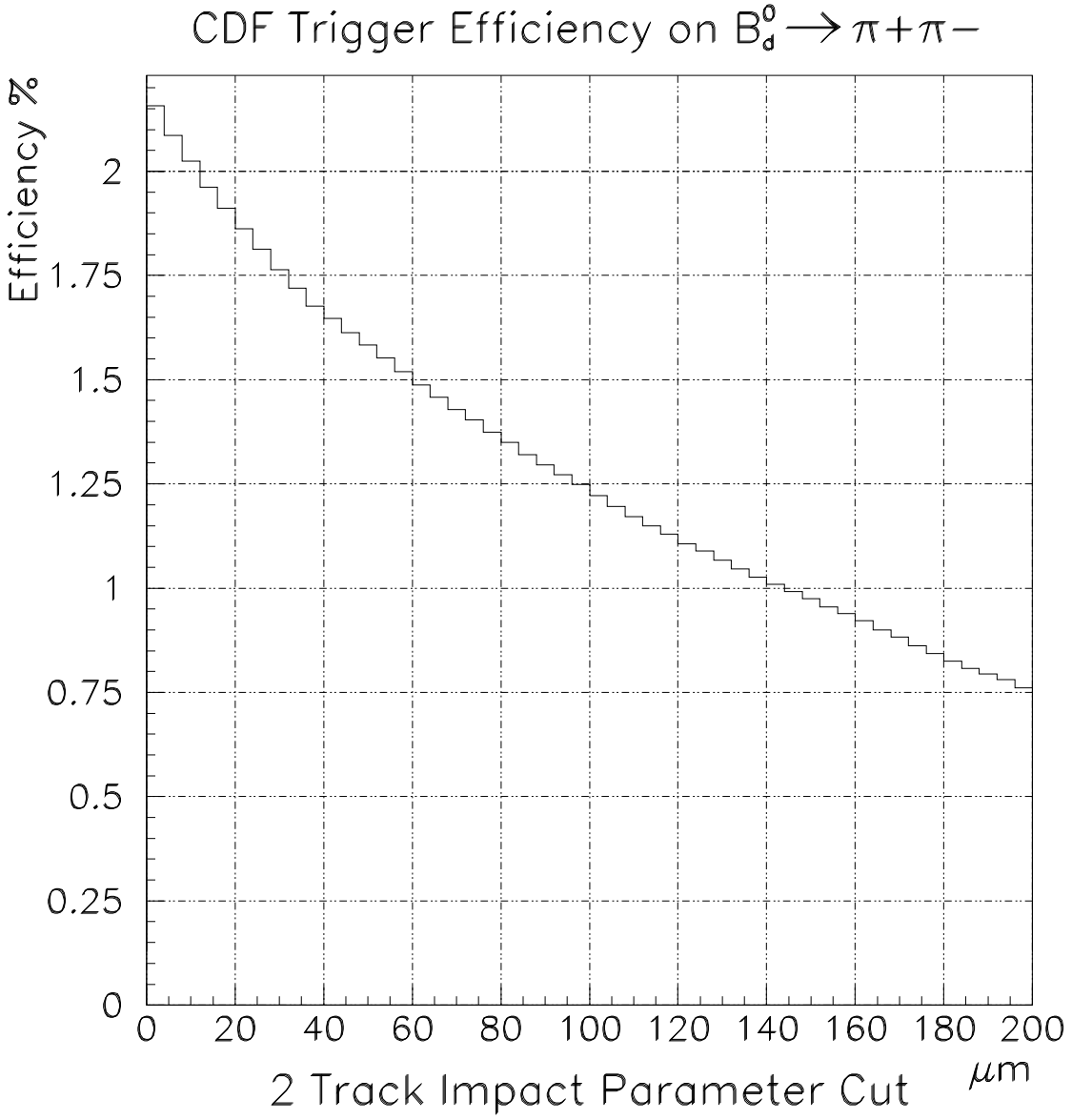

Figure 5.5: Dependence of signal Level 2 efficiency on the impact parameter cut applied on both pions. Efficiency of the cuts $\vec{P}_{tB} \cdot \vec{X}_v > 0$ and $\mid d_B \mid < 140$ μm is assumed 100 %.

Cut	Effic. (10^{-6})	Cross Sec. (nb)	Effic. (10^{-6})	Cross Sec. (nb)
$100\,\mu m < \mid d \mid < 1\,mm$	6.6 $\pm$1.9	340 ± 100	25 ± 4	1320 ± 190
$\vec{P_{tB}} \cdot \vec{X_v} > 0$	2.7 ± 1.2	140 ± 63	6.6 ± 1.9	340 ± 100
$\mid d_B \mid < 140\,\mu m$				

Table 5.3: L2 trigger efficiency and cross section obtained using CDF offline quantities (columns 2 and 3) and the SVT simulation (columns 4 and 5).

5.3.2.3 Variations

Slight variations on the set of cuts described above have been introduced [86] in order to cope with different trigger scenario. Three different options were proposed for L1 (depending on instantaneous luminosity conditions):

- Scenario A: $L \leq 1 \times 10^{32}\, Hz\, cm^{-2}$ and $396\, ns$ beam crossing
  - 2 tracks with $P_t > 2\, GeV/c$ and $P_t^1 + P_t^2 > 5.5\, GeV/c$
  - $\Delta\phi < 135°$
  - Opposite Charge
- Scenario B: $1 \times 10^{32}\, Hz\, cm^{-2} \leq L \leq 2 \times 10^{32}\, Hz\, cm^{-2}$ and $132\, ns$ beam crossing
  - 2 tracks with $P_t > 2.25\, GeV/c$ and $P_t^1 + P_t^2 > 6.0\, GeV/c$
  - $\Delta\phi < 135°$
  - Opposite Charge
- Scenario C: $1 \times 10^{32}\, Hz\, cm^{-2} \leq L \leq 2 \times 10^{32}\, Hz\, cm^{-2}$ and $396\, ns$ beam crossing
  - 2 tracks with $P_t > 2.5\, GeV/c$ and $P_t^1 + P_t^2 > 6.5\, GeV/c$
  - $\Delta\phi < 135°$
  - Opposite Charge

At level 2 two different sets of cuts, one to collect $B_d \to \pi^+\pi^-$ and the other to accept also $B_s^0 \to D_s n\pi$ decays, are foreseen.

- $B_d^0 \to \pi^+\pi^-$ (common to A, B and C)
  - $100\, \mu m < \mid d \mid < 1\, mm$
  - $\mid d(B) \mid < 140\, \mu b$ and $\vec{P}_t\,(B) \cdot \vec{X}_v > 0$
  - $\Delta\phi > 20°$
- B_s^0 decays (common to A, B and C)
  - $120\, \mu m < \mid d \mid < 1\, mm$
  - $\vec{P}_t\,(B) \cdot \vec{X}_v > 0$
  - $2° < \Delta\phi < 90°$

Table 5.4 reports the L2 trigger rates for the different trigger choices estimated using the methods and samples already introduced in the previous section. All scenario seem reasonably tailored to the CDF II environment.

Scenario	$B^0 \to \pi\pi$ selection	B_s selection	$B^0 \to \pi\pi$ .OR. B_s
A	360 ± 100 nb	394 ± 105 nb	560 ± 125 nb
B	196 ± 74 nb	280 ± 89 nb	336 ± 97 nb
C	84 ± 48 nb	196 ± 74 nb	224 ± 79 nb

Table 5.4: Level 2 trigger cross section for the three Level 1 scenarios of [86, 85].

5.3.3 Extending the $B \to \pi^+\pi^-$ Trigger to the $B_s \to D_s\pi/3\pi$ Topology

Among the cuts reported in section 5.3.2.3, a set of cuts for the collection of B_s decays has been introduced.
Technically, the biggest change is in the angular cut at level 2, which is reduced. This take into account the fact that $B_s^0 \to D_s n\pi$ shows tracks which are closer on average.
Also the cut $\mid d(B) \mid < 140\,\mu b$ has been removed: this is a cut which is applicable at trigger level only when the two trigger tracks are the sole decay products of the B meson. This is no longer the case in $B_s^0 \to D_s n\pi$.
In order to keep the background rejection at the same level, the L2 impact parameter cut is raised so to keep this trigger bandwidth close to that of the $B \to \pi^+\pi^-$ trigger (see figure 5.6).

We will see in the next chapters that the slight changes operated to build the $B_s \to D_s\pi/3\pi$ trigger open a broad range of physics possibilities far beyond the collection of a single B_s decay mode.

5.4 Conclusions

In this chapter we have introduced two tools: the Two Track Trigger and the μ+track trigger.
A muon plus track trigger would give access to B decays with a soft lepton tag and to softer $B \to \ell + X$. From the studies performed we conclude that this trigger approach can be implemented in CDF II.
The Two Track Trigger was primarily optimized for the collection of a specific decay mode of the B meson ($B \to \pi^+\pi^-$). From the estimated trigger efficiency on $B_d \to \pi^+\pi^-$ we have that $\approx 5,000$ $B_d \to \pi^+\pi^-$ events will be collectable on tape in 1 fb^{-1} of integrated luminosity. Besides the original use of the TTT for $B_d \to \pi^+\pi^-$, we have detailed some extended uses to collect $B_s \to D_s n\pi$ decays. These results confirm the feasibility of the Two Track Trigger and its compatibility with the CDF environment.

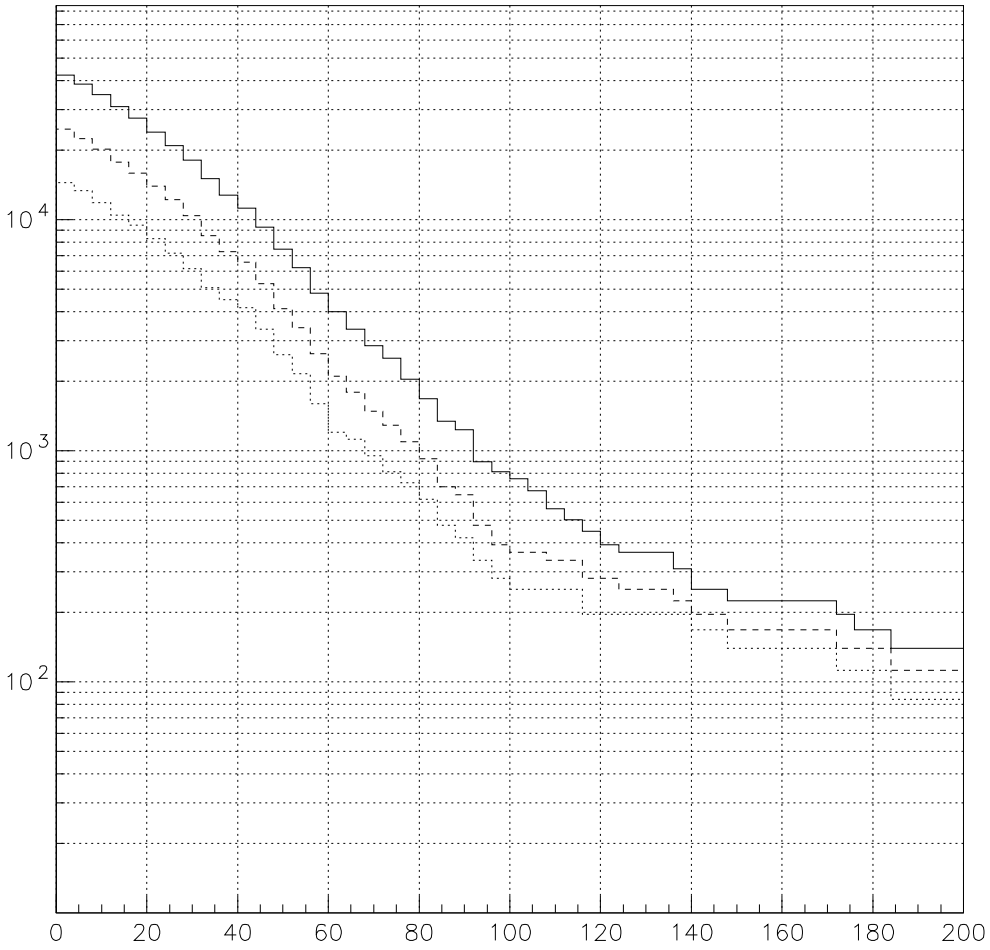

Figure 5.6: B_s-only trigger: dependence of L2 cross section (nb) on the impact parameter cut (micron) on both tracks (from full SVT simulation V1.2) for the three scenarios A, B ad C (from top to bottom).

Part II

The Trigger at Work

The Trigger at Work

The discussion is divided in two parts: the first part begins with chapter 6 which is a wide survey of the capabilities of the hadronic B trigger. Its purpose is that of identifying what decays are significantly collected by the CDF II hadronic B trigger. This survey radically changes the attitude towards the $B_s \to D_s\pi$ trigger: initially foreseen as a tool for the collection of $B_s \to D_s\pi$ decays it is evolving towards a generic tool for B physics. In consideration of this we wonder (chapter 7) about the possibility of really using this tool in such a different perspective: this issue, partly covered in chapter 6 will be addressed also in chapter 8 which details and extends to the case of this generic tool the studies reported in chapter 5. The attention is then (chapter 9) focused on the highest statistics sample, investigating the resolution achievable in that case for the CP violation parameters. This sample's importance goes beyond the physics interest because it can be used as a diagnostic tool of the physics performance of CDF II and SVT in particular.
Chapter 10 justifies the assumptions made in chapter 9 concerning the analysis efficiency and signal to background ratio. Since no optimized search has been performed on this decay mode in Run I, we decide to focus on this task in chapter 10 in order to obtain the best possible estimate of the event yield and signal to background ratio based on real Run I data. The analysis optimization will be useful not only for improving our estimates but also for preparing the Run II search of the $B_d\,(t) \to D^{(*)\mp}\pi^{\pm}$ signal.

The second part of the discussion is focused on the hardware implementation of the trigger, its realization, test and start of operation: chapter 12 describes the issues addressed in the first phase of the SVT setup, mainly concerning the interoperation of the various SVT sub-devices; chapter 13 details the latest results on the SVT performance within the first attempt of observing Tevatron collisions with the renewed CDF II detector.

Chapter 6

A Survey of Accessible Decays

The purpose of this chapter is that of exploring the potential of CP violation studies from the two-track trigger in run II in a more complete way. We evaluate the expected yields for several interesting candidate modes, and propose a list of the "minimally feasible" decays that are worth further consideration.

6.1 Introduction

The work in this chapter is meant to approach B physics issues from the point of view of a future CDF II experimenter, who has certain data sets available and wants to understand the feasibility of the many CP -related measurements for which some interest was recently expressed in literature.

We initially put together a preliminary list of B decays for which some interest was recently expressed in literature.

This list has been integrated with "gossip level" information collected at the last "CP violation in Run II and Beyond" workshop (Sept. 23-25 1999). The resulting list of decays underwent a further selection with some sort of preliminary requirements which look to us as baseline requirements for a CDF II analysis based on well understood tools and detector responses: for example, modes with neutral particles in the final state and non exclusive modes were excluded.
The resulting list of decays is then completely specified up to the final daughters; a rough estimate of the BR's is done using the most up to date information available[1]. Each of these (≈ 30) decays is then generated with standard montecarlo tools and undergoes a parametric trigger simulation, in order to obtain an acceptance estimate. The final result is an estimate of the number of collected events per fb^{-1} of integrated luminosity in CDF II which gives a first idea of the feasible analyses.

6.2 Candidate Decays

The first rough selection is based on the spires/slac preprints published in the last few years concerning the collection of B decays for the measurement of B physics

[1]Either from the references reported for each channel or from the PDG

parameters. Candidate B decays are required to satisfy the following requirements:

- Final decay products are totally hadronic
- No neutral particles are present in the final decay products (at least in a significant fraction of the total decay amplitude)
- Only B_d and B_u decays are considered

The first requirement is driven by the desire of investigating CDF II capabilities in doing totally hadronic B physics, while the second feature is required in order to simplify the reconstruction. The large value of x_s predicted by the standard model [88] would introduce additional difficulties in the disentanglement of CP violation effects in B_s decays. We thus choose to exclude these, apart from some reference modes used as benchmarks.

A first selection of possible decays is contained in tables 6.1 (for well known and understood measurements) and 6.2 (which lists more uncertain measurements): table 6.1 reports modes in which we have direct interest or are described in phenomenological papers with complete information including branching ratio estimates, projected CP violation effect and detailed description of the method. All the modes for which no complete and accurate information was available, and those occasionally mentioned as interesting without further details are listed in table 6.2.

For completeness and comparison with other works, we add a short list (table 6.3) of B_s decays which might be useful for a general reference on the hadronic trigger acceptance.

A brief description of each table's column follows. The first two columns in each table report the decay mode and the literature references in which that mode was mentioned, when available. The following column ("param.") reports the quantity which could be measured collecting a significant sample for that mode. In some decay modes only a fraction of the total branching ratio to the final state is considered *effective* for the analysis: this is for example the case of measurements based on intermediate resonances like the analyses based on Dalitz plots. An estimate of the branching ratio involved is reported in the table (" BR's Involved"): the value reported is replaced by the *effective* branching ratio for the measurement of the interesting quantity when such an estimate is available.
Many of the measurements reported involve the extraction of an asymmetry as the final model-independent physics observable. In these cases we report the expected SM asymmetry if available (" Exp. Asym." column).
When the measurement for the extraction of the relevant parameters is known or described in literature, we mention it in the column labelled "How" with one of the following short labels:

- **tda** means that the experimental quantity which needs to be measured is the Time Dependent Asymmetry in the B meson decay
- **tdr** indicates that all we need to measure is the lifetime evolution of the decay rate

- **brm** is used when only the measurement of the branching ratio is needed to extract the parameter
- **asy** means that the CP asymmetry needs to be measured
- **dpa** indicates the modes for which the asymmetry (either time-dependent or not) is measured only on a subset of the sample selected through the use of a Dalitz plot

Decay	Reference(s)	param.	How	BR's Involved	Exp. Asym.	Comments
• $B_d^\circ \to D^{*\mp}\pi^\pm$	[89]	$2\beta+\gamma$	tda††	$3\cdot10^{-3}$	0.02	Visible in Run I?
$B_d^\circ \to \bar{D}^\circ K_s$	[90]	$2\beta+\gamma$	tda††	$2\cdot10^{-5}$	0.4	Needs a D° flavor tag
$B_d^\circ \to D^{**\circ} K_s$	[90]	$2\beta+\gamma$	tda††		0.4	Automatic D Flavor Tag
						$D^{**\circ} = (D_1^\circ, D_2^{*\circ})$
$\circ\, B^\pm \to D^\circ K^\pm$	[91]	$Sin\,(2\gamma)$	brm	10^{-7}	-	in the PDG notation
$\circ\, B_d^\circ \to \left(D^\circ, \bar{D}^\circ, D_{1,2}\right)\left(K^{*\circ}, \bar{K}^{*\circ}\right)$	[93, 94]	$Sin^2\,(\gamma)$	brm	10^{-5}	-	[92]
						similar to [92]
						needs $K^{*\circ} \overset{66\%}{\to} K^+\pi^-$
$\circ\, B_d^\circ \to \left(D^{\circ *}, \bar{D}^{\circ *}, D_{1,2}^*\right)\left(K^{*\circ}, \bar{K}^{*\circ}\right)$	[93, 94]	$Sin^2\,(\gamma)$	brm		-	analogous to [92]
						needs $K^{*\circ} \overset{66\%}{\to} K^+\pi^-$
$B_d \to D^\circ K_s, \bar{D}^\circ K_s, D_1^\circ K_s$	[95, 90]	$Sin\,(2\beta+2\gamma)$,	tdr	$2\cdot10^{-5}$[90]	-	Has a similar $B_s \to D\phi$
		$Sin\,(2\beta)$				DCS contamination [90]
						solved requiring
				10^{-7}		$D \to K^+\pi^-$ like in [92]
$\circ\, B^\pm \to K^{*\pm}\rho^\circ$	[96]		tda	$5\cdot10^{-6}$	-0.135	
• $B^\pm \to \pi^\pm\rho^\circ$	[96]		tda	$9\cdot10^{-6}$	-0.03	
• $B^\circ \to \pi^+\pi^-, K\pi, KK$	[96, 97, 98,		tda	$4.7\cdot10^{-6}$	0.254	
	99, 100,					
	101, 102]					
• $B^\circ \to \phi K_s$	[96]		tda	$9\cdot10^{-6}$	0.35	
• $B^\pm \to \rho^\circ\pi^\dagger$	[103, 104,	α	dpa	$3.5\cdot10^{-5}$	$0.33 - 0.34Sin\,(\gamma)$	
	105, 106]					
$\circ\, B^\circ \to D^+D^-$	[107, 108]	$Sin\,(2\beta)$	tda			
$B^\circ \to D^{*+}D^{*-}$	[109]	$Sin\,(2\beta)$	tda	$6\cdot10^{-4}$[109]		Dilution: $D^{*+}D^{*-}$
						is not a CP
						eigenst. Ang. Anal. [108]
						Requires Neutrals (γ)

Table 6.1: Candidate B decay channels with literature references, physics parameter resulting from the measurement, branching ratio, expected asymmetry (if applicable) and a quick method description. Table notes are reported in the following

Decay	Reference(s)	param.	How	BR's Involved	Exp. Asym.	Comments
$\circ\, B^\circ \to D^{*+} D^{*-} K_s$	[109]	$Sin\,(2\beta)$	tda	10^{-2}		
$\circ\, B^\circ \to \rho^\circ \rho^\circ$	[96]		tda	$1 \cdot 10^{-6}$	-0.46	$\chi_{c0}\pi^\pm$ interference
$\bullet\, B^\pm \to \pi\pi\pi$	[103, 104, 105]	γ	dpa	$3.5 \cdot 10^{-5}$	$0.33 - 0.34 Sin\,(\gamma)$	$\chi_{c0}\pi^\pm$ interference
				10^{-6} eff.		$\rho^+\rho^-$ interference
$\bullet\, B^\pm \to K^+ K^- \pi^\pm$	[106]	γ	asy	$1.5 \cdot 10^{-5}$	$0.44 - 0.45 Sin\,(\gamma)$	
$\circ\, B \to D^+ D^- K_s$	[110, 111, 112]	$Cos\,(2\beta)$	dpa	$35 \cdot 10^{-4}$		through $D^{**\pm} D^\mp$
				10^{-4} eff.		Few % Penguins
$\circ\, B^\circ \to D^\pm \pi^\mp K_s$	[112]	$Cos\,(4\beta + 2\gamma)$	dpa	$27 \cdot 10^{-5}$		through $B_d^\circ \to D_s^{**+} \pi^-$
				10^{-5} eff.		$\bar{B}_d^\circ \to D^+ K^{*-}$
						$B_d, \bar{B}_d \to D^{**\circ} K_s$
$\bullet\, B \to D^\circ_{\rm CP} \pi^+ \pi^-$	[110, 111, 112]	$Cos\,(2\beta)$	dpa	$1 - 10 \cdot 10^{-4}$		through $D^{**\pm} \pi^\mp$, $D_{\rm CP} \rho^\circ$
$D^\circ_{\rm CP} \to \pi^+\pi^-, K^+K^-, K \circ \bar{K}^\circ$				$1 - 10 \cdot 10^{-6}$		No Penguins

Table 6.1: Candidate B decay channels with literature references, physics parameter resulting from the measurement, branching ratio, expected asymmetry (if applicable) and a quick method description. Table notes are reported in the following page.

† Looks difficult due to the need of simultaneous measurements on neutral channels [113]
†† in the measurement of $\left(B \to f/\bar{B} \to \bar{f}, B \to \bar{f}/\bar{B} \to f\right)$
NOTE THAT the states D_1° and D_2° above mentioned are defined as $\frac{D^\circ \pm \bar{D}^\circ}{\sqrt{2}}$ and have nothing to do with the $D_1\left(2420\right)^\circ$ and $D_2\left(2460\right)^{\circ *}$ states mentioned in the PDG.

Decay	Reference(s)	param.	How	BR's Involved	Exp. Asym.
$\bullet\, B_d^\circ \to K^{*+}\pi^-, K^\circ\phi$	[114, 115]	γ???	brm	$2-1\cdot10^{-5}$	-
$B^\circ \to K^{*\circ}K_s$				10^{-7}[116]	
$B^\circ \to K^{*\circ}\bar{K}^{*\circ}$					
$\circ\, B^+ \to K^+K_s$					
$\circ\, B^+ \to K_s\pi^+$	[15]				
$\bullet\, B^\circ \to D_s^\pm K^\mp$	[117]				
$\bullet\, B^\pm \to \phi K^\pm$					
$B^\circ \to (K, K^*)\, X$	[118]	CP viol.	asy	10^{-4}	-0.1
$B^\circ \to (D, D^*)\, X$	[119]	CP viol.	asy	10^{-4}	0.01
$B^\circ \to (D_s^+, D_s^{*+})\, X$	[120, 121]	V_{ub}	asy	10^{-1}	-

Table 6.2: Candidate B decay channels with literature references, physics parameter resulting from the measurement, branching ratio, expected asymmetry (if applicable) and a quick method description. See section 6.9 for an explanation of the $\bullet$ and $\circ$ symbols.

Decay
$\circ\, B_s \to K^{*\circ}\bar{K}^{*\circ}$
$B_s \to K^{*+}K^{*-}$
$B_s \to \bar{D}^\circ\phi$
$\circ\, B_s \to \bar{D}^\circ K^{*\circ}$
$\bullet\, B_s \to D_s\pi$
$\bullet\, B_s \to D_s\pi\pi\pi$

Table 6.3: Some candidate B_s decay channels. See section 6.9 for an explanation of the $\bullet$ and $\circ$ symbols. These channels are used mainly as controls for cross checking the result of this simulation with the expectations for these modes.

6.3 "Visibility Thresholds"

Let's assume that we collect a sample of size N of a given exclusive decay (e.g. $B_d \to D^{*+}\pi^-$ or $B^+ \to D^\circ K^+$). The usefulness of this sample in measuring the goal parameter ($2\beta + \alpha$ or γ in the examples) depends on the connection between the resolution on that parameter and the number of collected events. We know, for example, that for the measurement of a time dependent asymmetry the tagging algorithm attenuates the asymmetry and worsens by an $(\epsilon D^2)^{-\frac{1}{2}}$ factor the asymmetry resolution.
An essential distinction is thus that between channels which need a flavor tagging in the subsequent analysis and those which are based solely on an "event counting" strategy (like $B^+ \to D^\circ K^+$). The number of events required in the former approach is larger. This suggests that we define a "visibility threshold" for each decay channel which depends on the approach leading to the measurement of the "goal parameter". Given that the ϵD^2 factor roughly reduces the number of *effective events* by a factor ≈ 10, we will assume that the thresholds on the number of collected events can be lowered by a factor 10 for these decays in which the **brm** measurement is used (see tables 6.1 and 6.2).
We expect a rather sizeable background for these fully hadronic channels. We believe it will be impossible to observe channels which show less than ≈ 100 collectable $events/fb$, and hard if the collected sample is less than ≈ 1000 collectable $events/fb$.

6.4 Trigger Simulation

The acceptance estimate is done for two distinct L2 trigger selections, both based on the selection of two tracks which are supposed to be the decay products of a parent decaying within the detector volume:

- $B \to \pi\pi$ **Trigger**
  - **Level 1** Two XFT Tracks, above the $2\,GeV/c$ threshold. Among all possible $2\,GeV/c$ pairs, we look for those having $P_t^1 + P_t^2$ above the $5.5\,GeV/c$ threshold, opposite charge and $0^\circ \leq \Delta\phi \leq 135^\circ$.
  - **Level 2** Two SVT Tracks with $100\,\mu m \leq |d_0| \leq 1\,mm$. All level 1 cuts are then repeated on these two tracks with the improved L2 resolution and a tightened $\Delta\phi$ cut $20^\circ \leq \Delta\phi$. The intersection of the two tracks is identified and the quantity $\vec{P}_t \cdot \vec{X}_v$ of the parent particle in the vertex is calculated in the approximation of straight tracks. The cuts applied are then $\vec{P}_t \cdot \vec{X}_v > 0$ and $|d_B| < 140\mu m$ (d_B is the impact parameter for the parent particle).
- **Hadronic** B **Trigger**
  - **Level 1 (identical to the** $B \to \pi\pi$ **one)**: Two XFT Tracks, above the $2\,GeV/c$ threshold. Two of them are required to have $P_t^1 + P_t^2$ above the $5.5 GeV/c$ threshold, opposite charge and $0^\circ \leq \Delta\phi \leq 135^\circ$.

– **Level 2** (Also this level's selection is close to that described in the $B \to \pi\pi$ trigger with the following differences: the impact parameter cut is raised to $120\,\mu m$, the angular cut is changed to $2^\circ \leq \Delta\phi \leq 90^\circ$ and the d_B cut is dropped)
Two SVT Tracks with $120\,\mu m \leq |d_0| \leq 1mm$. All level 1 cuts are then validated on these two tracks, further adding $2^\circ \leq \Delta\phi \leq 90^\circ$ The intersection of the two tracks is identified and the quantity $\vec{P}_t \cdot \vec{X}_v$ of the parent particle in the vertex is calculated linearizing the particle trajectories. $P_t \cdot X_v > 0$ is then required.

6.4.1 Simulation Strategy

Each trigger is simulated parametrically using montecarlo data based on the `BGEN` [122] parametric B hadron montecarlo. This tool generates b quarks with p_t and rapidity distributions parametrized according to the next to leading log calculations: b quarks are fragmented to B mesons using the Peterson parameterization [123], while B hadrons decays are generated using the QQ [124] program.
In our `BGEN` configuration the final simulated event contains only one B together with its decay products: all the other $p\bar{p}$ products are not simulated. This means that the trigger efficiency will be actually under-estimated because we disregard all the events in which the trigger selection involves tracks from particles different from the B decay products. The probability that this happens is however smaller than that of catching the B daughters and we choose not to include this effect in the simulation.
Track parameters are smeared after generation in order to take into account the different resolution and efficiency with which these are known at the different trigger levels. Each trigger selection is then applied to the corresponding smeared parameters. In order to guarantee the event reconstructability, we include in the final efficiency estimate also the requirement that all the final decay products of the B are within the detector fiducial volume.
The final event yield is thus the result of a selection based on the parametric simulation of the trigger path and a rough acceptance requirement for the whole event, including parameterized detector and trigger inefficiencies.

6.4.2 Simulation Parameters

This section describes all the numerical details needed for the reproduction of the results we will obtain. We will first deal with the parameterizations of the XFT and SVT track fitters and then give the details of the event generation.

XFT tracks are defined as tracks with $|P_t| \geq 1.5\,GeV/c$ which have $|z| \leq 155\,cm$ between the inner and outer COT nominal radii (assumed to be $40\,cm$ and $137\,cm$).

Track parameters are smeared according to:

$$\begin{aligned}\sigma_{P_t}^{XFT} &= 0.015 P_t^2\, GeV/c \\ \sigma_{\phi_0}^{XFT} &= 4.8\, mrad\end{aligned}$$

A 5% inefficiency is added in order to keep into account track detection inefficiency.

SVT tracks are defined as tracks with $|P_t| \geq 2\, GeV/c$, hitting the four innermost SVX II layers. The $3D$ track extrapolation at each detector layer is required to have the $|z|$ coordinate falling within the region $[0.1125, 7.3329] \cup [7.5387, 14.7591] \cup [16.6204, 23.8408] \cup [24.0466, 31.267] \cup [31.492, 38.7124] \cup [38.9182, 46.1386]$ cm (corresponding to the nominal z location of the SVX II ladders).
Track parameters are smeared according to:

$$\begin{aligned}\sigma_{P_t}^{SVT} &= 0.013 P_t^2\, GeV/c \\ \sigma_{d_0}^{SVT} &= 35\, \mu m \\ \sigma_{\phi_0}^{SVT} &= 1\, mrad\end{aligned}$$

And a 7.8% ($\approx 0.98^4$) track inefficiency is assumed for hit detection effects. An additional 5% SVT pattern inefficiency has been taken into account.

Offline tracks are defined as tracks which are within COT geometrical acceptance [4]: $|z| \leq 155\, cm$ between the inner and outer COT nominal radii and $|P_t| \geq 0.4\, GeV/c$ is required. Track parameters are smeared according to the offline nominal resolutions [4]:

$$\begin{aligned}\sigma_{P_t}^{Off} &= \sqrt{(0.0009 P_t)^2 + 0.0066^2}\, GeV/c \\ \sigma_{d_0}^{Off} &= 30\, \mu m \\ \sigma_{\phi_0}^{Off} &= 0.5\, mrad \\ \sigma_{z_0}^{Off} &= 3\, mm \\ \sigma_{\cot\theta}^{Off} &= 0.004\end{aligned}$$

The sample is made of single B (or $\bar{B}$) events with $P_t^b \geq 0$ and $|\eta_b| \leq 5$ generated with `BGEN`. In each case decays have been forced in the specific channel described in tables 6.4, 6.7.
The primary vertex position has been generated according to a three dimensional Gaussian distribution which models the expected geometry of the Tevatron luminous region:

$$\begin{aligned}\sigma_x^{beam} &= 25\, \mu m \\ \sigma_y^{beam} &= 25\, \mu m \\ \sigma_z^{beam} &= 28\, cm\end{aligned}$$

6.4.3 Simulation Results

The trigger efficiency ϵ_{trig} is defined for all of the above channels as the fraction of generated B events passing the trigger cuts.
Fully contained events are defined as events for which all tracks in the decay under study are *offline* tracks (as defined above). The fraction of trigger events which passes this requirement is noted as ϵ_{acc}. Both quantities (ϵ_{trig} and ϵ_{acc}) are reported for both the $B \to \pi\pi$ ($\epsilon^{\pi\pi}_{trig}$ and $\epsilon^{\pi\pi}_{acc}$) and the hadronic B (ϵ^{HAD}_{trig} and ϵ^{HAD}_{acc}) triggers.

We report in tables 6.5 and 6.8 the efficiency obtained from the above described parameterized trigger simulation in ≈ 50000 B decays. For each decay and trigger channel we give in tables 6.6 and 6.9 the estimate of the total number of expected events, assuming a B_d production cross section of $3.35 \pm 0.68\,\mu b$ (in $|y| \leq 1$ and $P_t \geq 6\,GeV/c$ [125]).
Only statistical errors, as propagated from the MC statistics, and cross section uncertainty are included in the final errors. BR are evaluated on their mean value, as collected from the references mentioned with the corresponding channel. Upper limits and/or values from the PDG are used when no other source is available.
For $\Gamma\left(B_s \to K^* \bar{K}^*\right)$ a reference value of 10^{-6} is assumed.

6.5 Comparison with Previous Results

Studies of the acceptance for some of the decay modes considered in this note were available and thus used whenever possible as cross checks of the results obtained.
The resulting efficiencies for $B_d \to \pi\pi$ [126, 127, 128], $B^+ \to D^\circ K^+$ [92, 129, 130], $B_s \to D_s\pi$ and $B_s \to D_s\pi\pi\pi$ [126, 127] all agree with the results found in this work.

6.6 Inclusive Modes

The acceptance for some inclusive decays has been also tested with the same method above mentioned, excluding the requirement of having the decay products "fully contained" in the detector.
The trigger ability of collecting such modes is important because:

- important information can be extracted from inclusive modes (inclusive branching fractions, cross section etc.)
- such inclusive samples give the possibility of reconstructing arbitrary decays at the offline level

In order to obtain a faithful simulation of the inclusive modes we decided to switch to a more accurate (and thus time-consuming) $p\bar{p}$ simulator, capable of better describing both the b fragmentation and production processes.
A generic **pythia** [131] B sample has been tested through the parameterized simulation: 200000 $b\bar{b}$ events have been generated in order to measure the trigger acceptance to a generic b sample. All the event particles are considered trigger candidates

and thus processed by our parametric simulator.
The resulting efficiency is estimated to be $(0.3 \pm 0.013)\,\%$, with an equivalent cross section for the sample of $37 \pm 10\,\mu b$. This gives an equivalent b *cross section* of our trigger of approximately $110 \pm 20\,nb$.
This means that we cannot squeeze the bandwidth allocated for the two track trigger below this value unless we accept to waste some real b physics. On the other hand, this cross section corresponds to a Level 3 output rate of about $10\,Hz$ that is, about 10% of the total storage bandwidth: a compromise will be needed between the bandwidth assigned for b physics studies using the two track trigger and all the rest.
The use of pythia for the generation of more realistic b events gives rise also to the production of a model for all what lies beneath the b production. This means that many different candidate sources are available for the production of triggering tracks: the inclusive cross section quoted above includes combinations like two tracks coming from the fragmentation or decay products of one or both b quarks and even from other underlying interactions.
One might argue that we could actually get rid of most of those events since the bulk of the analyses performed with the two track trigger data will be based on an exclusive reconstruction of the B decay. Also inclusive modes are however present in this sample and any cut performed in order to further reduce those $110\,nb$ cuts out physics data potentially useful for flavor tagging calibration, inclusive measurements and even the reconstruction of unforeseen decays.

An example of this is the trigger sensitivity to $B_s \to D_s\pi$ and $B_s \to D_s\pi\pi\pi$ when the D_s decay isn't constrained. This has been done using exactly the same machinery and B_s sample as the inclusive case; the only exception is that we exclude the full containment requirement for the final decay products.
The resulting efficiency is estimated to be:

$$\epsilon_{D_s\pi} = 0.002 \pm 0.0002$$
$$\epsilon_{D_s\pi\pi\pi} = 0.0022 \pm 0.0002$$

Which correspond to these Level 2 cross sections:

$$\sigma_{D_s\pi} = 220 \pm 70\,pb$$
$$\sigma_{D_s\pi\pi\pi} = 690 \pm 200\,pb$$

This translates into an accept rate of about $0.1\,Hz$ for $B_s \to D_s n\pi$ alone using this trigger: more than 1 event out of every thousand coming through the two track trigger is expected to be actually a B_s decay! The challenge of collecting such a large sample of B_s decays is nevertheless impressive.

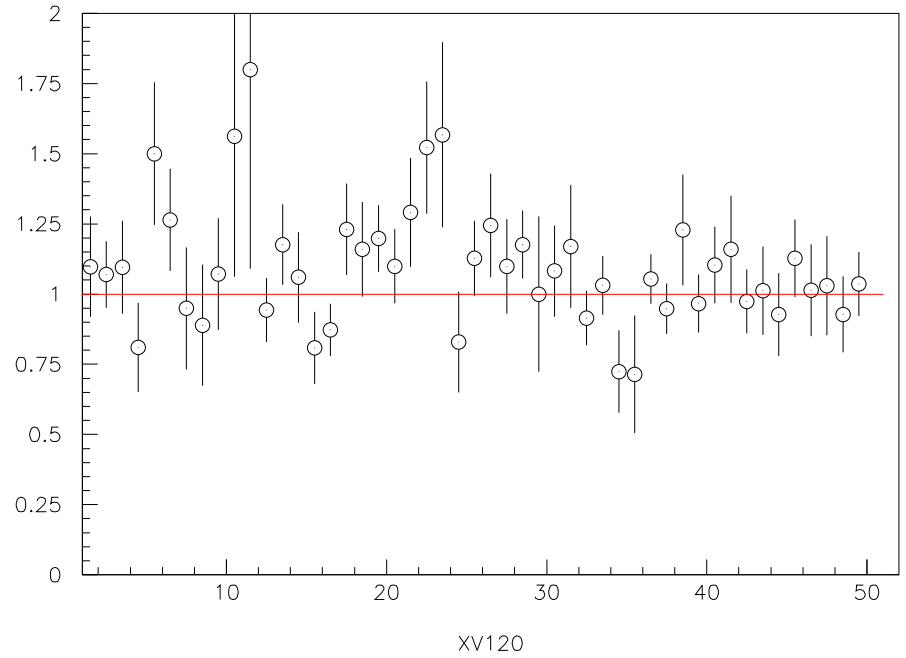

Figure 6.1: Event yield ratio for the two set of cuts proposed within the n-body trigger. See text for a detailed description of the plot.

6.7 Cuts Fine Tuning

A variant of the official trigger cuts has been suggested in some studies devoted to the $B^{\pm} \to D^{\circ}K^{\pm}$ channel [132]. The optimization in that case replaces some of the L2 cuts: $\vec{P}_t \cdot \vec{X}_v > 0.2$ and $|d_0| > 100\,\mu m$ take over $\vec{P}_t \cdot \vec{X}_v > 0$ and $|d_0| > 120\,\mu m$. The former (xv cut from now on) has already been proposed in [133], where its improvement for the collection of a $B^+ \to DK^+$ is shown.

The latter (which We'll refer to as the 120 choice) is in fact the "default" choice made in previous works.

Both choices are known (see [133]) to result in the same trigger rate. We made a comparison of efficiency for the two options based on all the exclusive modes discussed. Figure 6.1 reports the efficiency ratio for the two simulations carried on with the two different set of cuts. Each point corresponds to a different physics decay taken from the tables previously reported. The y axis in the plot is the ratio $\frac{\epsilon_{xv}}{\epsilon_{120}}$ between the trigger efficiencies in the two cases. This ratio is greater than 1 (red line) for 31 of the 44 channels reported.
In addition, the efficiency for the same two cuts has been simulated in the same manner for a generic $B^{\pm} + B_d + B_s$ sample of 650000 events. The efficiency ratio obtained is $\frac{\epsilon_{xv}}{\epsilon_{120}} = 1.1 \pm 0.06$.
These two observation led us to the conclusion that the best choice is the xv option, but for consistency with CDF choices we decided to pursue anyway our study assuming the 120 option.

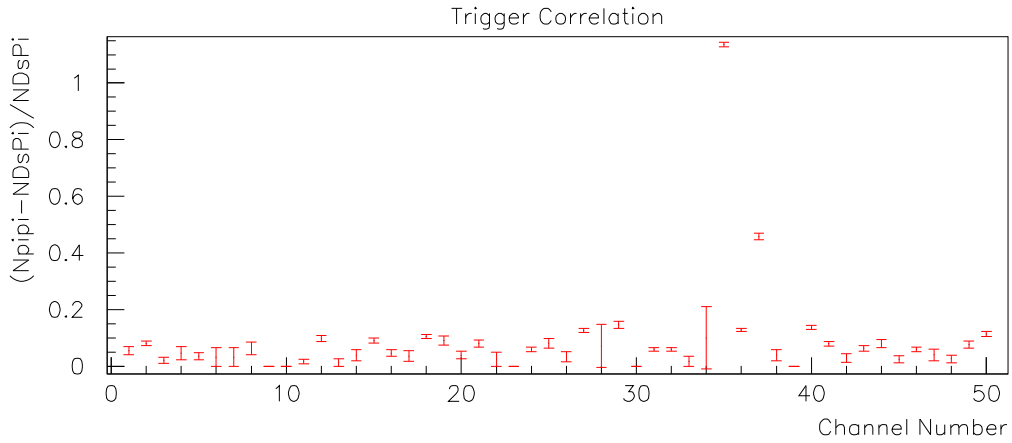

Figure 6.2: Contribution of the $B \to \pi^+\pi^-$ trigger for each decay: each point corresponds to a different decay mode, listed in arbitrary order on the x axis. The y scale reports the number of events selected by the $B \to \pi^+\pi^-$ and not by the $B_s \to D_s\pi$ trigger for that channel, divided by the $B_s \to D_s\pi$ trigger yield. Only two channels show significant contributions from the $B \to \pi^+\pi^-$ trigger: channel 35 ($B \to \pi^+\pi^-$) and 37 ($B \to \rho\pi$).

6.8 The $B_s \to D_s\pi$ Trigger as a Generic B Tool

From the results so far obtained it can easily be argued that the $B_s \to D_s\pi$ trigger use goes beyond the collection of $B_s \to D_s\pi$ decays.
In fact we've seen that the size of the collectable sample is interesting for many of the channels examined in this survey. The $B_s \to D_s\pi$ trigger should be interpreted as a generic tool for hadronic B physics at CDF rather than a B_s trigger alone. One might argue then that the power of the OR'ed $B \to \pi^+\pi^- \vee B_s \to D_s\pi$ trigger is probably even greater. Figure 6.2 shows for each decay proposed the size of the contribution of the $B \to \pi^+\pi^-$ trigger (measured in units of the yield of the $B_s \to D_s\pi$ trigger) taking out the events in common to the two streams.
The $B \to \pi^+\pi^-$ contribution is negligible for practically all the decay modes apart from $B_d \to \pi\pi$ for which the $B \to \pi^+\pi^-$ trigger was specifically tuned.

The next issue to address in order to accept the $B_s \to D_s\pi$ trigger as a generic tool for hadronic B physics is suggested by the previous consideration: given that the fine tuning for a specific channel results in a $\times 2$ improvement with respect to our *all hadronic B trigger*, is it possible to achieve similar improvements for other hadronic decays? The study reported in section 6.7 show that no really significant improvement seems to be easily at hand. This suggests that the possibility of strongly improving the $B \to \pi^+\pi^-$ yield comes primarily from the peculiarity of a two-body decay and that the two trigger channels essentially discriminate two-body and multi-body B decays very well.

6.9 Conclusions

If no further *ad-hoc* fine tuning is planned for each channel, tables 6.6 and 6.9 can be used as a first-sight reference for CDF II abilities in detecting and analyzing the specific channels quoted and channels with similar topologies.
Different symbols in tables 6.1, 6.2, 6.6 and 6.9 are used to distinguish modes belonging to the three classes based on visibility thresholds (see section 6.3): blank rows are for less than $\approx$ 100 collectable $events/fb$, $\circ$ rows for less than $\approx$ 1000 collectable $events/fb$ and $\bullet$ for more than $\approx$ 1000 collectable $events/fb$.
Even if this is just a partial survey of the CDF II possibilities for B physics in run II, we were able to identify more than 20 potentially interesting exclusive decay modes of the B meson accessible at our experiment. Out of those, many were so far never considered as candidates for a measurement in our environment and are often proposed as interesting tools at B factories. About half of the sizeable exclusive decays collected by the two track trigger have an event yield which is larger than 1000 events per year.
Outstanding signals opening intriguing physics opportunities have been identified: $B_d \to D^{(*)\pm}\pi^{\mp}$ ($B_d \to D^{*\pm}\pi^{\mp}$ and $B_d \to D^{\pm}\pi^{\mp}$) is the mode with the largest event yield we could identify. This will be one of the golden benchmarks of the two track trigger and is also known to be potentially useful for CP violation measurements. Other modes, like $B \to \pi\pi\pi$, might give access to measurement techniques never used in B physics at CDF, like the measurement of a time dependent asymmetry with the aid of a Dalitz plot analysis.

A similar survey is being performed on the Λ_b and B_s decays, giving rise to very encouraging results for many different exclusive decays interesting for B physics.

In 1 fb^{-1} a reasonable lower limit on the number of useful reconstructable events is given by the sum of all event yields for modes with $> 1000\, events$: about $240 \cdot 10^3$ events in total. This corresponds to a cross section of about $240\, pb$ which brings the S/B level in this trigger to the order of 1/500.

Even if the requirement on the allocated bandwidth for this trigger is huge ($\approx$ 30%) compared to the total available CDF II throughput, we claim that this sample is worth the effort: given its novelty in the hadronic environment realistic projections on the eventual loss resulting from limitations of the bandwidth are very difficult but are also known to be present. Any cut below the $110\, nb$ level would mean throwing away B physics possibilities for our experiment.

Decay	Complete Decay	Total BR
$B \to \pi\pi$	-	$4.7 \cdot 10^{-6}$
1. $B \to D^{*\mp}\pi^{\pm}$	$D^{*-} \to \bar{D}^{\circ}\pi^{-}, D^{\circ} \to K^{-}\pi^{+}$	$7.9 \cdot 10^{-5}$
2. $B \to D^{*\mp}\pi^{\pm}$	$D^{*-} \to \bar{D}^{\circ}\pi^{-}, D^{\circ} \to K_s\pi^{+}\pi^{-} \to \pi^{+}\pi^{-}\pi^{+}\pi^{-}$	$4 \cdot 10^{-5}$
3. $B \to D^{*\mp}\pi^{\pm}$	$D^{*-} \to \bar{D}^{\circ}\pi^{-}, D^{\circ} \to K^{-}\pi^{+}\pi^{+}\pi^{-}$	$1.5 \cdot 10^{-4}$
1. $B \to D^{\circ}K_s$	$D^{\circ} \to K^{-}\pi^{+}, K_s \to \pi^{+}\pi^{-}$	$5 \cdot 10^{-7}$
2. $B \to D^{\circ}K_s$	$D^{\circ} \to K_s\pi^{+}\pi^{-}, K_s \to \pi^{+}\pi^{-}$	$2.5 \cdot 10^{-7}$
3. $B \to D^{\circ}K_s$	$D^{\circ} \to K^{-}\pi^{+}\pi^{+}\pi^{-}, K_s \to \pi^{+}\pi^{-}$	$9.7 \cdot 10^{-7}$
1. $B \to D^{\circ}K^{*\circ}$	$D^{\circ} \to K^{-}\pi^{+}, K^{*\circ} \to K^{+}\pi^{-}$	$2.5 \cdot 10^{-7}$
2. $B \to D^{\circ}K^{*\circ}$	$D^{\circ} \to K_s\pi^{+}\pi^{-}, K^{*\circ} \to K^{+}\pi^{-}$	$1.3 \cdot 10^{-7}$
3. $B \to D^{\circ}K^{*\circ}$	$D^{\circ} \to K^{-}\pi^{+}\pi^{+}\pi^{-}, K^{*\circ} \to K^{+}\pi^{-}$	$4.9 \cdot 10^{-7}$
$B \to D_{1,2}K^{*\circ}$	$D_{1,2} \to (\pi^{+}\pi^{-}, K^{+}K^{-}), K^{*\circ} \to K^{+}\pi^{-}$	$\sim 10^{-8}$
1. $B \to D^{\circ *}K^{*\circ}$	$D^{\circ *} \to D^{\circ}\pi^{\circ}, D^{\circ} \to K^{-}\pi^{+}, K^{*\circ} \to K^{+}\pi^{-}$	$< 10^{-7}$
2. $B \to D^{\circ *}K^{*\circ}$	$D^{\circ *} \to D^{\circ}\pi^{\circ}, D^{\circ} \to K_s\pi^{+}\pi^{-}, K^{*\circ} \to K^{+}\pi^{-}$	$< 5 \cdot 10^{-8}$
3. $B \to D^{\circ *}K^{*\circ}$	$D^{\circ *} \to D^{\circ}\pi^{\circ}, D^{\circ} \to K^{-}\pi^{+}\pi^{+}\pi^{-}, K^{*\circ} \to K^{+}\pi^{-}$	$< 2 \cdot 10^{-7}$
$B \to D_1 K_S$	$D_1 \to (\pi^{+}\pi^{-}, K^{+}K^{-}), K_s \to \pi^{+}\pi^{-}$	$\sim 4 \cdot 10^{-8}$
$B \to \phi K_S$	$\phi \to K^{+}K^{-}, K_s \to \pi^{+}\pi^{-}$	$3 \cdot 10^{-6}$
$B \to D^{+}D^{-}$	$D^{\pm} \to K^{\mp}\pi^{\pm}\pi^{\pm}$	$3 < \cdot 10^{-6}$
1. $B \to D^{*+}D^{*-}$	$D^{*-} \to \bar{D}^{\circ}\pi^{-}, D^{\circ} \to K^{-}\pi^{+}$	$4 \cdot 10^{-7}$
2. $B \to D^{*+}D^{*-}$	$D^{*-} \to \bar{D}^{\circ}\pi^{-}, D^{\circ} \to K_s\pi^{+}\pi^{-}$	$2 \cdot 10^{-7}$
3. $B \to D^{*+}D^{*-}$	$D^{*-} \to \bar{D}^{\circ}\pi^{-}, D^{\circ} \to K^{-}\pi^{+}\pi^{+}\pi^{-}$	$7.8 \cdot 10^{-7}$
1. $B \to D^{*+}D^{*-}K_s$	$D^{*-} \to \bar{D}^{\circ}\pi^{-}, D^{\circ} \to K^{-}\pi^{+}, K_s \to \pi^{+}\pi^{-}$	$4.5 \cdot 10^{-6}$
2. $B \to D^{*+}D^{*-}K_s$	$D^{*-} \to \bar{D}^{\circ}\pi^{-}, D^{\circ} \to K_s\pi^{+}\pi^{-}, K_s \to \pi^{+}\pi^{-}$	$2.3 \cdot 10^{-6}$
3. $B \to D^{*+}D^{*-}K_s$	$D^{*-} \to \bar{D}^{\circ}\pi^{-}, D^{\circ} \to K^{-}\pi^{+}\pi^{+}\pi^{-}, K_s \to \pi^{+}\pi^{-}$	$8.8 \cdot 10^{-6}$
$B \to \rho^{\circ}\rho^{\circ}$	$\rho^{\circ} \to \pi^{+}\pi^{-}$	10^{-6}
$B \to D^{+}D^{-}K_s$	$D^{\pm} \to K^{\mp}\pi^{\pm}\pi^{\pm}, K_s \to \pi^{+}\pi^{-}$	$7 \cdot 10^{-6}$
$B \to D^{+}\pi^{-}K_s$	$D^{\pm} \to K^{\mp}\pi^{\pm}\pi^{\pm}, K_s \to \pi^{+}\pi^{-}$	$1 \cdot 10^{-5}$
$B \to D^{\circ}_{\mathrm{CP}}\pi^{+}\pi^{-}$	$D^{\circ}_{\mathrm{CP}} \to \pi^{+}\pi^{-}, K^{+}K^{-}$	$1 - 10 \cdot 10^{-6}$
$B \to K^{*+}\pi^{-}$	$K^{*+} \to K_s\pi^{+} \to \pi^{+}\pi^{-}\pi^{+}$	$2 \cdot 10^{-6}$
$B \to K^{*\circ}K_s$	$K^{*\circ} \to K^{+}\pi^{-}, K_s \to \pi^{+}\pi^{-}$	$4 \cdot 10^{-8}$
$B \to K^{*\circ}K^{*\circ}$	$K^{*\circ} \to K^{+}\pi^{-}$	$? \times 0.43$
$B \to D_s^{\pm}K^{\mp}$	$D_s^{\pm} \to \phi\pi^{\pm}, \phi \to K^{+}K^{-}$	$7 \cdot 10^{-6}$

Table 6.4: Estimate of the total BR for B_d° decays as described in the text.

Decay	Total BR	$\epsilon^{\pi\pi}_{trig}$ [%]	$\epsilon^{\pi\pi}_{acc}$ [%]	ϵ^{HAD}_{trig} [%]	ϵ^{HAD}_{acc} [%]
$B^\circ \to \pi\pi$	$4.3 \cdot 10^{-6}$	$1.0 \pm .05$	100 ± 8	$.5 \pm .04$	100 ± 10
1. $B^\circ \to D^\pm \pi^\mp$	$2.7 \cdot 10^{-4}$	$.3 \pm .02$	60 ± 10	$.5 \pm .03$	60 ± 9
1. $B^\circ \to D^{*\pm} \pi^\mp$	$7.9 \cdot 10^{-5}$	$.4 \pm .03$	50 ± 9	$.4 \pm .03$	60 ± 9
2. $B^\circ \to D^{*\pm} \pi^\mp$	$4 \cdot 10^{-5}$	$.2 \pm .02$	50 ± 10	$.3 \pm .03$	60 ± 10
3. $B^\circ \to D^{*\pm} \pi^\mp$	$1.5 \cdot 10^{-4}$	$.08 \pm .01$	50 ± 20	$.2 \pm .02$	60 ± 10
1. $B^\circ \to D^\circ K_s$	$5 \cdot 10^{-7}$	$.1 \pm .02$	60 ± 20	$.3 \pm .02$	70 ± 10
2. $B^\circ \to D^\circ K_s$	$2.5 \cdot 10^{-7}$	$.02 \pm .006$	40 ± 40	$.1 \pm .02$	60 ± 20
3. $B^\circ \to D^\circ K_s$	$9.7 \cdot 10^{-7}$	$.008 \pm .004$	50 ± 60	$.2 \pm .02$	50 ± 10
1. $B^\circ \to D^\circ K^{*\circ}$	$2.5 \cdot 10^{-7}$	$.3 \pm .03$	50 ± 9	$.5 \pm .03$	50 ± 8
2. $B^\circ \to D^\circ K^{*\circ}$	$1.3 \cdot 10^{-7}$	$.1 \pm .02$	50 ± 20	$.3 \pm .02$	40 ± 9
3. $B^\circ \to D^\circ K^{*\circ}$	$4.9 \cdot 10^{-7}$	$.1 \pm .02$	40 ± 10	$.3 \pm .03$	40 ± 9
$B^\circ \to D_{12} K^{*\circ}$	$1 \cdot 10^{-8}$	$.3 \pm .02$	50 ± 10	$.4 \pm .03$	50 ± 8
1. $B^\circ \to D^{*\circ} K^{*\circ}$	$1 \cdot 10^{-7}$	$.3 \pm .02$	40 ± 9	$.4 \pm .03$	50 ± 8
2. $B^\circ \to D^{*\circ} K^{*\circ}$	$5 \cdot 10^{-8}$	$.1 \pm .02$	50 ± 10	$.3 \pm .03$	50 ± 9
3. $B^\circ \to D^{*\circ} K^{*\circ}$	$2 \cdot 10^{-7}$	$.09 \pm .01$	50 ± 20	$.2 \pm .02$	50 ± 10
$B^\circ \to D_1 K_s$	$4 \cdot 10^{-8}$	$.09 \pm .01$	50 ± 20	$.2 \pm .02$	60 ± 10
$B^\circ \to \phi K_s$	$3 \cdot 10^{-6}$	$.01 \pm .005$	100 ± 80	$.1 \pm .02$	80 ± 20
$B^\circ \to D^+ D^-$	$3 \cdot 10^{-6}$	$.1 \pm .02$	30 ± 10	$.4 \pm .03$	40 ± 7
1. $B^\circ \to D^{*+} D^{*-}$	$4 \cdot 10^{-7}$	$.3 \pm .03$	40 ± 8	$.5 \pm .03$	40 ± 6
2. $B^\circ \to D^{*+} D^{*-}$	$2 \cdot 10^{-7}$	$.07 \pm .01$	20 ± 9	$.2 \pm .02$	40 ± 10
3. $B^\circ \to D^{*+} D^{*-}$	$7.8 \cdot 10^{-7}$	$.05 \pm .01$	40 ± 20	$.2 \pm .02$	40 ± 10
1. $B^\circ \to D^{*+} D^{*-} K_s$	$4.5 \cdot 10^{-6}$	$.1 \pm .02$	20 ± 9	$.3 \pm .02$	40 ± 8
2. $B^\circ \to D^{*+} D^{*-} K_s$	$2.3 \cdot 10^{-6}$	$.02 \pm .007$	20 ± 20	$.1 \pm .02$	40 ± 10
3. $B^\circ \to D^{*+} D^{*-} K_s$	$8.8 \cdot 10^{-6}$	$.01 \pm .005$	40 ± 50	$.08 \pm .01$	40 ± 20
$B^\circ \to \rho^\circ \rho^\circ$	$1 \cdot 10^{-6}$	$.3 \pm .03$	80 ± 10	$.4 \pm .03$	70 ± 10
$B^\circ \to D^+ D^- K_s$	$7 \cdot 10^{-6}$	$.05 \pm .01$	30 ± 20	$.2 \pm .02$	40 ± 10
$B^\circ \to D^\pm \pi^\mp K_s$	$1 \cdot 10^{-5}$	$.07 \pm .01$	50 ± 20	$.2 \pm .02$	40 ± 10
$B^\circ \to D^\circ_{CP} \pi^+ \pi^-$	$1 \cdot 10^{-5}$	$.3 \pm .03$	50 ± 10	$.5 \pm .03$	60 ± 9
$B^\circ \to K^{*+} \pi^-$	$2 \cdot 10^{-6}$	$.2 \pm .02$	80 ± 20	$.2 \pm .02$	80 ± 20
$B^\circ \to K^{*\circ} K_s$	$4 \cdot 10^{-8}$	$.008 \pm .004$	70 ± 80	$.1 \pm .02$	80 ± 20
$B^\circ \to K^{*\circ} K^{*\circ}$	$1.7 \cdot 10^{-8}$	$.3 \pm .02$	70 ± 10	$.5 \pm .03$	60 ± 9
$B^\circ \to D_s^\pm K^\mp$	$4.1 \cdot 10^{-6}$	$.2 \pm .02$	50 ± 10	$.4 \pm .03$	60 ± 10
1. $B^\circ \to D^\circ \rho^\circ$	$1.5 \cdot 10^{-5}$	$.3 \pm .03$	50 ± 10	$.5 \pm .03$	50 ± 8
2. $B^\circ \to D^\circ \rho^\circ$	$7 \cdot 10^{-6}$	$.1 \pm .02$	50 ± 10	$.3 \pm .02$	50 ± 10
3. $B^\circ \to D^\circ \rho^\circ$	$3 \cdot 10^{-5}$	$.1 \pm .02$	50 ± 20	$.3 \pm .02$	60 ± 10
$B^\circ \to \rho^\circ K_s$	$2.6 \cdot 10^{-5}$	$.01 \pm .005$	90 ± 70	$.1 \pm .02$	70 ± 20
$B^\circ \to D_s K^+$	$7 \cdot 10^{-6}$	$.2 \pm .02$	50 ± 10	$.4 \pm .03$	60 ± 10

Table 6.5: Simulated trigger efficiency. For each simulated trigger channel ($\pi\pi$ and HAD refer to different trigger selection criteria as explained in section 6.4) We report the fraction of produced events which triggered in that specific channel, and the fraction of these which is made entirely of *offline* tracks.

Decay	Total BR	$\epsilon_{tot}^{\pi\pi}$ [%]	$N_{1fb^{-1}}^{\pi\pi}$	ϵ_{tot}^{HAD} [%]	$N_{1fb^{-1}}^{HAD}$	$N_{1fb^{-1}}^{HAD+\pi\pi}$
$\bullet B^\circ \to \pi\pi$	$4.3 \cdot 10^{-6}$	$1.0 \pm .05$	4700 ± 2000	$.5 \pm .04$	2300 ± 980	4900 ± 2100
$\bullet 1.\ B^\circ \to D^\pm \pi^\mp$	$2.7 \cdot 10^{-4}$	$.2 \pm .02$	41000 ± 9600	$.3 \pm .03$	78000 ± 17000	81000 ± 18000
$\bullet 1.\ B^\circ \to D^{*\pm} \pi^\mp$	$7.9 \cdot 10^{-5}$	$.2 \pm .02$	13000 ± 3100	$.2 \pm .02$	19000 ± 4200	20000 ± 4600
$\bullet 2.\ B^\circ \to D^{*\pm} \pi^\mp$	$4 \cdot 10^{-5}$	$.1 \pm .01$	3800 ± 950	$.2 \pm .02$	6700 ± 1600	7100 ± 1600
$\bullet 3.\ B^\circ \to D^{*\pm} \pi^\mp$	$1.5 \cdot 10^{-4}$	$.04 \pm .009$	6200 ± 1900	$.1 \pm .02$	16000 ± 4100	17000 ± 4200
$1.\ B^\circ \to D^\circ K_s$	$5 \cdot 10^{-7}$	$.06 \pm .01$	31 ± 8.6	$.2 \pm .02$	85 ± 20	92 ± 21
$2.\ B^\circ \to D^\circ K_s$	$2.5 \cdot 10^{-7}$	$.008 \pm .004$	2 ± 1.1	$.08 \pm .01$	20 ± 5.2	21 ± 5.3
$3.\ B^\circ \to D^\circ K_s$	$9.7 \cdot 10^{-7}$	$.004 \pm .003$	3.8 ± 2.8	$.08 \pm .01$	74 ± 19	74 ± 19
$\circ 1.\ B^\circ \to D^\circ K^{*\circ}$	$2.5 \cdot 10^{-7}$	$.2 \pm .02$	40 ± 9.3	$.3 \pm .02$	67 ± 15	71 ± 16
$\circ 2.\ B^\circ \to D^\circ K^{*\circ}$	$1.3 \cdot 10^{-7}$	$.07 \pm .01$	8.7 ± 2.3	$.1 \pm .02$	16 ± 3.8	17 ± 4.1
$\circ 3.\ B^\circ \to D^\circ K^{*\circ}$	$4.9 \cdot 10^{-7}$	$.06 \pm .01$	27 ± 7.6	$.1 \pm .02$	58 ± 14	60 ± 14
$B^\circ \to D_{12} K^{*\circ}$	$1 \cdot 10^{-8}$	$.1 \pm .02$	$1.3 \pm .3$	$.2 \pm .02$	$2.3 \pm .5$	$2.3 \pm .5$
$\circ 1.\ B^\circ \to D^{*\circ} K^{*\circ}$	$1 \cdot 10^{-7}$	$.1 \pm .02$	11 ± 2.7	$.2 \pm .02$	20 ± 4.6	22 ± 5
$2.\ B^\circ \to D^{*\circ} K^{*\circ}$	$5 \cdot 10^{-8}$	$.07 \pm .01$	$3.4 \pm .9$	$.2 \pm .02$	7.4 ± 1.7	7.4 ± 1.8
$\circ 3.\ B^\circ \to D^{*\circ} K^{*\circ}$	$2 \cdot 10^{-7}$	$.05 \pm .01$	9 ± 2.7	$.1 \pm .01$	20 ± 5.1	21 ± 5.2
$B^\circ \to D_1 K_s$	$4 \cdot 10^{-8}$	$.04 \pm .01$	$1.7 \pm .5$	$.1 \pm .02$	5.7 ± 1.4	6 ± 1.4
$\bullet B^\circ \to \phi K_s$	$3 \cdot 10^{-6}$	$.01 \pm .005$	35 ± 16	$.1 \pm .02$	340 ± 84	350 ± 85
$\circ B^\circ \to D^+ D^-$	$3 \cdot 10^{-6}$	$.04 \pm .01$	130 ± 39	$.2 \pm .02$	550 ± 130	560 ± 130
$1.\ B^\circ \to D^{*+} D^{*-}$	$4 \cdot 10^{-7}$	$.1 \pm .02$	44 ± 11	$.2 \pm .02$	67 ± 16	69 ± 16
$2.\ B^\circ \to D^{*+} D^{*-}$	$2 \cdot 10^{-7}$	$.01 \pm .005$	2 ± 1	$.06 \pm .01$	12 ± 3.3	13 ± 3.4
$3.\ B^\circ \to D^{*+} D^{*-}$	$7.8 \cdot 10^{-7}$	$.02 \pm .006$	14 ± 5.4	$.06 \pm .01$	47 ± 13	49 ± 13
$\circ 1.\ B^\circ \to D^{*+} D^{*-} K_s$	$4.5 \cdot 10^{-6}$	$.03 \pm .008$	140 ± 46	$.1 \pm .01$	420 ± 110	450 ± 110
$2.\ B^\circ \to D^{*+} D^{*-} K_s$	$2.3 \cdot 10^{-6}$	$.006 \pm .003$	14 ± 8.3	$.04 \pm .009$	86 ± 27	86 ± 27
$\circ 3.\ B^\circ \to D^{*+} D^{*-} K_s$	$8.8 \cdot 10^{-6}$	$.004 \pm .003$	34 ± 26	$.03 \pm .008$	260 ± 86	260 ± 86
$\circ B^\circ \to \rho^\circ \rho^\circ$	$1 \cdot 10^{-6}$	$.2 \pm .02$	220 ± 49	$.3 \pm .03$	290 ± 64	330 ± 72
$\circ B^\circ \to D^+ D^- K_s$	$7 \cdot 10^{-6}$	$.02 \pm .006$	110 ± 45	$.09 \pm .01$	600 ± 150	630 ± 160
$\bullet B^\circ \to D^\pm \pi^\mp K_s$	$1 \cdot 10^{-5}$	$.04 \pm .009$	390 ± 120	$.1 \pm .01$	1000 ± 250	1000 ± 260
$\bullet B^\circ \to D^\circ_{CP} \pi^+ \pi^-$	$1 \cdot 10^{-5}$	$.2 \pm .02$	1700 ± 400	$.3 \pm .02$	2700 ± 600	2900 ± 640
$\bullet B^\circ \to K^{*+} \pi^-$	$2 \cdot 10^{-6}$	$.2 \pm .02$	300 ± 70	$.2 \pm .02$	350 ± 81	400 ± 91
$B^\circ \to K^{*\circ} K_s$	$4 \cdot 10^{-8}$	$.006 \pm .003$	$.2 \pm .1$	$.1 \pm .01$	3.8 ± 1	3.8 ± 1
$B^\circ \to K^{*\circ} \bar{K}^{*\circ}$	$1.7 \cdot 10^{-8}$	$.2 \pm .02$	$3.2 \pm .7$	$.3 \pm .03$	5.1 ± 1.1	5.4 ± 1.2
$\circ B^\circ \to D_s^\pm K^\mp$	$4.1 \cdot 10^{-6}$	$.1 \pm .02$	510 ± 120	$.2 \pm .02$	980 ± 220	1000 ± 220
$\bullet 1.\ B^\circ \to D^\circ \rho^\circ$	$1.5 \cdot 10^{-5}$	$.2 \pm .02$	2500 ± 590	$.3 \pm .02$	3700 ± 830	3900 ± 870
$\bullet 2.\ B^\circ \to D^\circ \rho^\circ$	$7 \cdot 10^{-6}$	$.07 \pm .01$	510 ± 130	$.1 \pm .02$	1000 ± 240	1100 ± 250
$\bullet 3.\ B^\circ \to D^\circ \rho^\circ$	$3 \cdot 10^{-5}$	$.06 \pm .01$	1700 ± 480	$.1 \pm .02$	4200 ± 1000	4300 ± 1000
$\bullet B^\circ \to \rho^\circ K_s$	$2.6 \cdot 10^{-5}$	$.01 \pm .005$	310 ± 140	$.1 \pm .01$	2400 ± 620	2400 ± 620
$\bullet B^\circ \to D_s K^+$	$7 \cdot 10^{-6}$	$.1 \pm .02$	880 ± 210	$.2 \pm .02$	1700 ± 380	1700 ± 380

Table 6.6: Expected sample size. For each simulated trigger channel ($\pi\pi$ and HAD refer to different trigger selection criteria as explained in section 6.4) We report the fraction of produced events which triggered in that specific channel and is made entirely of *offline* tracks, together with the number of events expected with this efficiency and the given cross section in $1fb^{-1}$ of int. luminosity. The last column reports the number of events collected with the logical OR of the two triggers. See section 6.9 for an explanation on the initial $\circ$ or $\bullet$ symbol.

Decay	Complete Decay	Total BR
1. $B \to D^\circ K^\pm$	$D^\circ \to K^-\pi^+$	$7.5 \cdot 10^{-8}$
2. $B \to D^\circ K^\pm$	$D^\circ \to K_s\pi^+\pi^-$	$3.8 \cdot 10^{-8}$
3. $B \to D^\circ K^\pm$	$D^\circ \to K^-\pi^+\pi^+\pi^-$	$5.2 \cdot 10^{-8}$
$B \to K^{*\pm}\rho^\circ$	$\rho^\circ \to \pi^+\pi^-, K^{*+} \to K_s\pi^+, K_s \to \pi^+\pi^-$	$1.7 \cdot 10^{-6}$
$B \to \pi^\pm\rho^\circ$	$\rho^\circ \to \pi^+\pi^-$	$9 \cdot 10^{-6}$
$B \to \pi^+\pi^-\pi^\pm$	-	$3.5 \cdot 10^-5$
$B \to K^+K^-\pi^\pm$	-	$1.5 \cdot 10^-5$
$B \to K^\pm K_s$	$K_s \to \pi^+\pi^-$	$? \times 0.68$
$B \to \pi^\pm K_s$	$K_s \to \pi^+\pi^-$	$? \times 0.68$
$B \to \phi K^\mp$	$\phi \to K^+K^-$	$1.2 \cdot 10^{-5}$

Table 6.7: Estimate of the total BR for B_u^+/B_u^- decays as described in the text.

Decay	Total BR	$\epsilon_{trig}^{\pi\pi}$ [%]	$\epsilon_{acc}^{\pi\pi}$ [%]	ϵ_{trig}^{HAD} [%]	ϵ_{acc}^{HAD} [%]
1. $B^\pm \to D^\circ K^\pm$	$7.5 \cdot 10^{-8}$	$.4 \pm .03$	60 ± 10	$.5 \pm .03$	70 ± 9
2. $B^\pm \to D^\circ K^\pm$	$3.8 \cdot 10^{-8}$	$.1 \pm .02$	50 ± 20	$.3 \pm .02$	50 ± 10
3. $B^\pm \to D^\circ K^\pm$	$5.2 \cdot 10^{-8}$	$.1 \pm .02$	60 ± 20	$.3 \pm .03$	50 ± 10
$B^\pm \to K^{*\pm}\rho^\circ$	$1.7 \cdot 10^{-6}$	$.08 \pm .01$	70 ± 20	$.2 \pm .02$	60 ± 20
$B^\pm \to \pi^\pm\rho^\circ$	$9 \cdot 10^{-6}$	$.4 \pm .03$	80 ± 10	$.3 \pm .03$	80 ± 10
$B^\pm \to \pi^+\pi^-\pi^\pm$	$3.5 \cdot 10^{-5}$	$.5 \pm .03$	70 ± 10	$.6 \pm .04$	80 ± 10
$B^\pm \to K^+K^-\pi^\pm$	$1.5 \cdot 10^{-5}$	$.4 \pm .03$	60 ± 10	$.5 \pm .03$	70 ± 10
$B^\pm \to K^\pm K_s$	$6.8 \cdot 10^{-6}$	$.01 \pm .005$	50 ± 50	$.03 \pm .008$	80 ± 40
$B^\pm \to \pi^\pm K_s$	$1.6 \cdot 10^{-5}$	$.01 \pm .005$	100 ± 80	$.03 \pm .008$	70 ± 40
$B^\pm \to \phi K^\pm$	$1.2 \cdot 10^{-5}$	$.2 \pm .02$	90 ± 20	$.3 \pm .03$	90 ± 10

Table 6.8: Simulated trigger efficiency. For each simulated trigger channel ($\pi\pi$ and HAD refer to different trigger selection criteria as explained in section 6.4) We report the fraction of produced events which triggered in that specific channel, and the fraction of these which is made entirely of *offline* tracks.

Decay	Total BR	$\epsilon_{tot}^{\pi\pi}$ [%]	$N_{1fb^{-1}}^{\pi\pi}$	ϵ_{tot}^{HAD} [%]	$N_{1fb^{-1}}^{HAD}$	$N_{1fb^{-1}}^{HAD+\pi\pi}$
$\circ$1. $B^{\pm} \to D^{\circ}K^{\pm}$	$7.5 \cdot 10^{-8}$	$.3 \pm .02$	20 ± 4.5	$.3 \pm .03$	25 ± 5.5	28 ± 6.1
2. $B^{\pm} \to D^{\circ}K^{\pm}$	$3.8 \cdot 10^{-8}$	$.07 \pm .01$	$2.6 \pm .7$	$.1 \pm .02$	4.9 ± 1.2	5.4 ± 1.3
3. $B^{\pm} \to D^{\circ}K^{\pm}$	$5.2 \cdot 10^{-8}$	$.08 \pm .01$	3.9 ± 1	$.2 \pm .02$	7.8 ± 1.9	8.2 ± 1.9
$\circ B^{\pm} \to K^{*\pm}\rho^{\circ}$	$1.7 \cdot 10^{-6}$	$.05 \pm .01$	83 ± 24	$.1 \pm .01$	170 ± 43	180 ± 45
$\bullet B^{\pm} \to \pi^{\pm}\rho^{\circ}$	$9 \cdot 10^{-6}$	$.3 \pm .03$	2900 ± 640	$.3 \pm .02$	2300 ± 520	3400 ± 730
$\bullet B^{\pm} \to \pi^{+}\pi^{-}\pi^{\pm}$	$3.5 \cdot 10^{-5}$	$.3 \pm .03$	12000 ± 2600	$.4 \pm .03$	15000 ± 3200	16000 ± 3500
$\bullet B^{\pm} \to K^{+}K^{-}\pi^{\pm}$	$1.5 \cdot 10^{-5}$	$.2 \pm .02$	3600 ± 810	$.3 \pm .03$	4700 ± 1000	5300 ± 1200
$\circ B^{\pm} \to K^{\pm}K_s$	$6.8 \cdot 10^{-6}$	$.006 \pm .003$	40 ± 25	$.03 \pm .008$	190 ± 63	200 ± 67
$\circ B^{\pm} \to \pi^{\pm}K_s$	$1.6 \cdot 10^{-5}$	$.01 \pm .005$	190 ± 87	$.02 \pm .006$	310 ± 120	340 ± 130
$\bullet B^{\pm} \to \phi K^{\pm}$	$1.2 \cdot 10^{-5}$	$.2 \pm .02$	2300 ± 520	$.3 \pm .03$	3600 ± 790	3800 ± 830

Table 6.9: Expected sample size. For each simulated trigger channel ($\pi\pi$ and HAD refer to different trigger selection criteria as explained in section 6.4) We report the fraction of produced events which triggered in that specific channel and is made entirely of *offline* tracks, together with the number of events expected with this efficiency and the given cross section in $1fb^{-1}$ of int. luminosity. The last column reports the number of events collected with the logical OR of the two triggers. See section 6.9 for an explanation on the initial $\circ$ or $\bullet$ symbol.

Decay	Complete Decay	Total BR
$B_s \to K^{*\circ}\bar{K}^{*\circ}$	$K^{*\circ} \to K^{\pm}\pi^{\mp}$	?
$B_s \to K^{*+}K^{*-}$	$K^{*\mp} \to K^{\circ}\pi$, $K^{\circ} \to \pi\pi$	?
1. $B_s \to \bar{D}^{\circ}\phi$	$D^{\circ} \to K^{-}\pi^{+}$, $\phi \to K^{+}K^{-}$	$1.1 \cdot 10^{-7}$
2. $B_s \to \bar{D}^{\circ}\phi$	$D^{\circ} \to K_s\pi^{+}\pi^{-}$, $K_S \to \pi^{+}\pi^{-}$, $\phi \to K^{+}K^{-}$	$5.3 \cdot 10^{-8}$
3. $B_s \to \bar{D}^{\circ}\phi$	$D^{\circ} \to K^{-}\pi^{+}\pi^{-}\pi^{+}$, $\phi \to K^{+}K^{-}$	$2.2 \cdot 10^{-7}$
1. $B_s \to \bar{D}^{\circ}\bar{K}^{*\circ}$	$D^{\circ} \to K^{-}\pi^{+}$, $K^{*\circ} \to K^{\pm}\pi^{\mp}$	$4.6 \cdot 10^{-6}$
2. $B_s \to \bar{D}^{\circ}\bar{K}^{*\circ}$	$D^{\circ} \to K_s\pi^{+}\pi^{-}$, $K_S \to \pi^{+}\pi^{-}$, $K^{*\circ} \to K^{\pm}\pi^{\mp}$	$2.2 \cdot 10^{-6}$
3. $B_s \to \bar{D}^{\circ}\bar{K}^{*\circ}$	$D^{\circ} \to K^{-}\pi^{+}\pi^{-}\pi^{+}$, $K^{*\circ} \to K^{\pm}\pi^{\mp}$	$9 \cdot 10^{-6}$
$B_s \to D_s\pi$	$D_s \to \phi\pi$, $\phi \to K^{+}K^{-}$	$5.3 \cdot 10^{-5}$
$B_s \to D_s\pi\pi\pi$	$D_s \to \phi\pi$, $\phi \to K^{+}K^{-}$	$1.4 \cdot 10^{-4}$

Table 6.10: Estimate of the total BR for B_s decays as described in the text.

Decay	Total BR	$\epsilon^{\pi\pi}_{trig}$ [%]	$\epsilon^{\pi\pi}_{acc}$ [%]	ϵ^{HAD}_{trig} [%]	ϵ^{HAD}_{acc} [%]
$B_s \to K^* \bar{K}^*$	$1 \cdot 10^{-6}$	$.2 \pm .02$	70 ± 10	$.4 \pm .03$	60 ± 10
$B_s \to K^{*+} K^{*-}$	$1 \cdot 10^{-6}$	$.1 \pm .02$	80 ± 20	$.2 \pm .02$	80 ± 20
1. $B_s \to \bar{D}^\circ \phi$	$1.1 \cdot 10^{-7}$	$.2 \pm .02$	60 ± 10	$.5 \pm .03$	60 ± 8
2. $B_s \to \bar{D}^\circ \phi$	$5.3 \cdot 10^{-8}$	$.1 \pm .01$	40 ± 10	$.2 \pm .02$	40 ± 10
3. $B_s \to \bar{D}^\circ \phi$	$2.2 \cdot 10^{-7}$	$.1 \pm .02$	50 ± 20	$.3 \pm .03$	50 ± 9
1. $B_s \to \bar{D}^\circ \bar{K}^{*0}$	$4.6 \cdot 10^{-6}$	$.3 \pm .03$	40 ± 9	$.5 \pm .03$	50 ± 8
2. $B_s \to \bar{D}^\circ \bar{K}^{*0}$	$2.2 \cdot 10^{-6}$	$.2 \pm .02$	60 ± 20	$.3 \pm .03$	50 ± 9
3. $B_s \to \bar{D}^\circ \bar{K}^{*0}$	$9 \cdot 10^{-6}$	$.1 \pm .02$	50 ± 20	$.3 \pm .03$	50 ± 10
$B_s \to D_s^\pm \pi^\mp$	$5.3 \cdot 10^{-5}$	$.3 \pm .02$	60 ± 10	$.4 \pm .03$	60 ± 10
$B_s \to D_s^\pm \pi^\mp \pi^+ \pi^-$	$1.4 \cdot 10^{-4}$	$.2 \pm .02$	40 ± 10	$.3 \pm .03$	40 ± 9

Table 6.11: Simulated trigger efficiency. For each simulated trigger channel ($\pi\pi$ and HAD refer to different trigger selection criteria as explained in section 6.4) We report the fraction of produced events which triggered in that specific channel, and the fraction of these which is made entirely of *offline* tracks.

Decay	Total BR	$\epsilon^{\pi\pi}_{tot}$ [%]	$N^{\pi\pi}_{1fb^{-1}}$	ϵ^{HAD}_{tot} [%]	$N^{HAD}_{1fb^{-1}}$	$N^{HAD+\pi\pi}_{1fb^{-1}}$
$\circ B_s \to K^* \bar{K}^*$	$1 \cdot 10^{-6}$	$.2 \pm .02$	71 ± 17	$.2 \pm .02$	97 ± 22	110 ± 24
$B_s \to K^{*+} K^{*-}$	$1 \cdot 10^{-6}$	$.09 \pm .01$	34 ± 8.7	$.2 \pm .02$	72 ± 17	78 ± 18
1. $B_s \to \bar{D}^\circ \phi$	$1.1 \cdot 10^{-7}$	$.1 \pm .02$	6 ± 1.4	$.3 \pm .02$	12 ± 2.6	12 ± 2.7
2. $B_s \to \bar{D}^\circ \phi$	$5.3 \cdot 10^{-8}$	$.04 \pm .01$	$.9 \pm .3$	$.1 \pm .01$	$2.1 \pm .5$	$2.2 \pm .5$
3. $B_s \to \bar{D}^\circ \phi$	$2.2 \cdot 10^{-7}$	$.07 \pm .01$	6.4 ± 1.7	$.2 \pm .02$	14 ± 3.2	14 ± 3.3
$\circ$1. $B_s \to \bar{D}^\circ \bar{K}^{*0}$	$4.6 \cdot 10^{-6}$	$.1 \pm .02$	230 ± 56	$.2 \pm .02$	400 ± 91	430 ± 96
$\circ$2. $B_s \to \bar{D}^\circ \bar{K}^{*0}$	$2.2 \cdot 10^{-6}$	$.09 \pm .01$	78 ± 20	$.2 \pm .02$	130 ± 31	140 ± 33
$\circ$3. $B_s \to \bar{D}^\circ \bar{K}^{*0}$	$9 \cdot 10^{-6}$	$.06 \pm .01$	230 ± 62	$.2 \pm .02$	590 ± 140	600 ± 140
$\bullet B_s \to D_s^\pm \pi^\mp$	$5.3 \cdot 10^{-5}$	$.2 \pm .02$	3400 ± 790	$.3 \pm .02$	5800 ± 1300	6200 ± 1400
$\bullet B_s \to D_s^\pm \pi^\mp \pi^+ \pi^-$	$1.4 \cdot 10^{-4}$	$.07 \pm .01$	3800 ± 1000	$.1 \pm .02$	7500 ± 1800	7700 ± 1800

Table 6.12: Expected sample size. For each simulated trigger channel ($\pi\pi$ and HAD refer to different trigger selection criteria as explained in section 6.4) We report the fraction of produced events which triggered in that specific channel and is made entirely of *offline* tracks, together with the number of events expected with this efficiency and the given cross section in $1fb^{-1}$ of int. luminosity. The last column reports the number of events collected with the logical OR of the two triggers. See section 6.9 for an explanation on the initial $\circ$ or $\bullet$ symbol.

Chapter 7

Perspectives

We have shown that even if the TTT (Two Track Trigger) data sample is collected for specific analyses ($B_d \to \pi\pi$ and $B_s \to D_s\pi$), the selection is favorable to many other hadronic B decays.
In principle we might take further advantage of several b physics measurements by selectively improving the trigger optimization.
In this chapter we will discuss the possibilities open by these considerations and introduce the issues we will address in the next chapters.

7.1 Not Only J/ψ

The potentialities of the fully hadronic and *semileptonic* B trigger should now be much clear: B physics at CDF II will no longer be exclusively done on the J/ψ and the single lepton trigger samples. This opens a broad range of new possibilities for an hadronic experiment, which are still far from being completely understood.
The two types of trigger strategies described in chapter 5 are quite new in our environment and need deeper insight and strong results in order to be fully exploited: one of our goals in chapter 6 has been precisely that of refining and systematically frame the trigger possibilities for a broad range of decay modes.
In the case of the $\mu + track$ trigger the work is still at a preliminary level, but promising results have been obtained. This channel is considered an important exploitation *per se* and as a fundamental expedient in the case that running conditions unpredictably vanish the realizability of the hadronic trigger.

We will focus our studies on a specific decay channel. The ideal goal would be that of having our tools ready as soon as possible: first of all for what concerns the trigger optimization (in particular for the channels we are interested in). Moreover it would be nice to have a baseline analysis strategy ready even before the data samples are available: we can't, of course, totally refine the analysis approach before having the data samples at hand, but we might prepare the baseline strategy so that we can refine it and critically revise even the trigger strategy as soon as the first real data samples are available.

7.2 Possible Candidates

We must restrict our interest to a small set of analyses, one or two but not more. New ideas and proposals are continuously produced, and the effort to study their implementation in the CDF II framework is a large project.
Apart from $B \to J/\psi K_s$, current CDF II plans are focused on two exclusive decay channels which should be, so far, pretty familiar: $B \to \pi^+\pi^-$ and $B_s \to D_s\pi$. There are several interesting issues still open and worth some discussion. Some of these will be introduced in section 7.2.1.

A new very interesting perspective came to our attention and we want to briefly discuss and motivate it in section 7.2.2

7.2.1 Afterthoughts on $B_d \to \pi^+\pi^-$ and $B^\pm \to K^\pm D^\circ$

Level 1 and 2 triggers strategies for the $B_d \to \pi^+\pi^-$ have been fairly optimized, but some more effort is needed in order to study what needs to be done at Level 3. Given the recent results [128] on the combined analysis of $B \to \pi^+\pi^-$, $B \to K\pi$ and $B \to K^+K^-$ we should also try to find a common trigger strategy for these channels, which are accepted by the first two trigger levels with reasonable efficiency.
$B^\pm \to K^\pm D^\circ$ is a newcomer in CDF [132] and its feasibility has been fairly detailed in [132, 134]. However, a better understanding of the level 3 strategy and a critical review of the level 1 and 2 approaches should result in a better exploitation of this channel. Last, the use of newly approved detectors, TOF in particular, might result in improved analysis and trigger performances for both analyses.

7.2.2 Clean CKM Information From $B_d(t) \to D^{(*)\mp}\pi^\pm$?

It has been known for many years [17] that $B_d(t) \to D^{(*)\mp}\pi^\pm, \rho^\pm, a_1^\pm$ modes may involve observable CP violating effects. This decay is a case of non-CP eigenstate decays, for which CDF still has no firm results and projections.

Another striking fact makes this decay rather appealing: there might be the possibility of reconstructing the $B_d(t) \to D^{(*)\mp}\pi^\pm$ channel with small statistics on Run I data. In particular, the single electron trigger stream, which contains $\mathcal{O}(10^6)$ B decays, might allow the reconstruction of a small signal.
The high P_t requirement on the lepton at trigger level makes the extrapolation to the Run II situation (and the $\mu + track$ trigger in particular) rather difficult, but the challenge is very appealing!
Apart from the direct measurement of CP violation this decay mode is interesting for a number of reasons:

- From chapter 6 we know that the two track trigger yield should be of the order of 300 $B_d(t) \to D^{(*)\mp}\pi^\pm$ events/day. The large statistics expected suggests its use as an on-line monitoring tool for the performance of SVT based triggers.
- Two facts make it one of the best candidates for several Run II control studies:
  - The expectations on the size of the collectable sample

  - The fact (see the modes listed in chapter 6) that this mode's topology is close to that of many others relevant to CP violation studies

  This suggests the use of $B_d(t) \to D^{(*)\mp}\pi^{\pm}$ as a tool for measuring with good precision (thanks to the large statistics):

  - The **dilution** of the tagging algorithms (note, for instance, that the same mode has been used as a control sample in the measurement of $Sin(2\beta)$ [135])
  - The tagging **efficiency** for all the cases in which decay modes with a similar final state are used for asymmetry measurements.
  - **Tagging asymmetries**: if the asymmetry for $B_d(t) \to D^{(*)\mp}\pi^{\pm}$ is beyond the CDF II reach but is known with sufficient absolute accuracy from other sources (experimental or theoretical), its measurement provides a precise measurement of eventual asymmetries in the tagging algorithms.

- The large number of particles in the final state of this mode makes it extremely sensitive also to issues related to the tracking system like detector efficiency and reconstruction performance. The reconstruction of this mode and an understanding of the event yield will provide insight also in these issues.

For what concerns CP violation, $B_d(t) \to D^{(*)\mp}\pi^{\pm}$ allows in principle [17] the determination of the CKM phase $\phi = -2\beta - \gamma$ from a measurement of the observables:

$$\begin{array}{ll} \Gamma\left(B_d(t) \to f\right) & \Gamma\left(B_d(t) \to \bar{f}\right) \\ \Gamma\left(\bar{B}_d(t) \to \bar{f}\right) & \Gamma\left(\bar{B}_d(t) \to f\right) \end{array}$$

Furthermore, there's no need to determine all the four BR, but it suffices to measure one of the two asymmetries:

$$\begin{aligned} \mathcal{A}_{CP}(t) &= \frac{\Gamma\left(B_d(t) \to \bar{f}\right) - \Gamma\left(\bar{B}_d(t) \to f\right)}{\Gamma\left(B_d(t) \to \bar{f}\right) + \Gamma\left(\bar{B}_d(t) \to f\right)} \\ \mathcal{A}_{CP}(t) &= \frac{\Gamma\left(B_d(t) \to f\right) - \Gamma\left(\bar{B}_d(t) \to \bar{f}\right)}{\Gamma\left(B_d(t) \to f\right) + \Gamma\left(\bar{B}_d(t) \to \bar{f}\right)} \end{aligned} \tag{7.1}$$

The BR's involved in the reconstruction of this mode are rather large [13]:

$$\mathrm{BR}\left(B_d \to f\right) = (2.76 \pm 0.21) \cdot 10^{-3}.$$

Let's focus on a particular decay chain: we know that $D^{*\mp}(2010) \to D^{\circ}\pi^{\pm}$ is the preferred decay channel for the $D^{*\mp}$ ($\approx 68\%$). The secondary decay can reasonably chosen among:

$$\begin{array}{lll} B^{\circ} \to \pi^{+} & D^{*\mp} & \approx 0.3\% \\ & \hookrightarrow \pi^{+}K^{-}\pi^{+} & \approx 4\% \\ & \hookrightarrow \pi^{+}K^{-}\rho^{+} & \approx 6\% \\ & \hookrightarrow \pi^{+}K^{-}X & \approx 53\% \end{array} \tag{7.2}$$

Each of these channels requires a different approach, since the final products show relevant differences for the signal reconstruction: the first one involves only charged final decay products, but shows the smallest combined BR ($\mathcal{O}(10^{-4})$); the second signal listed involves a final state with neutral particles, difficult to detect at CDF, but has a slightly larger combined BR ($\mathcal{O}(1.5 \cdot 10^{-4})$). The K^- inclusive decay is by far the one with the largest combined BR ($\mathcal{O}(10^{-3})$) but the feasibility of its reconstruction in the CDF environment is uncertain and needs to be studied.

Let's take the first decay as a prototype: $B^\circ \to \pi^+ D^{*\mp} \to \pi^+ K^- \pi^+$. The asymmetry to be measured is $\mathcal{A}_{CP}(t) \sim 0.02$; assuming that we need an asymmetry resolution of the order of $\delta\mathcal{A} \approx 5 \cdot 10^{-3}$, with an ϵD^2 factor optimistically estimated around 5% we need a sample of $N = (\epsilon D^2 \delta\mathcal{A}) \approx 10^4$ $B \to f$ decays.
A priori this approach looks feasible: we know that the mode $B \to J/\psi K_s$ has a combined BR for the final products $\mu^+\mu^-\pi^+\pi^-$ which is $4 \cdot 10^{-4}$ and that CDF II expects to collect $\mathcal{O}(10^4)$ of these events in Run II.
We also know from chapter 6 that the event yield for this mode given by the two track trigger alone is about in the right range: $10^4 - 10^5$ events.
The large BR suggests that also an approach based on the $\mu + track$ trigger could be feasible, with the lepton involved being used either as an automatic flavor tag for the B meson or as a decay product of the D°. In the former case the use of a leptonic trigger would improve the ϵD^2 factor and possibly compensate for the loss in signal efficiency due to the low ($\sim 10\%$) B semileptonic BR. In the latter case, the stiff lepton requirement might be compensated by the larger branching ratio involved for the D° meson.

In addition, the decay chain we are approaching presents many handles. These should result in a good efficiency for the analysis and trigger on this channel.

What can be done for the study of this channel, presently? First of all, of course, a more detailed feasibility study can be done. A background study would also be needed, and run I data might give valid insights in what will be the S/N situation.

7.3 Conclusions

Our goal is to contribute to the study of the trigger channels discussed above (the two track trigger in particular) and to define the selection criteria to be used by the offline analysis for the isolation of one or more interesting channels ($B_d(t) \to D^{(*)\mp}\pi^\pm$, $B^\pm \to K^\pm D^\circ$, $B \to \pi^+\pi^-$). Our personal preference goes to the $B_d(t) \to D^{(*)\mp}\pi^\pm$ decay, both for its novelty in our environment and for its promising perspectives.
The two track trigger still needs the identification of a clear level 3 strategy for the collection of the interesting decays despite bandwidth limitations. In the next four chapters we will deal first with the level 3 issues and then with the offline selection criteria for $B_d(t) \to D^{(*)\mp}\pi^\pm$.

Chapter 8

Level 3 of the Hadronic B Trigger

Chapter 6 clearly demonstrates that the $B_s \to D_s\pi$ trigger is in fact a superb general purpose tool for the study of CP -related B physics at CDF. So far we don't have evidence of good discriminants at level 3 which might help us in further beating the unwanted background: even if practically all we collect with the $B_s \to D_s\pi$ trigger seems to come from real B events, it can be argued that only a small fraction of the data will be usable and used in the analysis. On the other hand, if the bandwidth allocation has to be further limited for this trigger (e.g. when the Tevatron will reach larger luminosities), we must identify discriminants for a level 3 selection which are general enough not to preclude the best exploitation of the collected sample! This is the reason why we will try in this chapter first of all to improve our knowledge on the required bandwidth for the $B_s \to D_s\pi$ trigger, and then to identify good discriminants in the sense explained above.

8.1 A Better Estimate of the Required Bandwidth

Controlling the hadronic B L3 trigger rate is of primary importance, given the large L3 rate expected for this stream. The official trigger table [136] assumes an average rejection factor at L3 of the order of $\times 50$. This is not acceptable for the multibody part of that trigger unless we want to reject a good fraction of hadronic B physics: section 6.6 shows that out of about $400\,nb$ coming out from level 2 for this channel, an estimated 25% comes from B physics alone.
We will certainly be asked by the whole CDF collaboration to reduce the allocated bandwidth as much as possible: it is important to remember that the trigger bandwidth is one of the most precious and limited resources of hadronic experiments. With this goal in mind we need to define at our best what is the real bandwidth required to keep the B content in realistic conditions and eventually propose new non-destructive handles for the limitation of the bandwidth.

Note: Along this chapter we will often deal with estimates based on real data and simulations which yield statistically limited results. In order to better exploit the information contained in these results, we choose to quote confidence intervals rather than statistical errors which would have a much less evident meaning.

Ref. [85] and [137] give estimates for the behavior of the $B \to \pi\pi$ trigger based on Run I real data samples and including the effects of a level 3 validation of the trigger cuts. Our aim in this section is that of obtaining a similar estimate in the case of the $B \to D_s\pi$ trigger (see [136]).
From [85] it can be inferred that a confirmation of the L2 cuts with offline tracks applied to the $B \to \pi^+\pi^-$ trigger yields an $\approx \times 2$ reduction of the level 2 rate. Given the strict similarity of the $B \to \pi^+\pi^-$ and $B \to D_s\pi$ triggers, it is expected that also the $B \to D_s\pi$ trigger might gain the same rejection factor.
This factor, if confirmed, would be more important in the $B \to D_s\pi$ trigger case since the $\pi\pi$ path throughput can be made small with mass cuts, while the $B \to D_s\pi$ stays large and takes the largest fraction of the bandwidth.

8.2 Effect of L3 Confirmation of L2 Cuts

In order to verify this hypothesis, the following steps are ideally needed:

1. Take a sample, like the one used in [85] (the two track special sample taken in order to study the feasibility of the $B \to \pi^+\pi^-$ trigger), allowing the study of the TTT yield

2. Apply the $B \to D_s\pi$ trigger cuts on offline quality tracks for this sample

3. Estimate the resulting cross section for an "offline quality" $B \to D_s\pi$ trigger

The comparison of the results with the already known estimate of the $B \to D_s\pi$ L2 cross section would then be straightforward.
There are however two obstacles to this procedure: first of all the somewhat uncertain knowledge on the total integrated luminosity of the two samples we will use in sections 8.2.3 and 8.2.4, the latter in particular. The second obstacle is connected to the small statistics available in our studies: the sample used in section 8.2.3 yields a handful of events after all the trigger cuts are applied and thus of poor statistical significance.
In order to best use the statistics available we choose to **replace** step 3 above and instead look at the ratio between the $B \to D_s\pi$ and $B \to \pi^+\pi^-$ cross sections before and after the offline confirmation of the L2 cuts.
If this ratio stays the same we expect a $\times 2$ rejection for the $B \to D_s\pi$ trigger too.

8.2.1 Samples and Triggers

We use two different samples for this study. The first is the same used in [85] and consists of a set of special runs taken explicitly for SVT trigger studies. This sample was acquired with the only request of two tracks in the event with a P_t cut which is 50% efficient at about $2\,GeV$ and 99% at $2.2\,GeV$. The effect of the inefficiency between $2.0\,GeV$ and $2.2\,GeV$ is negligible with respect to the error introduced by the uncertainty on the B production cross section alone [85].

In order to obtain an estimate with better statistical significance, we examine also a different sample of about $4.2\,pb^{-1}$ in integrated luminosity. This sample is a special μ + *track* trigger taken during run Ic, requiring at level 1 the presence of a muon in the central muon detectors (CMU and CMP) with a $P_t > 6\,GeV/c$ cut (50% efficiency is at about $2.5\,GeV/c$ and flattens at about the nominal cut value). The level 2 requirement is that the identified muon falls has P_t larger than $3.5\,GeV$ (50% efficient at $3\,GeV$ and 99% at $3.6\,GeV$) and that an additional track has P_t larger than $5\,GeV$ (50% efficient at $4\,GeV$ and 99% at $5.1\,GeV$). Finally, the event is required to have a L3 muon with $P_t \geq 3\,GeV$.
In the subsequent study the muon is treated as a tagging tool for the "other B" in the event and is thus excluded from the set of candidate SVT triggering tracks.

8.2.2 Trigger Simulation

Ideally we would need to run our data sample through a simulation of the three trigger levels: an XFT simulator for L1, an SVT simulator for L2 and a reconstruction software analogous to the L3 behavior. However, taking advantage of the fact that each cut is then reconfirmed at offline-quality, we skip the intermediate steps. All the simulations in this chapter are thus carried on at offline level: We use the offline CTC track set in replacement of the L1 XFT track list and then emulate the SVT output with the SVX+CTC simultaneous fit.
This means that we will not be able to reproduce the intermediate L1 and L2 expected rates, but on the other hand greatly simplifies the study.
An obvious candidate cut for L3 cleanup is a cut on the SVX fit quality. This might be both an overall quality cut or the confirmation that the number of silicon hits matches that used by SVT or both requirements at the same time. I choose to apply the strict confirmation of the L2 requirement: 4 silicon hits reconstructed by the offline clustering algorithm.
Measuring and cutting on the tracks impact parameter requires the knowledge of the primary vertex position in each event. This is usually well approximated by the average beam position for the set of events belonging to the same run.
The data sample we are using does not contains the offline information on the beam position, which had to be reconstructed on the basis of the sample itself. Since we were not able to retrieve the same beam position used in [137] and [85], the simulation results are not expected to be exactly the same but will still be statistically compatible with what previously found.

8.2.3 Simulation Results

Table 8.1 reports the event count for different trigger scenarios and different trigger simulations.
Each row corresponds to a trigger scenario:

- $B \to \pi^+\pi^-$ **rev. 1** corresponds to the $B \to \pi^+\pi^-$ trigger selection designed for the low luminosity configuration of the Tevatron (including, for example, a $30^\circ < \Delta\Phi < 160^\circ$ cut). This configuration is simulated as a benchmark of

	This Work	[85] SVTSIM	L2 (SVTSIM) Xsec. (nb)
$B \to \pi^+\pi^-$ rev. 1	4	12	340 ± 100
$B \to \pi^+\pi^-$ rev. 2	4	13	360 ± 100
$B \to D_s\pi$	2	14	394 ± 105
($B \to \pi^+\pi^-$ rev. 1) OR ($B \to D_s\pi$)	6	20	560 ± 125
($B \to \pi^+\pi^-$ rev. 2) OR ($B \to D_s\pi$)	5	-	-

Table 8.1: Event counts for different trigger scenarios: see section 8.2.3 for an explanation.

the results, in comparison with old CDF works which used exactly the same sample and trigger cuts.

- $B \to \pi^+\pi^-$ **rev. 2** corresponds to the offical $B \to \pi^+\pi^-$ trigger plan at low luminosities (including, for example, a $20° < \Delta\Phi < 135°$ cut) and is the selection currently described in the official trigger table plans for CDF II [136]

- $B \to D_s\pi$ corresponds to the $B \to D_s\pi$ trigger as specified in [136]

- **($B \to \pi^+\pi^-$ rev. 1).OR.($B \to D_s\pi$)** corresponds to the OR of the first and third trigger listed here

- **($B \to \pi^+\pi^-$ rev. 2).OR.($B \to D_s\pi$)** corresponds to the OR of the second and third trigger listed here

The first column contains the new results produced here, while the second and third column are the results contained in [85] and correspond to the offline (second column) and full SVT (third column) simulations of the corresponding triggers. The numbers in the last column are the L2 cross section estimate taken from the same note.

The results obtained here in the simulation of the original $B \to \pi^+\pi^-$ trigger somehow differ from those reported in [85]: 4 events against the 5 of [85]. The comparison of the techniques used in the two cases suggests that the difference presumably lies in the use of different beam position constants for the two analyses. From table 8.1 We see that [85] estimates a rate reduction for the validation of the $B \to \pi^+\pi^-$ trigger of:

$$\frac{N^{B\to\pi^+\pi^-}_{aftervalidation}}{N^{B\to\pi^+\pi^-}_{beforevalidation}} = \frac{5}{12} \text{ corresponding to } [0.17, 0.75] \,@\, 98\%\, CL \tag{8.1}$$

This corresponds to the trigger scenario originally proposed in [85] (i.e. what we refer to as " $B \to \pi^+\pi^-$ rev. 1"). From the new numbers quoted here we can evaluate the ratio of event yields for the $B \to \pi^+\pi^-$ and $B \to D_s\pi$ triggers before

and after track validation:

$$R_{before} = \frac{N^{B\to D_s\pi}_{beforevalidation}}{N^{B\to\pi^+\pi^-}_{beforevalidation}} = \frac{14}{12} \approx 1.2 \pm 0.34 \tag{8.2}$$

$$R_{after} = \frac{N^{B\to D_s\pi}_{aftervalidation}}{N^{B\to\pi^+\pi^-}_{aftervalidation}} = \frac{2}{4} \approx 0.5 \pm 0.35 \tag{8.3}$$

R_{before} and R_{after} are statistically compatible, with central values decreasing after the validation. This result suggests that the ratio R keeps constant or even decreases across the validation cuts, and thus that the $B \to D_s\pi$ cross section after validation is equal to or smaller than the $B \to \pi^+\pi^-$ cross section.
The strongest statistical evidence of this *clean-up* effect on the $B \to \pi^+\pi^-$ and $B \to D_s\pi$ triggers is given by the effect of these cuts on the OR of the two trigger samples:

$$\frac{N^{B\to\pi^+\pi^- ORB\to D_s\pi}_{aftervalidation}}{N^{B\to\pi^+\pi^- ORB\to D_s\pi}_{beforevalidation}} = \frac{6}{20} \text{ corresponding to } [0.1, 0.55]\,@\,98.7\%\,CL \tag{8.4}$$

Which means that the OR'ed trigger undergoes a rejection which is a factor 2 or better.
The absolute number of events passing all the $B \to D_s\pi$ trigger cuts (i.e. 2) alone provides another estimate of the expected L3 bandwidth required by this trigger after the confirmation cuts. For this purpose I use the 95% CL band for a Poisson distribution in the absence of background in the Feldman & Cousins approach: 2 events observed means $0.36 \leq \mu \leq 6.72$ at 95% CL. Adding to this the cross section/number of events scaling factor used in [85]:

$$\sigma_{B\to D_s\pi} = [0.36, 6.72] \times 28\,nb = [10, 190]\ nb\,@\,95\%\,CL$$

In conclusion, both direct and indirect estimates of the cross section for the reconfirmed hadronic trigger suggest that the trigger rate is reduced at least a factor of 2 by L3 confirmation.
The sample on which these measurements are done is small and a larger number of events is desirable for reconfirming this statement.

8.2.4 The $\mu + track$ Sample

A candidate sample for improving the statistics in this study is the μ plus track sample described in section 8.2.1. With a procedure similar to that used in analogous works [137], We simulate the usual set of triggers using the technique of section 8.2.3. The results are reported in table 8.2 where the rows have the same meaning of those from table 8.1. The first column in table 8.2 reports the results of the simulation as already carried on here for the two track special run. The second column is a recalculation of the results reported in [137] where a subset of this sample ($1.5\,pb^{-1}$) was used for the study of the background for the $B \to \pi^+\pi^-$ trigger. The last column reports the result from [137] rescaled to the integrated luminosity of the full

	This Work	[137] Like	[137] (rescaled)
$B \to \pi^+\pi^-$ rev. 1	152	377	-
$B \to \pi^+\pi^-$ rev. 2	240	544	437
$B \to D_s\pi$	228	891	-
($B \to \pi^+\pi^-$ rev. 1) OR ($B \to D_s\pi$)	347	1175	-
($B \to \pi^+\pi^-$ rev. 2) OR ($B \to D_s\pi$)	424	1313	-

Table 8.2: Event counts for different trigger scenarios: see section 8.2.4 for an explanation.

sample used here ($4.2\,pb^{-1}$). In the case of this sample only the ratio R after the validation cuts can be evaluated. In fact the full SVT simulation can't be applied to this sample due to the lack of statistics to produce correct beam alignment for SVTSIM in each of the many runs of the sample [1].

$$R_{after} = \frac{N^{B\to D_s\pi}_{aftervalidation}}{N^{B\to\pi^+\pi^-}_{aftervalidation}} = \frac{228}{240} \text{ corresponding to } [0.92, 0.98]\,@\,98\%\,CL \qquad (8.5)$$

This tells us with good statistical accuracy but uncertain systematics that the ratio R can be reasonably assumed to be roughly 1 after the validation of L2 cuts.
We can then conclude that the $B \to \pi^+\pi^-$ and the $B \to D_s\pi$ trigger are affected in a similar way by the L3 confirmation of L2 cuts. This means that, disregarding systematics effects due to the sample we are using, the expected bandwidth required by the $B \to D_s\pi$ trigger after L3 confirmation of the L2 cuts is within 10% from the one required by the $B \to \pi^+\pi^-$ trigger.

8.2.5 Conclusions

We have several indications that the cleanup of the multibody part of the Two Track Trigger will be of the order of 50%: thanks to the two track special run we can safely predict with poor statistical accuracy but little systematics $\sigma_{B\to D_s\pi}$ to lie in the interval $10-190\,nb$ at 95% confidence level. The same sample yields a cleanup ratio for the OR of the multibody and the two body hadronic triggers falling in the region $[0.1, 0.55]$ at about 99% CL.
Also a study based on a biased sample with larger statistics gives similar results, suggesting that $\sigma_{B\to D_s\pi} \approx \sigma_{B\to\pi^+\pi^-} = 140 \pm 63$.

8.3 Tightening the Level 3 Selection

What can we do in order to reduce the required bandwidth loosing as little as possible in terms of yield from the $B \to D_s\pi$ sample?

The answer depends on the cuts we can perform at level 3, which in turn depend on the physics quantities computable in real time by the level 3 farm. The list of

[1] remember that the beam was not kept stable in Run I

these quantities is still being defined and will depend on the performance of the L3 reconstruction algorithms. However, track reconstruction at the offline level will be available at level 3 at least for the trigger tracks, in order to confirm the L2 selection as suggested in the previous section. This suggests applying some kind of kinematic constraint based on the two track parameters not previously available.
We want this selection to be really discriminating on the physics content with as little as possible loss in acceptance for generic B decay modes. Is this possible at all? Topological requests are probably ideal in this perspective: 3D vertexing of the two tracks is a prime example.
Another approach, complementary but also logically descending from the previous one is that of selecting resonances directly at level three. This is of course an approach limited to the set of B decay modes which present common intermediate states, but could become pretty general: most of the modes shown in chapter 6 do contain intermediate charmed mesons (like $D^{\pm}$, D°, D^{*} and so on). The very same approach has been shown to be amazingly helpful in the case of $B \to \pi^{+}\pi^{-}$ selection at trigger level: in that case a tight cut about the candidate B invariant mass allows the reduction of the trigger cross section from $\approx 360\,nb$ down to about $10\,nb$.
There is however a difference we must take into account: the mass cut in the case of $B \to \pi^{+}\pi^{-}$ required the invariant mass of the trigger tracks to sit in a narrow window at the (large) nominal B mass value. A first problem arises because in the case of charmed decays, we should look for track pairs: in principle all the track pairs in the event should be tested, or at least all track pairs within some cone around the trigger pair (in the case of $B_d\,(t) \to D^{(*)\mp}\pi^{\pm}$, and thus probably of all decay modes with many tracks in the final state, the cone size however practically includes a whole hemisphere of the detector). The other problem we must take into account is that the invariant mass of the resonance we are looking for is significantly smaller than that of the B meson, and in particular sits in a mass region where the two track trigger spontaneously contains most of the bandwidth.
The conclusion is that we can't expect to obtain background rejections comparable to the ones obtained in the case of $B \to \pi^{+}\pi^{-}$, and that a detailed study is needed in order to better understand background contributions at this level.
We thus stick to the simplest way: selecting events on the basis of the invariant mass of *the two trigger tracks* fully reconstructed at level 3.

8.3.1 Invariant Mass at L3: the Signal Distribution

Borrowing the signals already discussed in 6, we can quickly obtain an estimate of the efficiency of this selection on the set of "significantly collectable" decay modes. We separate three sets of decay modes: the first contains the full set of decay modes proposed in 6. The second set contains only those decay modes for which more than 100 events are expected according to 6. The third set is like the previous one, but restricted to modes with event yields of 1000 or larger.
In each case we select the events after the complete selection reported in chapter 6, including the Level 1 and 2 trigger simulations and the requirement that the final B decay products are contained in the nominal acceptance of the central detector.

Mode	Fraction (%)
$D^*\pi$	$23-42$
$D^\circ_{\mathsf{CP}}\pi\pi$	$13-28$
$D^\circ\rho^\circ$	$0-10$
$D^\circ K^*$	$50-73$
$D^* K^*$	$17-36$
$D^{*+}D^{*-}K_s$	$27-60$
$D^{*+}D^{*-}$	$28-52$
$D^\circ K^+$	$19-34$
$D^\circ\phi$	$22-40$
Bandwidth	$2.2-9$

Mode	Fraction (%)
$D_s\pi$	$8-21$
ϕK^+	$0-2$
Bandwidth	$9-19$

Table 8.3: 98% Confidence limits for the fraction of the signal passing the trigger cuts which has the two trigger tracks invariant mass falling in the region $1.68-2.04\,GeV$. Only D° decaying into the charged $K\pi$ mode are considered. The right table refers to the same fraction calculated for events falling in the ϕ mass range $(0.82-1.22\,GeV)$. The last line of both tables reports the fraction of the total bandwidth corresponding to the mentioned mass cuts, estimated in section 8.3.2.

We then plot the trigger tracks invariant mass distribution M_{tt} for these three sets with various trigger selections. The result is reported in figure 8.1.

The bottom left plot of figure 8.1 is particularly significant: an important fraction of the interesting events is selected by the Two Track Trigger (TTT) assigning the two tracks to the decay of a D meson! Far from being fully efficient this selection might be however a powerful tool for quickly identifying a very small sub-stream of the TTT which is rich in terms of interesting signals. Provided that the background contribution is small enough, this is an handle with a bandwidth reduction power comparable to the L3 mass cut for the $B \to \pi^+\pi^-$ signal reconstruction.
In fact, the four bins containing the charm peak (bins 14-17, $1.68-2.04\,GeV$) correspond to a fraction of the signal which depends on the specific mode chosen: the two leftmost columns of table 8.3 report a list of the charmed B decays which should yield more than 10^3 events in $1\,fb^{-1}$ with the fraction of those having the two trigger tracks falling in the interval $1.68-2.04\,GeV$. An efficiency ranging between 10% and 30% is foreseen depending on the decay mode.

8.3.2 Invariant Mass at L3: the Background Distribution from Real Data

We now need to estimate of the background rejection for this raw invariant mass cut. One way of doing this is that of obtaining information on the shape of the invariant mass distribution after L3 confirmation. Given this shape, we can infer what's the fraction of the total bandwidth (i.e. the integral of the whole shape) which falls in the given invariant mass range.

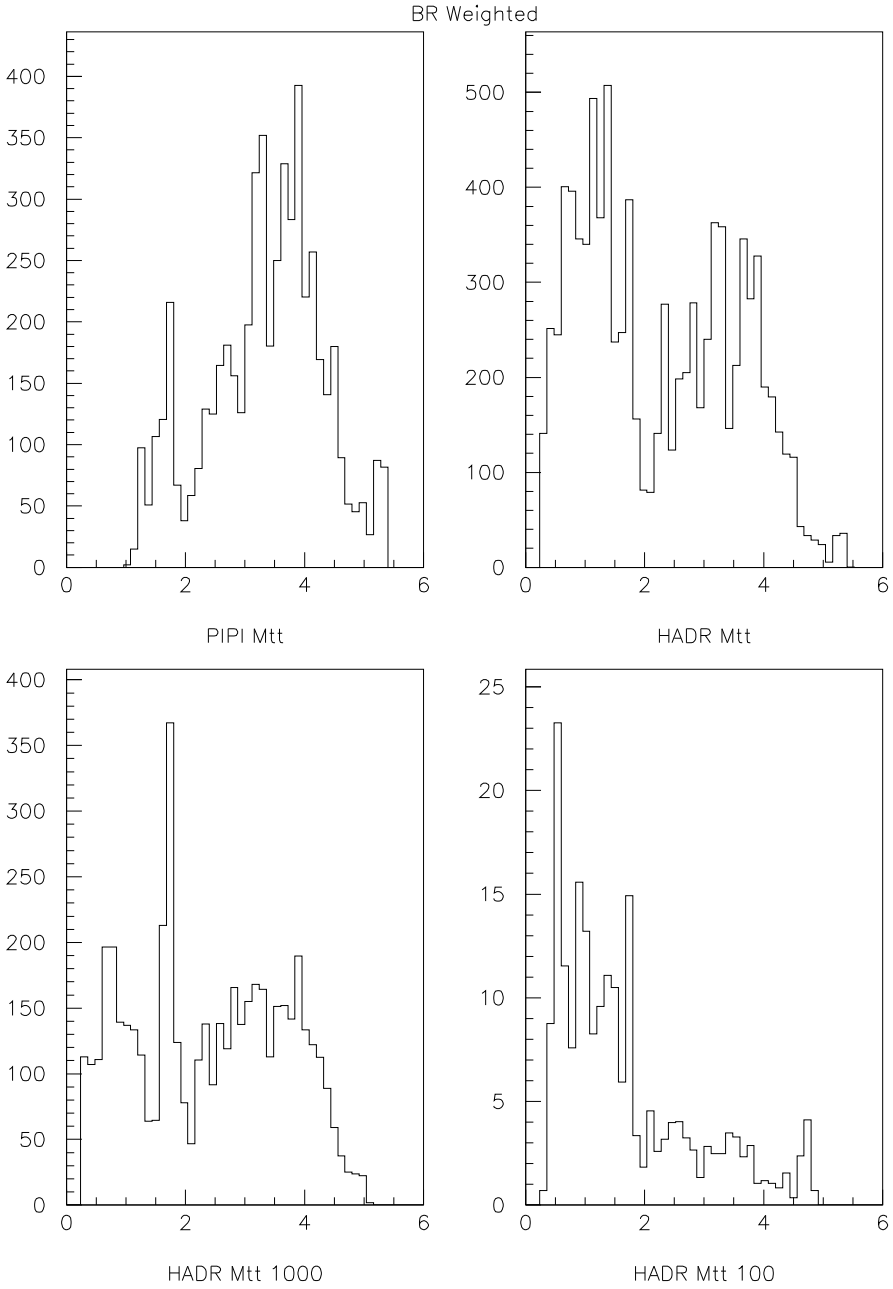

Figure 8.1: Invariant mass distribution for the two triggering tracks in the two track trigger for various B decay modes and trigger paths. Top plots: the histograms are filled with all decay modes listed in 6. Top Left plot is the result of the $B \to \pi^+\pi^-$ (a.k.a. high mass) trigger path. The Top right plot comes from the $B \to D_s\pi$ (a.k.a. low mass) trigger path. Bottom histograms contain the same distribution filtered through the logical or of the two trigger paths, selecting only decay modes which contribute with more than 1000 events (left) or between 1000 and 100 events (right) per inverse fb. The vertical scale in all histograms is homogeneous but arbitrary. Contributions are weighted by their branching ratio of the decay modes and are thus proportional to the number of events.

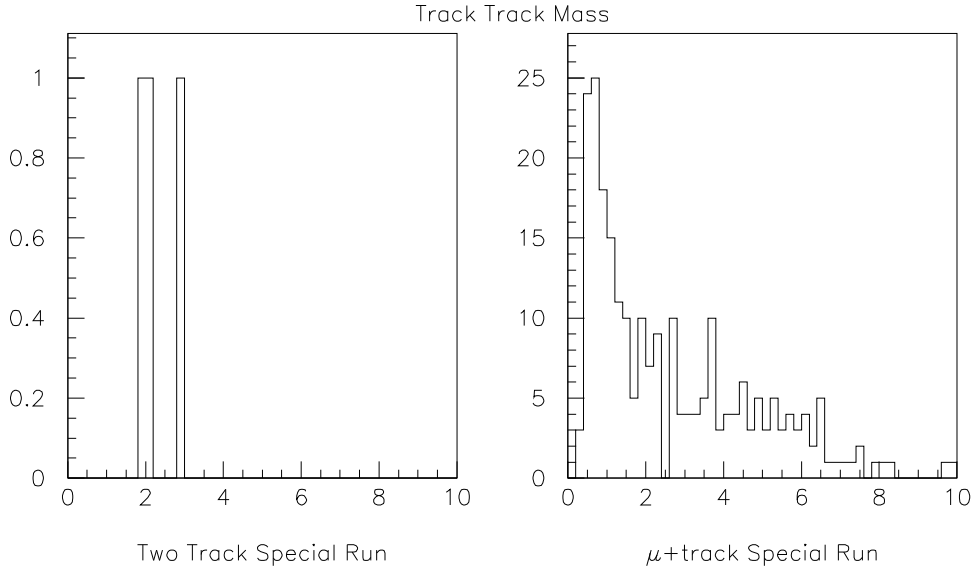

Figure 8.2: Invariant mass distribution for the two triggering tracks in the two track trigger special run (left) and in the $\mu+track$ special run (right) for the trigger paths already discussed in the L3 validation study. All plots report the distribution at the output of the multibody section of the two track trigger after L3 confirmation.

The equivalent cross section as estimated for a trigger which accepts trigger track pairs in the mass range $1.68 - 2.04\,GeV$ comes straightforward from the data in the left of figure 8.2: we count 1 event in that mass range, equivalent to $[0.05, 5.14] \times 28\,nb = [1.4, 144]\,nb\,@\,95\%\,CL$. Not much of an indication on the clean-up. On the other hand, the second sample (right plot of figure 8.2) gives in the same mass range 13 events out of a total of 227. This translates into the reduction of the trigger cross section down to $[2.2, 9]\,\%\,@98\%CL$ of the L3 value in the full mass range: $[3, 13]\,nb\,@98\%CL$ when one assumes the total multibody trigger cross section to be $140\,nb$ (see section 8.2.5).
A similar calculation can be performed for the ϕ resonance: table 8.3 reports also the efficiency of a cut about the ϕ resonance ($0.82 - 1.22\,GeV$). Again, the data in figure 8.3 gives a reduction of $9 - 19\%$, corresponding to about $21\,nb$.
Note that the improvement in the case of the D° resonance for the signal to background ratio ranges between 2 and 20 and looks much more interesting than that achievable in the case of the ϕ resonance (with S/B improvements of the order of 3 at most). This is the consequence of two distinct effects: the first is the presence of a larger background at low masses in figure 8.2 which yields larger background below the ϕ peak rather than that of the D°. The second effect which favors D° modes comes from table 8.3: the average probability of catching the two decay products of the $\phi \to K^+K^-$ decay in the trigger tracks is tiny and certainly smaller than the analogous probability for the $D^\circ \to K\pi$ decay.

8.3.3 The Invariant Mass Distributions in the TTT

The invariant mass distribution for the trigger tracks in the case of real data is something which is useful in many studies related to the TTT and that is certainly worth the work of performing the study on real run I data. We will thus discuss the features of these distributions beyond the purpose of estimating the trigger cross section for the range of mass cuts performed in the previous subsection: it is very important to acquire as much familiarity as possible with them in order to promptly understand Run II data.
We use for this study the same two samples already used for the study of the effect of the validation cuts on the TTT rate (see section 8.2.1). After the offline validation of the trigger cuts we take the trigger tracks and plot the invariant mass distribution. Figure 8.3 contains the invariant mass distribution for the two triggering tracks in the two track trigger special run. The trigger paths are those already discussed in the previous sections. These plots are a bit complicate to understand but really deserve some attention. Each box in figure 8.3 pertains to a given trigger path (the same discussed in section 8.2.3: $B \to \pi^+\pi^-$ Rev. 2, $B \to \pi^+\pi^-$ Rev. 1 and $B \to D_s\pi$). Each trigger path has an associated color (red for $B \to \pi^+\pi^-$ Rev. 2, blue for $B \to \pi^+\pi^-$ Rev. 1 and green for $B \to D_s\pi$). The box contains a continuous distribution, corresponding to the invariant mass values for the track pairs passing the trigger path pertaining to that box. In addition, the same box contains also dotted distributions. Those distributions represent the fraction of the continuous distribution which is contributed by events triggered also by one of the other two trigger paths. The color of the dots indicates which of the other two paths is considered. Here is an example: the $B \to D_s\pi$ two tracks mass distribution is the green continuous line in the bottom plot. The red dots in the bottom plot are the fraction of $B \to D_s\pi$ triggered events which are triggered also by the $B \to \pi^+\pi^-$ Rev. 2 trigger. Blue dots in the same plot are the fraction of $B \to D_s\pi$ triggered events which are triggered also by the $B \to \pi^+\pi^-$ Rev. 1 trigger.
Figure 8.4 reports exactly the same distribution for the muon+track trigger of section 8.2.4. We would like to stress again that the two figures are obtained from real Run I data.

A main feature of these distributions is immediately visible: the two body path yields events biased towards high masses, while the multibody path favors low invariant mass combinations. This is straightforward when one compares the continuous line of the top left plot in figure 8.4 (this is the invariant mass distribution for the two body path) with that in the bottom plot of the same figure (multibody path). In fact, even the events in common between the two paths (dotted distributions in the same two plots) present the same shape, suggesting that when one event sits in both plots either it presents an invariant mass which is *mid*-mass or it enters the two plots with different track combinations.
Another lesson we learn from these distributions is that the fraction of events which hits both paths is small but sizeable (compare the dotted and continuous distributions).

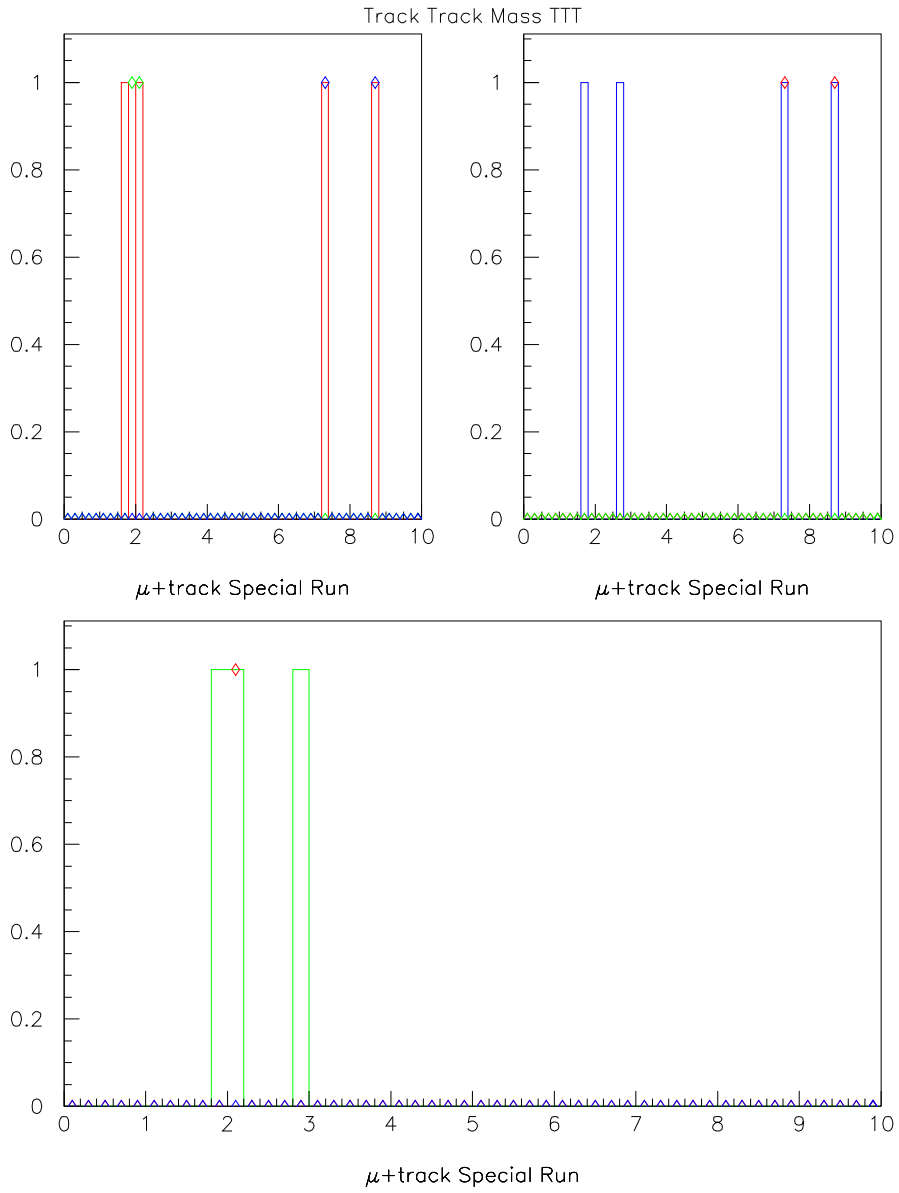

Figure 8.3: Invariant mass distribution for the two triggering tracks in the two track trigger special run for the trigger paths already discussed in the L3 validation study. Top left plot is for the high mass trigger in the final version. Top right is for the high mass trigger in the originally proposed version. Bottom plot is for the low mass trigger. Each histogram contains also the invariant mass distribution for the subset of triggering events which are selected also by one of the other two. These two distributions are superimposed using markers not connected with continuous lines. The marker color identifies the intersecting trigger (e.g. the low mass histogram is the green line in the bottom box, the intersecting high mass events are in red in the same histogram and the intersecting high mass events according to the original definition of the high mass trigger are in blue).

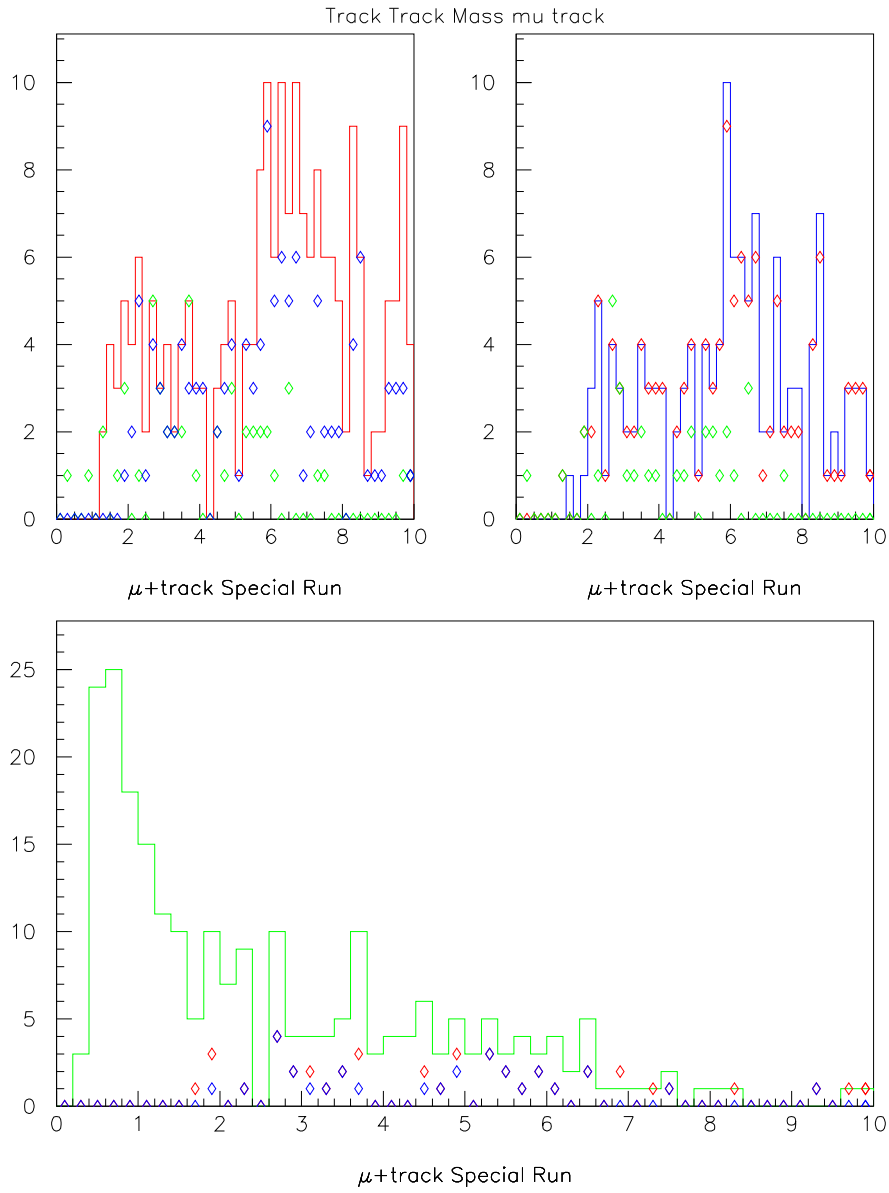

Figure 8.4: Invariant mass distribution for the two triggering tracks in the muon+track special run data for the trigger paths already discussed in the L3 validation study. Top left plot is for the high mass trigger in the final version. Top right is for the high mass trigger in the originally proposed version. Bottom plot is for the low mass trigger. Each histogram contains also the invariant mass distribution for the subset of triggering events which are selected also by one of the other two. These two distributions are superimposed using markers not connected with continuous lines. The marker color identifies the intersecting trigger (e.g. the low mass histogram is the green line in the bottom box, the intersecting high mass events are in red in the same histogram and the intersecting high mass events according to the original definition of the high mass trigger are in blue).

Finally, one might argue on the fairness of using the $\mu + track$ sample for estimates concerning the shape of the two track invariant mass distribution. The ideal sample for these studies would be that of figure 8.3, which has however too small statistics. In favor of this use comes the comparison of the corresponding plots in the two figures, which seem statistically compatible.

8.4 Conclusions

The $B_s \to D_s\pi$ trigger is a general purpose tool for the study of CP -related B physics at CDF and contains mostly B physics events. This is so striking that the CDF collaboration has been convinced to allocate about 1/3 of the total available bandwidth for this trigger alone. This is 1/3 of the most important resource in an hadronic experiment!
The hadronic trigger total bandwidth after level 2 is large and could become unacceptable for storage. Level 3 validation of the L2 cuts alone is capable of reducing the bandwidth down to the level of $150\,nb$.
A "charmonium expressline" from the hadronic B trigger is conceivable with good efficiency and rejection: its simplest implementation has been studied which requires the presence of a D resonance in the two tracks reconfirmed at L3. This has the advantage of being of minimal impact on the L3 algorithms with nevertheless good efficiency on interesting signals (30%) and good background rejection (5.5%), reducing the bandwidth down to a rate at which a data expressline is really feasible.

Chapter 9

Clean CKM Information from $B_d\,(t) \to D^{(*)\mp}\pi^{\pm}$

A reasonable multibody trigger strategy is now available. This strategy allows the collection of several charmed B decays, among which the one already encountered in chapters 6 and 7: $B_d\,(t) \to D^{(*)\mp}\pi^{\pm}$. Chapter 6 shows that the amount of events collectable in the $B_d \to D^{*\pm}\pi^{\mp}$ and $B_d \to D^{\pm}\pi^{\mp}$ decays ($B_d\,(t) \to D^{(*)\mp}\pi^{\pm}$ from now on) is quite large. Following the suggestions of [89] we want to explore the power of this sample in the extraction of useful CKM information (namely, $2\beta+\gamma$).

9.1 Introduction

I. Dunietz first suggested in [89] that the $B_d\,(t) \to D^{(*)\mp}\pi^{\pm}$ channel might be used in "first generation" experiments for the extraction of useful CKM information.
The measurement is based on a time-dependent study of four decay rates (either B_d or $\bar{B}_d$ decaying to $D^{(*)-}\pi^{+}$ or $D^{(*)+}\pi^{-}$). The time dependent expression of these rates contains a term proportional to $Sin\,(2\beta+\gamma)$, which is expected to be of $\mathcal{O}\,(10^{-2})$. The detection of this tiny oscillation will be the main issue in this analysis.
Since a precise measurement of 2β will be at the same time available, we can expect the analysis to produce a γ measurement up to discrete ambiguities.
Our purpose in this chapter is to set up a first rough analysis strategy, in order to obtain an estimate of the achievable resolution as a function of the size of the collected sample.

9.2 CP violation in non CP Eigenstates

Mixing induced CP violation measurements are usually performed on decays to CP eigenstates.
Nothing prevents us from seeing it also in decays to non-CP eigenstates. In the case

of a B_d decaying to a final state f or $\bar{f}$, this would show up as:

$$\Gamma\left(B(t) \to f\right) \neq \Gamma\left(\bar{B}(t) \to \bar{f}\right)$$
$$\Gamma\left(B(t) \to \bar{f}\right) \neq \Gamma\left(\bar{B}(t) \to f\right)$$

Let's introduce, in analogy with chapter 1, the notation:

$$\langle f|\, T\, \left|\bar{B}\right\rangle = Me^{i\phi}e^{i\alpha} = Me^{i\beta}$$
$$\langle f|\, T\, |B\rangle = M'e^{-i\phi'}e^{i\alpha'} = M'e^{-i\beta'}$$
$$\rho \equiv \frac{M}{M'} \quad A^2 \equiv M^2 + M'^2$$
$$\xi \equiv \alpha - \alpha' \quad \Phi \equiv 2\beta + \phi' + \phi$$

We are assuming the presence of one dominant amplitude for the decay process.
α and α' represent the CP even phases in the decay amplitudes, while ϕ, ϕ' are the CP odd ones.
We can now express the time evolution of the decay width for initially B_d or $\bar{B}_d$ states as [18]:

$$N\left(\overset{(-)}{B} \to f\right) \propto \frac{A^2}{2}e^{-\Gamma t}\left(1 \pm \frac{\rho^2-1}{\rho^2+1}Cos\left(\Delta m\, t\right) \pm \frac{2\rho}{\rho^2+1}Sin\left(\Delta m\, t\right)Sin\left(\Phi+\xi\right)\right) \quad (9.1)$$
$$N\left(\overset{(-)}{B} \to \bar{f}\right) \propto \frac{A^2}{2}e^{-\Gamma t}\left(1 \mp \frac{\rho^2-1}{\rho^2+1}Cos\left(\Delta m\, t\right) \pm \frac{2\rho}{\rho^2+1}Sin\left(\Delta m\, t\right)Sin\left(\Phi-\xi\right)\right) \quad (9.2)$$

This is, in fact, the case of $B_d(t) \to D^{(*)\mp}\pi^{\pm}$, where $\Phi = 2\beta + \gamma$ is expected to hold with good approximation.
Various observables can be built on the 4 basic ones reported in 9.1 and 9.2, the usual being:

$$\begin{aligned}\mathcal{A} &= \frac{\left[\Gamma\left(B \to f\right) + \Gamma\left(B \to \bar{f}\right)\right] - \left[\Gamma\left(\bar{B} \to f\right) + \Gamma\left(\bar{B} \to \bar{f}\right)\right]}{\left[\Gamma\left(B \to f\right) + \Gamma\left(B \to \bar{f}\right)\right] + \left[\Gamma\left(\bar{B} \to f\right) + \Gamma\left(\bar{B} \to \bar{f}\right)\right]} = \\ &= -\frac{2\rho}{\rho^2+1}Cos\left(\Delta m\, t\right)Cos\left(\xi\right)Sin\left(\Phi\right)\end{aligned}$$

In the case of $B_d(t) \to D^{(*)\mp}\pi^{\pm}$ we have $\rho \approx 0.02$ and ξ is expected to be $\approx 0\, mod\, \pi$, which thus results in an asymmetry amplitude of about 0.04.
Measuring such a small asymmetry should be performed carefully, since small sample pollutions and mistagging effects might strongly affect the measurement.
As an example, we report in figures 9.1 and 9.2 the $B/\bar{B} \to f/\bar{f}$ branching ratios and asymmetry evaluated for $\rho = 0.02$, $2\beta+\gamma = 132°$, $\xi = 0.01$. Various mistagging probability scenario are investigated.

Taking advantage of the full statistical power of the sample will presumably mean performing an unbinned likelihood fit for the 4 separate BR, measured as functions

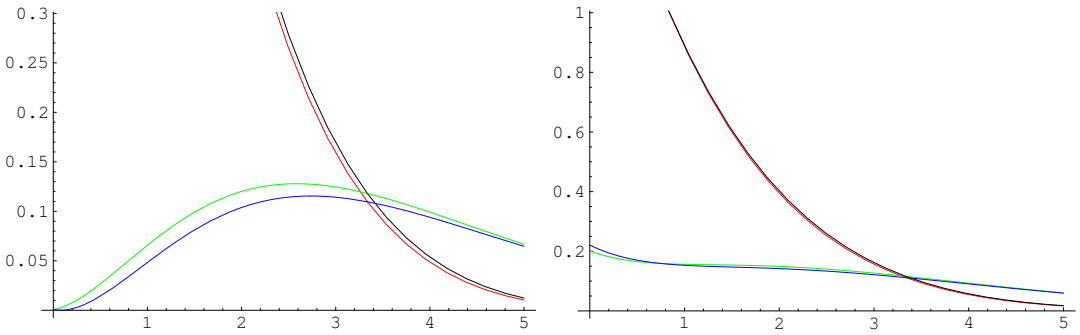

Figure 9.1: Left: the four BR for $B/\bar{B} \to f/\bar{f}$ (y axis, in arbitrary scale but relatively normalized) as a function of time (x axis, in ps). Right: the same BR with a 10% mistagging.

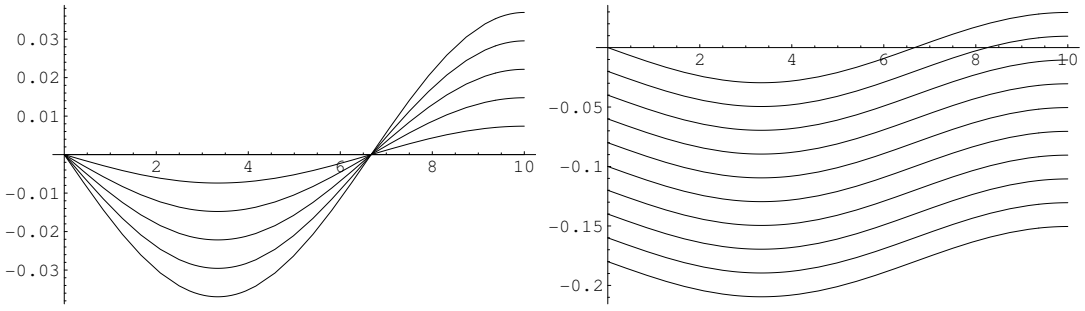

Figure 9.2: Left: expected time-dependent asymmetry as a function of mistagging (x axis is time in ps, y axis is asymmetry $\mathcal{A}$ as defined in the text), going from 0% to 50% both for B and $\bar{B}$ mesons. Right: expected asymmetry for various mistagging probabilities, assumed to be $10\% + x$ for B mesons and $10\% - x$ for $\bar{B}$ mesons, with x going from 0.01 to 0.09 (different curves).

of proper time τ.
If we assume a tagging efficiency ϵ for our tagging algorithm, a mistagging probability ζ for B mesons and $\bar{\zeta}$ for $\bar{B}$ mesons, we obtain:

$$N\left(\overset{(-)}{B} \to f\right) \propto \epsilon\left(1-\zeta-\bar{\zeta}\right)\frac{A^2}{2}e^{-\Gamma t}\left(\frac{1\pm\left(\bar{\zeta}-\zeta\right)}{1-\zeta-\bar{\zeta}} \mp \frac{\rho^2-1}{\rho^2+1}Cos\left(\Delta m\, t\right) \mp \frac{2\rho}{\rho^2+1}Sin\left(\Delta m\, t\right)Sin\left(\Phi+\xi\right)\right) \quad (9.3)$$

$$N\left(\overset{(-)}{B} \to \bar{f}\right) \propto \epsilon\left(1-\zeta-\bar{\zeta}\right)\frac{A^2}{2}e^{-\Gamma t}\left(\frac{1\pm\left(\bar{\zeta}-\zeta\right)}{1-\zeta-\bar{\zeta}} \pm \frac{\rho^2-1}{\rho^2+1}Cos\left(\Delta m\, t\right) \mp \frac{2\rho}{\rho^2+1}Sin\left(\Delta m\, t\right)Sin\left(\Phi-\xi\right)\right) \quad (9.4)$$

$$\mathcal{A} = \left(\bar{\zeta}-\zeta\right) - \frac{2\rho}{\rho^2+1}\left(1-\zeta-\bar{\zeta}\right)Cos\left(\Delta m\, t\right)Cos\left(\xi\right)Sin\left(\Phi\right) \quad (9.5)$$

The asymmetry 9.5 is now plagued by the ignorance of the mistagging probabilities ζ, $\bar{\zeta}$ which change both the offset and the amplitude of the time-dependent oscillation in $\mathcal{A}$ (see also fig. 9.2).
The quantities 9.3 and 9.4 can in principle be separately fitted, resulting in the simultaneous determination of ρ, $Sin\left(\Phi+\xi\right)$, $Sin\left(\Phi-\xi\right)$, ζ and $\bar{\zeta}$.
Additional statistical power can be obtained using both $B_d(t) \to D^{*\mp}\pi^{\pm}$ and $B_d(t) \to D^{\mp}\pi^{\pm}$. Assuming $\xi_{B_d(t)\to D^{*\mp}\pi^{\pm}} \approx \xi_{B_d(t)\to D^{(*)\mp}\pi^{\pm}} \approx 0\, mod\, \pi$ we can in fact merge together the two samples, and fit the four time dependent branching ratios with the same expressions 9.3 and 9.4. Moreover, we might rely on the assumption that the mistagging probabilities ζ and $\bar{\zeta}$ depend only on the particular tagging algorithm chosen, and not on the final state. This would allow a separate determination of ζ and $\bar{\zeta}$ from other B_d or $B^{\pm}$ decay modes, thus leaving only ρ and Φ as free parameters.

9.3 A Toy Simulation

Now that the framework is clear, we can attempt a first rough study of the achievable resolution on Φ and ρ. For this purpose we wrote a toy monte-carlo simulator which generates directly the lifetime distributions for the 4 different decay modes, as defined in expressions 9.4 and 9.3. With this tool it is possible to study several different dependencies of the resolution on the interesting physics parameters:

1. The value of the parameters
2. The size of the sample
3. The signal to background ratio

9.3.1 Background-Free Resolutions

In the following we will assume that ζ, $\bar{\zeta}$, Δm, Γ are known from some other measurement.
All the *toy experiments* have been carried on varying one of the parameters in a certain range, and keeping all the others at their *reference* values. These values are

Parameter	Value
Sample size	$300000\,evts$
Δm	$0.471\,ps^{-1}$
Γ	$0.651\,ps^{-1}$
ζ	0.3
$\bar{\zeta}$	0.3
ϵ	0.1
ρ	0.02
$\Phi = 2\beta + \gamma$	112°
ξ	0
$c\tau$ region	$[1, 4]\ ps^{-1}$
binning (for binned fit only)	$51\,bins$

Table 9.1: Reference values used for the toy simulations.

reported in table 9.1. For numerical reasons the fitted quantities are not the relevant physics quantities (ρ and Φ), but rather simple functions of them which have a clear role in equations 9.3 and 9.4: ρ^2 and $\frac{2\rho}{1+\rho^2} Sin\,(2\beta + \gamma)$. An additional parameter (a global normalization of the 4 fitted functions) is added in the case of binned fit.
Samples of toy measurements were generated varying, one at a time, each of the above mentioned parameters. The resulting conclusion is that in the explored range there's no appreciable dependency of the resolution on the measured quantities from the corresponding physics parameters.
Figure 9.3 shows the behavior of the deviation from the true value of the fitted parameters as a function of the parameter's value: for each value of the physics parameter being stepped, the experiment is repeated many times; each experiment produces a point in the resolution vs parameter plot. The contour plots of the resulting density distributions are reported.
The same distributions are shown both in the case of binned and unbinned fit.
The conclusion is that no correlation is present between the parameter's values and the fit resolution, both for the binned and unbinned fit in a wide range of the parameters about the reference values.

The dependency of the fitted parameter's resolutions on the binning in the case of a *binned* fit has also been explored. Figure 9.4 reports once again the density profile for the resulting fit resolution repeatedly calculated for a set of different binnings. The number of bins (x axis in the plots) is referred to the $[0, 12.5]\,ps$ region, while the fit region is still the one reported in table 9.1 For comparison, the average deviation from the true value of the same two parameters in the case of an unbinned fit (evaluated on the configuration reported in table 9.1) are: 0.017 for $\frac{2\rho}{\rho^2+1} Sin\,(\Phi)$ and 0.01 for ρ^2 (see figure 9.5). The resolutions depend on the binning. Comparing fig. 9.4 and fig. 9.5 we verify that the asymptotic value of the resolution on the fitted parameters for large number of bins extrapolates to the unbinned resolution. The unbinned fit thus looks the best choice as far as parameter determination is

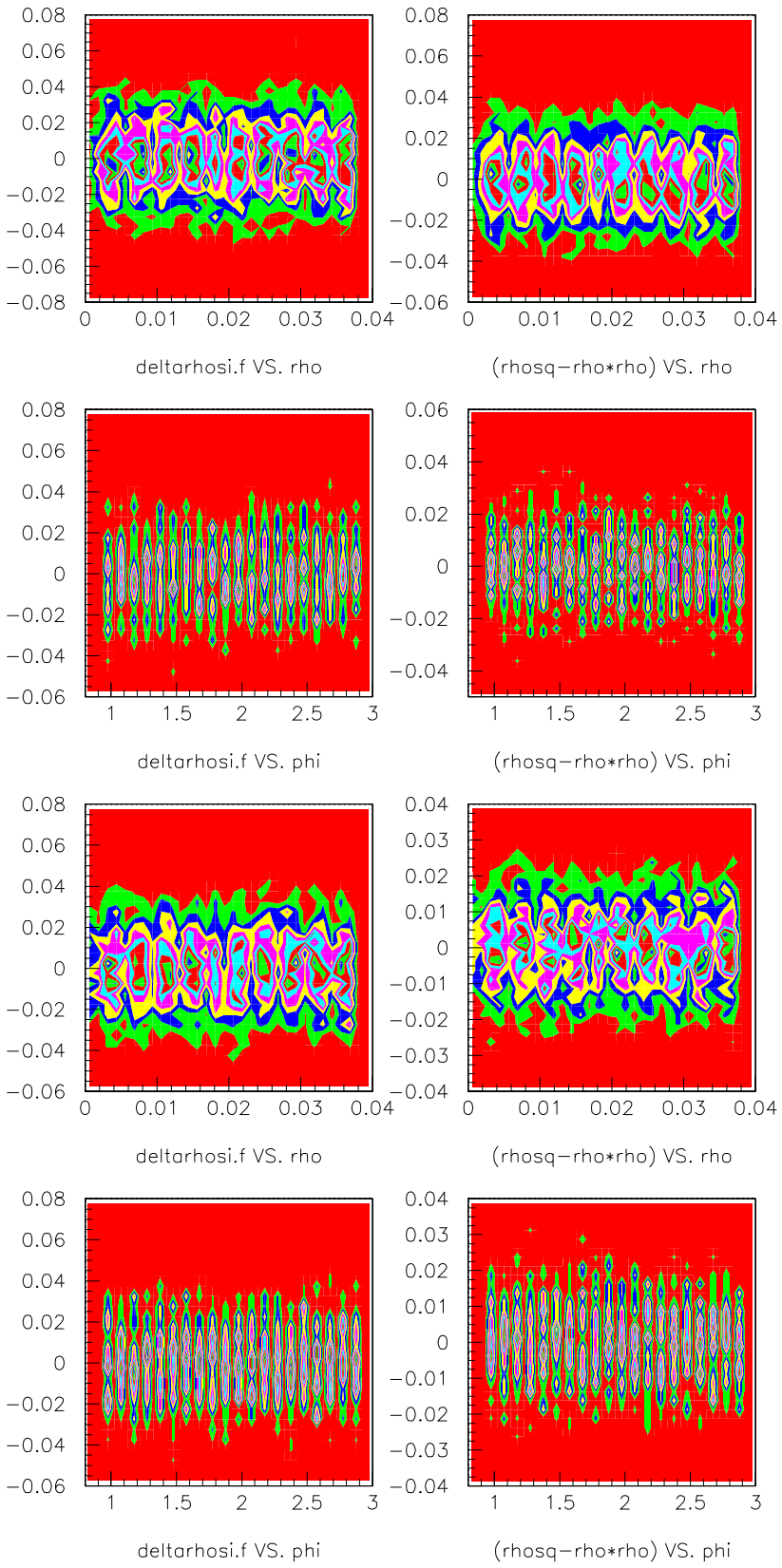

Figure 9.3: Distribution of the deviation from the true parameter value for ρ^2 (right column) and $\frac{2\rho}{\rho^2+1}Sin\,(\Phi)$ (left column) as a function of ρ (odd rows) or Φ (even rows). In the top two rows the binned fit is used, while the two bottom rows contain the corresponding plots in the case of unbinned fit.

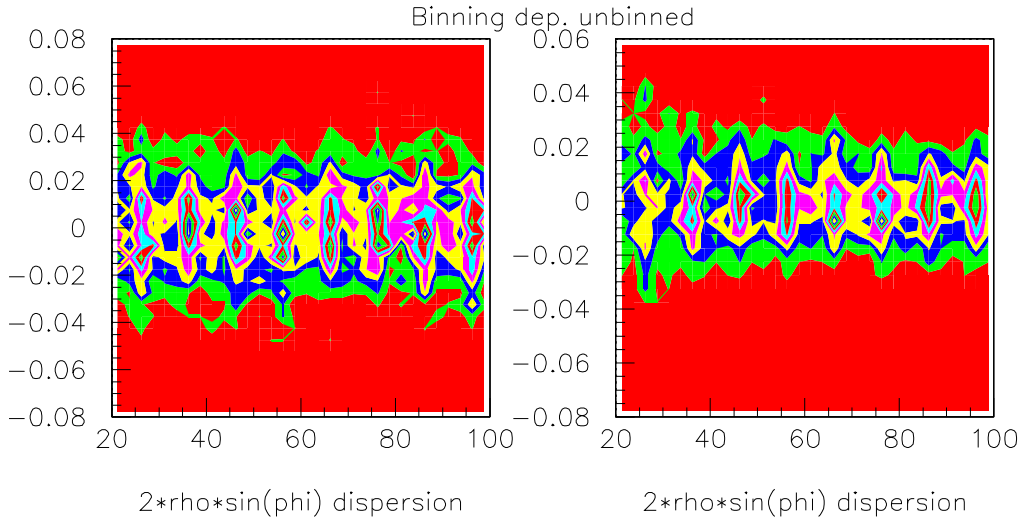

Figure 9.4: Contour plot for the toy montecarlo resolution on the fit parameters ρ^2 (right plot) and $\frac{2\rho}{\rho^2+1}Sin(\Phi)$ (left plot) repeatedly calculated for each value of the binning reported in abscissa.

concerned.

The size of the sample we expect to collect in $2\,fb^{-1}$ for $B_d(t) \to D^{(*)\mp}\pi^{\pm}$ is estimated to fall between about $10000 - 100000$ events using $B_d(t) \to D^{*\mp}\pi^{\pm}$ only, and raise up to about 300000 events when also $B_d(t) \to D^{\mp}\pi^{\pm}$ is included.
The fitted parameter resolutions decreases as the size N of the tagged sample grows. In fact this is expected to be roughly $\propto \frac{1}{\sqrt{N}}$. This is what has been checked in the last toy experiment, where the sample size has been logarithmically scaled. Figures 9.6 and 9.7 report the results of such simulation, respectively in the case of binned and unbinned fit.
The approximate behavior of the resolution is the expected one for all parameters and all types of fits. The resulting resolution is thus such that we will not certainly be able to measure ρ, but might allow an evidence of nonzero $\frac{2\rho}{\rho^2+1}Sin(\Phi)$. Moreover, the integration of a total luminosity of $30\,fb^{-1}$ would allow the sample size to increase by another factor 15, thus collecting roughly $5 \cdot 10^6$ events.

9.3.2 Background Effects

The parameter resolutions are expected to worsen due to the presence of a background of size S with a signal of size N. The behavior is expected to be roughly proportional to $\frac{\sqrt{S+B}}{S}$.
We consider a S/B ratio of about $1:1$ a safe assumption given that CDF has already been capable of reconstructing $B_d(t) \to D^{\mp}\pi^{\pm}$ in the Run I sample obtaining such background (see [138]). A more sound justification of this assumption will be

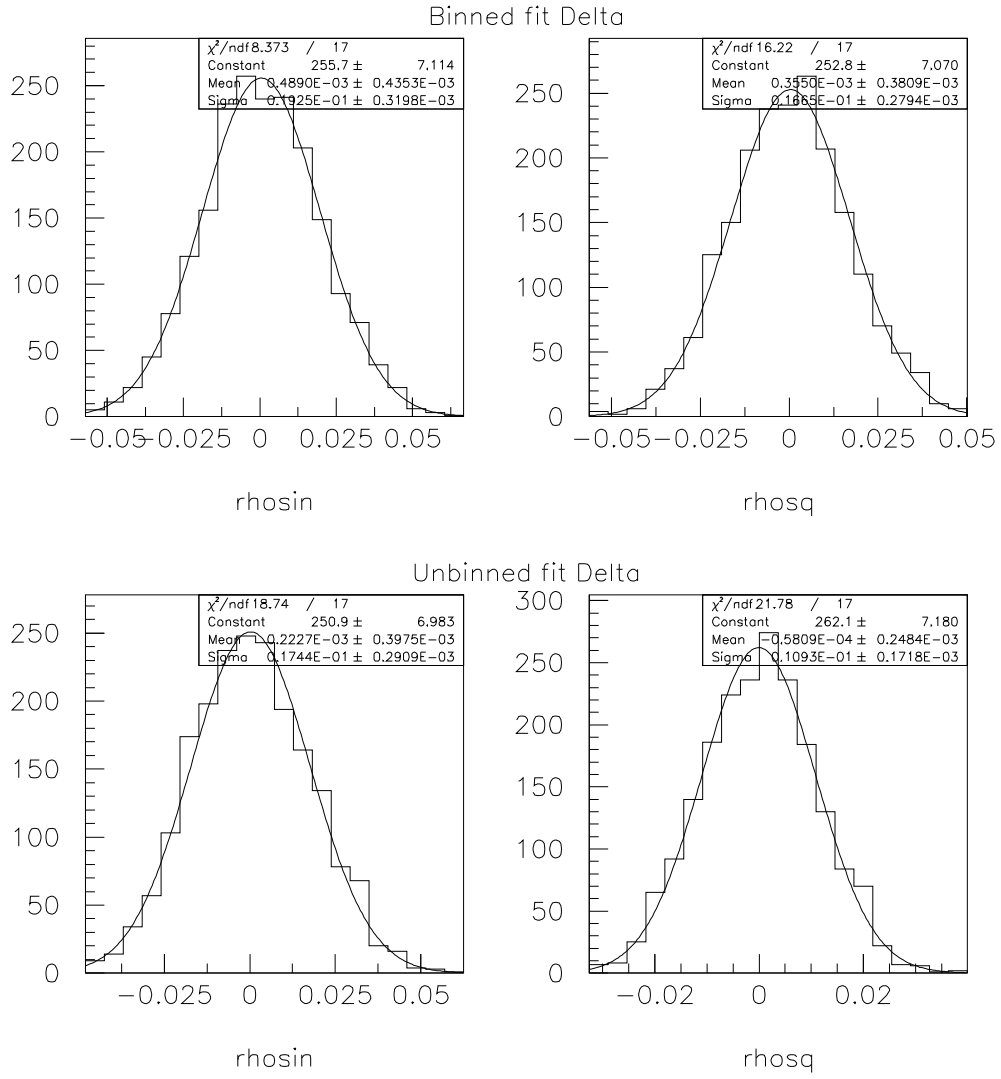

Figure 9.5: Deviation from the true value of the two fit parameters ρ^2 (right plot) and $\frac{2\rho}{\rho^2+1}Sin\,(\Phi)$ (left plot) calculated for a set of toy experiments configured as described in table 9.1.

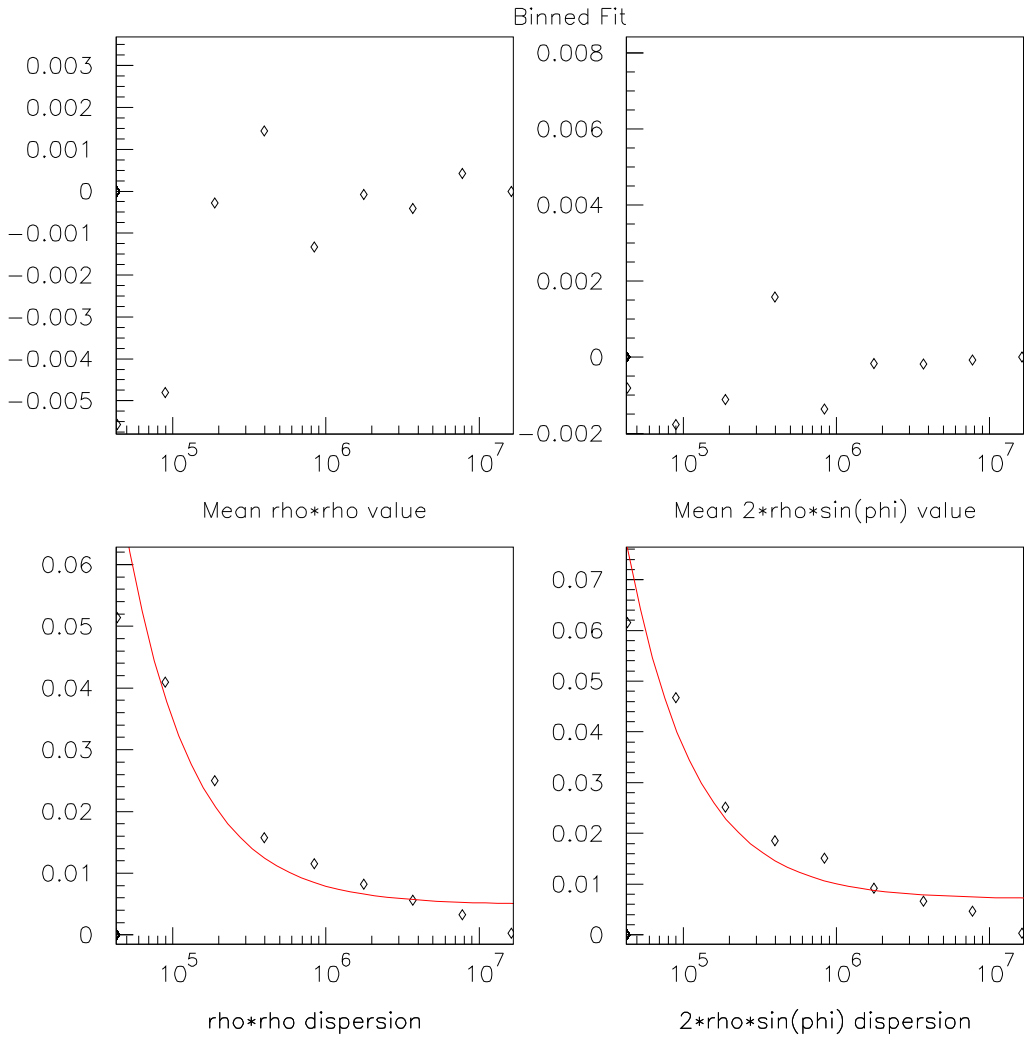

Figure 9.6: Evolution of the mean value (top plot) and the variance (bottom plots) of the deviation from the true value of the two fit parameters ρ^2 (left plot) and $\frac{2\rho}{\rho^2+1}Sin(\Phi)$ (right plot) calculated for a set of toy experiments at various sample sizes (x axis). All other parameters are given in 9.1. The y axis of the bottom plots reports the quantity scaled by a factor $\sqrt{2}$ to take into account the effect of a S/B ratio of about $1:1$ (see section 9.3.2). The x axis reports in all cases the number N of collected events at trigger level (and not ϵN)

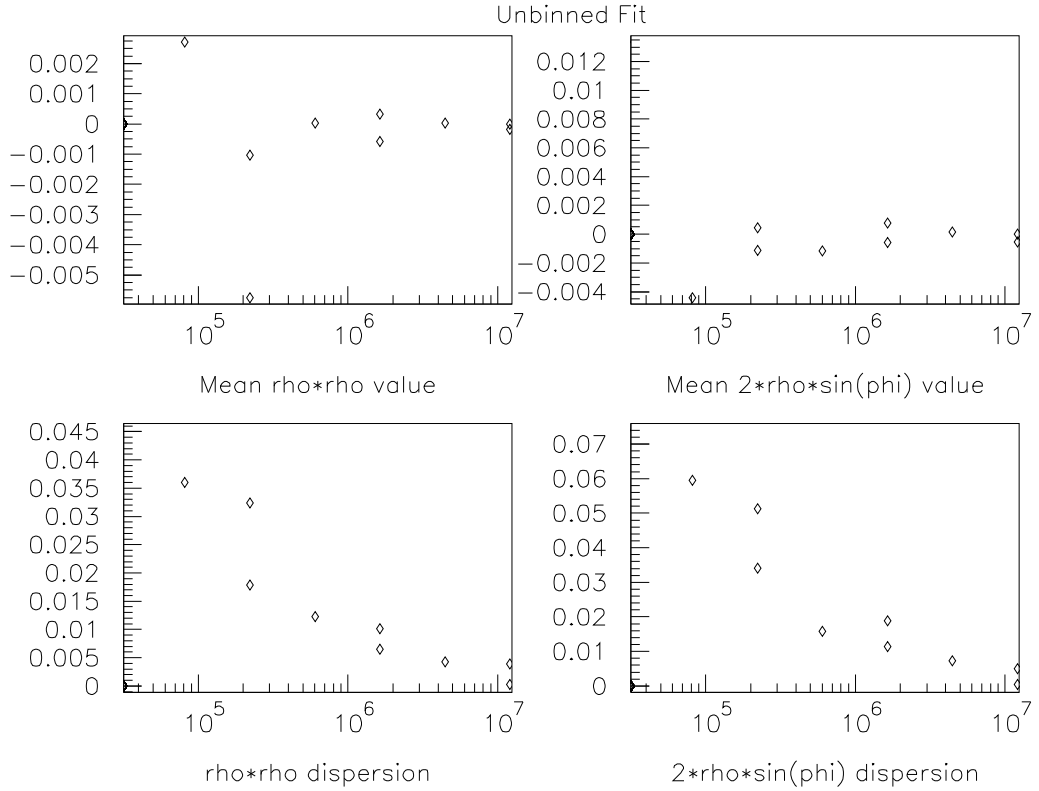

Figure 9.7: Evolution of the mean value (top plot) and the variance (bottom plots) of the deviation from the true value of the two fit parameters ρ^2 (left plot) and $\frac{2\rho}{\rho^2+1}Sin\,(\Phi)$ (right plot) calculated for a set of toy experiments at various sample sizes (x axis). All other parameters are given in 9.1. The y axis of the bottom plots reports the quantity scaled by a factor $\sqrt{2}$ to take into account the effect of a S/B ratio of about $1:1$ (see section 9.3.2). The x axis reports in all cases the number N of collected events at trigger level (and not ϵN)

however given in the next three chapters.
This means that we can roughly expect the fit resolution to worsen by a factor $1.4 \approx \sqrt{2}$ due to the presence of the background in $B_d(t) \to D^{(*)\mp}\pi^{\pm}$. This factor has already been taken into account in the vertical scales of figures 9.6 and 9.7.

Note also that it is reasonable to expect a smaller background where a D^* is involved, due to the narrow $m_{D^{*\pm}} - m_{D^{\pm}}$ difference.

9.3.3 Input Parameters

Equations 9.3 and 9.4 clearly require a knowledge of other physics inputs which *a priori* might induce a critical bias in the fit results.
I thus tried to quantify this effect studying the mean value and width of the residual distribution for the most interesting fit parameter (nominally $2\frac{\rho}{1+\rho^2}Sin(\Phi)$) in various toy experiments.
The most critical parameters are ζ, $\bar{\zeta}$ and ξ. For each of them in fact the fit requires an input value which plays a critical role in equations 9.3 and 9.4 and thus in the fit.
Two set of experiments in which the measurement is repeatedly performed varying either ξ or $\left(\zeta, \bar{\zeta}\right)$ and keeping the other quantities at their reference value (see table 9.1) show that both the bias and the resolution effects are negligible in our case.
Figure 9.8 shows the results of the study on the ξ dependency of the fit, shown as the measured mean value and width of the fitted parameter deviation from the true input value.
Figure 9.9 shows the deviation from the true value of $2\frac{\rho}{1+\rho^2}Sin(\Phi)$ as ζ and $\bar{\zeta}$ vary in a wide range of values (from 0 to 0.5).
From these studies we conclude that the assumption $\xi = 0$ is rather safe in the expected parameter range, and that a knowledge of ζ and $\bar{\zeta}$ of the order of $5 - 10\%$ is sufficient.

9.4 Conclusions

A parametric study for the feasibility of measuring $2\beta+\gamma$ from the $B_d(t) \to D^{(*)\mp}\pi^{\pm}$ decay has been performed. We expect to collect roughly 10^5 of these events in Run II with a total integrated luminosity of $2\,fb^{-1}$ and about $5 \cdot 10^6$ when $30\,fb^{-1}$ are integrated.
Even if this is probably the largest exclusive hadronic B decay that CDF will collect in Run II, the expected asymmetry is very small and close to the final experimental resolution: assuming a S/B ratio of $1:1$ the parameter $\frac{2\rho}{\rho^2+1}Sin(2\beta+\gamma)$ will be measured with a resolution varying from 1% to 5% (independently from the parameters values) where the expected value is 4% in the case of maximal CP violation within the SM.
At this level the measurement is still limited by statistics, while the input parameters determination shouldn't be critical in the fit.

On the other hand, the tiny and probably unmeasurable CP violation effects

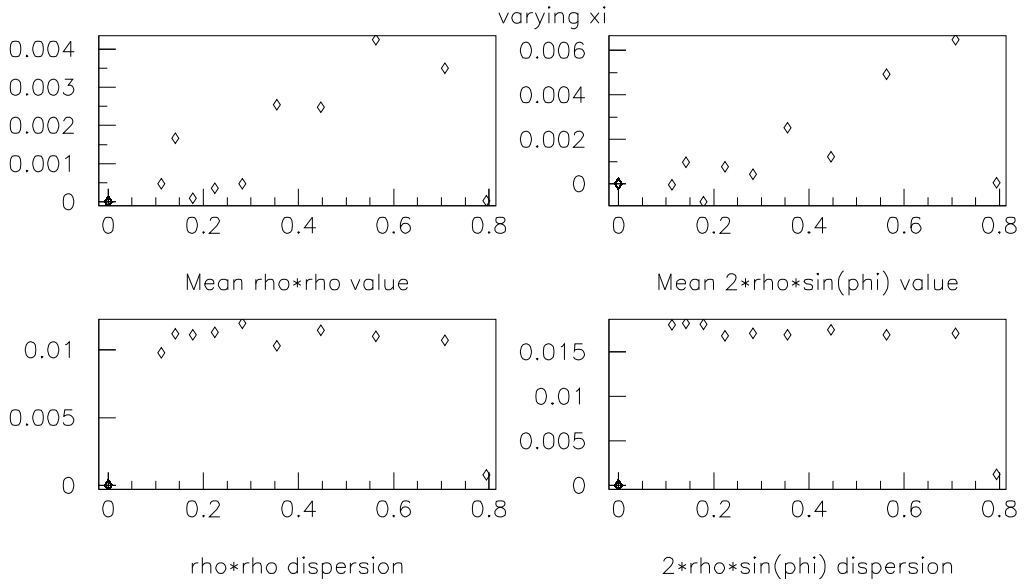

Figure 9.8: Mean value (top plots) and width (bottom plots) of the deviation from the input value of ρ^2 and $2\frac{\rho}{1+\rho^2}Sin\,(\Phi)$ as ξ is changed (x axis).

make this big exclusive sample a good candidate for performing dilution,tagging and efficiency studies in the two track trigger sample.

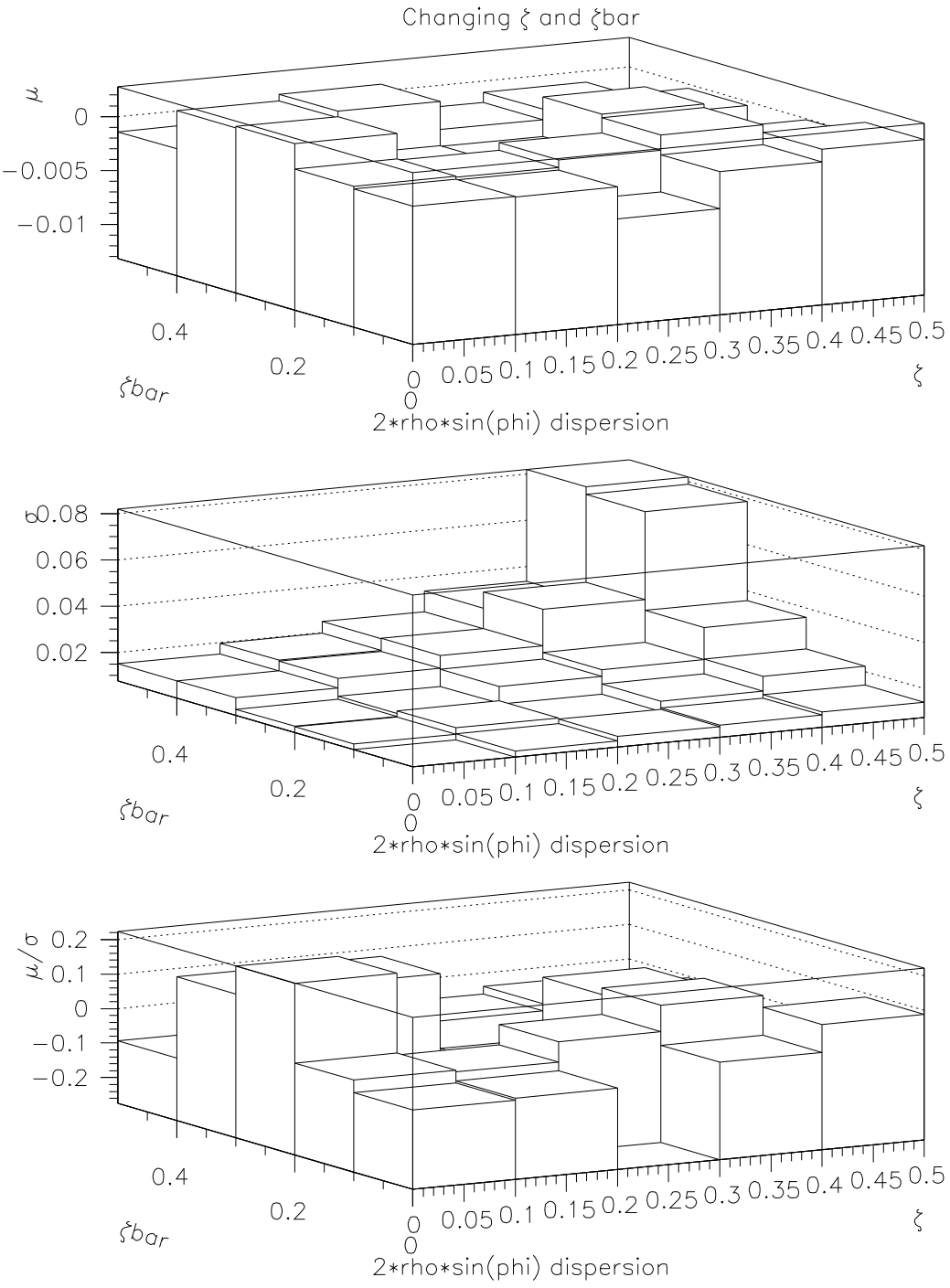

Figure 9.9: Mean value μ (top) width σ (center) and μ/σ of the deviation from the input value of $2\frac{\rho}{1+\rho^2}Sin\,(\Phi)$ as ζ and $\bar{\zeta}$ are changed (x and y axis).

Chapter 10

Background Estimates for $B_d(t) \to D^{(*)\mp}\pi^{\pm}$

The largest uncertainty in the study performed in chapter 9 comes from the fact that we have no firm estimate for the achievable signal to background ratio for the decay mode $B_d(t) \to D^{(*)\mp}\pi^{\pm}$. The purpose of this chapter is to obtain an estimate from the data at hand.
There are currently 2 two different ways to estimate the S/B ratio we are interested in. The first one, presented in section 10.1, comes from the observation of B decay modes similar to $B_d(t) \to D^{(*)\mp}\pi^{\pm}$. The other method (section 10.2) is based on a direct search on Run I with Run II-like requirements. This search covers many different charm decays of the B meson, including $B_d(t) \to D^{(*)\mp}\pi^{\pm}$.
Both methods are based on the same trigger sample, requiring a single inclusive lepton of transverse momentum ranging between $5\,GeV/c$ and $8\,GeV/c$.

10.1 Hadronic B Signals in Run I

Hadronic B decays have recently been observed in Run I data [139]. They are the $B^{\pm} \to D^{\circ}\pi^{\pm}$ and $B_d \to D^{+}\pi^{-}$ modes. For the sake of our study we will be mainly interested in the neutral B decay (cf. section 10.1.4).
We will first discuss the sample preselection, common to both modes, and then we will detail each search separately.

10.1.1 The Inclusive Lepton Sample

The inclusive electron and muon samples are the basis for most of the CDF I searches in B physics. These samples are selected at trigger level by requiring the presence of a rather stiff ($5 - 8\,GeV/c$) track corresponding to either a segment tracked by the central muon detector or a significant energy release in the electromagnetic calorimeter. Simulations suggest that about 20% of these leptons come from b decays (see section 6.6). The total integrated luminosity of the inclusive lepton sample in Run I is about $101\,pb^{-1}$ both for the muon and electron data set.
Quality requirements are then applied to the trigger lepton. The only sample so far

examined for this search has been the inclusive electron sample because it is known to be much cleaner than that of the inclusive muon sample (electron identification in CDF is more accurate than muon identification). We will thus describe the electron selection criteria.
Central electrons in CDF I are identified using the information from the electromagnetic calorimeter, a set of strip (measuring the Φ position) and wire chambers (measuring the z position) placed between the outer side of the COT and the electromagnetic calorimeter (*pre-shower* detector) and at about 6 radiation lengths (*shower* detector). These detectors are used to measure the position and lateral profile of the shower in ϕ and z. Standard quality cuts include the matching of the extrapolated track seen by the tracking system to the preshower and shower detectors. Calorimetric quantities are also checked, comparing the energy released in the hadronic calorimeter to that released in the electromagnetic calorimeter and the contamination of the adjacent electromagnetic towers. The set of cuts used is:

- $P_t^e \geq 8\,GeV/c$
- $\frac{Hadronic\,Energy}{Electromagnetic\,Energy} < 0.04$
- Distance between the track extrapolation to the shower-max detector and the shower energy centroid $\Delta x < 1.5\,cm$
- Same as above but in the z direction: $\Delta Z < 3.0\,cm$
- $\chi^2_{strip} < 10.0$: this is the quality cut on the fit to the electromagnetic shower profile in the strip (ϕ) chamber
- $\chi^2_{wire} < 10.0$: this is the quality cut on the fit to the electromagnetic shower profile in the wire (z) chamber
- The fraction of energy released by the shower in electromagnetic towers other than the one the track points to is required to be small: $L_{shr} < 0.2$

These are the standard requirements for a good quality electron in CDF Run I. Since in this study the electron is assumed to be a "spectator" (i.e. a product of the "opposite side" b decay) in the search for the exclusive decays (which are totally hadronic), no stricter requirement is applied for this particle: in particular track quality requirements (e.g. silicon hits) are not imposed.

10.1.2 A Charged B Decay With Charm

The charged mode reconstruction is performed in three steps:

- lepton validation
- D° search
- Candidate B search

All selection cuts have been chosen to maximize the significance $\frac{S}{\sqrt{S+B}}$ on a montecarlo sample representing the signal S and a sideband interpolation in order to estimate the background B from the real data.

Candidate D° mesons are identified in [139] requiring the raw candidate mass to be within $\pm 200 MeV/c$ of the D° mass. The $K\pi$ pairs selected in this way and the resulting candidate D meson are required to satisfy:

- $P_t^D \geq 2\, GeV/c$
- $0.25\, cm > c\tau_D > 0.01\, cm$
- $P_t^K \geq 0.6\, GeV/c$
- $P_t^\pi \geq 0.5\, GeV/c$
- (Number of silicon hits from the K) + (number of silicon hits from the π) $\geq$ 3
- χ^2 probability for the mass constrained fit $> 0.1\%$

The D° mesons selected in this way are matched with π candidates to form possible B^+ mesons. The requirements applied to the B^+ combinations are:

- $P_t^\pi \geq 0.7\, GeV/c$
- Number of silicon hits for the non D° pion ≥ 3
- Maximum z separation between the B decay products $\leq 4\, cm$
- $P_t^B \geq 7\, GeV/c$
- $0.2\, cm > c\tau_B > 0.01\, cm$
- Transverse decay length of the B meson $L_{xy}^B \geq 0.03\, cm$
- Separation from the trigger lepton: $\Delta\Phi_{B-lepton} \geq 78^\circ$
- Isolation of the B meson: for all tracks in $\Delta R = \sqrt{\Delta\eta^2 + \Delta\Phi^2} \leq 1$

$$r = \frac{P_t^B}{P_t^B + \Sigma_{i=1}^n P_t^i} \geq 0.4$$

- χ^2 probability for the B decay fit with mass-constraint on the $D^\circ > 0.1\%$

The result of this search in the electron sample is reported in figure 10.1 with the invariant mass distribution for the candidate B mesons. The B signal is searched by directly fitting the B mass distribution with an unbinned Gaussian signal plus linear background model (either fixing or releasing the average B mass and width). A signal of about 8 ± 4 events is found.

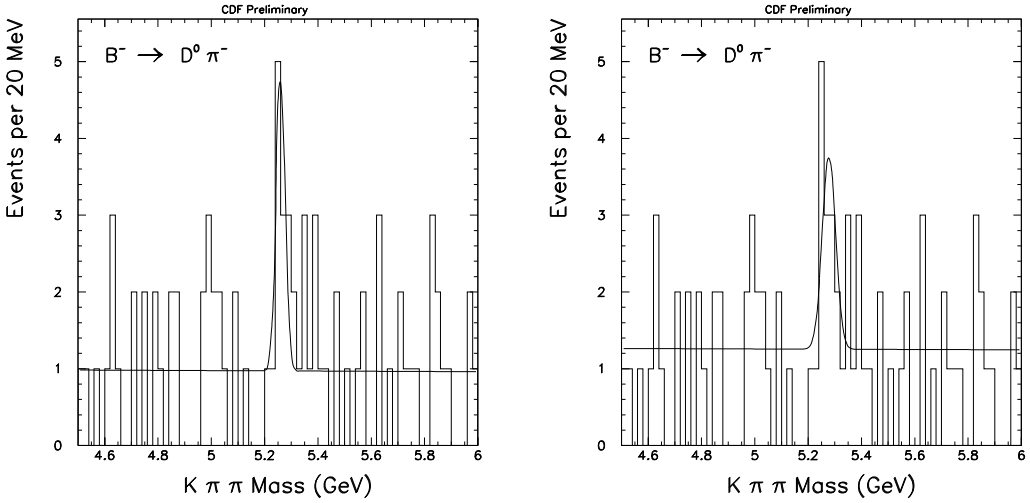

Figure 10.1: Fit to the invariant mass distribution for the candidates $B^{\pm} \to D^{\circ}\pi^{\pm}$ with $D^{\circ} \to K\pi$. The left plot shows the free linear+Gaussian fit. The mean of the Gaussian is $5.26^{+0.01}_{-0.009}\,GeV/c^2$ and the width is $0.017^{+0.01}_{-0.008}\,GeV/c^2$. The number of signal events is $8.1^{+3.8}_{-3.5}$. The right plot shows the unbinned fit results. The fit is performed fixing the mean of the Gaussian at the PDG mass of the B° ($5.279\,GeV/c^2$) and the width at the resolution expected by the simulation of the same decay ($0.025\,GeV/c^2$). The number of signal events is $9.5^{+4.0}_{-3.5}$.

10.1.3 Another B Decay With Charm

An analogous search is performed on the same sample for evidence of $B^{\circ} \to D^{+}\pi^{-}$ with $D^{+} \to K^{-}\pi^{+}\pi^{+}$. The optimized charged D selection criteria are similar to the previous ones:

- $P_t^D \geq 3\,GeV/c$
- $0.2\,cm > c\tau_D > 0.0125\,cm$
- $P_t^K \geq 0.6\,GeV/c$
- $P_t^{\pi_1} \geq 0.4\,GeV/c$
- $P_t^{\pi_2} \geq 0.4\,GeV/c$
- Number of silicon hits from the K+number of silicon hits from the two $\pi \geq 3$
- χ^2 probability for the mass constrained fit $> 0.01\%$
- Maximum z separation between the D^{+} decay products $\leq 3.5\,cm$

Also the B search is performed with very similar cuts:

- $P_t^{\pi} \geq 0.9\,GeV/c$

- Number of silicon hits for the non-D^+ pion ≥ 3
- Maximum z separation between the B decay products $\leq 4\,cm$
- $P_t^B \geq 7.5\,GeV/c$
- $0.2\,cm > c\tau_B > 0.01\,cm$
- Transverse decay length of the B meson $0.5\,cm \geq L_{xy}^B \geq 0.025\,cm$
- Separation from the lepton: $\Delta\Phi_{B-lepton} \geq 78^\circ$
- Isolation of the B meson: for all tracks in $\Delta R = \sqrt{\Delta\eta^2 + \Delta\Phi^2} \leq 1$

$$r = \frac{P_t^B}{P_t^B + \Sigma_{i=1}^n P_t^i} \geq 0.5$$

- χ^2 probability for the B decay fit with mass constraint on the $D^\circ > 0.01\%$
- Electron transverse momentum $P_t^e \geq 9\,GeV/c$

The result is reported in figure 10.2 with the invariant mass distribution for the candidate B mesons. The B signal is searched by directly fitting the B mass distribution with an unbinned Gaussian signal plus linear background model and leaving the candidate B mass and width fixed (right plot) or floating (left plot). A signal of about 5 ± 4 events is found.

10.1.4 Extrapolation to $B_d\,(t) \to D^{(*)\mp}\pi^\pm$

The mentioned charm decay modes are strictly connected to the one we are studying. In particular, the final state of the neutral (section 10.1.3) mode is equal to that of our signal. Given the fact that $B_d\,(t) \to D^{(*)\mp}\pi^\pm$ has a slightly different topology but another very narrow resonance to rely on, we expect a similar analysis to produce better signal efficiency with comparable or better signal to background ratio. The narrow $D^* - D^\circ$ mass difference resonance is in fact a powerful discriminant between signal and background which will somewhat enhance the $B_d\,(t) \to D^{(*)\mp}\pi^\pm$ efficiency with respect to $B_d \to D^+\pi^-$.
A first rough estimate of the achievable $B_d\,(t) \to D^{(*)\mp}\pi^\pm$ signal to background ratio is thus obtained assuming the same S/B of the reconstructed $B^\circ \to D^+\pi^-$, obtained from figure 10.2. In the left plot we count 38+27 events in the two sidebands $[4.8, 5.2]\ GeV/c^2$ and $[5.4, 5.8]\ GeV/c^2$. The width of the fitted Gaussian is $\sigma \approx 0.017 \pm 0.013$ which yields an estimate of the background sitting below a $\pm 3\sigma$ interval around the Gaussian center of 8.3 ± 6.4 events. The corresponding S/B ratio is 0.78 ± 0.77.
From the right plot a similar calculation yields a S/B ratio of 0.44 ± 0.37.

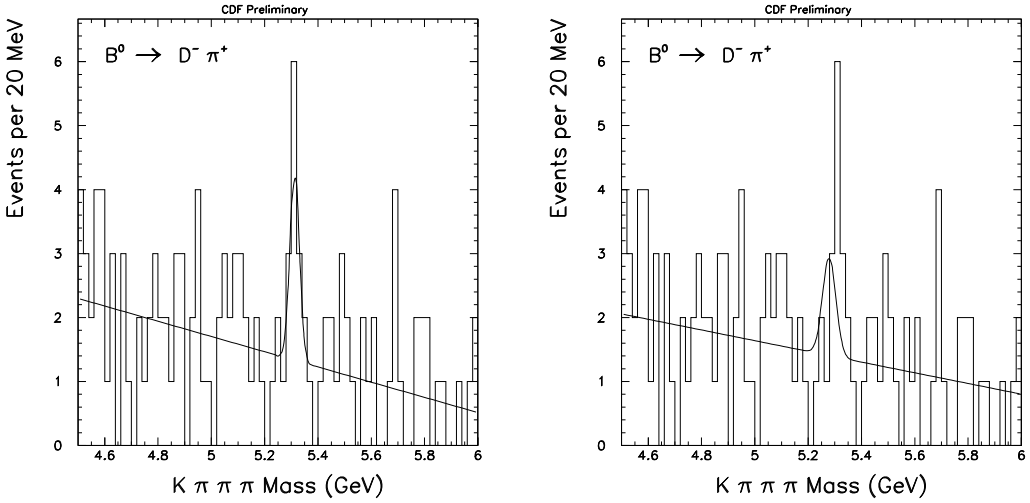

Figure 10.2: Fit to the invariant mass distribution for the candidates $B_d \to D^+\pi^-$ with $D^+ \to K^+\pi^-\pi^-$. The left plot shows the free linear+Gaussian fit. The mean of the Gaussian is $5.31^{+0.01}_{-0.02}\,GeV/c^2$ and the width is $0.017^{+0.012}_{-0.013}\,GeV/c^2$. The number of signal events is $4.8^{+3.9}_{-3.3}$. The right plot shows the unbinned fit results. The fit is performed fixing the mean of the Gaussian at $5.279\,GeV/c^2$ and the width at $0.025\,GeV/c^2$. The number of signal events is $4.8^{+3.9}_{-3.3}$.

10.2 Run II Projections From Run I Data

A search for generic charmed B decays has been performed on the same sample discussed in section 10.1 in order to estimate the Run II possibilities. The study [140] is basically a broad search for B resonances decaying to reconstructed charm and n pions in the inclusive lepton sample of Run I. No particular fine tuning was performed and no evidence for $B \to D\,n\pi$ could be claimed.
The interest in this study lies in the fact that the set of cuts performed is very close to that planned for the two track trigger sample:

- The lepton in the sample is excluded from the search and the search was performed in the *away side* from the trigger lepton, requiring the tracks to sit in the $\Delta\Phi_{track-lepton} > 90°$ region
- $|\Delta z| < 5\,cm$ is required among the candidate B daughters
- $D° \to K\pi$ is searched in the sample, with *SVT-like* cuts:
  - $\left|\frac{d}{\sigma_d}\right| > 1$ for both the kaon and the pion, which means a large impact parameter deviation from 0
  - The $D°$ candidate mass is required to sit in the range $[1.84, 1.88]\ GeV/c^2$
- A soft pion ($P_t > 0.2\,GeV/c$) is added to the $D°$ in order to form the D^*

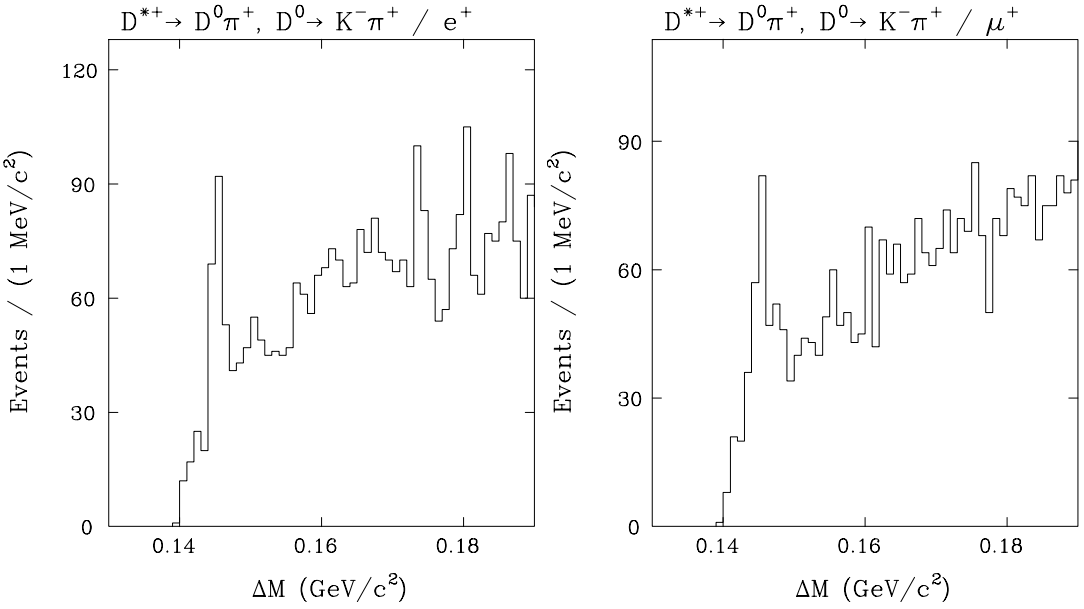

Figure 10.3: $m(D^*) - m(D)$ mass difference distribution in the inclusive electron (left) and inclusive muon (right) samples.

- The D^* candidate mass is required to sit in the range $[0.144, 0.147]$ GeV/c^2 from the candidate D° mass
- The proper decay length ct of the candidate B meson is required to be larger than $100\,\mu m$

The d/σ and the ct cuts mimic in fact the behavior of the two track hadronic trigger. The result of the $B_d(t) \to D^{(*)\mp}\pi^{\pm}$ search are 3 (1) events in the inclusive electron (muon) sample sitting in the range $[5, 5.6]$ GeV/c^2 for the $B_d(t) \to D^{(*)\mp}\pi^{\pm}$ mode. Both samples show a narrow $m(D^*) - m(D)$ peak of about 150 events each (figure 10.3).

10.2.1 Extrapolation to $B_d(t) \to D^{(*)\mp}\pi^{\pm}$

An estimate of the S/B ratio is not so easy since we have no signal evidence from the sample.
Let's start from the D^* sample reconstructed in this analysis. About 150 D^* are seen in the electron channel plus a similar amount in the muon channel. About 70% of those should come from B decays if we assume $f_{c\bar{c}} \approx 0.3$. Assuming an analysis efficiency $\epsilon \approx 0.7$ and using the PDG branching fractions, we find out that the expected number of $B_d(t) \to D^{(*)\mp}\pi^{\pm}$ is approximately:

$$N\left(B_d(t) \to D^{(*)\mp}\pi^{\pm}\right) = n(D^*) \times \epsilon \times (1 - f_{c\bar{c}}) \times \frac{\mathcal{B}\left(B_d(t) \to D^{(*)\mp}\pi^{\pm}\right)}{\mathcal{B}(B \to D^* X)} \approx 0.02$$

Let's assume that the reconstructed B width is the same as the one measured in section 10.1: $0.025\,GeV/c^2$. A $\pm 3\sigma$ window about the B mass yields about 0.75

signal events expected in the electron sample and 0.25 in the muon sample. This translates in a S/B ratio of about 1/40 from the electron sample and 1/10 from the muon sample and is in good agreement with no observation.

10.3 Conclusions

From the Run I studies performed so far we can draw that the expected S/B ratio for the $B_d(t) \to D^{(*)\mp}\pi^{\pm}$ decay should sit somewhere between 1/6 and 3/4. However, we should bear in mind two important facts: the first one is that the error on these estimates are very large, close to 100%. The other is that none of these analyses is really optimized for our search: the charmed decay of section 10.1.4 is identical to $B_d(t) \to D^{(*)\mp}\pi^{\pm}$ in terms of final state particles, but less powerful in terms of discriminating variables. This suggests that an optimization of the cuts in our specific case might yield better S/B ratios and probably even better signal efficiency. The study described in sections 10.2 and 10.2.1 has the advantage of being somewhat directed to the specific search of $B_d(t) \to D^{(*)\mp}\pi^{\pm}$. The signal yield estimate is however very poor and the analysis cuts are poorly optimized and thus improvable.
We therefore insist that an optimized analysis might be able to achieve a performance in terms of signal to background ratio of the order of 1/1.

Chapter 11

An Optimized $B_d(t) \to D^{(*)\mp}\pi^{\pm}$ Search in Run I Data

All the searches for hadronic decays of the B meson but those for the $D^{\circ}\pi^{+}$ and $D^{+}\pi^{-}$ have not been really optimized in CDF Run I.
Performing this optimization for $B_d(t) \to D^{(*)\mp}\pi^{\pm}$ is worth for several reasons: first of all to obtain the best achievable estimate of the S/B ratio in the Run I sample and a projection for Run II. The second reason is the opportunity of identifying better discriminants between signal and background while performing a preliminary fine-tuning of the analysis cuts. A third reason is, of course, the possibility of actually seeing a signal.
The first part of this chapter deals with a first rough estimate of the signal. After that we will detail the strategy for the fine tuning of the analysis cuts and describe in detail the real and simulated samples used. We will then describe the process of cut optimization, identifying the final analysis cuts, the efficiency of this analysis on the sample, the signal yield and S/B projections.

11.1 Signal Yield Estimate

We already know that the inclusive lepton sample contains the largest number of $b\bar{b}$ pairs in a single CDF I data stream (see section 10.2.1). Since the number of expected signal events is rather small (see section 10.2.1) we choose to tune our search on this sample.

To roughly estimate the signal in the inclusive lepton data set we assume that out of $5 \cdot 10^6$ events 20% are $b\bar{b}$. One of these quarks is assumed to decay leptonically, while $\approx 37.5\%$ of the opposite side b quarks give a B_d or a $\bar{B}_d$. This leaves us with roughly $4 \cdot 10^5$ B_d mesons. The combined branching ratio for the chain $B_d \to \pi D^* \to \pi D^{\circ} \to K\pi$ is obtained from the latest PDG information:

$$\mathcal{B} = (2.76 \pm 0.21) \cdot 10^{-3} \times (67.7 \pm 0.5) \cdot 10^{-2} \times (3.83 \pm 0.09) \cdot 10^{-2} = (7.16 \pm 0.57) \cdot 10^{-5}$$

This thus gives us about 30 $B_d \to \pi D^* \to \pi D^{\circ} \to K\pi$ events in the sample. Assuming a signal efficiency of about 5% (just like in the $B \to D^{+}\pi^{-}$ analysis), we draw an expected signal size of 1.4 events.

11.2 Analysis Strategy

Given the small signal expected, we will not be able to see a significant signature of this decay mode. Cut optimization and the refinement of all the tools necessary to a true analysis will however give us a better understanding of what we can expect from Run II. The analysis will be divided in three steps, described in the next three sections: first we will focus on the data sample and on the generation of the simulated signal. A first rough reconstruction attempt will then be performed on a sample of D^* selected from the inclusive electron sample: this will give us a feeling for the performance and quality of our reconstruction algorithm. We will then optimize the choice of the analysis cuts and estimate both the signal acceptance and background rejection. The last step will then be the application of these criteria to the full data sample available.

11.3 The Data Sample

In order to perform a good optimization of the analysis cuts we need both a good background sample and a clean signal sample. The former is very difficult to model and we thus choose to rely on the real data. The simulated signal is rather simpler to obtain: most of the care will be put in the selection of a sensible set of generation parameters and preselection cuts.

11.3.1 The Inclusive Lepton Sample

The data sample we will rely on has been collected in Run Ib (1992-1996) requiring the presence of a single high P_t lepton and no other cuts. The transverse momentum cut for the lepton ranges between 6 and $8\,GeV/c$ (see figure 11.1). In order to gain independence from the momentum threshold turn-on of the trigger, we will preselect the lepton requiring a momentum larger than $8\,GeV/c$. The trigger lepton will be interpreted as a decay product of the away side b quark (that is, the one which is not candidate for the $D^*\pi$ reconstruction). From the past CDF experience [141] we know that candidates originating from the b quark *opposite* to the one producing the trigger lepton will be preferentially in the opposite hemisphere with respect to the trigger lepton. In order to reduce the combinatorics in the search for our signal we choose to preliminarly exploit this feature, restricting the signal search to tracks well separated from the trigger lepton. Figure 11.2 shows the distribution of $\Delta R_{t-\ell}$ for the 4 decay products of the B_d meson superimposed to the $\Delta R_{t-\ell}$ distribution for the *background* sample $\left(\text{the variable } R \text{ being defined as usual: } \Delta R = \sqrt{(\Delta\Phi_{t-\ell})^2 + (\Delta\eta_{t-\ell})^2}\right)$. These distributions come from a simulated signal sample (the one described in section 11.3.2) and a subset of the data sample used in the analysis. Requiring the tracks to sit in the range $\Delta R > 2$ from the lepton allows a first effective skimming of the data sample.

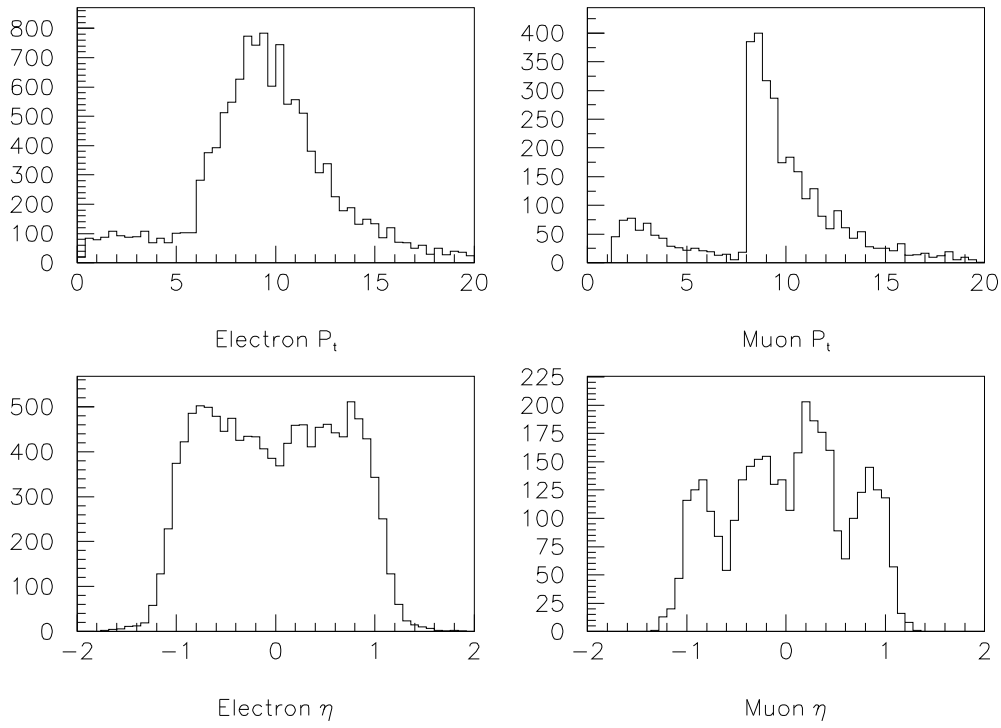

Figure 11.1: Transverse momentum (top) and rapidity (bottom) distribution for the lepton in the inclusive electron (left) and muon (right) samples collected in CDF Run Ib.

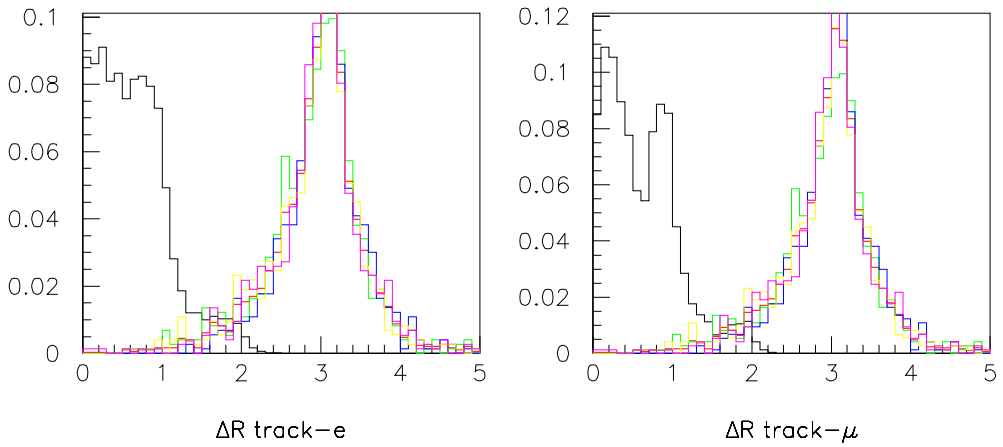

Figure 11.2: $\Delta R = \sqrt{(\Delta\Phi_{t-\ell})^2 + (\Delta\eta_{t-\ell})^2}$ distribution for the inclusive lepton data sample (leftmost distribution in both figures) and for the 4 decay products in the simulated signal sample (4 rightmost superimposed distributions in both the left and right figures). The left figure is for the inclusive electron sample, while the right one is for the inclusive muon.

11.3.2 The Montecarlo Sample

In order to have a good understanding of the features of the signal, we need to produce a large-enough simulated sample of signal with features as close as possible to the ones of the true $D^*\pi$ events which pass the inclusive lepton trigger.
The raw signal generation is performed using PYTHIA [131] version 6.115. Events with at least a B_d or a $\bar{B}_d$ are selected. Either the B_d or the $\bar{B}_d$ (in turn) are forced to decay in the corresponding Cabibbo allowed $D^{*-}\pi^+$ mode, while the opposite b quark is required to decay semileptonically after hadronization.
The final montecarlo file needs to contain both the case in which the b decayed semileptonically while the B_d decayed through the completely forced $D^*\pi \to D\pi\pi \to K\pi\pi\pi$ chain and the CP conjugated case in which the $\bar{b}$ decayed semileptonically while the $\bar{B}_d$ decayed through the completely forced $D^*\pi \to D\pi\pi \to K\pi\pi\pi$. This is achieved in two separate generations. The first generation step selects semileptonic b decays and forces[1] :

- every B_d to decay to $D^{*-}\pi^+$
- every D^{*-} to decay to $\bar{D}^\circ\pi^-$
- every $\bar{D}^\circ$ to decay to $K^+\pi^-$

[1]Note that following the method described even D^* and D° produced by other means than $B \to D^*\pi$ are forced as well. The montecarlo sample will be primarily used to measure the event yield and in this perspective this is a small effect. We choose not to address this problem for the sake of simplicity.

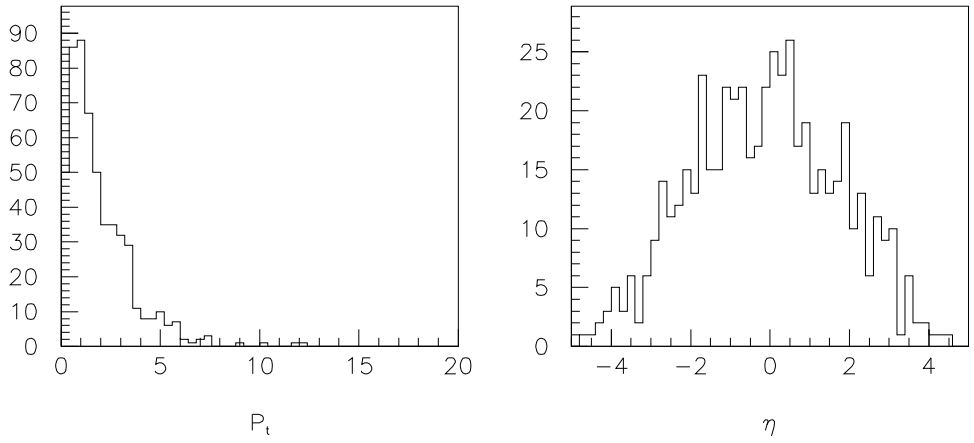

Figure 11.3: Lepton transverse momentum (left) and rapidity (right) distribution for semileptonic b decays filtered with the selections described in 11.3.2 but removing the lepton acceptance restrictions and generating b events with loose P_t and η requirements.

the CP conjugated modes of those in this list are not forced in this case.
The second generation step selects the CP conjugated with semileptonic $\bar{b}$ and then forces **only** the CP conjugated modes of those reported in the previous list.

The two resulting simulated samples are then merged together and treated as a single montecarlo file with larger statistics. This has the advantage that we don't need to force simultaneously the D^* and the $\bar{D}^*$ decays (and similarly for the D and $\bar{D}$) in each subsample, making the simulated events closer to reality.

The generated events are filtered requiring the effective presence of a B_d decaying along the correct chain and the presence of a lepton of high enough ($8\,GeV/c$) transverse momentum. The result is then fed to a parametric simulator of the $CDFI$ detector and events are selected on the basis of the presence of a lepton passing requirements equivalent to those of the inclusive lepton trigger.
In order to obtain an efficient production of decays successfully passing through all the described machinery, we need to perform a tuning of the ranges of momentum and rapidity in which the b quarks are produced. Trigger leptons are "central" and "stiff", that is must satisfy $|\eta| \leq 1.2$ and $|P_t| \geq 8\,GeV/c$.
Producing unbiased b events in PYTHIA would result in a lepton momentum and η distribution as the ones reported in figure 11.3 which are clearly very inefficient for our acceptance cuts. On the other hand, generation cuts cannot be set too "central" or "stiff" because this would result in a distortion of the kinematical distributions of the b quark. The final choice has been to produce b quarks in the ranges $|\eta| \leq 3$ and $\hat{P}_t \geq 4$. Figure 11.4 shows the resulting b η and P_t distributions in the montecarlo sample after the requirement that the lepton is identified in the detector with large enough P_t. These look consistent with the cuts imposed at generator level and

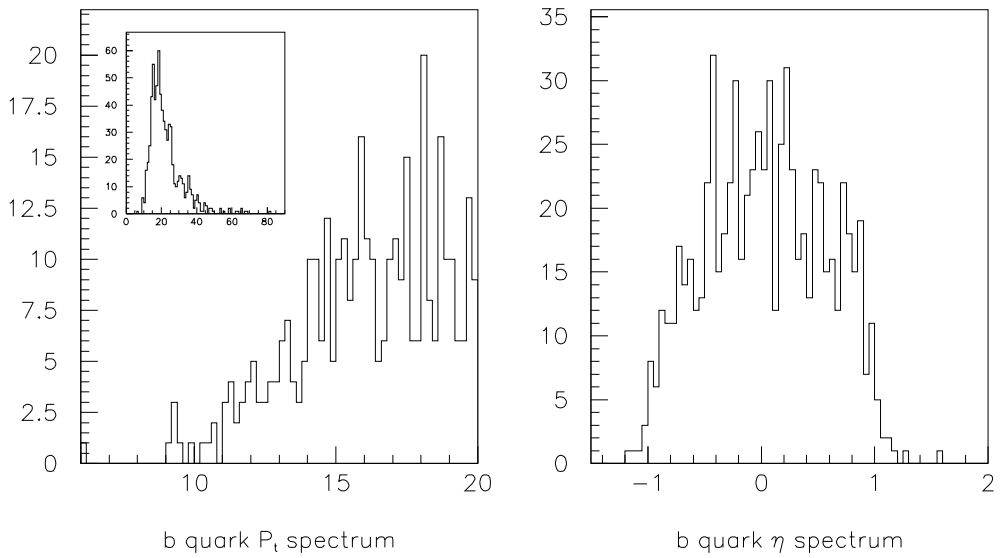

Figure 11.4: b quark transverse momentum (left) and rapidity (right) distribution for semileptonic b decays filtered with the selections described in section 11.3.2 and the final tuned production cuts on the b quark.

give an acceptable production efficiency for the sample: the η and P_t distributions shaping of the b quarks is dominated by the trigger requirements rather than the generation cuts.

The final simulated signal sample is based on the generation of 1,000,000 pythia events, yielding 755 inclusive electron triggered events with $B_d \to D^*\pi \to D^\circ\pi\pi \to K\pi\pi\pi$ on the other side.

11.4 Testing the Analysis Code

The signal reconstruction is based on analysis routines that we developed from scratch. We need to perform a validation of these routines. This is done studying the generated sample with two different techniques: the first one relies on the montecarlo information in order to correctly identify the track combinations which will yield the $B_d(t) \to D^{(*)\mp}\pi^{\pm}$ signal ("*divine*" reconstruction). We then apply exactly the same code we use for the real data to the simulated signal, without the *divine* information and compare the two results in order to evaluate the performance of the analysis code.

The *divine* reconstruction performs a simultaneous fit of the whole $B_d \to D^*\pi \to D^\circ\pi\pi \to K\pi\pi\pi$ decay chain after identifying the tracks produced in the B_d decay. Events preselection is identical to that performed by the analysis code: $\Delta R_{t-\ell} \geq 2$, $|m_D - m_D(PDG)| \leq 0.1\,GeV$, $|m_{D^*} - m_{D^*}(PDG)| \leq 0.1\,GeV$, $0.14 \leq m_D - m_D^* \leq$

$0.16\,GeV$. We will show that these cuts are loose in comparison with the widths of the reconstructed resonances and thus should not compromise the signal yield. Figure 11.5 shows the results of the divine reconstruction applied to the sample generated as described in section 11.3.2.

The *regular* analysis code is written in a totally independent way, thus giving the opportunity of cross checking the two programs. The corresponding distributions for the *regular* signal search program applied to the simulated sample are reported in figure 11.6 The two sets of distributions look compatible and this gives us confidence in the reconstruction code. A detailed cross check between the two methods has been carried on, explicitly searching the *divine* combinations found by the real data fitter and checking the consistency of the fitted variables between the two reconstructions. In all cases the difference between the reconstructed variables for the two methods is exactly zero.

This exercise allows us to perform a first estimate of the detection efficiency for our signal in the CDF I detector: we know that 755 events have been generated and passed through the detector simulator and the reconstruction program. The invariant mass distribution for the reconstructed B mesons in figure 11.6 shows exactly 200 candidate events sitting in the range $5.279 \pm 0.1\,GeV$, corresponding to a 2σ interval about the nominal B_d mass central value, while we have 52 events sitting outside this region and within $5.279 \pm 0.2\,GeV$. This yields a signal estimate of about 148 events, corresponding to an acceptance of: $\frac{148}{755} \approx 20\%$.
A detailed study of the various effects in the reduction of the initial signal down to this scale is reported in the following table:

Cut	Events	Fraction (%)
None	755	100
Detector Acceptance	302	40
$\lvert m_D - m_D(PDG)\rvert \leq 0.1GeV$	279	37
$\lvert m_{D^*} - m_{D^*}(PDG)\rvert \leq 0.1GeV$	276	36
$\Delta R_{t-\ell} \geq 2$	185	24

The first row reports the number of generated events. The following rows report the number of events in the divine reconstruction which pass the given cut.

11.5 A First Glimpse

The next step in the analysis preparation is testing the performance of the analysis code on a known signal sample. This has been already performed on the montecarlo sample in section 11.4, but we have the chance of performing a cross check also on a subset of the inclusive lepton sample, enriched in D^{*+} decays. Running our code on this sample gives us the opportunity of performing a check on a sample very close to the one we want to use.

The inclusive lepton plus D^* sample contains about 200 identified D^* decays to $D^\circ\pi$ with $D^\circ \to K\pi$. We will not discuss the detail of the cuts producing this sample, but only stress that they include the requirement that the D^* decay products sit in a fiducial cone around the trigger lepton. This is complementary to the $\Delta R_{t-\ell} > 2$ cut

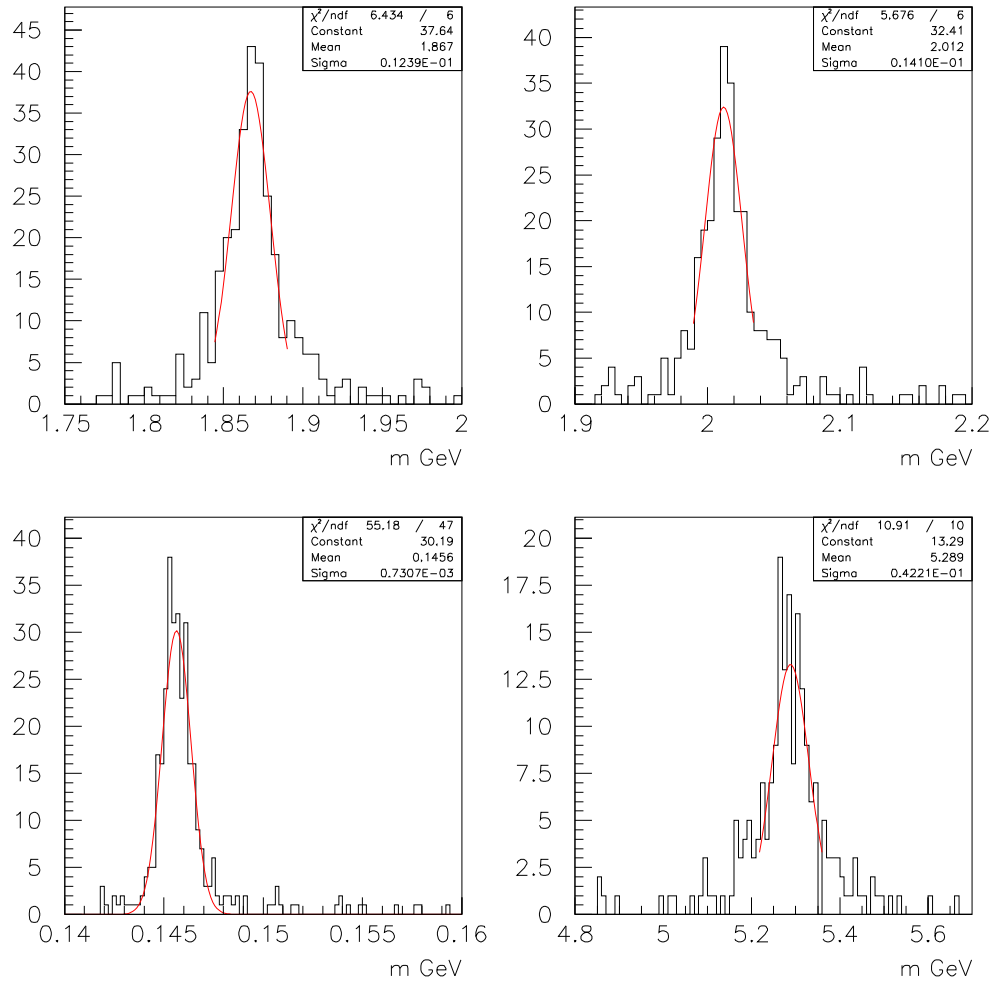

Figure 11.5: Reconstruction of the simulated signal using the standard CDF reconstruction code driven by a *divine* choice of the track combinations. Plots show the invariant mass distribution of the candidate D° (top left), D^{*} (top right), B_d° (bottom right) mesons. The bottom left plot shows the reconstructed $D^{*} - D^{\circ}$ invariant mass difference distribution.

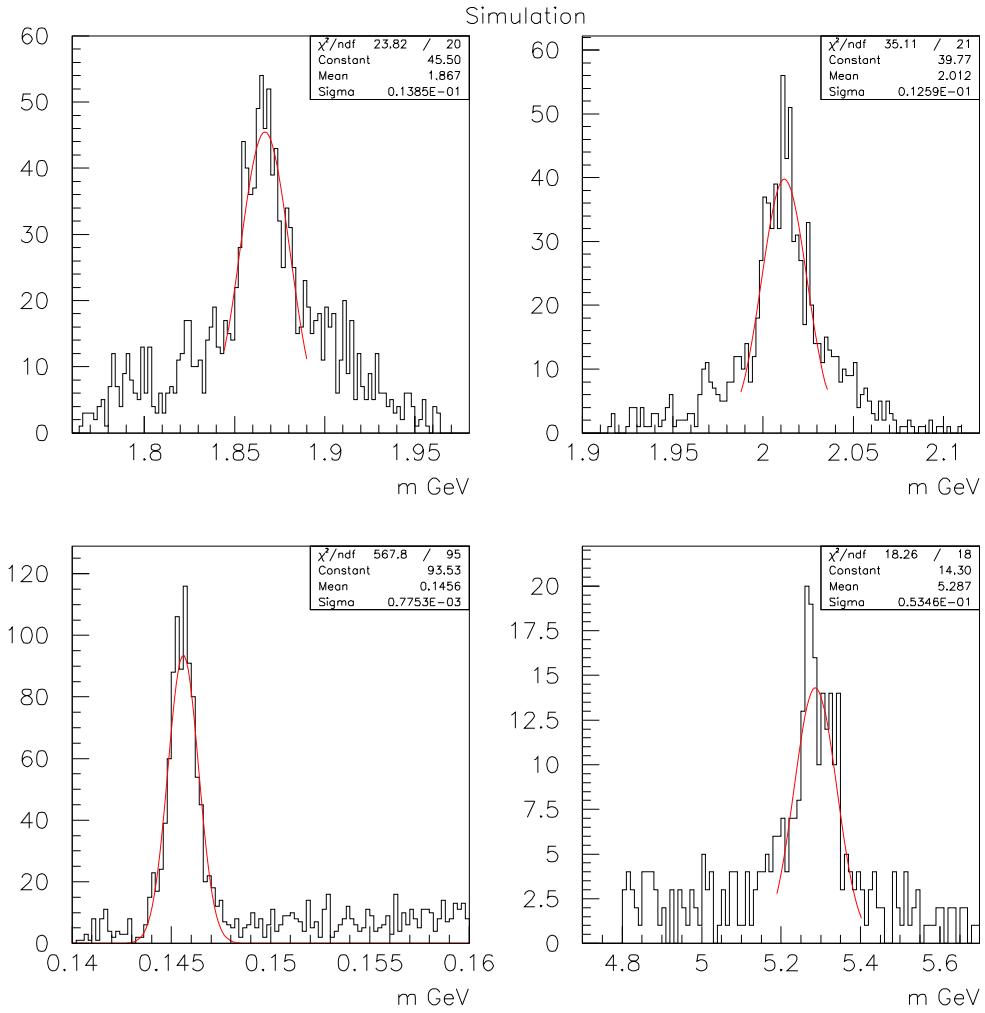

Figure 11.6: Reconstruction of the simulated signal using the standard CDF reconstruction code. Plots show the invariant mass distribution of the candidate D° (top left), D^* (top right), B_d° (bottom right) mesons. The bottom left plot shows the reconstructed $D^* - D^\circ$ invariant mass difference distribution.

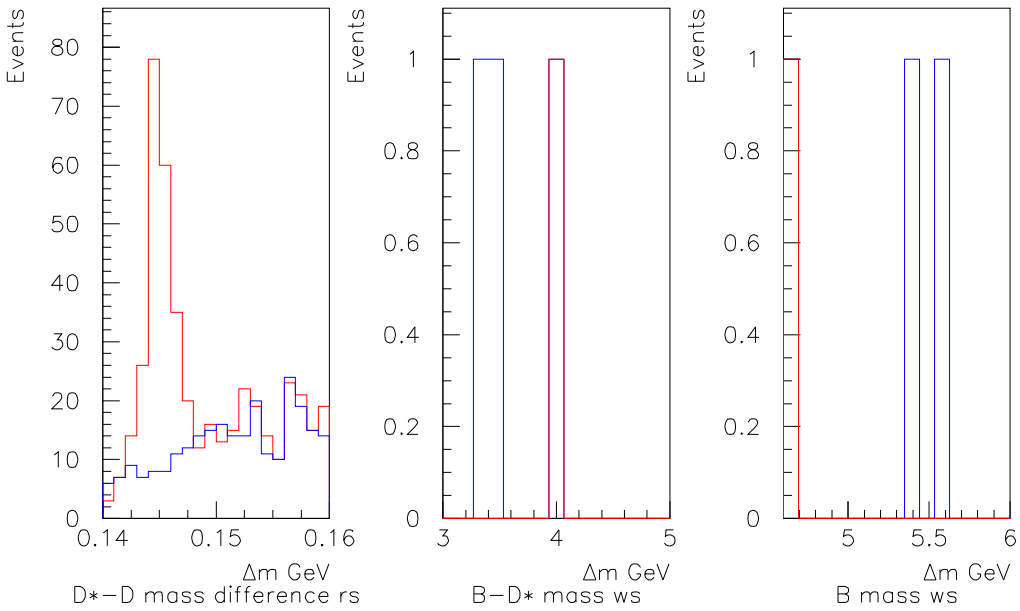

Figure 11.7: Reconstructed D^* decays in the preselected D^* sample. The leftmost plot shows the Δm_{D^*-D} distribution. The expected peak shows up in the right charge association and disappears (underlying line) when the wrong charge combinations are picked. The central histogram shows an analogous plot for the candidate B mesons reconstructed further associating a pion to the D^*. The rightmost histogram shows the candidate B mass distribution for the same events.

we are requiring on the D^* candidate tracks and therefore we decide to temporarily drop this requirement in the analysis.

The results of the search are reported in figure 11.7 The cuts chosen in this case are far from being optimized, and were picked exclusively relying on common sense: the most important point at this step is that we are able to see the physics signal of the D^* meson.

11.6 Cuts Optimization

Both the simulated signal and the analysis code are now well understood and ready for the tuning of the analysis cuts.
The initial sample of real data, after the $\Delta R_{t-\ell}$ selection is reduced to 140080 4-tracks combinations. We preliminarly choose the variables which look promising for the selection of our signal. The list of candidate quantities is reported in table 11.1.

Figure 11.8 reports the distribution of each of these variables taken individually for the simulated signal and for the data sample we are analyzing. This figure already gives a first rough idea of which among the listed parameters is potentially

Variable	Description	Charge	Sidebands
$\pi_4 P_t$	Transverse momentum of the D° pion	≥ 0.12	≥ 2.2
$K_3 P_t$	Transverse momentum of the D° kaon	≥ 0.93	≥ 2.5
$\pi_2 P_t$	Transverse momentum of the D^* pion	–	≥ 0.32
χ^2 fit	χ^2 for the 4 tracks combined fit	≤ 13.4	≤ 6.9
Δm	mass difference between the reconstructed D° and D^*	$[0.143, 0.148]$	$[0.143, 0.148]$
L^D_{xy}/σ	Transverse plane decay path of the reconstructed D° meson projected along its momentum and measured in terms of its resolution	–	–
$\pi_1 P_t$	Transverse momentum of the D^* pion	≥ 1.49	–
L^B_{xy}/σ	Transverse plane decay path of the reconstructed B° meson projected along its momentum and measured in terms of its resolution	–	–
B mass	Invariant mass distribution of the candidate B meson	–	–
ISO	$ISO = \frac{P_t^B}{P_t^B + \Sigma P_t^i}$ where the sum is extended to all the non-B tracks contained in a $\Delta R_{B-t} < 1$ cone about the B meson	≥ 0.04	≥ 0.095
$\Delta R_{B-\ell}$	ΔR between the candidate B meson and the triggering lepton	–	–
L^B_{xy}/L^D_{xy}	ratio of the reconstructed B and D mesons decay lengths projected along their momenta	–	–
$c\tau_D$	transverse decay length of the D meson	–	–
$c\tau_B$	transverse decay length of the B meson	–	–
$c\tau_B/c\tau_D$	ratio of the transverse decay lengths of the B and D mesons	–	–
$\pi_1\, d/\sigma$	Impact parameter of the B° pion measured in terms of its resolution	≥ 0.07	≥ 0.045
$\pi_2\, d/\sigma$	Impact parameter of the D^* pion measured in terms of its resolution	≥ 0.6	≥ 0.5
$K_3\, d/\sigma$	Impact parameter of the D° kaon measured in terms of its resolution	≥ 0.03	≥ 0.36
$\pi_4\, d/\sigma$	Impact parameter of the D° pion measured in terms of its resolution	≥ 1.46	≥ 1.6
P_t^D	transverse momentum of the reconstructed D° meson	≥ 2.5	≥ 3.4
$P_t^{D^*}$	transverse momentum of the reconstructed D^* meson	≥ 0.012	≥ 1.4
P_t^B	transverse momentum of the reconstructed B° meson	≥ 7.1	≥ 7
$P_t^D \cdot X_v$	transverse momentum of the reconstructed D° meson projected along its decay direction	≥ 0.03	≥ 0.01
$P_t^B \cdot X_v$	transverse momentum of the reconstructed B° meson projected along its decay direction	≥ 0.04	≥ 0.04

Table 11.1: Potential discriminants for the isolation of the $B_d\,(t) \to D^{(*)\mp}\pi^\pm$ signal from background. The values reported in the last two columns are the ones optimized following the prescriptions of section 11.6.

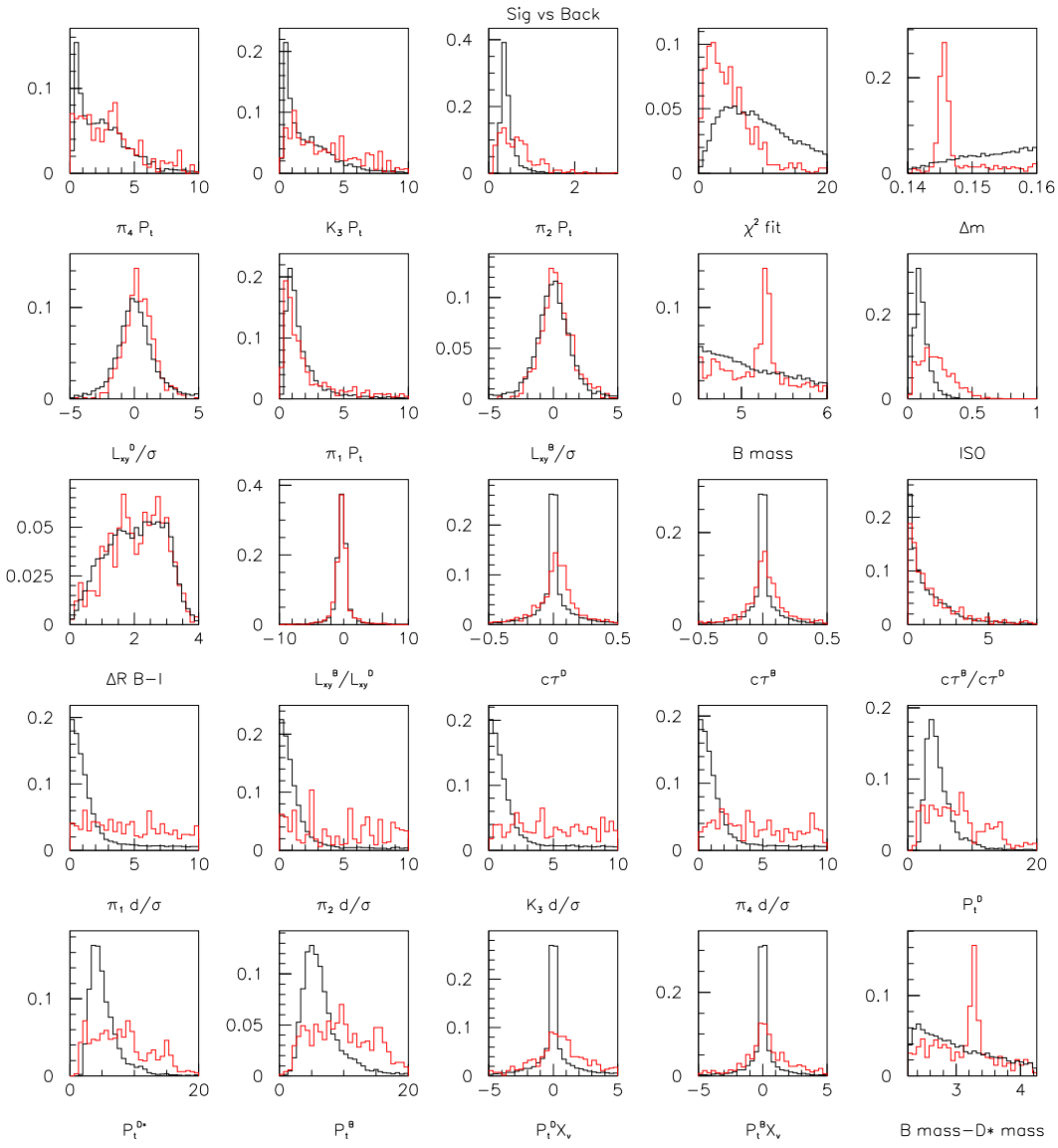

Figure 11.8: Simulated signal (red) and real data (black) distributions in the variables described in section 11.6.

a good discriminant between signal and background. Another interesting view of the same situation is rendered by figure 11.9 where the signal to background ratio is reported as a function of the same variables of figure 11.8. Even if in many cases the choice of the cuts to be performed looks obvious at least in a first approximation, we choose to rely on a numerical optimization for the final evaluation.
The quantity we want to optimize is the so-called *significance* of the signal in the final B meson invariant mass distribution, defined as:

$$\varsigma = \frac{S}{\sqrt{S+B}} \tag{11.1}$$

Where S and B are defined as the signal and background event counts in a given mass region. This quantity usually represents the effects of signal and noise statistics in the expression for the resolution of an asymmetry measurement of a signal S with background B.
We choose $[5.179, 5.379]$ as the mass window, corresponding to about 95% of the reconstructed B mesons in the simulated signal analysis of figure 11.6.

We now have to precisely define the *signal* and *background* sample. The former is unambiguously defined as the number of simulated events passing the analysis cuts and falling in the mentioned mass region. This number must be rescaled by the ratio $\frac{N_{produced}}{N_{simulated}}$, where $N_{simulated}$ is the number of montecarlo events generated for this study (755) and $N_{produced}$ is the number of signal events we expect to be produced in the sample we are analyzing (29, as explained in section 11.1).

Defining the background is more difficult essentially because we don't have a "clean sample of background", but instead we are relying on the analysis sample itself. Two different definitions of the background seem interesting in this context: the first one uses two sidebands in the mass spectrum of the candidate B mesons. In this case we will define as background events those falling in the intervals $[5.079, 5.179]$ and $[5.379, 5.479]$.
An alternative background definition is based on the charge assignment for each track: given the 4 tracks there is only 1 way of combining the charges in such a way that they actually correspond to a sensible combination from the physics point of view. In this combination the following track pairs have opposite charge:

- the two decay products of the D°
- the soft pion produced by the D^* and the kaon emitted by the D°
- the pion produced by the B° and the D^* decay pion
- the trigger lepton and the B° decay pion

That is, given the charge of the lepton all other charges are uniquely identified if we ignore CP violation effects (which are negligible at the level of our signal).
We can thus consider the (several) *wrong* charge assignments sitting below the candidate B° mass peak as a model of the background.

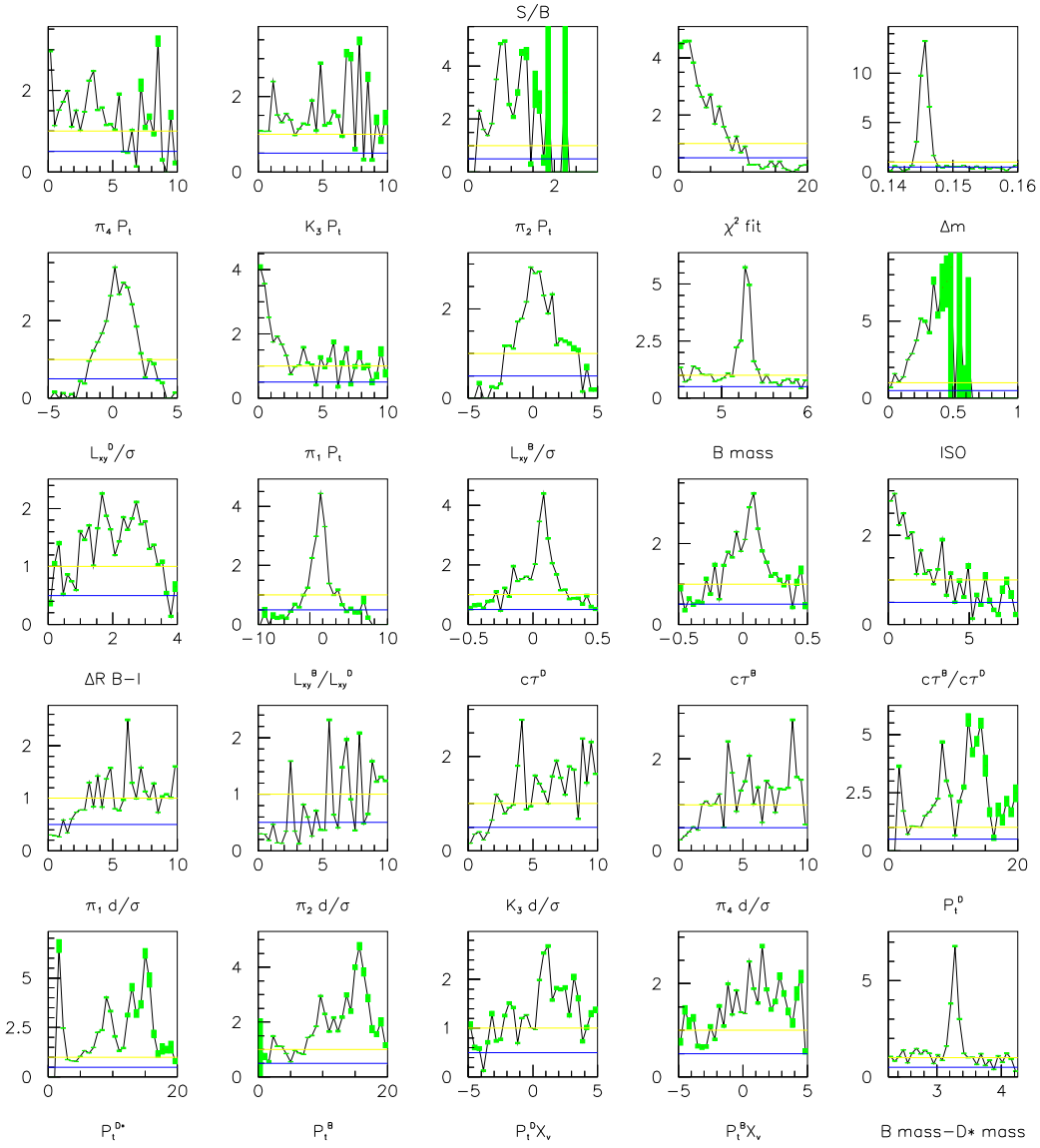

Figure 11.9: Signal to background ratio evaluated using the montecarlo sample as signal and the real data sample as background reported as a function of the variables described in section 11.6. The boxes show for each bin in each histogram the statistical error of the S/B ratio. Horizontal lines are drawn at S/B values of 1 and 0.5.

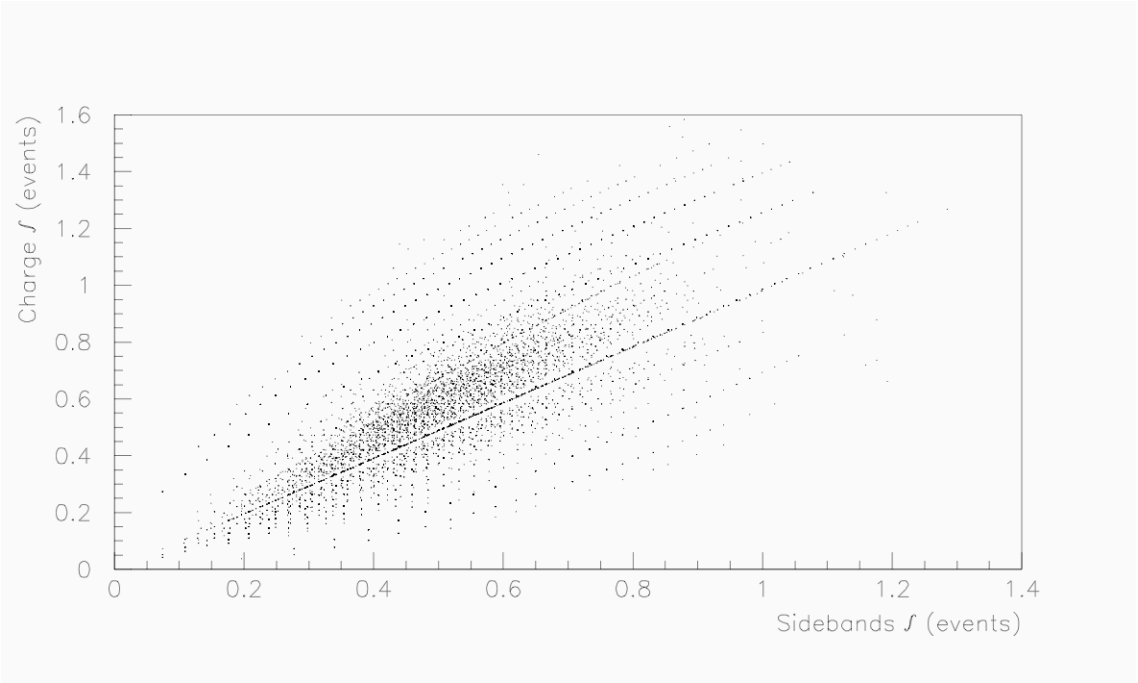

Figure 11.10: This plot reports on the x axis $\frac{S}{\sqrt{S+B}}$ defined using the measurement of the background based on the sidebands in the B° mass distribution. The y axis reports the same quantity calculated estimating the background on the basis of the charge assignment.

The *sideband* estimate of the background has the advantage of giving a good description of the background below the reconstructed B peak under the assumption that the background distribution is linear at the B resonance. This is a reasonable assumption for combinatorial background without resonances but is a poor description for the fraction of background coming from B physics.

On the other hand, the *charge*-based background estimate probably better describes the real background sitting below the B peak but is affected by another difficulty: the background yield estimated with this method is probably optimistic since we are excluding from the possible background the same charge combination as the signal.

Figure 11.10 shows the correlation between the ς parameter defined using the two different ways of estimating the background to our signal: each point in the histogram corresponds to a set of cuts randomly chosen for all the variables of table 11.1. The two background definitions seem to yield slightly different ς values and we choose to consider them separately. Given the small statistics of the final sample and the availability of an intermediate preselected manageable sample, we choose to optimize both definitions and eventually discuss separately the two results.

We can now switch to the problem of maximizing ς. This operation is performed simultaneously on most of the variables listed in table 11.1, using standard multidimensional maximization techniques. Each cut is defined as an interval defined

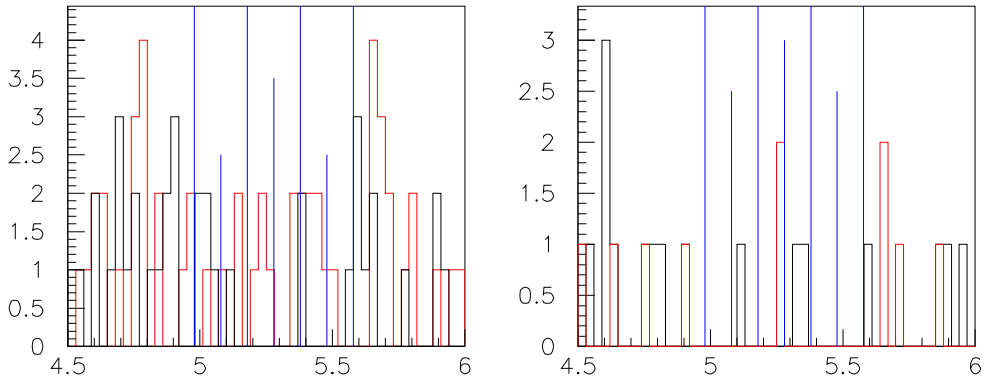

Figure 11.11: Invariant mass distribution for the B meson candidates from the electron sample. The left plot shows the candidates passing all the selection cuts corresponding to the optimization of ς based on charge discrimination between signal and background. The right plot corresponds to the cuts obtained using the sidebands to estimate the B background. Both plots report the right sign (red) and wrong sign charge (black) combinations. Blue vertical lines are traced at $\pm\,[0, 0.1, 0.2, 0.3]\ GeV$.

by one or two parameters which are then optimized maximizing the significance. The choice for the initial values is reported in table 11.2. The choice is based on the visual comparison of the signal and background distributions reported in figure 11.8.

The resulting set of cuts after the optimization is reported in the last two columns of table 11.1. Each column refers to a different choice of the background definition. The resulting estimate for the signal significance and event yields are reported in table 11.3.

11.7 Analysis Results

Both sets of optimized cuts yield close significance estimates, with rather different signal yields. We apply both set of cuts to the inclusive electron sample, preselected as described in section 11.3.1.
We evaluate the signal size counting the correct sign combinations which fall in the mass range $[5.179, 5.379]$ for the candidate B meson.

The result is reported in figure 11.11 in terms of invariant mass distribution of the candidate B mesons mass distribution. Table 11.3 reports the evaluation of the significances, event yields and efficiencies based on those distributions.

Variable	Description	Cut Definition	Initial Value
$\pi_4 P_t$	Transverse momentum of the D° pion	$\geq x_1$	≥ 2.4
$K_3 P_t$	Transverse momentum of the D° kaon	$\geq x_2$	≥ 1
$\pi_2 P_t$	Transverse momentum of the D^* pion	$\geq x_3$	≥ 0
χ^2 fit	χ^2 for the 4 tracks combined fit	$\leq x_4$	≤ 15
Δm	mass difference between the reconstructed D° and D^*	$[x_5, x_6]$	$[0.144, 0.148]$
L^D_{xy}/σ	Transverse plane decay path of the reconstructed D° meson projected along its momentum and measured in terms of its resolution	$[x_7, x_8]$	$[-7, 7]$
$\pi_1 P_t$	Transverse momentum of the D^* pion	$\geq x_9$	$\geq 0.$
L^B_{xy}/σ	Transverse plane decay path of the reconstructed B° meson projected along its momentum and measured in terms of its resolution	$[x_{10}, x_{11}]$	$[-7, 7]$
B mass	Invariant mass distribution of the candidate B meson	–	–
ISO	$ISO = \frac{P_t^B}{P_t^B + \Sigma P_t^i}$ where the sum is extended to all the non-B tracks contained in a $\Delta R_{B-t} < 1$ cone about the B meson	$\geq x_{12}$	≥ 0
$\Delta R_{B-\ell}$	ΔR between the candidate B meson and the triggering lepton	$\geq x_{13}$	≥ 0
L^B_{xy}/L^D_{xy}	ratio of the reconstructed B and D mesons decay lengths projected along their momenta	$\geq x_{14}$	0
$c\tau_D$	transverse decay length of the D meson	$[x_{15}, x_{16}]$	$[-2, 2]$
$c\tau_B$	transverse decay length of the B meson	$[x_{17}, x_{18}]$	$[-2, 2]$
$c\tau_B/c\tau_D$	ratio of the transverse decay lengths of the B and D mesons	$\geq x_{19}$	≥ 0
$\pi_1\, d/\sigma$	Impact parameter of the B° pion measured in terms of its resolution	$\geq x_{20}$	≥ 0
$\pi_2\, d/\sigma$	Impact parameter of the D^* pion measured in terms of its resolution	$\geq x_{21}$	≥ 0.1
$K_3\, d/\sigma$	Impact parameter of the D° kaon measured in terms of its resolution	$\geq x_{22}$	≥ 0.03
$\pi_4\, d/\sigma$	Impact parameter of the D° pion measured in terms of its resolution	$\geq x_{23}$	≥ 1.5
P_t^D	transverse momentum of the reconstructed D° meson	$\geq x_{24}$	≥ 1.5
$P_t^{D^*}$	transverse momentum of the reconstructed D^* meson	$\geq x_{25}$	≥ 1.4
P_t^B	transverse momentum of the reconstructed B° meson	$\geq x_{26}$	≥ 4
$P_t^D \cdot X_v$	transverse momentum of the reconstructed D° meson projected along its decay direction	$\geq x_{27}$	≥ 0.05
$P_t^B \cdot X_v$	transverse momentum of the reconstructed B° meson projected along its decay direction	$\geq x_{28}$	≥ 0.05

Table 11.2: Critical region and initial value of the fit parameters for the optimization of the signal significance in this search. The values reported in the last column are the initial values of the optimization process.

Method	ς_{Charge} $\left[\sqrt{events}\right]$	$\varsigma_{Sidebands}$ $\left[\sqrt{events}\right]$	MC Signal $[events]$	ϵ $[\%]$
Charge	2.24 ± 0.24	1.3 ± 0.13	5 ± 0.44	17 ± 1.5
Sidebands	1.16 ± 0.2	1.4 ± 0.16	2.5 ± 0.3	8.6 ± 1
Method	ς_{Charge} $\left[\sqrt{events}\right]$	$\varsigma_{Sidebands}$ $\left[\sqrt{events}\right]$	Signal $[events]$	ϵ $[\%]$
Charge	2.45 ± 0.64	0 ± 10	6 ± 3.45	21 ± 12
Sidebands	$0. \pm 2.2$	1.1 ± 0.9	1.5 ± 2.9	5 ± 10

Table 11.3: Results of the cuts optimization following the two different strategies (rows) for the definition of the background described in the text. Disregarding the optimization chosen, ς is evaluated in both ways for comparison. The top table refers to the cuts optimization (section 11.6), while the bottom one refers to the evaluation on the real data alone (section 11.7). The signal is defined in both tables as the right charge combinations falling in the $[5.179, 5.379]$ mass range for the candidate B meson less the background estimated with the given method.

Method	ξ_{Charge}	$\xi_{Sidebands}$
Charge	1 ± 0.1	0.57 ± 0.05
Sidebands	0.74 ± 0.12	0.91 ± 0.08
Method	ξ_{Charge}	$\xi_{Sidebands}$
Charge	1 ± 0.4	0 ± 1.6
Sidebands	0 ± 1.4	0.75 ± 0.6

Table 11.4: Results of the cuts optimization following the two different strategies for the definition of ξ described in the text. Disregarding the optimization chosen, ξ is evaluated in both ways for comparison. The top table refers to the cuts optimization, while the bottom one refers to the evaluation on the real data alone, where the signal is defined as the right charge combinations falling in the $[5.179, 5.379]$ mass range for the candidate B meson.

11.8 Run II Extrapolations

The quantity $\frac{S}{\sqrt{S+B}}$ can be seen as the product of a factor independent from the sample statistics ($\sqrt{\frac{S}{S+B}}$) and another factor which scales as $\sqrt{S}$ with the sample size. Since the sample size is uncertain, it is probably more useful to have a measurement of $\xi = \sqrt{\frac{S}{S+B}}$ which is independent from the event yield expectations. We therefore report the estimated values of this variable in table 11.4, organized like table 11.3.

11.9 Conclusions

We performed a complete optimization of the analysis cuts for the full reconstruction of the $B_d \to D^{*\mp}\pi^{\pm}$ decay on Run I data. The expected event yield is not large

enough to let us hope in any visible signal, but table 11.3 shows that the analysis results are in agreement with what expected from the simulation, both in terms of estimated event yield and significance. The simulated and the real data give us the possibility of estimating the scale factor ξ, which somewhat determines the significance of the signal events in an hypothetic measurement. In chapter 9 we roughly assumed a value of $\xi = \frac{1}{\sqrt{2}} \approx 0.71$. We now know that an analysis such as the one we have optimized in this chapter yields a value of ξ compatible with our assumption.

Chapter 12

Setting Up the Silicon Vertex Tracker

Starting from summer 1999, all the SVT board prototypes have been collected together in one of the final SVT crates at Fermilab (B0 from now on). At that time all the boards needed to assemble a single SVT wedge were available. Many of them have been finalized at the end of summer 1999, after the final test of compatibility and functional performance made at B0. Many tests have been performed on a board by board basis at first, and on board groups then: thermal environment compatibility (especially for the AMboard, which is the *hottest* board in the system: see section 12.2), communication with external DAQ devices, protocol uniformity among boards and more specific and complex functional tests on each board. We will first deal with single board-hardware tests and then discuss inter-operative tests. However, the reader should keep very clear in mind that even if logically distinct in some cases these tests were carried on at the same time or in a different order than just from the simplest to the most complex, either because of the impossibility of serializing some of the steps or for the simple lack of resources.

12.1 Single Board Tests

We initially discuss basic functional tests which had to be performed first in order to verify the possibility of even keeping the SVT devices powered with continuity in safe and sane conditions. After verification of these basic steps, single board functionality has been addressed. This phase can be divided in two different steps. The first one is a real stand-alone procedure and deals with the basic board functionality, while the second step consists in the verification of the board's ability of interacting with other SVT boards. Given the pipelined structure of SVT, the functional verification of each SVT board strongly relies on the performance of adjacent boards. However, thanks to the modularity of the data stream flowing through SVT elements, we were able to conceive a *bootstrap* procedure for the functional test.

12.1.1 Basic Functionality

The first step of each board's check has been a simple electrical test, aimed to the verification of design schematics in the realization of the design; every kind of problems can, and in fact does, happen in this phase: short circuits occurred while soldering, wrongly positioned, oriented and connected devices, errors in the realization of the printed circuit board and so on: paradoxically, the first version of the associative memory chip bugs were such that its behavior was much closer to the expected one when the device wasn't powered! After this phase, simple functional tests were performed: checking the VME interface, internal registers and memories and simple I/O operations are the first logical steps in the board debugging. This meant more than once the reiteration of individual chip programming or even hardware design. Each test step required the development of semi-automatic electric tests with the help of a pattern-generator and a logic analysis system, the design of device-specific low-level code for the access to registers, memories and programs of each module.

12.1.2 Simple Board Interoperation and Complex Functionality Test

After the VME I/O test, the following step is that of checking the custom SVT I/O ports. Precisely with this goal in mind, the simplest I/O capable SVT board (the Merger) was designed first, including features aimed to the goal of testing and debugging other board's I/O features.
The most important of these features is probably the duplication of the received and sent data in special circular buffers (*spy buffers*): spy buffers greatly simplified this debugging step, allowing a standard procedure of checking sent vs received data.
After the I/O debugging, each board's complex functions needed to be tested: one or more Mergers used as VME accessible input generators and output read-outs allowed variable speed tests of the I/O and internal mechanisms. In the case of lack of Mergers, other boards capable of VME access to the input and output registers were used. Each board's test requires at this stage the finalization of the low level access routines, the development of specific test algorithms and of reliable software simulator of the expected hardware behavior.

In fact we developed the so called hardware-level (aka bit-level) simulator mostly at the time of each board's functional test. In some cases the simulator was developed even before the actual board was available.

12.2 An Example: the Thermal Performance of the AMboard

Each procedure described above might look straightforward and easy at first sight, but in fact involves many interesting (but also many boring) details. As a *worked example* we present here the results of the two thermal tests aimed to verify that

the AMboard (which can be considered one of the most temperature-critical SVT component) can reliably work in the thermal conditions of the SVT crates.

12.2.1 Introduction

The AMboard is one of the most critical SVT boards from the point of view of thermal behavior: the presence of mezzanine boards (AMplugs) on most of the board's surface, and the fact that each AMplug is filled with thermal sensitive dissipating devices (AMchips, RoboClock and Glue0) might create a potential problem if the board cooling is insufficient. Moreover, we didn't have a certain thermal specification for the AMchips.
For this reason we have divided the test in two parts:

- a rough "thermal specification" test (the *Italian* test), in which we have thermally stressed an AMplug in order to provide an approximate temperature range in which the devices can work without problems
- an "in situ" test (the *B0* test), in which we tried to reproduce as much as possible the real operating environment of the AMboard

To insure that the board was effectively working, we adopted a rather "standardized" testing procedure known among the SVT people as "random test". We will first briefly define what this test procedure is, and then we will report the results of the two thermal tests.

12.2.2 The *random test* procedure

The *random test* (RT) consists of a standard set of routines initially built to test the performance and reliability of the associative memory section of SVT (the Associative Memory Sequencer and the Associative Memory Boards). In order to be extensively usable as a test tool for SVT, the RT includes the possibility of generating input data and read the output stream(s) of the SVT chain under test with a variety of devices (the Hit Buffer, the Merger, the Hit Finder). In each configuration the random test, through a plethora of options (defining the input device, the output device, the data streams under test and so on), is capable of checking the hardware behavior against the software simulation included within the RT itself. In fact the program evolved to an `ANSI C` library for the detailed hardware simulation of each board in the chain. This simulation is the basis for the offline simulation of SVT in the Run II analysis package and also for the simulators used in the SVT monitoring software.

The input data to the RT chain is randomly generated in variable size and content distribution, thus allowing the test of the data flow through boards in a variety of conditions.

Also the hardware initialization is handled by the same program, providing the ability of arbitrarily generating or loading from predefined files the content of the memories which define each board's configuration.

The random test, in the configuration in which we have chosen to operate, is defined as follows: we use one AMboard, an AMS board and a Merger board. The Merger is kept in "test mode": 1 input and 1 output are used to feed and read the output of the AMS through VME I/O calls. Random *events* are generated as follows: every 260 events a set of random hits H is generated and randomly loaded into the AMchips, after remapping through a copy of the map loaded into the AMS. Every event is then generated extracting a set of 20 to 100 hits (the size is randomly chosen between these limits) from H, and adding to them an end event word, with the event tag in the end event word cycling through all its possible values. This defines an SVT event, which is then fed to the AMS, through the VME-Merger path. The AMS output is read through the Merger input (via VME operations) and compared with what expected by a software simulation of the devices.
Even if the set of hits and patterns and the maps used in this test are different from the real working conditions of SVT, this procedure has the advantage of thoroughly checking all the bit configurations in the AMchip in a random way.

12.2.3 The *Italian* test

The goal of this test is that of providing a confidence interval for the operational temperature of the AMboard.
We set up the boards in a crate located in Pisa, using a low speed VME CPU. Three thermal sensors are glued to an AMchip, a "RoboClock" and a "glue 0" chip (the three main components of the AM plugs) on the same AMplug stuffed with AMchips version 3.2.
The AMplug is mounted on an easily accessible position on the AMboard (slot 12). The AMS clock is 30MHz.
The thermal stabilization is achieved using a temperature controlled soldering iron, thermally connected to AMplug 12, and a variable cooling flow of air at room temperature. To reach higher temperatures, an air heater is then used, bringing the chips up to $80\,^{\circ}C$. Detailed temperature information is reported on table 12.1.
At every temperature steps, the random test is left working for about 30 min. while the temperature is kept stable. During all the test the random test was running without errors. This brings us to the conclusion that the AMboard can work at temperatures as high as $75\,^{\circ}C$.

12.2.4 The *B0* test

Our goal in this test is that of reproducing as much as possible the effective cooling of the SVT crates on the AMboard and then probe the various components temperature to verify if and how the AMboard temperature falls within optimal working conditions.
We are provided with a crate, a high speed CPU and a low speed CPU mounted in a true CDF trigger crate, complete of an operational cooling circuit. The crate is full of TDC boards, and the free slot between our AMboard and the AMS is filled with a dummy board.

Time	RoboClock temp. $^{\circ}C$	Glue 0 Temp. $^{\circ}C$	AMchip temp $^{\circ}C$	Comments
14:43	53.5	43	32	Test not running RoboClock on P3 heater off
15:13	55.5	47.8	36.2	Test running
15:40	60.5	54.9	47	Test running heater on
16:11	64	59	52.5	Same
16:56	67.7	62.5	56	Same
17:40	80	78	75	Test running air heater on

Table 12.1: Temperatures of the various AMplug components tested in the *Italian* part of the thermal test.

The AMboard is filled with AMplugs, and configured as reported in table 12.2. After 1hr from crate power-up with the rack door closed, the hottest chip on AMplug 4 is at a temperature of $20^{\circ}C$.
The test is performed then in various steps and conditions:

1. at first the plug with thermal probes is used as a "passive" board, disabling the patterns and watching the temperature while the random test is running on all the plugs of version 3.1 Both fast and slow CPUs are used. The AMS clock is 20MHz.

2. After this, we load in the AMS an "ad hoc" microcode, written to perform an infinite loop of input operations on all the chips of the AMboard. This was done to perform at full clock speed the most "heating" operation conceivable in the AMchips. The AMS clock is $20\,MHz$.

3. Next, the random test is used again, this time enabling also the board instrumented with thermal probes, keeping it running for a long period of time. The AMS clock is $20\,MHz$

4. The AMS clock is then replaced with a $32\,MHz$ one, and the special microcode (2) is run again. We don't expect the random test to work in this condition, since the RoboClock timing isn't fine tuned. The purpose of this phase is just that of probing the board temperatures in a "worst case" configuration.

5. finally, a $28\,MHz$ clock is placed in the AMS, and the random test is left running for as long as possible, after having configured the AMboard correctly (see [142]).

Note that in all the cases (detailed temperature measurements are reported in table 12.3) the chips temperature never goes above $25^{\circ}C$. Even if the temperature goes well below the range of temperatures at which the board was previously tested,

AMplug Slot Number	Plug type (AMchip version)	Plug ID	Comments
AM0	2	115	Old black-case AMchips
AM1	3.1	112	Working AMchips with shift bug
AM2	3.1	?	Plug had no ID #
AM3	2	108	
AM4	3.2	102	Plug with temp. probes
AM5	3.1	110	
AM6	2	104	
AM7	3.1	103	
AM8	2	111	
AM9	3.1	101	
AM10	2	114	
AM11	2	107	
AM12	2	105	
AM13	3.1	?	Plug had no ID #
AM14	2	106	
AM15	3.1	100	

Table 12.2: AMplugs identification on the AMboard, during the *B0* test.

no failure of the board is encountered.
While the random test is running in various conditions, we are also able to detect how the temperature changes in the various phases of the test: since the pattern generation and download on the AMboard takes some time (during which no other operations are performed on the AMchips) we are able to see (fig. 12.1) the temperature of the RoboClock and glue chips raising (during the input/output cycles) and then lowering again (during the update of AM patterns). Unexpectedly, the most stable device during the random test is the AMchip itself! In any case temperature changes of less than $1°C$ along the test cycles.

12.2.5 Conclusions

The AMboard has shown a good stability in a wide range of temperatures (from $16°C$ up to $80°C$), and is not expected to have excessive heating problems in the final SVT setup. We expect the AMchips to be working, in the final crate, at a temperature between $15°C$ and $20°C$, while all the commercial devices will work within thermal specifications.

12.3 The Vertical Slice Test

The SVT Vertical Slice Test (*VST* from now on) is the ideal completion of the previous stand-alone testing phase: it means essentially putting all the available boards together and assembling the first working prototype of a full SVT slice.

Running Time	RoboClock temp. $^{\circ}C$	Glue 0 Temp. $^{\circ}C$	AMchip temp $^{\circ}C$	Comments
1hr	20.1	17.0	15.2	AMS in test mode
1'	23.6	21.2	15.9	(1), PPC CPU, 20MHz
5'	23.7	21.4	16.0	(1), PPC CPU, 20MHz
20'	23.6	21.3	15.9	(1), PPC CPU, 20MHz
1'	23.3	21	16	(1), 68K CPU, 20MHz
5'	23.4	20.9	16	(1), 68K CPU, 20MHz
20'	23.5	21	16	(1), 68K CPU, 20MHz
1'	23.5	21.2	16.5	(2), 20MHz
5'	23.4	21.6	18.5	(2), 20MHz
20'	23.4	21.6	18.6	(2), 20MHz
60'	23.2	21.5	18.4	(2), 20MHz
1'	23.3	21	16.5	(3), 68K CPU, 20MHz
5'	23.5	21.1	16	(3), 68K CPU, 20MHz
20'	23.4	21	15.8	(3), 68K CPU, 20MHz
15h 35'	23.5	21.1	16	(3), 68K CPU, 20MHz
1'	24.1	22.3	16	(4), 68K CPU, 32MHz
30'	25	24	20.4	(4), 68K CPU, 32MHz
5'	24.6	22.5	16.2	(3), 68K CPU, 28MHz
20'	24.7	22.6	16.2	(3), 68K CPU, 28MHz
18h 35'	25.1	23	16.5	(3), 68K CPU, 28MHz

Table 12.3: Temperatures of the various AMplug components tested in the various conditions of *B0* part of the thermal test, as described in the text.

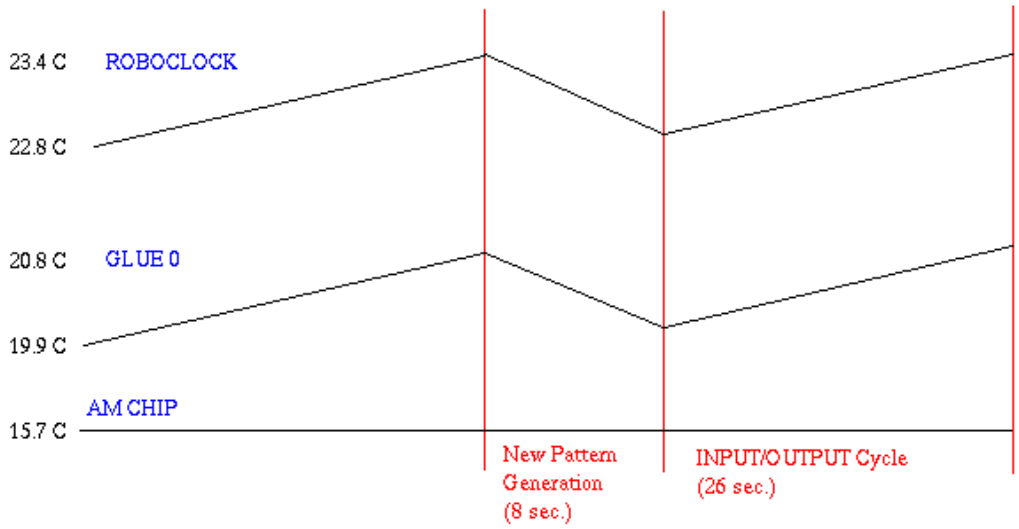

Figure 12.1: Thermal behavior of the AMplug components during the random test in phase (3) of the *B0* test.

This gave us the possibility of settling in the final environment, testing the boards interaction and the data flow through the SVT pipeline.

12.3.1 Goals and Structure of the Vertical Slice Test

The ultimate goal of the VST was that of verifying the hardware performance and the behavior of the system in realistic conditions.
Intermediate goals spontaneously rose from March 1999 on, as soon as new boards were available and thus their integration in the test was possible.
The kernel around which all the devices were added was the AM system (AMb, AMS and HB), which was already known to perform well from previous tests. Hit Finders were added next and extensively reprogrammed in order to use them as random input sources, coupled to the random test. At the same time the fiber optic link to the silicon vertex detector readout (G-link) and its interface with the Hit Finder boards were available and tested. Shortly after, also the Spy Control board was available and integrated in the test. In the late phase of the VST, also the TF was added and used as final element in the chain.
In parallel to the random test training of the available SVT wedge (section 12.2.2), we were able to freely access and use the "logic analysis system" based on the spy buffer registers and the spy control board. This feature was in fact used to develop and test the spy monitoring software (SMS). The purpose of the SMS is that of providing an on-line diagnostic tool for SVT while taking data. Basically, the spy buffers of several SVT boards are read and matched against each other. The events flowing through SVT are thus fed to a software simulation of the SVT boards and checked against the hardware output for consistency. At the same time secondary monitoring tasks like simple data statistics and consistency checks are performed.

12.3.2 Detailed Simulation of the Hardware Behavior

Having the data flowing through the whole SVT slice was already a goal by itself, but would have been rather incomplete without being integrated with a diagnostic system capable of detecting faults due to misconfiguration or hardware/software bugs. This is another reason which brought us to develop and thoroughly test a modular library of software simulators which reproduce in all the possible details the behavior of the actual hardware. The library modularity naturally descends from the structure of SVT and basically follows the device granularity at the board level. This means that a set of standard `ANSI C` routines and data structures were organized in a set of object-like tools, each representing a board and the access "methods" needed to perform the I/O from the objects in a manner as similar as possible to the real boards.
The Object Oriented-like structure of the code was strongly suggested by the modular structure of SVT and by our previous experience in the development of quick and dirty debugging tools. However we chose not to develop the library in object-oriented languages in order to maintain the possibility of using the same actual code in heterogeneous environments like a workstation, the offline environment, the on-

line environment and the crate cpu.
The simulated internal registers and the data streams are designed to be easy to access and understand by an human, giving the ability to compare them with the actual hardware output.
At the same time we developed accessory tools like data stream unpacking routines, data stream sorters and comparison tools and simple demo programs.

12.4 Conclusions

The preparation of SVT for the first tests involved several steps, which culminated in the test of a complete SVT *slice*.

The vertical slice test successfully ran for months. The modular configuration was modified several times during the test in order to adapt the set-up to the available hardware, running as long as human resources allowed to. The expertise and knowledge accumulated during this phase were of great importance for the integration of SVT in the commissioning run and for the integration in the real data taking phase of CDF II.
We refined and started to develop new software for the handling and diagnostics of SVT, ending up with a set of standard routines for the access of the actual hardware by diagnostic and DAQ software and for the modular simulation of the SVT hardware.
This library is being integrated in the on-line hardware monitoring tools and was extensively used in the realization of the first version of the Run II offline software simulator of SVT.

Chapter 13

First SVT Whimpers

The SVT test during the October 2000 commissioning run was very successful. Even if the detector configuration was far from the specifications required by SVT we were able to identify tracks and fit them later on. The test served as a first step towards the development of the tools and diagnostics needed for the beginning of Run II, but also demonstrated SVT's flexibility. We were able to interface to the SVX II output data stream and to the L2 DAQ system without problems.
We will first deal with the hardware and software configuration during the commissioning run, and then show the results obtained.

13.1 The CDF Commissioning Run

The CDF II configuration in the commissioning run was significantly different from the final one. Many detector and trigger components were still under commissioning. This meant, in some cases, that the real part was substituted by a mock-up or a fraction of the device built with spare parts. In other cases this could go down to the complete absence of the device. This is for example the case of the XFT interface towards SVT and of the SVT interface to the L2 trigger. In this section we will describe the structure of the available SVX II detectors and the choices we made in order to check SVT at our best.

13.1.1 SVX II Barrel 4

SVX II wasn't ready for the Commissioning Run roll-in. However, an ad hoc barrel (Barrel 4) built with spare parts and lower quality silicon detectors was assembled. Only 4 SVX II wedges were stuffed with silicon layers, leaving the rest of the barrel empty. During commissioning it was realized that one of the inner 4 silicon layers in each wedge was dead in the east half-barrel. We then decided to restrict our attention to the west half-barrel, which had all the 4 inner silicon layers (namely layer 1, 2, 3 and 4) in good shape.
In principle the east barrel problem could be solved reconfiguring the corresponding SVT wedges to use the outer silicon layer instead of the dead one, but this would have

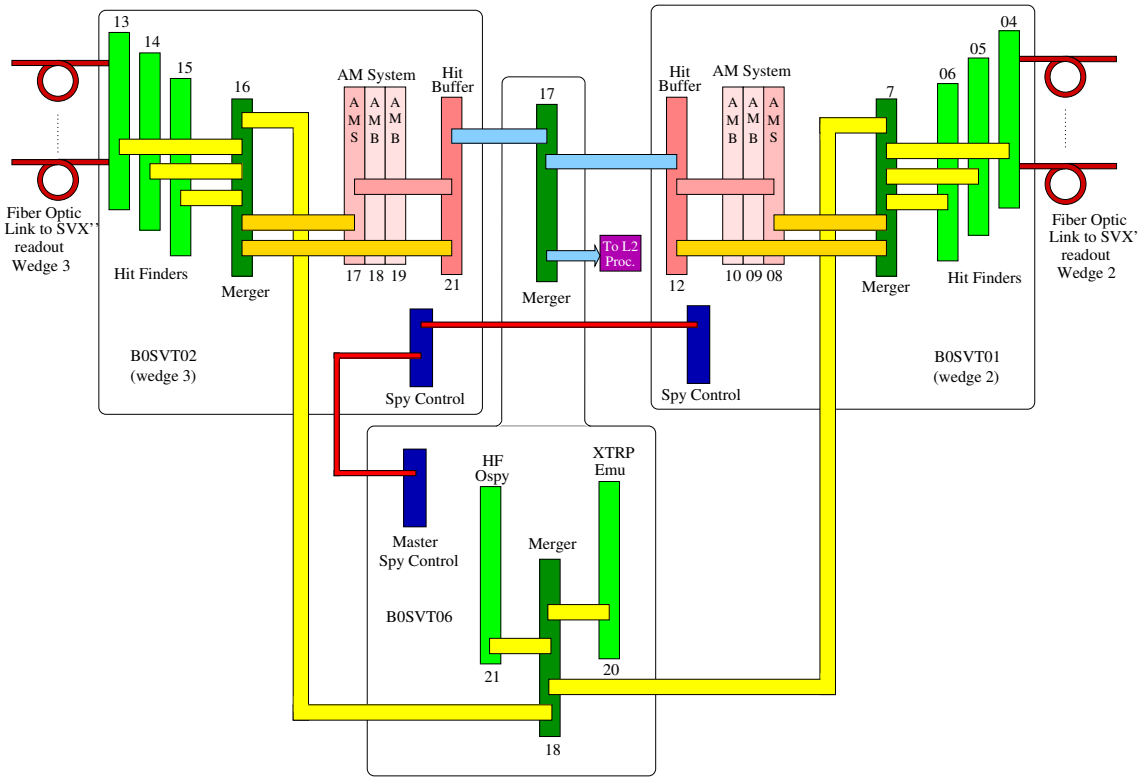

Figure 13.1: SVT layout in the commissioning run.

required an additional effort in order to generate new patterns for that configuration. We thus decided to let go the east half-barrel.

13.1.2 SVT Configuration

Figure 13.1 reports the organization of SVT in the commissioning run.

The SVT interface towards L1 was still missing at the time of the commissioning run. This means that the XFT information wasn't available for SVT processing. We decided to setup a fake L1 source, with the aid of an "XTRP emulator", an Hit Finder board and a Merger in order to test the SVT performance as a fitter working on the silicon detector alone.
The XTRP emulator (XTRPe) consisted of a reprogrammed Hit Finder board which received the Level 1 "accept" signal and the Level 1 event information from the crate backplane. This information was then propagated in the SVT data stream. The XTRPe was needed in order to label the SVT stream with the correct event tag, taken from the L1 information.
The AM system still required the presence of tracks coming from XFT in order to flag a candidate pattern. For this reason the XFT section of the SVT patterns was loaded with the coordinate of the same "XFT" hit for every pattern. In this way, the presence of that particular hit in every event allowed SVT to work independently from the XFT data. Another HF was used as a data source producing fake

XFT tracks, with the hit coordinate corresponding to that programmed in the AM patterns. With this patch, the SVT pattern recognition was artificially restricted to the silicon detector alone.
The output of the two "XTRP emulators" was merged and sent to the two SVT wedges instead of the regular XTF boards output.

In order to perform the SVT alignment, two different configurations for the output were planned:

- Alignment mode: this is the configuration as reported in figure 13.1, where the track fitter is excluded from the chain, and the hit buffer output goes directly to L2. As we will see in section 13.1.3, this is needed in order to determine the SVT fitting constants.

- Track fitting mode: this is the normal working configuration for SVT, with the track fitter output of all wedges merged together and sent to the L2 decision crate.

Due to timing constraints and various difficulties, we were not able to include the TF in the commissioning run. SVT ran most of the time in the *track alignment mode*. Notwithstanding this, we were able to produce very appealing results.

13.1.3 The SVT Alignment

Every times that some geometrical change occur in the detector, the set of patterns and constants (see sections 4.3.1 on page 56 and 4.3.2 on page 57) of SVT should in principle be generated. This is certainly true at the beginning of a new run, with an unknown detector geometry and beam position.
In the following sections we generally will call *alignment* the set of procedures needed to build a set of patterns (for the pattern recognition stage) and constants (for the track fitting stage) consistent with the hardware geometry and including misalignment effects. The engineering run setup didn't gave us the opportunity of performing a feedback from SVT on the beam position, we thus had to perform a beam position measurement and correction of the track parameters at a later stage of data analysis (beam alignment).
In the next subsections we will detail the algorithms used, both for the generation of patterns and constants (*detector alignment*) and for the track parameters correction due to the randomly positioned beam (*beam alignment*).

13.1.3.1 Detector Alignment

Track identification and beam profile measurement in SVT was possible independently from any offline reconstruction of the Silicon VerteX segments thanks to the Principal Component Analysis algorithm described earlier (see sections 4.3.1 and 4.3.2). In fact the core of this algorithm is a "bootstrap procedure" which consists

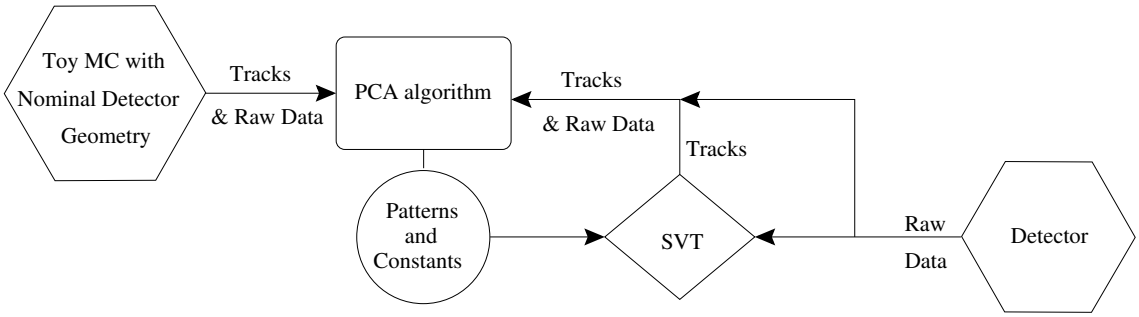

Figure 13.2: The iterative algorithm applied for the generation of patterns and constants in SVT starting from the nominal detector geometry.

in starting from a training sample of raw detector data generated with a toy Montecarlo simulating the nominal detector geometry (see figure 13.2). This sample is used to apply the PCA and extract a first set of constants (defining both the constraints and the track parameters) and patterns available for each wedge. The patterns are chosen to have wide roads[1] (in order to compensate the uncertainty on the real detector geometry) but low efficiency (this is the price we have to pay since the size of the pattern set is defined once for all by the SVT hardware).
This set of patterns and constants is loaded into SVT and thus used to identify real detector tracks. This new set of tracks is used in a new iteration of the PCA algorithm which produces a more realistic set of constants and patterns.
The last stage of the algorithm can in principle be repeated in order to obtain better constants and patterns. In the case of the engineering run a single iteration of the machinery was sufficient to produce a good quality set of parameters.
In practice, the TF section of SVT was not included in the engineering run most of the time. This means that most of the algorithm described in 13.2 was implemented via software.
Two different implementations of the SVT algorithm were used in the production of the final SVT tracks: the earlier available produced SVX segments without using the COT information. Later on we were able to use also the offline COT track and try the PCA analysis on real data.

The detailed structure of the algorithm used is reported in figure 13.3. An AC++ program dumps offline quality COT tracks and SVT road-hit sets into ASCII files. Tracks and roads are then combined in all possible pairs and fed to the linear fitter, initially loaded with nominal constants. The PCA algorithm is then re-applied to the set of tracks identified and produces the "aligned" constants. These constants can be applied to the oncoming segments and roads in order to obtain the final set of SVT tracks.
In the case of sole SVX segments, the COT dump and the track-road combination stages are excluded, with roads and SVT road-hit data flowing directly to the linear fitting stage.

[1] See section 4.3.1

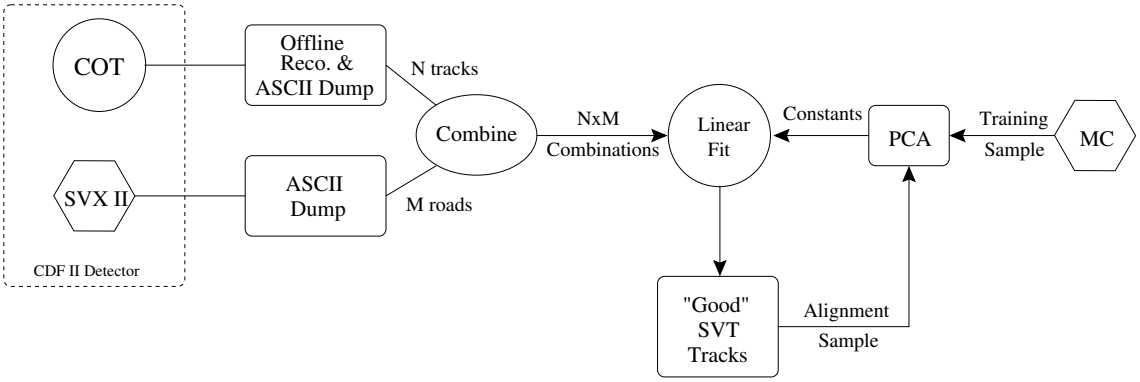

Figure 13.3: The algorithm used for the generation of patterns and constants in SVT starting from the nominal detector geometry.

13.1.3.2 Beam Alignment

As previously stated, no beam steering was done during the commissioning run. For this reason we have to perform beam position correction for the track parameters produced by the SVT fitting algorithm. This procedure is performed with a simultaneous unbinned fit to the d_0, ϕ_0, z_0 distribution of the observed tracks, where z_0 is the z coordinate as measured by the COT alone. This distribution is expected to follow the law $d_0 = d_0^{true} + (x_{bea} + z_0\, x_{slope})\, Sin\,(\phi_0) - (y_{bea} + z_0\, y_{slope})\, Cos\,(\phi_0)$ when d_0, ϕ_0 are measured with respect to the nominal detector axis ($x_0 = y_0 = 0$) while the beam is displaced by x_{bea}, y_{bea} at $z = 0$ with a tilt of x_{slope} in the x direction and of y_{slope} in the y direction.

13.2 First Tracks

Two different track reconstruction algorithms have been used during the commissioning run:

- **Standalone SVX tracking**: this method consists in applying the SVT algorithm to the SVX data alone: removing COT information (due to the lack of XFT interfacing) means that the number of measured parameters decreases from 6 (4 SVX hits+2 COT parameters) down to 4 (SVX hit coordinates on layers 0,1,2 and 4 were used)

- **SVX+COT tracking**: using the offline measured COT track parameters we were able to feed SVT with both COT and SVX information, thus testing the performance of the SVT algorithm in its native environment

The most detailed studies have been performed on data coming from a single wedge (SVX wedge 2), with these two different strategies. The next sections will detail the results obtained.

Parameter	v_1	v_2	v_3	v_4	c
f_1	3328.21	-7622.2	5411.43	-1241.6	-231.18
	w_1	w_2	w_3	w_4	b
d_0	-2.50041	0.29527	1.88430	-0.66608	-0.10942
ϕ_0	-0.65938	0.23805	0.72942	-0.30549	0.85797
c	0.080774	-0.041188	-0.101974	0.062201	-0.109425

Table 13.1: Fit parameters (d_0, c, ϕ_0) and constraint (f_1) coefficients for the nominal detector geometry with standalone SVX II tracking. The coefficient names are consistent with the ones used in section 4.3.2 (page 57 and ff.).

13.2.1 Standalone SVX II Tracking with SVT

Having 4 input coordinates instead of 6 means that the number of fit constraints goes from 3 (6 coordinates-3 track parameters=3 constraints) down to 1 (4 coordinates-3 track parameters=1 constraint).
Using a detector simulation based on the nominal detector geometry and including multiple scattering effects, we end up with the set of constants reported in table 13.1 Having only one constraint of course reduces the discriminating power of the pattern recognition, thus allowing a larger number of fake hit combinations being identified as real tracks. Despite this and the hostile environment in which SVT was running (don't forget that also the quality of the silicon detector was rather poor), the quality of the parameters measured by SVT looks incredibly good.
Figure 13.4 reports the distribution of the fit constraint f_1 calculated with the constants of table 13.1. This figure very well describes the situation: we are clearly able to identify physical tracks and isolate them from the unphysical background at a certain level. Choosing tracks for which f_1 sits in the range $[-80, 80]$ we clearly clean up the sample from the combinatorial hit background.

Given the limited power of this reconstruction due to the lack of COT information, performing the whole alignment iteration is not very significant. In fact, the only quantity affected by such a procedure is the constraint reported in figure 13.4 which already looks fairly well aligned.

We thus decide to stick on the nominal quantities and look at the measured track parameters.

Since no COT information is used, no easy reference information is available for the track parameters measured by this version of the SVT algorithm.

The most significant distribution is probably that of the measured impact parameter as a function of the azimuthal angle ϕ_0. This is reported in the top left inset of figure 13.5 after the cut on the constraint f_1. The bulk of the set of physical tracks is easily recognizable in this figure by the highest density set. The presence of beam misalignment reflects onto a sinusoidal dependency of the impact parameter on ϕ_0 which yields also information on the beam position in the transverse plane. After beam position fit and subtraction we obtain the impact parameter reported in the lower left inset of the same figure, where now d_0 is, as expected, independent from ϕ_0. The beam position and slope are mea-

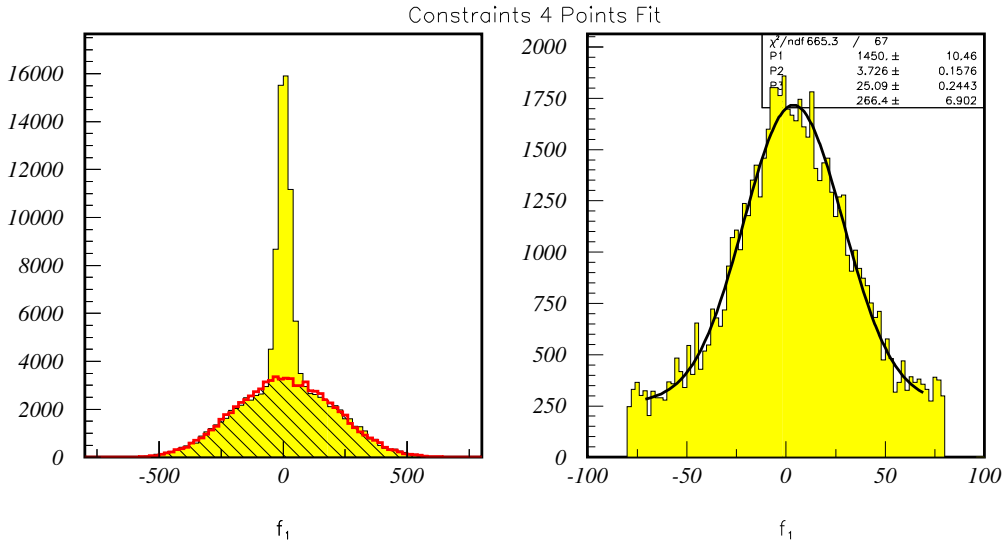

Figure 13.4: Left: distribution of the value of the fitting constraint f_1 from the data coming from the SVT wedge corresponding to SVX wedge 2 during the commissioning run. The linearization constants are the ones reported in table 13.1. The wider histogram superimposed corresponds to the distribution of f_1 values for random hit combinations within a road. Right Gaussian+constant fit to the previous distribution, zoomed in.

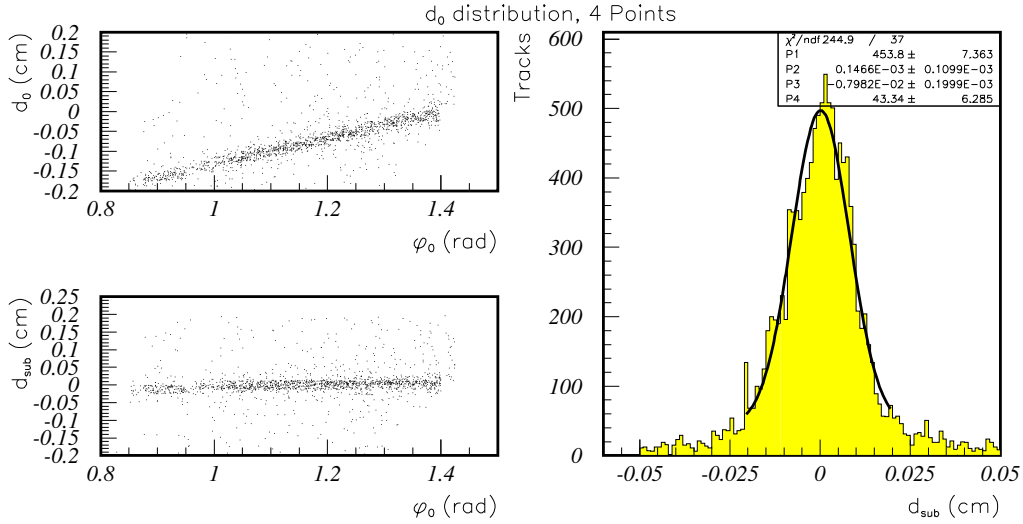

Figure 13.5: Track parameters for the commissioning run data of wedge 2. The parameters are calculated using only silicon data. Top left: measured impact parameter (cm) vs the azimuthal angle ϕ_0 (rad). Bottom left: same distribution as the top left plot but after beam alignment. Right: impact parameter distribution after beam subtraction.

sured with a fit on the (d_0, ϕ_0, z_0) distribution of the expected dependency $d_0 = d_0^{true} + (x_{bea} + z_0\, x_{slope})\, Sin\,(\phi_0) - (y_{bea} + z_0\, y_{slope})\, Cos\,(\phi_0)$ to the sample. The resulting beam parameters are:

x_{beam} at $z_0 = 0$	$0.0473\, cm$
beam slope along x	$-0.4058\, mrad$
y_{beam} at $z_0 = 0$	$0.3087\, cm$
beam slope along y	$-0.5742\, mrad$

The width of the impact parameter distribution after beam alignment is reported in the right plot of figure 13.5: in the Gaussian approximation of the central peak, the d_0 width is about $80\,\mu m$. This is much larger than the expected $\approx 45\,\mu m$, but we must bear in mind that this measurement is performed without the full detector information the SVT algorithm needs.

13.2.2 Full COT+SVX II Tracking with SVT

The results obtained on-the-fly from the SVT hardware were very encouraging. The next step in our strategy is then that of testing the full SVT algorithm together with the alignment procedures. The best strategy is that of somehow faking the XFT information with something roughly equivalent: the offline COT tracks. We thus fed the SVT with the commissioning run raw data and fake XFT information extracted from the offline fit. This procedure fully exercises the SVT algorithm and allows improvements on the track measurements.
First of all, given that we have now 6 parameters for each track, we expect to have 3 independent fit constraints. After iterating the alignment procedure once, we obtain the constraints distributions detailed in figure 13.6. The top series of 3 histograms reports the distributions for constraints $f1, f2$ and $f3$ after detector alignment. The set of physical tracks is easily distinguishable from the underlying bulk of random background combinations. The bottom series of histograms reports a zoom in of the top distributions, with the details of a Gaussian signal+constant background fit. Table 13.2 reports the fitting constants obtained after detector alignment. The resulting power in terms of pattern recognition and parameters resolution is what we want to analyze now.
Let's start from the pattern recognition: in the case of wedge 2 we start with an initial sample of 16072 silicon hit combinations at the track fitting level. Figure 13.6 shows the constraint distributions for the above silicon hit combinations paired with each COT track in the event. The constraint distribution suggests that we can safely cut on the 3 constraints requiring physical tracks to sit in the region $(f_1, f_2, f_3) \in [-12, 12] \times [-120, 120] \times [-150, 150]$ which yields 6767 tracks. This is equivalent, but more accurate, to a cut on the 6 d.o.f. χ^2 at $\approx 97\%$. So the second stage of the pattern recognition (pattern matching is already performed on this sample) yields a $3\times$ clean-up in terms of fake tracks due to pure combinatorics.

For what concerns intrinsic track parameters fit, figure 13.7 reports the difference between input (COT) and measured track curvature and azimuthal angle ϕ_0.

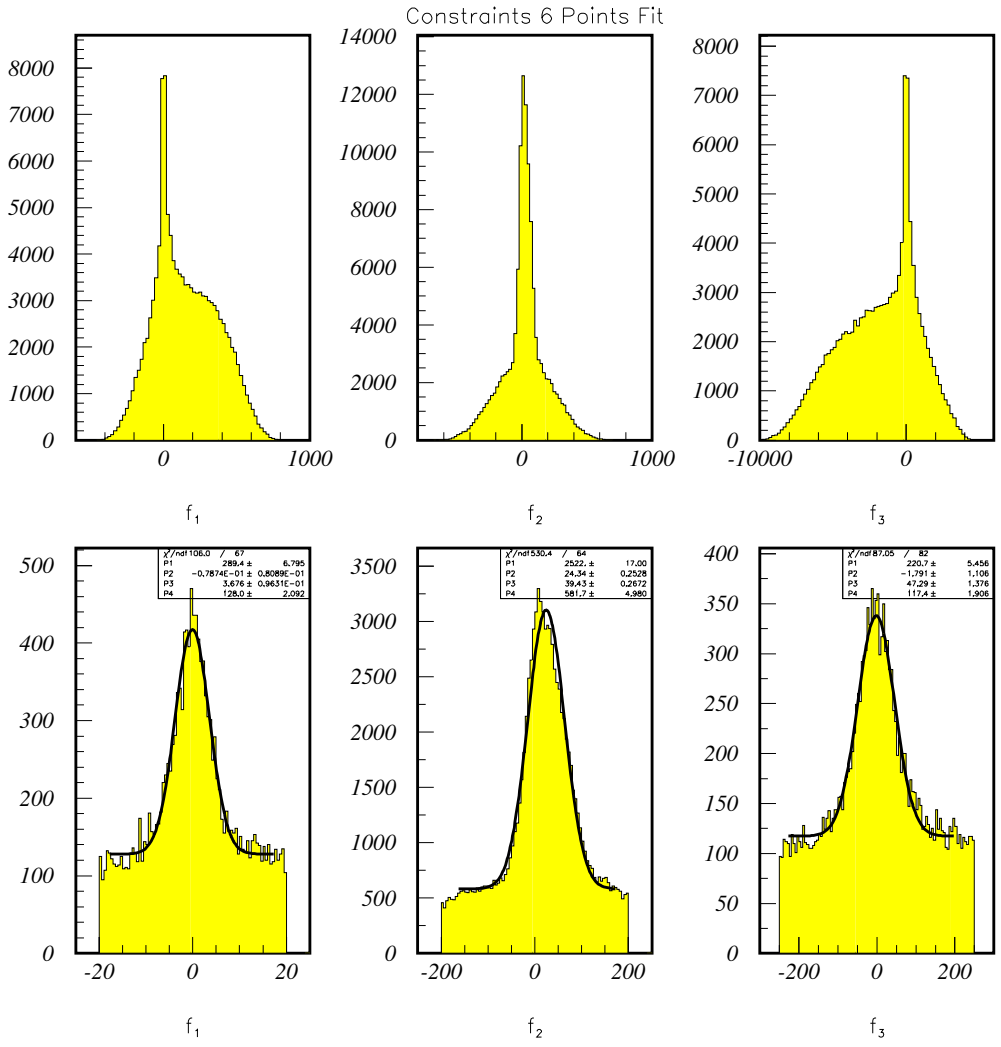

Figure 13.6: Constraints distributions in the SVX+COT analysis: the top row reports the full constraints ($f1, f2$ and $f3$) distributions. The bottom row reports the same distributions zoomed in the region about 0, with a fit in the hypothesis of Gaussian signal plus constant background: $p_4 + p_0 \cdot e^{-\left(\frac{x-p_1}{2p_2}\right)^2}$.

Par.	v_1	v_2	v_3	v_4	v_5	v_6	c
f_1	-386.8	204.05	666.9	-467.15	9942.6	539.2	-483.9
f_2	3854.3	-7740.0	4917.4	1022.3	-73.071	74.12	-281.45
f_3	-4588.8	1366.1	5376.6	-2234.9	-316.24	-6563.15	+5613.7
	w_1	w_2	w_3	w_4	w_5	w_6	b
d_0	0.96657	0.45496	-0.080964	-0.3535	13.446	-0.65023	.64869
ϕ_0	-0.075371	-0.0076263	0.051868	0.031256	-2.6857	0.55754	0.38268
c	0.0035062	-0.0028042	-0.005685	0.0049685	0.86759	-0.010826	0.009487

Table 13.2: Fit parameters (d_0, c, ϕ_0) and constraints (f_1, f_2, f_3) coefficients for SVX II+COT tracking. The former are those corresponding to the nominal detector geometry, while the latter are calculated iterating the alignment procedure. The coefficient names are consistent with the ones used in section 4.3.2 (page 57 and ff.).

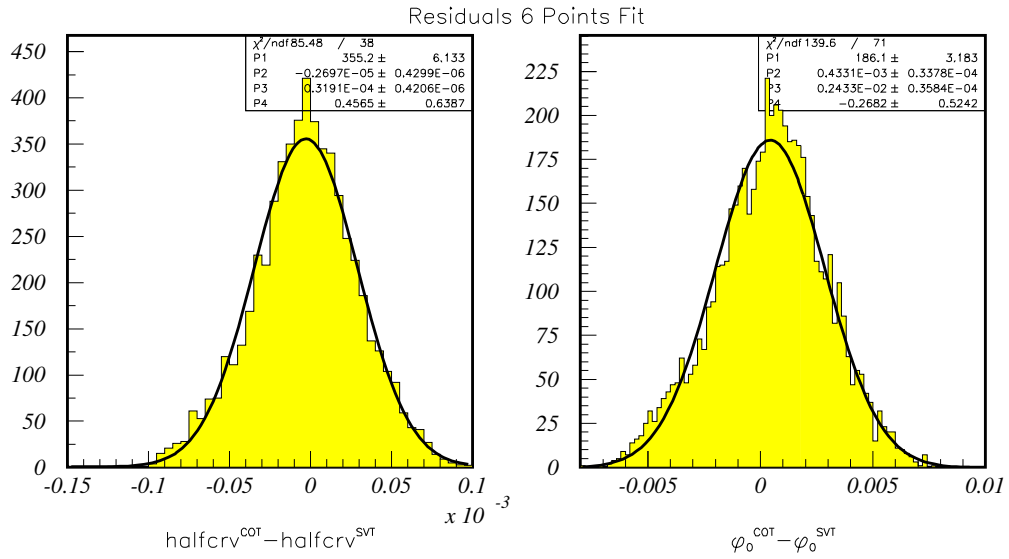

Figure 13.7: Difference between the COT and SVT measurements of the tracks curvature (left) and ϕ_0 (right).

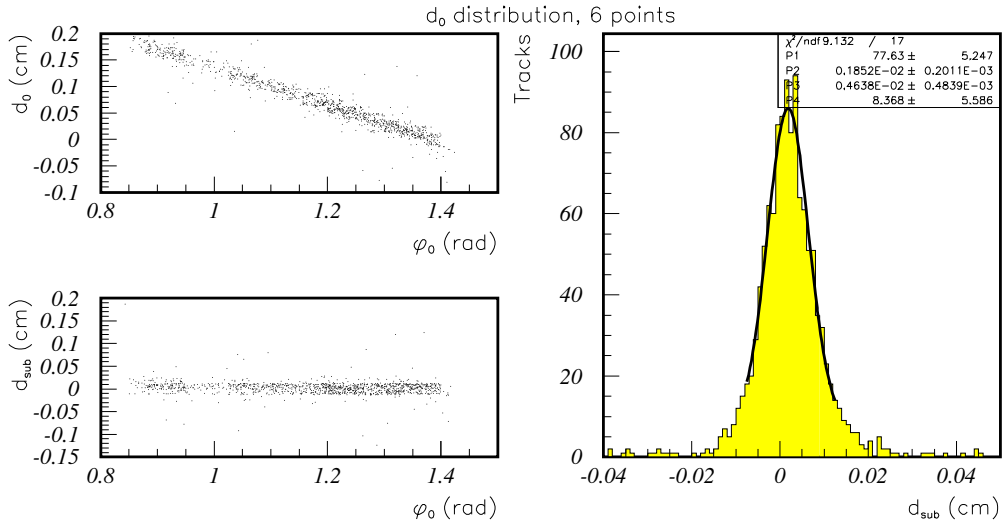

Figure 13.8: Impact parameter distributions for the commissioning run data of wedge 2. The parameters are calculated using COT+SVX II data. Top left: measured impact parameter (cm) vs the azimuthal angle ϕ_0 (rad). Bottom left: same distribution as top left plot but after beam alignment. Right: impact parameter distribution after beam subtraction.

The measured widths are $2.7 \cdot 10^{-5}\,cm$ (corresponding to a P_t resolution of roughly $\frac{0.13\%}{P_t^2\,[GeV]}$) and $4.2\,mrad$. This is a rather remarkable achievement by itself: resolutions are comparable to the ones expected from the offline algorithms (see [4]).
The last performance we have to check is that on the impact parameter measurement. We thus repeat the procedure already described in the case of the SVX II standalone fit: The distribution of d_0 as a function of the azimuthal angle ϕ_0 is reported in the top left inset of figure 13.8 after the cut on the fit constraints. After beam position fit and subtraction we obtain the impact parameter reported in the lower left inset of the same figure, where now d_0 is, as expected, independent from ϕ_0. The resulting beam parameters are:

x_{beam} at $z_0 = 0$	$0.0726\,cm$
beam slope along x	$0.7764\,mrad$
y_{beam} at $z_0 = 0$	$0.3612\,cm$
beam slope along y	$1.632\,mrad$

The width of the impact parameter distribution after beam alignment is reported in the right plot of figure 13.8: in the Gaussian approximation of the central peak, the d_0 width is about $47\,\mu m$.
Given the small number of tracks per event in the commissioning run data, basically due to the lack of a suitable L1 trigger, we were not able to collect many events with more than 1 fitted SVT tracks.
The interest in those would be that track pairs allow to totally disentangle the

intrinsic beam width from the impact parameter measurement error due to finite detector resolution (see, for example, [143]).

Another interesting analysis is however possible: SVT has low but sizeable track detection efficiency also below the nominal 2 GeV/c threshold in P_t. In order to disentangle the intrinsic resolution on the beam position we thus look for track pairs disregarding their P_t value. The number of track pairs is still not enough to draw statistically significant conclusions from the method proposed in [143]. On the other hand, the intrinsic symmetric structure of SVT suggests another useful approach: we study the distribution of the (x_0, y_0) coordinates of the point of minimum distance of each charged track from the beam axis. The distribution of these points is reported in figure 13.9. The statistics of events with track pairs is small for a 2D study such the one reported in [143], but is however still enough to study the dispersion of the (x_0, y_0) coordinates.

The (x_0, y_0) distribution clearly shows two distinct eigenvectors, due to the fact that a single wedge in the silicon detector doesn't measures the two coordinates with the same accuracy. In fact, given the structure of the detector, this should be straightforward: the coordinate parallel to the detector layers is measured with better accuracy than the perpendicular one.

Transforming with a simple rotation about the z axis the (x_0, y_0) coordinates into the pair (x_0^*, y_0^*) which correspond respectively to the perpendicular and parallel direction to the silicon ladders, yields the top right distribution of figure 13.9. The resolution on those new variables is then measurable by the width of the distribution of the $\Delta x_0^*, \Delta y_0^*$ quantities, reported in the bottom left and bottom right plots of figure 13.9.

13.3 Conclusions

The SVT performance during the commissioning run was more than satisfactory. In fact, SVT was one of the devices in the best shape during the whole run. The main limitations in its operation were due to the lack of external hardware components, like the XTRP interface to SVT and the Level 2 processors. Notwithstanding the bad quality of the silicon detectors used, which were chosen among the ones rejected for the construction of SVX II, SVT was able to obtain useful information out of the detector: determine detector alignment, perform internal and beam alignment and measure track parameter resolution. The performance in terms of parameter resolution was very close to the design specifications.

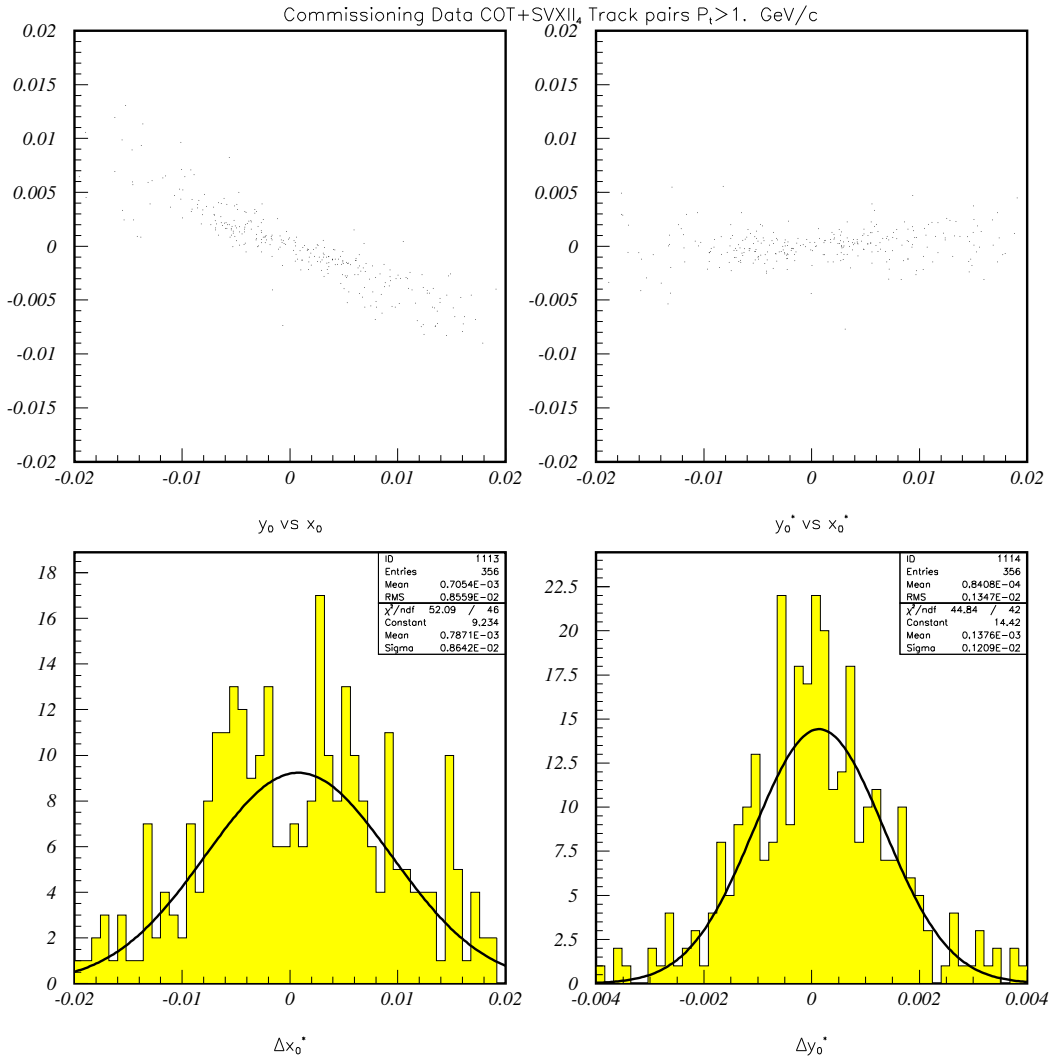

Figure 13.9: Distribution of the coordinates of the closest approach of each track to the beam axis in the transverse plane. Top Left: distribution of the closest points. Top Right: the same distribution after a rotation about the z axis of $0.4245\,rad$ (see text). The bottom histograms are the distributions of Δx_0^* (left) and Δy_0^* (right) for track pairs in the same event. The different width reflects the different resolution of the silicon detectors for the track position in the transverse plane: measurements in the ladder direction (y_0^*) are more accurate than those in any other direction, and in particular in the perpendicular one (x_0^*).

Bibliography

[1] D. Boutigny et al. BaBar technical design report. SLAC-R-0457.

[2] M. T. Cheng et al. A Study of CP violation in B meson decays: Technical design report. BELLE-TDR-3-95.

[3] The BTeV collaboration. BTeV preliminary technical design report. Technical report, FERMILAB, 1999.

[4] The CDF collaboration. CDF II technical design report. Technical report, FERMILAB, 1996. FERMILAB-Pub-96/390-E.

[5] The CDF Collaboration. Measurements of the CP-Violation Parameter $Sin\,(2\beta)$ in $B \to J/\psi K_s$ Decays. *Physical Review D*, 1999. FERMILAB-PUB-99/225-E.

[6] T. D. Lee and C. N. Yang. Question of Parity Conservation in Weak Interactions. *Phys. Rev.*, 104:254, 1956.

[7] C. S. Wu et al. Experimental test of parity conservation in beta decay. *Phys. Rev.*, 105:1413, 1957.

[8] R. Garwin et al. Observation of the Failure of Conservation of Parity and Charge conjugation in Meson Decays: The Magnetic Moment of the Free Muon. *Phys. Rev.*, 105:1415, 1957.

[9] L. Grodzins M. Goldhaber and A. W. Sunyar. Helicity of Neutrinos. *Phys. Rev.*, 117:1015, 1958.

[10] N. Cabibbo. Unitary Symmetry and Leptonic Decays. *Phys. Rev. Lett.*, 10:531, 1963.

[11] M. Kobayashi and T. Maskawa. *Progr. Theor. Phys.*, 49:652, 1973.

[12] L. Wolfenstein. Parameterization of the Kobayashi-Maskawa Matrix. *Phys. Rev. Lett.*, 51:1945, 1983.

[13] The Particle Data Group. *The Particle Data Book*. The European Physical Journal C. Springer, 1998.

[14] C. S. Lim T. Inami. *Prog. Th. Phys.*, 65:297, 1981.

[15] M. Neubert. Determination of the Weak Phase $\gamma = \arg V_{ub}^*$. In *Heavy Flavours 8, Southampton, UK*, 1999. hep-ph/9910530.

[16] I. Dunietz D. Atwood and A. Soni. *Phys. Rev. Lett.*, 78:3257, 1997.

[17] I. Dunietz. Clean CKM Information From $B_d \to D^{(*)\mp}\pi^{\pm}$. *Physics Letters B*, 427:179, 1998.

[18] I. Dunietz R. Aleksan et al. CP Violation Using non-CP Eigenstate Decays of Neutral B Mesons. *Nuclear Physics B*, 361:141, 1991.

[19] M. Gronau and D. Wyler. *Phys. Lett. B*, 265:3257, 1991.

[20] ed. P. F. Harrison and ed. H. R. Quinn. The BaBar physics book: Physics at an asymmetric B factory. Papers from Workshop on Physics at an Asymmetric B Factory (BaBar Collaboration Meeting), Rome, Italy, 11-14 Nov 1996, Princeton, NJ, 17-20 Mar 1997, Orsay, France, 16-19 Jun 1997 and Pasadena, CA, 22-24 Sep 1997.

[21] The KTeV Collaboration. Observation of Direct CP Violation in $K_{S,L} \to \pi\pi$ decays. FERMILAB-PUB-99/150-E.

[22] M. Gronau. Elimination of Penguin Contributions to CP Asymmetries in B Decays Through Isospin Analysis. *Phys. Lett. B*, 265:389, 1991.

[23] R. Fleischer. New Strategies to Extract β and γ from $B_d \to \pi^+\pi^-$ and $B_s \to K^+K^-$. CERN-TH/99-79 hep-ph/9903456, 1999.

[24] R. Fleischer. Recent Theoretical Developments in CP Violation in the B System. CERN-TH/99-242 hep-ph/9908340, 1999.

[25] R. Aleksan, B. Kayser, and D. London. In Pursuit of Gamma. DAPNIA/SPP 93-23 NSF-PT-93-4 UdeM-LPN-TH-93-184 Hep-Ph/9312338, 1993.

[26] S. Bailey and P. Maksimović. Prospects for Measuring γ With $B_s \to D_s^{\pm}K^{\mp}$. CDF/ANAL/BOTTOM/CDFR/4863.

[27] A. E. Snyder and H. R. Quinn. Measuring CP Asymmetry in $B \to \rho\pi$ without ambiguities. *Phys. Rev.*, D48:2139, 1993.

[28] I. Dunietz A. Dighe and R. Fleischer. *Eur. Phys. J.*, C6:647, 1999.

[29] R. Fleischer. *Phys. Rev.*, D60:073008, 1999.

[30] G. Sciolla et al. The BaBar drift chamber. *Nucl. Instrum. Meth.*, A419:310, 1998.

[31] I. Adam et al. DIRC, the internally reflecting ring imaging Cherenkov detector for BaBar. *IEEE Trans. Nucl. Sci.*, 45:657, 1998. hep-ex/9712001.

[32] Jochen Schwiening. DIRC, the internally reflecting ring imaging Cerenkov detector for BaBar: Properties of the quartz radiators. 1997. hep-ex/9707035.

[33] Jochen Schwiening. DIRC, a new type of particle identification system for BaBar. *Nucl. Instrum. Meth.*, A408:211, 1998. hep-ex/9712018.

[34] I. Adam et al. An internally reflecting Cherenkov detector (DIRC): Properties of the fused silica radiators. *IEEE Trans. Nucl. Sci.*, 45:450, 1998.

[35] Christophe Yeche. The DIRC, the particle identification detector of BaBar. *Nucl. Phys. Proc. Suppl.*, 75B:356–358, 1999.

[36] M. Zito. DIRC: The particle identification detector of BaBar. DAPNIA-SPP-00-07.

[37] J. Brose. BaBar CsI calorimeter design and first beam test results. *Nucl. Instrum. Meth.*, A379:495, 1996.

[38] A. Bondar. The BELLE detector. *Nucl. Instrum. Meth.*, A408:64, 1998.

[39] G. Alimonti et al. The BELLE silicon vertex detector. *Nucl. Instrum. Meth.*, A453:71–77, 2000.

[40] A. Abashian et al. The K_l/μ detector subsystem for the BELLE experiment at the KEK B-factory. *Nucl. Instrum. Meth.*, A449:112–124, 2000.

[41] N. Morgan. Resistive plate counters for the BELLE detector at KEK B. Prepared for 3rd International Workshop on Resistive Plate Chambers and Related Detectors (RPC 95), Pavia, Italy, 11- 12 Oct 1995.

[42] S. McMahon. First data from the BaBar experiment at PEP II. *Nucl. Instrum. Meth.*, A446:70, 2000.

[43] P. Grosso. BaBar: B-physics potentials and prospects. *Nucl. Instrum. Meth.*, A446:84, 2000.

[44] B. Aubert et al. Measurement of the B° meson properties using partially reconstructed $B^\circ \to D^{*-}\pi^+$ and $B^\circ \to D^{*-}\ell^+\nu_\ell$ decays with the BaBar detector. 2000. hep-ex/0008053.

[45] David G. Hitlin. First CP violation results from BaBar. 2000. hep-ex/0011024.

[46] Marie-Helene Schune. Physics results from BaBar and prospects. 2000. hep-ex/0011100.

[47] Francesca Di Lodovico. First physics results at BaBar. 2000. hep-ex/0012005.

[48] B. Aubert et al. A study of time-dependent CP-violating asymmetries in $B^\circ \to J/\psi K_s^\circ$ and $B^\circ \to \psi\,(2s)\,K_s^\circ$ decays. 2000. hep-ex/0008048.

[49] Hiroaki Aihara. A measurement of CP violation in B° meson decays with Belle. 2000.

[50] B. Aubert et al. Measurement of the branching fractions for $B^\circ \to D^{*-}\pi^+$ and $B^\circ \to D^{*-}\rho^+$. 2000. hep-ex/0008051.

[51] B. Aubert et al. Exclusive B decays to charmonium final states. 2000. hep-ex/0008050.

[52] Gerhard Raven. Measurements of inclusive and exclusive B decays to charmonium with BaBar. 2000. hep-ex/0010067.

[53] B. Aubert et al. Measurement of inclusive production of charmonium states in B meson decays. 2000. hep-ex/0008049.

[54] B. Aubert et al. Measurement of branching fractions for two body charmless B decays to charged pions and kaons at BaBar. 2000. hep-ex/0008057.

[55] B. Aubert et al. A measurement of the branching fraction of the exclusive decay $B^\circ \to K^{*\circ}\gamma$. 2000. hep-ex/0008055.

[56] B. Aubert et al. Study of inclusive $D_s^{(*)\pm}$ production in B decays and measurement of $B^\circ \to D^{*-}D_s^{(*)+}$ decays using a partial reconstruction technique. 2000. hep-ex/0008056.

[57] B. Aubert et al. Search for $B \to K^+\ell^+\ell^-$ and $B^\circ \to K^{*\circ}\ell^+\ell^-$. 2000. hep-ex/0008059.

[58] Natalia Kuznetsova. Search for $B^+ \to K\ell\ell$ and $B^\circ \to K^\circ\ell\ell$. 2000. hep-ex/0010071.

[59] Theresa J. Champion. Studies of charmless two-body, quasi-two-body and three- body B decays. 2000. hep-ex/0011018.

[60] J. Olsen. Charmless hadronic B decays at BaBar. 2000. hep-ex/0011031.

[61] Colin Jessop. First results in exclusive radiative penguin decays at BaBar. 2000. hep-ex/0011054.

[62] Gloria Vuagnin. B decays to D_s^* and D^*. 2000. hep-ex/0011096.

[63] B. Aubert et al. A measurement of the charged and neutral B meson lifetimes using fully reconstructed decays. 2000. hep-ex/0008060.

[64] Fernando Martinez-Vidal. Measurement of B° and $B^\pm$ lifetimes and $B^\circ\bar{B}^\circ$ mixing with fully reconstructed B decays in BaBar. 2000. hep-ex/0009051.

[65] Chih hsiang Cheng. B lifetime measurements with exclusively reconstructed B decays. 2000. hep-ex/0011007.

[66] B. Aubert et al. Measurement of the time dependence of $B^\circ\bar{B}^\circ$ oscillations using inclusive dilepton events. 2000. hep-ex/0008054.

[67] Shahram Rahatlou. A study of $B^\circ\bar{B}^\circ$ oscillations with full reconstructed B mesons with the BaBar detector. 2000. hep-ex/0011006.

[68] Christophe Yeche. Preliminary BaBar results on B° mixing with dileptons and on lifetime with partially reconstructed B° decays. 2000. hep-ex/0011010.

[69] B. Aubert et al. A measurement of the $B^\circ\bar{B}^\circ$ oscillation frequency and determination of flavor-tagging efficiency using semileptonic and hadronic B° decays. 2000. hep-ex/0008052.

[70] K. Abe et al. Measurement of $B^\circ_d\bar{B}^\circ_d$ mixing rate from the time evolution of dilepton events at the Upsilon(4S). 2000.

[71] The CDF II Collaboration. Proposal for the enhancement of the CDF II detector: An inner silicon layer and a time of flight. Technical report, CDF institutions, 1998. Presented to the Fermilab Director and PAC.

[72] N. Lockyer T. Gao, J. Heinrich. Universal Curves for dE/dx in Run I Using J/Ψ Dataset. CDF Note 5479, 1999.

[73] W. R. Leo. *Techniques for Nuclear and Particle Physics Experiments.* Springer, 1994.

[74] The CDF Collaboration. Measurement of $B^\circ - \bar{B}^\circ$ flavor oscillations using jet charge and lepton flavor tagging in $p\bar{p}$ collisions at $\sqrt{s} = 1.8tev$. *Physical Review D*, 60:2003, 1999. FERMILAB-PUB-99/019-E.

[75] A. Nippe M. Gronau and J. Rosner. Method for flavor tagging in neutral B meson decays. *Physical Review D*, 47:1988, 1993.

[76] The CDF Collaboration. Measurement of $B^\circ - \bar{B}^\circ$ flavor oscillation frequency and study of same side flavor tagging of b mesons in $p\bar{p}$ collisions. *Physical Review D*, 59:2001, 1998. FERMILAB-PUB-98/188-E.

[77] G. J. Feldman and Robert D. Cousins. Unified Approach to The Classical Statistical Analysis of Small Signals. *Phys. Rev. D*, 57:3873, 1998.

[78] L. Ristori M. Dell'Orso. *Nuclear Instruments & Methods A*, 278:436, 1989.

[79] S. Belforte et al. Svt technical design report. Technical report, INFN, 1996. CDF/DOC/TRIGGER/PUBLIC/3108.

[80] A. Cerri. Comparing SVT and Offline Tracking in the Quest for SVT Efficiency and Over-Efficiency. CDF/MEMO/TRIGGER/CDFR/4710.

[81] C. Bigongiari. Study of the SVT efficiency using a J/ψ data sample. CDF/DOC/TRIGGER/CDFR/4823.

[82] The CDF Collaboration. Transverse Momemntum Distributions of Charged Particles Produced in $p\bar{p}$ Collisions at $\sqrt{s} = 1.8TeV$. *Phys. Rev. Lett.*, 61:1819, 1988. CDF/PUB/MIN_BIAS/PUBLIC/0576.

[83] G. Punzi A. Cerri. Muon+Track trigger rates from full SVT simulation. CDF/DOC/TRIGGER/CDFR/5135.

[84] G. Gagliardi G. Punzi, S. Donati. A $B_d \to \pi^+\pi^-$ trigger for CDF. In *Workshop on B physics at hadron colliders, Snowmass*, June 1993. CDF Note 2358.

[85] S. Donati. Two Track Trigger With Full SVT Simulation. CDF Note 3780.

[86] J. Lewis I. Yu. Two Track Trigger for Run II and Eficiencies for B Hadronic Decays. CDF Note 4095.

[87] S. Donati G. Punzi. $B_d \to \pi^+\pi^-$ Trigger Studies With Run Ia Data. CDF Note 3167.

[88] S. Laplace A. Höcker, H. Lacker and F. Le Diberder. A new Approach to a Global Fit of the CKM Matrix. LAL 01-06, hep-ph/0104062, 2001.

[89] I. Dunietz. Clean CKM Information From $B_d \to D^{(*)\mp}\pi^{\pm}$. *Physics Letters B*, 427:179, 1998.

[90] B. Kayser and D. London. Exploring CP Violation With $B_d^\circ \to DK_s$ Decays. NSF-PT-99-5 UdeM-GPP-TH-98-47 hep-ph/9909561, 1999.

[91] I. Dunietz D. Atwood and A. Soni. *Phys. Rev. Lett.*, 78:3257, 1997.

[92] Giovanni Signorelli. Studio di Fattibilità della Misura dell'Angolo γ del Triangolo di Unitarietà a CDF. Master's thesis, Università degli Studi di Pisa, 1997/98.

[93] I. Dunietz. CP Violation With Self-Tagging B_d Modes. *Physics Letters B*, 270:75, 1991.

[94] R. Aleksan, B. Kayser, and D. London. In Pursuit of Gamma. DAPNIA/SPP 93-23 NSF-PT-93-4 UdeM-LPN-TH-93-184 Hep-Ph/9312338, 1993.

[95] M. Gronau and D. London. How To Determine all The Angles of the Unitarity Triangle From $B_d^\circ \to DK_s$ and $B_s^\circ \to D\phi$. *Phys. Lett.*, B253:483, 1991. hep-ph/9606217.

[96] A. Ali. CP Violation and Prospects at B Factories and Hadron Colliders. DESY 99-049 hep-ph/9904427, 1999.

[97] R. Fleischer. New Strategies to Extract β and γ from $B_d \to \pi^+\pi^-$ and $B_s \to K^+K^-$. CERN-TH/99-79 hep-ph/9903456, 1999.

[98] R. Fleischer. New Strategies to Extract CKM Phases From Non-Leptonic B Decays. CERN-TH/99-243 hep-ph/9908341, 1999.

[99] J. Matias R. Fleischer. Searching for New Physics in Non-Leptonic B Decays. CERN-TH/99-164 hep-ph/9906274, 1999.

[100] The CLEO Collaboration. Study of Charmless Hadronic B Decays Into the Final States $K\pi$, $\pi\pi$, and KK, with the first observation of $B \to \pi^+\pi^-$ and $B \to K^0\pi^0$. CLEO CONF 99-14.

[101] R. Fleischer. Recent Theoretical Developments in CP Violation in the B System. CERN-TH/99-242 hep-ph/9908340, 1999.

[102] M. Gronau. Elimination of Penguin Contributions to CP Asymmetries in B Decays Through Isospin Analysis. *Phys. Lett. B*, 265:389, 1991.

[103] M. Neubert. Determination of the Weak Phase $\gamma = \arg V_{ub}^*$. In *Heavy Flavours 8, Southampton, UK*, 1999. hep-ph/9910530.

[104] A. E. Snyder and H. R. Quinn. Measuring CP Asymmetry in $B \to \rho\pi$ without ambiguities. *Phys. Rev.*, D48:2139, 1993.

[105] H. R. Quinn H.J. Lipkin, Y. Nir and A. E. Snyder. *Phys. Lett.*, B265:389, 1991.

[106] T. N. Pham. CP-Violating Asymmetry in B Decays to 3 Pseudoscalar Mesons. In *QCD Euroconference 99, Montpellier*, 1999.

[107] R. Fleischer. Theoretical Aspects of CP Violation in the B System. Talk Given at the "B Physics Workshop", Fermilab, 1999, 1999.

[108] H. Quinn I. Dunietz et al. How to Extract CP Violating Asymmetries From Angular Correlations. *Phys. Rev.*, D43:2193, 1993.

[109] P.J. O'Donnel T.E. Browder, A. Datta and S. Pakvasa. Measuring β in $B \to D^{*+}D^{*-}K_s$. UH-511-930-99 UT-PT-99-08 hep-ph/9905425, 1999.

[110] I. Dunietz. On determining CKM angles α and β. In *Heavy Flavours 8, Southampton, UK*, 1999.

[111] A. Le Yaouanc J. Charles et al. *Physics Letters B*, 425(433):375(441), 1998. hep-ph/9801363.

[112] B. Kayser and D. London. B Decay CP Asymmetries, Discrete Ambiguities and New Physics. NSF-PT-99-4 UdeM-GPP-TH-98-48 hep-ph/9909560, 1999.

[113] M. Gronau. CP Violation and B Physics. SLAC-PUB-8221 hep-ph/9908343, 1999.

[114] J.L. Rosner M. Gronau. New Information on B Decays to Charmless VP Final States. TECHNION-PH-99-33 EFI 99-40 hep-ph/9909478, 1999.

[115] J.L. Rosner. CP Violation in the Standard Model. Talk Given at the "B Physics Workshop", Fermilab, 1999, 1999.

[116] B. Dutta and Sechul Oh. Charmless Hadronic B Decays and the Recent CLEO Data. hep-ph/9911263, 1999.

[117] J. L. Rosner B. Blok, M. Gronau. Annihilation, Rescattering and CP asymmetries in B Meson Decays. *Phys. Rev. Lett.*, 78:3999, 1997.

[118] X.-G. He T.E. Browder, A. Datta and S. Pakvasa. Large CP Violation in $B \to K^{(*)}X$ Decays. hep-ph/9807280, 1998.

[119] I. Dunietz and R.G. Sachs. Asymmetry Between Inclusive Charmed and Anticharmed Modes in $B^\circ, \bar{B}^\circ$ Decay as a Measure of CP Violation. *Physical Review*, 37:3186, 1987.

[120] A. Le Yaouanc R. Aleksan, M.Zito et al. Inclusive Decay of B Mesons Into D_s or D_s^*. LPT Orsay 99-36 DAPNIA/SPP 99-19 hep-ph/9906505, 1999.

[121] A. Le Yaouanc R. Aleksan, M.Zito et al. Measuring $|V_{ub}|$ With $B \to D_s^+ X_u$ Transitions. LPT Orsay 99-35 DAPNIA/SPP 99-18 hep-ph/9906504, 1999.

[122] P. Sphicas. A $b\bar{b}$ Monte Carlo Generator. CDF Note 2655, 1999.

[123] C. Peterson et al. *Physical review D*, 27:105, 1983.

[124] K. Read P. Avery and G. Trahern. Cornell Internal Note CSN-22, 1985.

[125] Todd A. Keaffaber et al. Measurement of the B Meson Differential Cross Section Using the Exclusive Decay $B \to J/\psi K$. CDF Note 4911.

[126] The CDF II Collaboration. Proposal for Enhancement of the CDF II Detector: An Inner Silicon Layer and A Time of Flight Detector. P-909, 1998.

[127] The CDF II Collaboration. Update to Proposal P-909: Physics Performance of the CDF II Detector with An Inner Silicon Layer and A Time of Flight Detector. P-909 update, 1999.

[128] F. Wuerthwein. Measuring γ to better Than 10° in Run II. CDF Note 5271.

[129] G. Signorelli. Increased L2 Trigger Efficiency for Multibody All-Hadronic B Decays. CDF Note 4970.

[130] G. Punzi G. Signorelli. Measurement of the CKM angle γ with $B^\pm \to DK^\pm$. CDF Note 4881.

[131] T. Sjostrand. *Comput. Phys. Commun*, 82:74, 1994.

[132] Giovanni Signorelli. Studio di Fattibilità della Misura dell'Angolo γ del Triangolo di Unitarietà a CDF. Master's thesis, Università degli Studi di Pisa, 1997/98.

[133] G. Signorelli. Increased L2 Trigger Efficiency for Multibody All-Hadronic B Decays. CDF Note 4970.

[134] G. Punzi G. Signorelli. Measurement of the CKM angle γ with $B^{\pm} \to DK^{\pm}$. CDF Note 4881.

[135] B. Aubert et al. Observation of CP violation in the B° meson system. 2001. hep-ex/0107013.

[136] The TDSWG. CDF Note 4718.

[137] S. Donati. Signal/Noise in $B \to \pi\pi$ samples estimated from Run Ic data. CDF Note 4212.

[138] C. Blocker M. Kirk. $B \to D\pi$ decay. CDF Note 5267.

[139] the CDF Collaboration A. Cerri. Fisica del flavor al tevatron. In *LEPTRE, XIII convegno sulla fisica al LEP*, 2001.

[140] F. Ukegawa. Looking for the $B \to Dn\pi$ Decays in the Inclusive Lepton Events. CDF Note 4212.

[141] The CDF Collaboration. Measurement of correlated $\mu - \bar{b}$ cross sections in $p\bar{p}$ collisions at $\sqrt{s} = 1.8\,TeV$. *Physical Review D*, 53:1051, 1996. FERMILAB-PUB-95/289-E.

[142] A. Semenov. Timing of AMboard. SVT internal note.

[143] L. Ristori A. Cerri, S. Donati. Measuring Beam Width and SVX Impact Parameter Resolution. CDF/MEMO/TRIGGER/CDFR/4189.